William & Mary
CHARTERED 1693

W&M ScholarWorks

Dissertations, Theses, and Masters Projects

Theses, Dissertations, & Master Projects

2000

Lamb wave diffraction tomography

Eugene V. Malyarenko
College of William & Mary - Arts & Sciences

Follow this and additional works at: https://scholarworks.wm.edu/etd

 Part of the Acoustics, Dynamics, and Controls Commons, and the Electrical and Computer Engineering Commons

Recommended Citation

Malyarenko, Eugene V., "Lamb wave diffraction tomography" (2000). *Dissertations, Theses, and Masters Projects.* Paper 1539623991.
https://dx.doi.org/doi:10.21220/s2-bsmy-8j59

This Dissertation is brought to you for free and open access by the Theses, Dissertations, & Master Projects at W&M ScholarWorks. It has been accepted for inclusion in Dissertations, Theses, and Masters Projects by an authorized administrator of W&M ScholarWorks. For more information, please contact scholarworks@wm.edu.

INFORMATION TO USERS

This manuscript has been reproduced from the microfilm master. UMI films the text directly from the original or copy submitted. Thus, some thesis and dissertation copies are in typewriter face, while others may be from any type of computer printer.

The quality of this reproduction is dependent upon the quality of the copy submitted. Broken or indistinct print, colored or poor quality illustrations and photographs, print bleedthrough, substandard margins, and improper alignment can adversely affect reproduction.

In the unlikely event that the author did not send UMI a complete manuscript and there are missing pages, these will be noted. Also, if unauthorized copyright material had to be removed, a note will indicate the deletion.

Oversize materials (e.g., maps, drawings, charts) are reproduced by sectioning the original, beginning at the upper left-hand corner and continuing from left to right in equal sections with small overlaps.

Photographs included in the original manuscript have been reproduced xerographically in this copy. Higher quality 6" x 9" black and white photographic prints are available for any photographs or illustrations appearing in this copy for an additional charge. Contact UMI directly to order.

Bell & Howell Information and Learning
300 North Zeeb Road, Ann Arbor, MI 48106-1346 USA
800-521-0600

Reproduced with permission of the copyright owner. Further reproduction prohibited without permission.

Reproduced with permission of the copyright owner. Further reproduction prohibited without permission.

Lamb Wave Diffraction Tomography

A Dissertation

Presented to The Faculty of the Department of Applied Science

The College of William and Mary

In Partial Fulfillment

Of the Requirements for the Degree of

Doctor of Philosophy

By

Eugene V. Malyarenko

October 2000

Reproduced with permission of the copyright owner. Further reproduction prohibited without permission.

UMI Number: 9999052

Copyright 2000 by
Malyarenko, Eugene Valentinovich

All rights reserved.

UMI Microform 9999052
Copyright 2001 by Bell & Howell Information and Learning Company.
All rights reserved. This microform edition is protected against
unauthorized copying under Title 17, United States Code.

Bell & Howell Information and Learning Company
300 North Zeeb Road
P.O. Box 1346
Ann Arbor, MI 48106-1346

Reproduced with permission of the copyright owner. Further reproduction prohibited without permission.

APPROVAL SHEET

This dissertation is submitted in partial fulfillment
of the requirements for the degree of

Doctor of Philosophy.

Eugene V. Malyarenko

Approved, October 2000

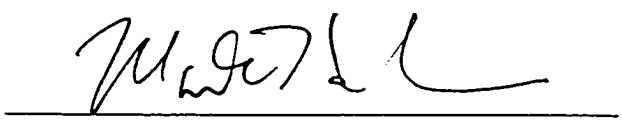

Mark Hinders

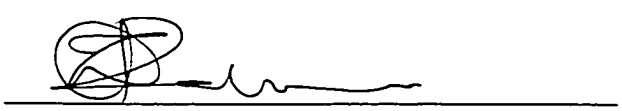

Zia-ur Rahman

(Department of Computer Science)

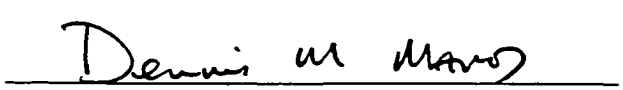

Dennis Manos

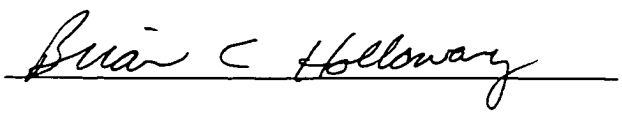

Brian Holloway

Reproduced with permission of the copyright owner. Further reproduction prohibited without permission.

Copyright

by

Eugene V. Malyarenko

2000

Reproduced with permission of the copyright owner. Further reproduction prohibited without permission.

To my family.

Reproduced with permission of the copyright owner. Further reproduction prohibited without permission.

Contents

Acknowledgments viii

List of Tables ix

List of Figures x

Abstract xviii

Chapter 1 Introduction 2

1.1 Lamb Waves 6

1.1.1 Basic theory 6

1.1.2 Excitation techniques 13

1.1.3 Application to NDE problems 20

1.2 Tomography 24

1.3 Initial state of the problem 29

1.3.1 Parallel Projection Lamb Wave Tomography 30

1.3.2 Single Projection Crosshole Lamb Wave Tomography 35

Chapter 2 Estimation of arrival times 39

2.1 Important concepts 39

2.1.1 Noise reduction issues 40

2.1.2 Estimation of arrival time in dispersive medium 42

2.2 Pattern matching techniques 55

2.3 Neural network approach 62

2.4 Time-frequency analysis 63

2.5 Wavelet transform analysis 76

2.6 Time-domain search 77

2.7 Generalized traveltime method 82

Reproduced with permission of the copyright owner. Further reproduction prohibited without permission.

2.8 Discussion 85

Chapter 3 Fan beam tomography **87**
3.1 General discussion of the method 88
3.2 Reconstruction of simulated defects 93
3.2.1 Circular array implementation 101
3.3 Practical implementation and experimental results 103
3.3.1 Adaptation to the new geometry 103
3.3.2 Data collection procedure 105
3.3.3 Discussion 135

Chapter 4 Double crosshole Lamb wave tomography **139**
4.1 The Algebraic Reconstruction Algorithm 141
4.2 Reconstruction of simulated defects 145
4.3 Double crosshole experiment 151
4.3.1 Double crosshole scanner 151
4.3.2 Experimental Results 156
4.4 Analysis of the results 167
4.5 Discussion 168

Chapter 5 Diffraction Tomography **170**
5.1 Review of the current state of Diffraction Tomography 170
5.1.1 Traveltime tomography 172
5.1.2 Non-iterative DT methods 174
5.1.3 Iterative DT methods 178
5.1.4 Performance evaluation 180
5.2 Choosing further direction 181
5.3 Ray tracing algorithms 185
5.3.1 Simulated annealing ray tracing 187
5.3.2 Discrepancy minimization ray tracing 189
5.4 Iterative image reconstruction 194
5.4.1 Curvilinear SIRT 194
5.4.2 Integrated reconstruction procedure 195
5.5 Double crosshole reconstructions 196
5.6 Reconstruction from six crosshole projections 199
5.7 Discussion 211

Reproduced with permission of the copyright owner. Further reproduction prohibited without permission.

Chapter 6 Conclusions and Future Work 214

Bibliography 222

Vita 235

Reproduced with permission of the copyright owner. Further reproduction prohibited without permission.

Acknowledgments

I am grateful to my advisor, Professor Mark Hinders for his clever guidance, encouragement and all kinds of invaluable support during my school years.

Thanks to my wife Dasha for being with me, and thanks to all our family for their permanent help, understanding and hope.

I would like to thank my committee members, Dr. Z. Rahman, Dr. D. Manos and Dr. B. Holloway for their useful comments, corrections and suggestions.

I would like to express my gratitude to Chris Domack, Jonathan Stevens and the team of Nascent Technology Solutions for their cooperation, help in building equipment, and support.

I would also like to thank my former advisor Professor I. Kucherov for forming my vision of acoustics and guided waves.

Big thanks to Jim McKeon for helping me accommodate in the lab.

Many people made this work happen. I am indebted to all of them, including Open Source, Linux and Free Software Internet communities.

Reproduced with permission of the copyright owner. Further reproduction prohibited without permission.

List of Tables

2.1 Phase delay measurement algorithm. Requires signal recording in two different locations. 52
2.2 Group delay measurement algorithm. 53
2.3 Pattern matching algorithm. 56
2.4 Adaptive pattern matching algorithm. 60
2.5 Measuring arrival time with Positive distribution 73
2.6 Time domain Group Delay measurement 79

5.1 Simulated Annealing Ray Tracing Algorithm 188
5.2 Bent ray SIRT reconstruction scheme 195

Reproduced with permission of the copyright owner. Further reproduction prohibited without permission.

List of Figures

1.1 Aloha Airlines accident: side view of the damaged aircraft. 4
1.2 Aloha Airlines accident: front view of the damaged aircraft. 4
1.3 Lamb waves in isotropic plates: isotropic plate of thickness 2d parallel to the xy-plane is placed in vacuum. The plate is infinite in both x and y directions. We are looking for waves propagating in the x-direction. 7
1.4 Phase velocity ($mm/\mu s$) dispersion curves in aluminum plates for the first three symmetric and antisymmetric modes. Phase velocity is plotted versus the product of frequency f (MHz) and plate thickness $2d$ (mm). 12
1.5 Group velocity ($mm/\mu s$) dispersion curves in aluminum plates for the first two symmetric and antisymmetric modes. Group velocity is plotted versus the product of frequency f (MHz) and plate thickness $2d$ (mm). 12
1.6 Lamb wave excitation with a method of variable incidence angle: a bulk compressional wave incident on the wedge-plate interface at angle θ creates shear and compressional transmitted waves. Their multiple reflections from plate boundaries lead to the formation of Lamb waves. Changing incidence angle θ allows for selective excitation of different modes existing at this particular frequency. 13
1.7 Three tomographic geometries used in the scope of this work. Dashed arrows indicate ray paths, curved arrows indicate sample (or source-receiver assembly) rotation after completion of the current projection. 25
1.8 Limitations of ultrasonic transmission and reflection tomography: unlike X-rays, ultrasound cannot penetrate densely packed clusters of strong scatterers. In such cases reflection tomography is more informative about the internal structure of the defect. 28

Reproduced with permission of the copyright owner. Further reproduction prohibited without permission.

1.9 Reconstruction of a 15 mm-diameter through hole in aluminum plate with parallel projection Lamb wave tomography: 18 projections, 160 steps. The size of the reconstructed area is 160 × 160mm. 31
1.10 Horizontal profile of the image (Fig. 1.9), taken at half-height, and schematic hole position. 31
1.11 Reconstruction of a 25.4 mm-diameter circular flat-bottom hole in aluminum plate with parallel projection Lamb wave tomography: 18 projections, 160 steps. The size of the reconstructed area is 160 × 160mm. 32
1.12 Horizontal profile of the image (Fig. 1.11), taken at half-height, and schematic defect position. 32
1.13 Reconstruction of a 25.4 mm-diameter through hole in a stitched graphite-epoxy composite plate with parallel projection Lamb wave tomography: 18 projections, 160 steps. The size of the reconstructed area is 160 × 160mm. 33
1.14 Reconstruction of an impact damage in a stitched graphite-epoxy composite plate with parallel projection Lamb wave tomography: 18 projections, 160 steps. The size of the reconstructed area is 160 × 160mm. 33
1.15 Reconstruction of a 25.4 mm-diameter through hole in aluminum plate with a single projection crosshole Lamb wave tomography: 40 × 40 steps, step size = 5mm. The size of the reconstructed area is 200×200mm. 36
1.16 Horizontal profile of the image (Fig. 1.15), taken at half-hight, and schematic hole position. 36
1.17 Reconstruction of a 25.4 mm-diameter circular flat-bottom hole in aluminum plate with parallel projection Lamb wave tomography: 40 × 40 steps, step size = 5mm. The size of the reconstructed area is 200×200mm. 37
1.18 Horizontal profile of the image (Fig. 1.17), taken at half-height, and schematic defect position. 37

2.1 Raw signal typical for our experiments. Note the presence of the excitation tone burst between 0 and 10 μs due to the electrical cross-influence. 43
2.2 Band-pass filtered signal. The colored noise left in the region 10-70 μs is produced by standing waves in the finite plate. 43
2.3 Band-pass filtered signal, standing plate waves were damped with clay. 44
2.4 Tone burst reflection from the water-aluminum interface. Wave packets do not spread in this nondispersive case. Arrival time is easy to find even after multiple reflections. 45

Reproduced with permission of the copyright owner. Further reproduction prohibited without permission.

2.5 Lamb waves: Rectangular envelope of the original tone burst spreads due to dispersion. The arrival time problem is no longer straightforward. 45
2.6 Typical tone burst used for Lamb wave excitation. Carrier frequency – 1.2 MHz, number of cycles – 13. 49
2.7 Typical tone burst used for Lamb wave excitation. Carrier frequency – 1.2 MHz, number of cycles – 5. 49
2.8 Fourier power spectra of two tone bursts of different duration (Figs 2.6 and 2.6). Bandwidth can be effectively controlled by changing the number of cycles in the tone burst. 50
2.9 Theoretical arrival times of the S_0 mode in a defect-free aluminum plate. To generate this pattern the source-receiver distance was changed the same way as in our crosshole scanner. 54
2.10 Typical shape of the leading edge of the fastest mode. It is difficult to accurately find the beginning of the wave packet. 57
2.11 Arrival times in a defect-free aluminum plate, obtained with adaptive pattern matching method. Comparison with theoretical times (Fig. 2.9) yields MS error $\delta_{ms} = 2.74$. 61
2.12 Arrival times in aluminum plate with 25.4 mm-diameter flat-bottom hole in the center, obtained with adaptive pattern matching method. 61
2.13 (a) – Wigner transform of the signal (c). The power spectrum is shown in (b). The Wigner distribution was computed according to (2.11), note severe artifacts at frequencies above the carrier frequency (peak frequency on the power spectrum (b)). 68
2.14 (a) – custom positive transform of the signal (c). The power spectrum is shown in (b). The time frequency distribution is based on the equation (2.16), note the absence of artifacts on the image. 72
2.15 Arrival times in a defect-free aluminum plate obtained with a time-frequency algorithm based on a positive distribution (2.16). Comparison with theoretical times (Fig. 2.9) yields MS error $\delta_{ms} = 2.188$. . . 74
2.16 Arrival times in aluminum plate with 25.4 mm-diameter flat-bottom hole in the center obtained with a time-frequency algorithm based on a custom positive distribution. 74
2.17 Arrival times in a defect-free aluminum plate obtained with a time-domain group delay measurement algorithm (Table 2.6). Comparison with theoretical times (Fig. 2.9) yields MS error $\delta_{ms} = 0.213$. 80

Reproduced with permission of the copyright owner. Further reproduction prohibited without permission.

2.18 Arrival times in aluminum plate with 25.4 mm-diameter flat-bottom hole in the center obtained with a time-domain group delay measurement algorithm. The defect shows up as a slowdown on the bottom line $t = 52\mu s$ around the ray 800. 80
2.19 Arrival times in a defect-free aluminum plate obtained with a method of generalized traveltimes. Comparison with theoretical times (Fig. 2.9) yields MS error $\delta_{ms} = 7.625$. 84
2.20 Arrival times in aluminum plate with 25.4 mm-diameter flat-bottom hole in the center obtained with a method of generalized traveltimes. 84

3.1 The Fan Beam geometry: M - geometrical center of the system; O - transmitter; $\pm\gamma_m$ - range of the fan beam; $\delta\gamma$ - angular distance between receivers; α - current projection angle; γ - current receiver angle. 89
3.2 Illustration of the fan beam reconstruction algorithm: α - current projection angle; image point P with coordinates (x, y); γ' - angle between the central ray OM and the direction on the point P being reconstructed. 91
3.3 Area coverage of the circular fan beam geometry: $\pm\gamma_m$ – fan beam opening angle; R – radius of the perimeter transducer array; r – radius of the most densely covered area where all fan beams intersect. 95
3.4 Dependence of the size of the reconstructed image on the fan beam opening angle: r – radius of the best-covered area; R – radius of the circular perimeter array of transducers; square - region displayed on the image. 96
3.5 Simulated ellipse reconstruction from fan beam projections with convolution-backprojection algorithm: 64 projections, 101 ray, padding with maximum. Note the artifacts and blurring. 98
3.6 Simulated ellipse reconstruction from fan beam projections with convolution-backprojection algorithm: 64 projections, 101 ray, padding with zeroes. 98
3.7 Simulated ellipse reconstructions from fan beam projections with convolution-backprojection algorithm: 16 projections. Resolution increases with the number of rays per projection. 99
3.8 Simulated ellipse reconstructions from fan beam projections with convolution-backprojection algorithm: 32 projections. Resolution increases with the number of rays per projection. 99

Reproduced with permission of the copyright owner. Further reproduction prohibited without permission.

3.9 Simulated ellipse reconstructions from fan beam projections with convolution-backprojection algorithm: 64 projections.Resolution increases with the number of rays per projection. 100
3.10 Simulated ellipse reconstructions from fan beam projections with convolution-backprojection algorithm: 128 projections. Resolution increases with the number of rays per projection. 100
3.11 Adapting fan beam geometry to a circular perimeter array of transducers: original configuration is described in terms of γ and $\delta\gamma$; new configuration uses ϵ and $\delta\epsilon$; note that $\delta\epsilon = 2\delta\gamma$. 102
3.12 Ray length calculation for the experimental fan beam geometry. . . . 104
3.13 Transducers with cone-shaped delay lines used for Lamb wave excitation at various frequencies. From left to right: 100 KHz $ValpeyFisher^{TM}$ transducer; 1.0 MHz and 2.25 MHz $Panametrics^{TM}$ transducers. . . 106
3.14 Schematic of the fan beam scanner. 107
3.15 Photo of the fan beam scanner in $W\&M$ NDE lab. 108
3.16 Fan beam measurement setup with P_2L_2. T and R are transmitting and receiving transducers. 110
3.17 P_2L_2 calibration plot. 112
3.18 Parabolic trends on velocity data obtained with P_2L_2. 114
3.19 Fan beam setup for P_2L_2 spike position measurement. 116
3.20 Comparison of projection data for defect-free aluminum plate and for a plate with 25.4 mm-diameter flat-bottom hole. Data represent position of the P_2L_2 spike in a fan beam tomographic experiment. 117
3.21 Residual parabolic trends on velocity data obtained with P_2L_2 spike position measurement. Velocities were computed from the arrival times in Fig. 3.20 118
3.22 Difference plot obtained as a result of subtraction of the plots in Fig. 3.21. Central hump represents the defect. Note the artifacts on both sides of the image. 120
3.23 Fan beam setup in waveform capture mode. 121
3.24 Software-extracted raw arrival times in aluminum plate with 25.4 mm-diameter flat-bottom hole. 125
3.25 Software-extracted raw arrival times in aluminum plate with five 15 mm-diameter through holes. 126
3.26 Raw velocities in aluminum plate with 25.4 mm-diameter flat-bottom hole. Velocities were calculated from the arrival times in Fig. 3.24. . . 127

Reproduced with permission of the copyright owner. Further reproduction prohibited without permission.

3.27 Raw velocities in aluminum plate with five 15 mm-diameter through holes. Velocities were calculated from the arrival times in Fig. 3.25. . 128
3.28 Smoothed velocities in aluminum plate with 25.4 mm-diameter flat-bottom hole. Velocities were obtained by smoothing data in Fig. 3.26 with a moving average filter of order 10. 129
3.29 Smoothed velocities in aluminum plate with five 15 mm-diameter through holes. Velocities were obtained by smoothing data in Fig. 3.27 with a moving average filter of order 10. 130
3.30 Fan beam reconstruction of single 25.4 mm-diameter flat-bottom hole in aluminum plate from raw (unfiltered) velocity data. The radius of the artifact-free circular area is 56 mm. The reconstructed defect is unrealistically large. 131
3.31 Fan beam reconstruction of single 25.4 mm-diameter flat-bottom hole in aluminum plate from smoothed velocity data. The radius of the artifact-free circular area is 56 mm. The size of the reconstructed defect is much closer to the reality than that in Fig. 3.30. 132
3.32 Resolution of the fan beam tomography: two simulated small ellipses. 134
3.33 Resolution of the fan beam tomography: two simulated ellipses of different size. 134
3.34 Noise reduction by averaging: A typical raw signal. 136
3.35 Noise reduction by averaging: Signal from Fig. 3.34 averaged 10 times. 136

4.1 Explanation of the ART algorithm for the double crosshole geometry: a - distance between transducers; pixels (m, n) are indexed as shown; ray enumeration order (i, j) is different for different projections. . . . 140
4.2 Simulated elliptical defect reconstructions from 1,2 and 3 crosshole projections with sequential ART algorithm: 20×20 pixels. 147
4.3 Simulated elliptical defect reconstructions from 1,2 and 3 crosshole projections with sequential ART algorithm: 50×50 pixels. 147
4.4 Simulated elliptical defect reconstructions from 1,2 and 3 crosshole projections with sequential ART algorithm: 100×100 pixels. 148
4.5 Sequential ART reconstructions of two simulated elliptical defects from 1,2 and 3 crosshole projections: 20×20 pixels. 148
4.6 Sequential ART reconstructions of two simulated elliptical defects from 1,2 and 3 crosshole projections: 50×50 pixels. 149

Reproduced with permission of the copyright owner. Further reproduction prohibited without permission.

4.7 Sequential ART reconstructions of two simulated elliptical defects from 1,2 and 3 crosshole projections: 100 × 100 pixels. 149
4.8 Block diagram of the data acquisition equipment for crosshole tomography. 152
4.9 Photo of the crosshole scanner in our lab. 153
4.10 Schematic of the crosshole scanner. 154
4.11 Sequential ART reconstruction of two circular flat-bottom holes in aluminum plate. Defect diameters: 29 and 25 mm. Distance between centers: 53 mm. Image size: 200 × 200 mm. $f = 1.2$ MHz. Note the level of "salt and pepper noise" throughout the image. 157
4.12 Sequential ART reconstruction of five equally spaced 15 mm-diameter through holes in aluminum plate. Image size: 200 × 200 mm. $f = 1.2$ MHz. Note the level of "salt and pepper noise" and distorted shape of the holes near the edges. 158
4.13 Sequential ART reconstruction of a rectangular thinning region in aluminum plate. Image size: 200 × 200 mm. $f = 2.2$ MHz. Note the level of "salt and pepper noise". 159
4.14 Sequential ART reconstruction of an oblong thinning region in aluminum plate. Image size: 200 × 200 mm. $f = 1.2$ MHz. Note the level of "salt and pepper noise". 160
4.15 SIRT reconstruction of two flat bottom holes. Image size: 200 × 200 mm. 161
4.16 SIRT reconstruction of five through holes. Image size: 200 × 200 mm. 162
4.17 SIRT reconstruction of a rectangular thinning region. Image size: 200× 200 mm. 163
4.18 SIRT reconstruction of an oblong thinning region. Image size: 200×200 mm. 164
4.19 SIRT reconstruction of adhesively bonded doubler in aluminum plate, 1 iteration. Different colors indicate: red – no adhesive; green - poor bond quality, adhesive sticks to only one side; blue – good bond quality. 165
4.20 SIRT reconstruction of adhesively bonded doubler in aluminum plate, 10 iterations. Different colors indicate: red – no adhesive; green – poor bond quality, adhesive sticks to only one side; blue – good bond quality. 166

5.1 To the derivation of the local form of Snell's law. 191
5.2 Ray path and bilinear interpolation. 191

Reproduced with permission of the copyright owner. Further reproduction prohibited without permission.

5.3 Image preparation for ray tracing: smoothing with averaging mask. . 193
5.4 Typical rays traced from left (transmitters) to right (receivers) on a smoothed terrain (Fig. 5.3B). 193
5.5 Aluminum plate with two circular thinnings. Image size: 200 × 200 mm. 197
5.6 Aluminum plate with five through holes. Image size: 200 × 200 mm. . 197
5.7 Aluminum plate with oblong thinning. Image size: 200 × 200 mm. . . 197
5.8 Six possible crosshole projections. 200
5.9 Lamb wave traveltime tomography with computer plug-in boards. . . 202
5.10 Subtracting SIRT reconstruction artifacts. Image size: 200 × 200 mm. 203
5.11 Horizontal artifact profiles taken at image quarter-height. 203
5.12 Straight and bent ray reconstructions of a 25.4 mm-diameter through hole in aluminum plate. Orders of averaging masks used: B - 17; C - 11. Image size: 200 × 200 mm. 206
5.13 Horizontal profiles of images (Fig. 5.12A,B,C) taken at half-height. . 206
5.14 Straight and bent ray reconstructions of the five 15 mm-diameter through holes in aluminum plate. Orders of averaging masks used: B - 17; C - 11. Image size: 200 × 200 mm. 208
5.15 Horizontal profiles of images (Fig. 5.14A,B,C) taken at half-height. . 208
5.16 Straight and bent ray reconstructions of an oblong 25x100 mm thinning region in aluminum plate. Orders of averaging masks used: B - 17; C - 11. Image size: 200 × 200 mm. 209
5.17 Horizontal profiles of images (Fig. 5.16A,B,C) taken at half-height. . 209
5.18 Straight and bent ray reconstructions of two simulated corrosion pits in aluminum plate with 23 shallow holes in each. Image size: 200 × 200 mm. 213

Reproduced with permission of the copyright owner. Further reproduction prohibited without permission.

Abstract

As the worldwide aviation fleet continues to age, methods for accurately predicting the presence of structural flaws, such as hidden corrosion and disbonds, that compromise airworthiness become increasingly necessary. Ultrasonic guided waves, Lamb waves, allow large sections of aircraft structures to be rapidly inspected. However, extracting quantitative information from Lamb wave data has always involved highly trained personnel with a detailed knowledge of mechanical waveguide physics. In addition, human inspection process tends to be highly subjective, slow and prone to errors. The only practical alternative to traditional inspection routine is a software expert system capable of interpreting data with minimum error and maximum speed and reliability. Such a system would use the laws of guided wave propagation and material parameters to help signal processing algorithms automatically extract information from digitized waveforms. This work discusses several practical approaches to building such an expert system.

The next step in the inspection process is data interpretation, and imaging is the most natural way to represent two-dimensional structures. Unlike conventional ultrasonic C-scan imaging that requires access to the whole inspected area, tomographic algorithms work with data collected over the perimeter of the sample. Combined with the ability of Lamb waves to travel over large distances, tomography becomes the method of choice for solving NDE problems. This work explores different tomographic reconstruction techniques to graphically represent the Lamb wave data in quantitative maps that can be easily interpreted by technicians. Because the velocity of Lamb waves depends on the thickness, the traveltimes of the fundamental modes can be converted into a thickness map of the inspected region. Lamb waves cannot penetrate through holes and other strongly scattering defects and the assumption of straight wave paths, essential for many tomographic algorithms, fails. Diffraction tomography is a way to incorporate scattering effects into tomographic algorithms in order to improve image quality and resolution. This work describes the iterative reconstruction procedure developed for the Lamb Wave tomography and allowing for ray bending correction for imaging of moderately scattering objects.

Reproduced with permission of the copyright owner. Further reproduction prohibited without permission.

Lamb Wave Diffraction Tomography

Reproduced with permission of the copyright owner. Further reproduction prohibited without permission.

Chapter 1

Introduction

On April 28, 1988, a Boeing 737-200, operated by Aloha Airlines Inc., experienced an explosive decompression and structural failure at 24,000 feet, while en route from Hilo to Honolulu, Hawaii [1]. Approximately 18 feet from the cabin skin and structure aft of the cabin entrance door and above the passenger floor line separated from the airplane during flight (Figures 1.1,1.2). One flight attendant was swept overboard during the decompression and is presumed to have been fatally injured; 7 passengers and 1 flight attendant received serious injuries. As a result of the accident, the airplane was determined to be damaged beyond repair. It was dismantled and sold for parts and scrap.

The National Transportation Safety Board determined that the probable cause of this accident was the failure of the Aloha Airlines maintenance program to detect the presence of significant disbonding and fatigue damage which ultimately led to to the failure of the lap joint at S-10L and the separation of the fuselage upper lobe.

The Safety Board emphasized the great importance of encouraging further

Reproduced with permission of the copyright owner. Further reproduction prohibited without permission.

research into improved corrosion detection and prevention methods.

Many areas of aircraft are difficult to inspect for corrosion. Within lap joints, for example, the corrosion can go undetected until it is so severe that the damage is visible from the condition of the outer skin. None of the various NDT inspection methods have proved universally effective. The Safety Board recommended the Federal Aviation Administration to challenge NDT equipment manufacturers with the specific needs for the aviation industry in order to develop improved, economical, state-of-the-art equipment, and to employ methods which minimize human performance inadequacies.

Inspection of plate-like metal structures is becoming one of the most important industrial issues. Built decades ago, military and civil aircraft, ships, waste storage reservoirs and railway tank cars, have been subjected to in-service stresses and harsh environmental conditions. Such long exposure inevitably leads to various kinds of structural damage, including corrosion, cracks, delaminations, fatigue etc. Different defects grow with different speeds and reach their critical states in different time periods. In order to reveal potential threats, periodic inspections should be scheduled, tailored for the particular application. Ultrasonic NDE is often an appropriate inspection method.

The most common ultrasonic inspection routine uses point measurements in a pulse-echo or through-transmission mode to estimate variations of plate properties with depth at a given location (Krautkramer [2]). This technique uses longitudinal and/or shear bulk waves and can get very high thickness resolution at high frequencies. For large areas, however, the ultrasonic transducer must be scanned over the entire

Reproduced with permission of the copyright owner. Further reproduction prohibited without permission.

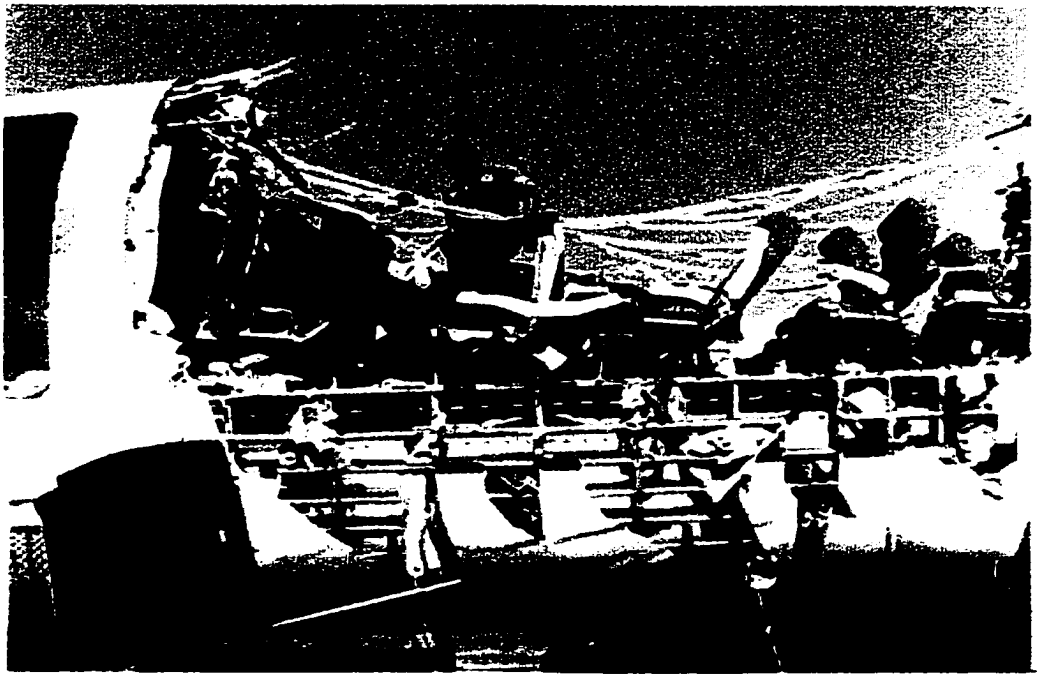

Figure 1.1: Aloha Airlines accident: side view of the damaged aircraft.

Figure 1.2: Aloha Airlines accident: front view of the damaged aircraft.

Reproduced with permission of the copyright owner. Further reproduction prohibited without permission.

region to map the structure. This conventional method, while very effective for small custom-built parts with complicated surfaces, becomes rather time-consuming and mechanically cumbersome for field inspection of large simple structures. To save time, inspection is carried out at randomly chosen spots of the surface, thus increasing the probability of missing a flaw.

This work concentrates on development of an alternative ultrasonic inspection technique which is optimized for large areas and capable of assessing their surface quality quickly and efficiently. This technique makes use of ultrasonic Lamb waves propagating along the plate for large distances and having properties which are very different from the properties of bulk waves.

This thesis is organized as follows:

- The first section of the Introduction covers the basic theory of lamb Waves in isotropic plates and various methods of excitation and detection. The second section introduces main concepts of tomography and briefly discusses various tomographic techniques. The third section describes the early results obtained with the Parallel Projection and the Single Crosshole Lamb wave tomographic techniques established by McKeon and Hinders before this work began.

- The second chapter discusses the construction of an accurate time delay estimation algorithm for Lamb Waves. The first section analyzes the signals, typically encountered in Lamb wave propagation experiments, explains the detection and noise reduction methods, and examines the issues associated with accurate velocity measurement of wave packets traveling in dispersive media. The other sections concentrate on particular approaches to the problem of arrival time

Reproduced with permission of the copyright owner. Further reproduction prohibited without permission.

extraction.

- Chapters 4 and 5 describe our work on the Fan Beam and Double Crosshole Lamb Wave tomography based on the straight-ray approximation. Both chapters contain theoretical, simulation, and experimental sections, as well as detailed analysis of the results and comparisons to other tomographic techniques.

- Chapter 5 concentrates on diffraction tomography. It begins with extensive review of the existing literature on the subject in order to identify approaches, applicable to Lamb wave tomography. In the later sections we describe our ray tracing routines and the iterative image reconstruction algorithm. The chapter concludes with analysis of experimental results and evaluation of practical merits of the newly developed method.

- The results for this thesis and the directions of further development are summarized in the Conclusions chapter.

1.1 Lamb Waves

1.1.1 Basic theory

The behavior of Lamb waves has been studied extensively by many authors since their first description by Lamb in 1917. A comprehensive review of the literature devoted to the Lamb wave propagation issues was written by McKeon [3]. The main mathematical approaches to the solution of Lamb wave problems together with the most general results and conclusions are summarized in several well known trea-

Reproduced with permission of the copyright owner. Further reproduction prohibited without permission.

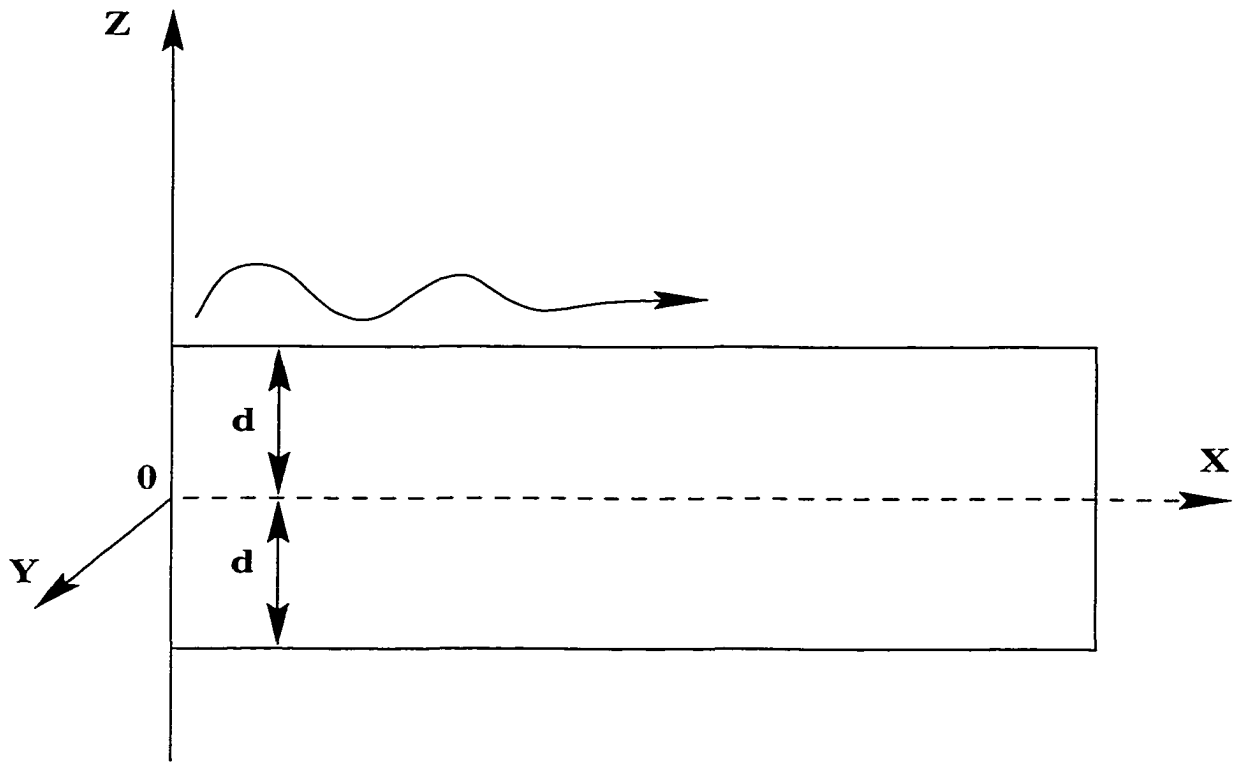

Figure 1.3: Lamb waves in isotropic plates: isotropic plate of thickness 2d parallel to the xy-plane is placed in vacuum. The plate is infinite in both x and y directions. We are looking for waves propagating in the x-direction.

Reproduced with permission of the copyright owner. Further reproduction prohibited without permission.

tises on wave propagation theory written by Viktorov [4], Achenbach [5], Graff [6], Brekhovskikh [7], Grinchenko [8], Rose [9], Auld [10] and others.

Below we briefly discuss the simplest and the most fundamental example of the Lamb wave theory: propagation of guided ultrasonic waves in a plate with traction-free boundaries [9]. The plate (Fig. 1.3) of thickness $2d$ is infinite in both the x and y directions; its boundaries $z = \pm d$ are stress-free. The wave propagates parallel to the x-axis and its behavior is governed by the equations of the theory of linear elasticity in the absence of external forces:

$$\rho \frac{\partial^2 U_i}{\partial t^2} = \frac{\partial T_{ik}}{\partial x_k} \tag{1.1}$$

$$T_{ij} = C_{ijkl} S_{kl} \tag{1.2}$$

$$S_{kl} = \frac{1}{2}\left[\frac{\partial U_k}{\partial x_l} + \frac{\partial U_l}{\partial x_k}\right] \tag{1.3}$$

where S_{ij} and T_{ij} are the components of the strain and stress tensors, ρ is the density of the plate material, U_i are the components of the elastic displacement vector, and C_{ijkl} are the components of a fourth order tensor of elastic constants which in the most general anisotropic case can be represented by a 2-D 6×6 matrix C_{IJ}. Repeating index summation is assumed everywhere.

Upon substitution (1.1) becomes:

$$\rho \frac{\partial^2 U_i}{\partial t^2} = C_{ijkl} \frac{\partial^2 U_l}{\partial x_j \partial x_k} \tag{1.4}$$

(1.4) should be solved together with traction-free boundary conditions which can be defined as:

Reproduced with permission of the copyright owner. Further reproduction prohibited without permission.

$$T_{ij}n_j \quad = 0 \quad |_{z=\pm d} \tag{1.5}$$

where $\vec{n}$ is a unit normal to the plate surface.

For isotropic materials all elements of the reduced matrix C_{IJ} can be expressed using only two independent values λ and μ, and (1.4) reduces to three equations

$$\rho\frac{\partial^2 U_i}{\partial t^2} = \mu\frac{\partial^2 U_i}{\partial x_j^2} + (\lambda+\mu)\frac{\partial^2 U_j}{\partial x_i \partial x_j} \tag{1.6}$$

which have to be solved together with the boundary conditions (1.5). The next step in the solution utilizes the method of potentials, or the method of partial waves, or a more recent method based on carrier waves. Although the method of potentials based on a Helmholtz decomposition of the vector wave field is very popular in the literature, it can be used only for isotropic plates. The method of partial waves ([10], [9]) describes Lamb waves as a result of constructive interference between longitudinal and shear waves bouncing between free surfaces of the plate. This method is more general. It works for anisotropic media and leads more directly to wave solutions and provides more insight into the physical nature of the guided waves. Recently published approach by Achenbach [11] shows that Lamb waves can also be analyzed on the basis of a carrier wave plus a superimposed thickness motion. The carrier wave describing the propagation along the plate is a solution of the reduced membrane wave equation, and the thickness motion has the same form for any carrier wave.

All three methods lead to the same results summarized below:

1. In a free isotropic plate, equations for the in-plane displacements (polarized

Reproduced with permission of the copyright owner. Further reproduction prohibited without permission.

along the y-axis) decouple from the system (1.6) with substituted boundary conditions.

2. The Lamb wave is a combination of coupled horizontal and vertical motions in the xz plane.

3. There exist symmetric and antisymmetric families of Lamb waves depending on the displacement symmetry with respect to the plate centerline $z = 0$.

4. Each family has corresponding dispersion equation:

$$\frac{\tan qd}{\tan pd} = -\frac{4k^2pq}{(q^2-p^2)^2} \quad \text{for symmetric modes} \tag{1.7}$$

$$\frac{\tan qd}{\tan pd} = -\frac{(q^2-p^2)^2}{4k^2pq} \quad \text{for antisymmetric modes} \tag{1.8}$$

where $p = \sqrt{\frac{\omega^2}{v_l^2} - k^2}$, $q = \sqrt{\frac{\omega^2}{v_t^2} - k^2}$, v_l and v_t are correspondingly longitudinal and shear bulk wave velocities in the plate material, k is the wave vector component in the direction of propagation (x-axis).

5. The phase velocity of a particular Lamb wave mode at a frequency ω can be calculated as

$$V_{ph} = \frac{\omega}{k} = \frac{\omega\lambda}{2\pi} \tag{1.9}$$

while the group velocity

$$V_g = \frac{d\omega}{dk} = \frac{V_{ph}}{1 - \frac{\omega}{V_{ph}}\frac{dV_{ph}}{d\omega}} \tag{1.10}$$

Reproduced with permission of the copyright owner. Further reproduction prohibited without permission.

Frequency dependence of both V_{ph} and V_g can be calculated numerically from the transcendental dispersion equations (1.7) or (1.8).

6. Numerical solution of (1.7) and (1.8) yields two families of curves $k(\omega)$ called modes. At a given frequency, in general, several modes can propagate, each having different phase velocity. Symmetric and antisymmetric modes are enumerated according to the order of their cut-off frequencies, S_n, A_n with $n = 0, 1, 2 \ldots$. All modes except the S_0 and A_0 have such frequencies defined as:

$$\omega_{cs} = n\pi\frac{V_t}{d};\ \ \omega_{cs} = \pi(n+\tfrac{1}{2})\tfrac{V_l^2}{V_t d} \quad \text{for symmetric modes} \tag{1.11}$$

$$\omega_{ca} = \pi(n+\frac{1}{2})\frac{V_t}{d};\ \ \omega_{ca} = n\pi\tfrac{V_l^2}{V_t d} \quad \text{for antisymmetric modes} \tag{1.12}$$

where n is a positive integer.

Below its cut-off frequency, each mode represents exponentially attenuating motion, becoming a standing wave with $V_{ph} = \infty$ and $V_g = 0$ at the cut-off frequency, and propagating along the plate only at higher frequencies. The higher the frequency the more modes coexist in the plate, and their phase velocities converge to the common limit - the velocity of the Rayleigh surface wave. To demonstrate the dispersive behavior of Lamb waves, (1.7) and (1.8) were solved numerically to plot phase and group velocity dispersion curves for several low-order modes in Fig. 1.4 and Fig. 1.5. Both velocities are expressed in $mm/\mu s$ and plotted versus the product of frequency f (MHz) and plate thickness $2d$ (mm).

Reproduced with permission of the copyright owner. Further reproduction prohibited without permission.

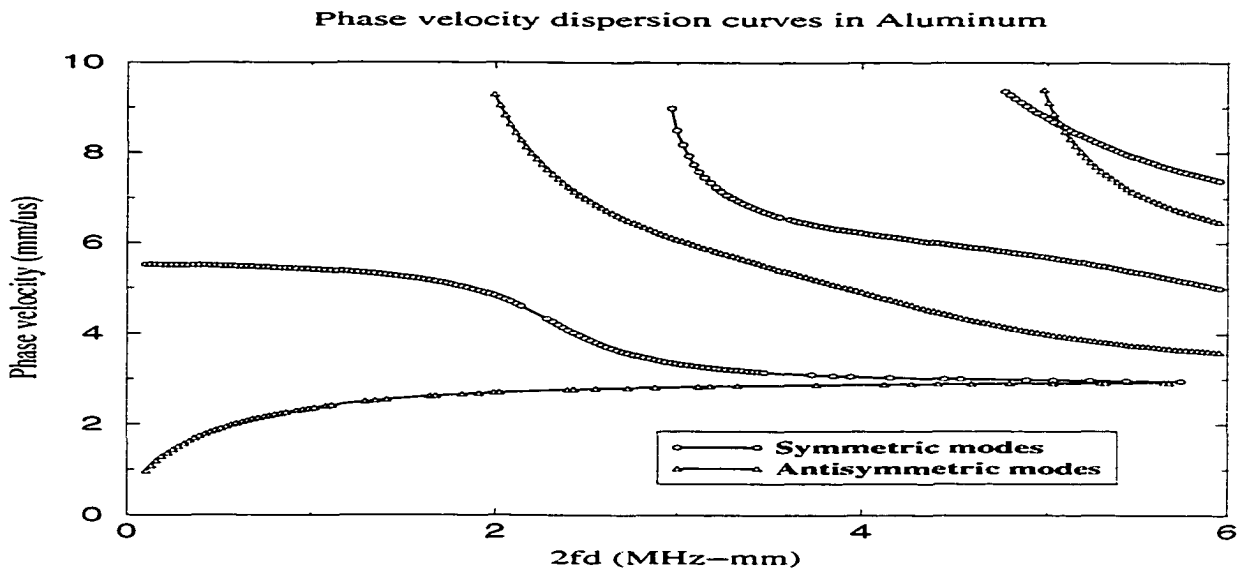

Figure 1.4: Phase velocity ($mm/\mu s$) dispersion curves in aluminum plates for the first three symmetric and antisymmetric modes. Phase velocity is plotted versus the product of frequency f (MHz) and plate thickness $2d$ (mm).

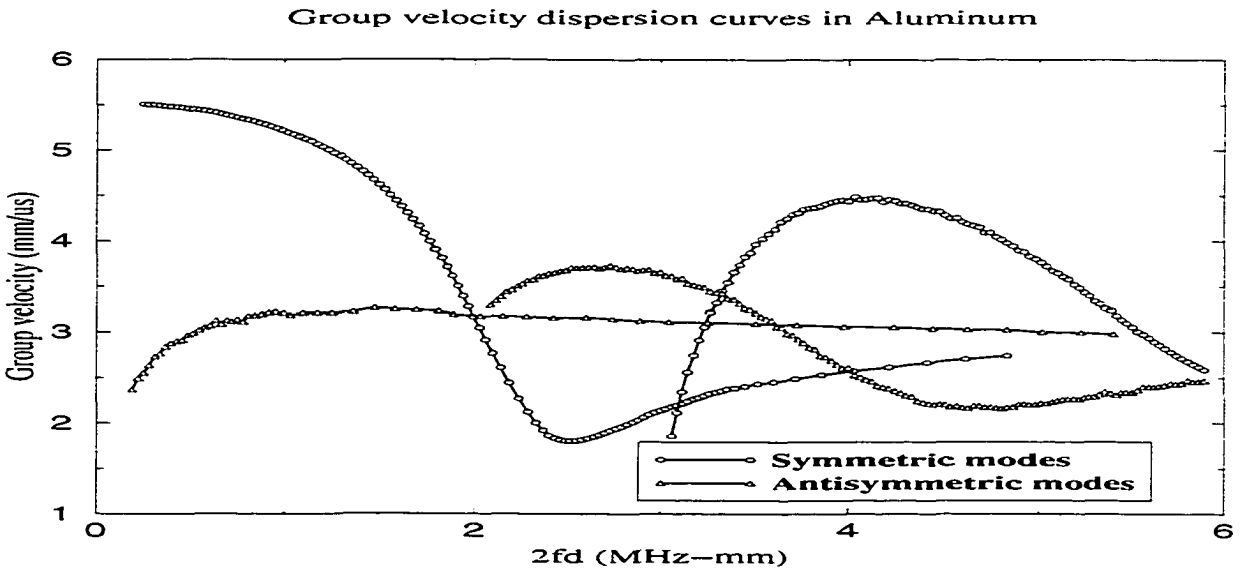

Figure 1.5: Group velocity ($mm/\mu s$) dispersion curves in aluminum plates for the first two symmetric and antisymmetric modes. Group velocity is plotted versus the product of frequency f (MHz) and plate thickness $2d$ (mm).

Reproduced with permission of the copyright owner. Further reproduction prohibited without permission.

1.1.2 Excitation techniques

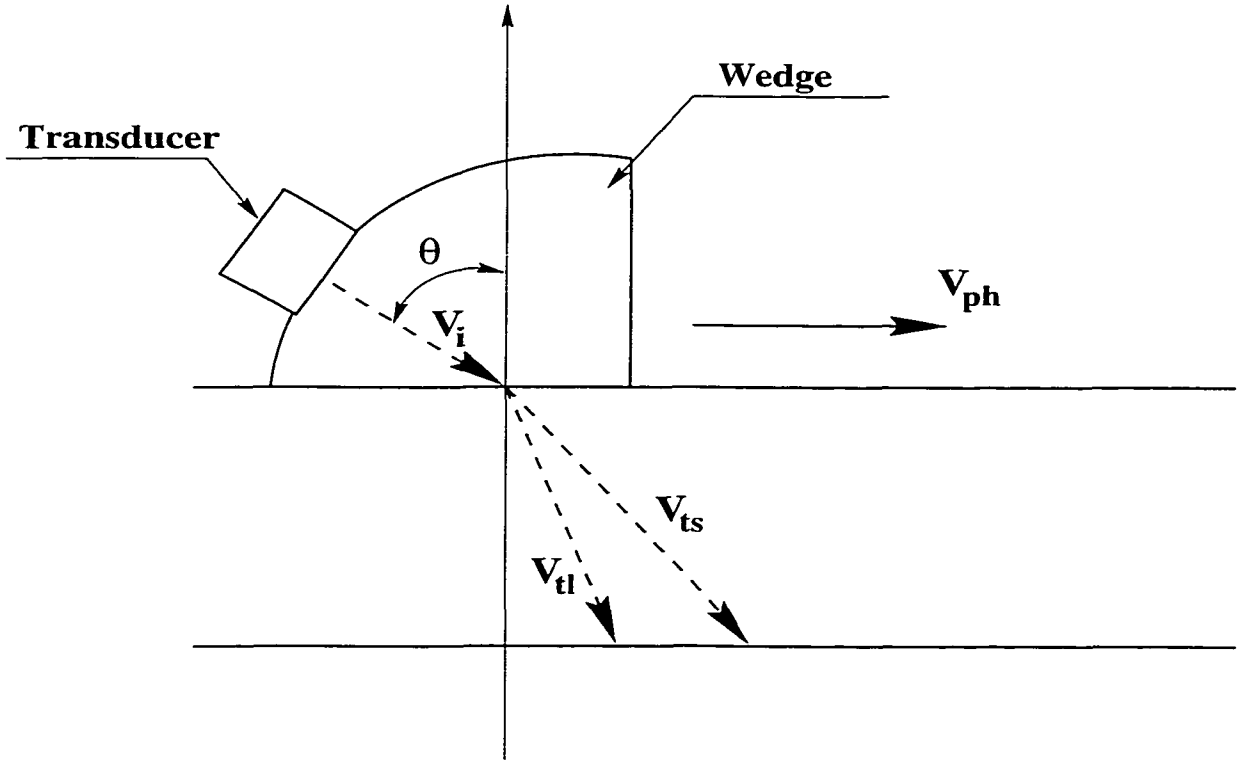

Figure 1.6: Lamb wave excitation with a method of variable incidence angle: a bulk compressional wave incident on the wedge-plate interface at angle θ creates shear and compressional transmitted waves. Their multiple reflections from plate boundaries lead to the formation of Lamb waves. Changing incidence angle θ allows for selective excitation of different modes existing at this particular frequency.

There exist a great variety of techniques to generate Lamb waves. The simplest and the most widespread method uses plate surface excitation by normal or shearing perturbations. If the excitation pulse is broadband enough, it can simultaneously generate several distinct modes at different frequencies. The energy of the initial pulse is distributed between these modes unequally. It may happen that the mode of interest receives only a small fraction of the input energy, while undesirable modes

Reproduced with permission of the copyright owner. Further reproduction prohibited without permission.

dominate and complicate the measurement process. Among the well-known methods of selective mode excitation are the phase-matched angle beam method and the comb method.

Variable incidence angle methods

The first method requires either a contact wedge (Fig.1.6) or an immersion tank to couple ultrasonic bulk waves into the plate at a chosen angle. Variable incidence angle creates preferable conditions for a particular mode and suppresses the others. This mechanism is based on Snell's law for refraction stating that the phase velocity V_{ph} of the expected Lamb waves propagating in the x direction (Fig.1.3) satisfies the relation [12]:

$$V_{ph} = \frac{V_l}{\sin\theta}$$

with V_l being the longitudinal velocity in the wedge material and θ being the incidence angle in the wedge. Since each mode has a different phase velocity V_{ph} at a given frequency ω, one can select the desired mode by tuning the angle θ. It is worth noting that the above is true only for plane wave incidence [9]. Real finite area wavefronts emanated by transducers are not planar and allow some variation of incidence angles around θ. This leads to a finite velocity interval of the excited Lamb waves.

The presence of surrounding liquid in the immersion implementation allows for the phenomenon of Leaky Lamb Waves (LLW). The plate displacement pattern is mode and frequency dependent. For some modes at certain frequencies, surface displacements have a large normal component allowing energy to leak into the surrounding liquid [9], [13]. Shear surface displacements, dominant under different

Reproduced with permission of the copyright owner. Further reproduction prohibited without permission.

conditions, do not allow for appreciable leaks into the fluid which does not support shear forces. Studying LLW reflection spectra, it is possible to gain insight into the Lamb Wave Propagation in complex composites and their interaction with defects (Bar-Cohen et al., [13]).

Resonant methods

The method of Time-Delay Periodic Linear Array (or the comb transducer) is a resonance technique that creates a specified phase displacement pattern on the surface of the plate to excite the desired mode with a given phase velocity at a given frequency. When all elements in the array are equally spaced and connected to the same source (in phase), the excited guided wave will have the same wave length as the transducer spacing [4]. If the elements are connected to different sources with appropriate phase shifts it is possible not only to control the wavelength of the resulting guided wave but also to make it propagate in a preferred direction [14], [15], [16]. The last effect is achieved due to the interference between waves, created by different parts of the array: the waves amplify each other along certain directions and cancel everywhere else. As a result, the excitation energy is used more efficiently and the wave can propagate further, which is very important in many large-scale pipe and plate inspection applications.

Coupling

Effective excitation of Lamb waves by surface disturbances strongly depends on the type of coupling between the ultrasonic transducer and the plate surface. In the worst case, when the coupling agent is vacuum, all the wave energy is reflected back to the transducer. In the ideal case when acoustic impedances of transducer, couplant

Reproduced with permission of the copyright owner. Further reproduction prohibited without permission.

and plate materials are equal, almost all of the wave energy would enter the plate. In practice, the acoustic impedance of the couplant should be as similar as possible to impedances of both transducer and plate materials. Most liquid couplants in bulk state do not support shear waves and are used for surface excitation with normal perturbations. Shear perturbations can be excited only by means of a rigid bond or a very viscous liquid couplant. However, in our lab we have successfully generated Lamb waves in aluminum plates with spring-loaded shear contact transducers using a very thin layer of water for coupling. Below we describe several Lamb Wave generation methods that do not require any special couplant (Hertzian contact, EMAT, laser generation, and air-coupled excitation).

Hertzian contact transducers

The zeroth order antisymmetric Lamb mode A_0 represents a flexural motion of the plate. At low values of the frequency-thickness product $2fd$ A_0 is strongly dispersive and thus is very sensitive to thickness variations (see Figures 1.4 and 1.5). Such motion can be effectively produced using point contact (Hertzian) transducers. In this region of strong dispersion the S_0 mode is faster than the A_0, but it is not excited because of the different symmetry. In experiments with small-aperture sources imposing normal surface traction (Degertekin et al [17]), the relative amplitude of the A_0 mode was nearly 70 dB higher than of the S_0 mode at low values of the frequency-thickness product ($2fd < 0.25 MHz \cdot mm$). Using this method the A_0 mode has been successfully excited in steel pipes and plates allowing for tomography and erosion/corrosion monitoring (Pei et al., [18], [19], Hildebrand et al., [20]). The Hertzian transducers used in these experiments consist of cylindric piezoelectric ele-

Reproduced with permission of the copyright owner. Further reproduction prohibited without permission.

ments machined from PZT-5H ceramic and bonded to steel rods. The rod diameter was chosen so that for a given frequency only the lowest order extensional mode is able to propagate in it producing displacements normal to the tested surface and thus exciting only antisymmetric Lamb modes. The rod end with a sharp spherical tip ensured single point of contact with the surface. Both transmitter and receiver rods were identically sensitive to the same mode. The couplant was not needed for the Hertzian transducers. In addition, the sharp tip could easily penetrate the pipe insulation layer which would otherwise have to be removed to get access to the tested surface. These advantages, together with their omni-directionality, make Hertzian transducers very useful for tomographic purposes.

Air-coupled transducers

Most air coupled transducers are capacitive devices vibrating under alternating voltage and emitting ultrasound waves into air. Due to the large acoustic impedance mismatch between gases and solid materials, the air-coupled transducers require specialized electronics with very high voltage pulsers and narrow-band, high-gain amplifiers. The total reflection losses in through transmission can exceed 120 dB [21] and manufacturers must use sophisticated combinations of matching layers in order to receive signals with acceptable signal-to-noise ratio. Current advances in technology have made it possible to overcome these limitations and manufacture air coupled transducers capable of performing most general inspection tasks including generation and detection of Lamb Waves.

EMATs

The electromagnetic-acoustic transducers (EMATs) exploit the principle that

Reproduced with permission of the copyright owner. Further reproduction prohibited without permission.

an electromagnetic wave incident on the surface of an electrical conductor induces eddy currents within the skin of the conductor [22]. In the presence of a static external magnetic field, Lorentz oscillatory forces act on the ions of the conductor and induce acoustic waves. A typical EMAT consists of a large magnet to produce the external field and a high-frequency coil to induce eddy currents in the sample skin. By varying the mutual orientation of the coil, magnet and the sample, it is possible to excite both normal and shear displacements in the sample. No coupling is required for the regular operation of EMATs, but the low signal-to-noise ratio and need for large magnets to excite useful levels of ultrasonic signals limits their practical application. In addition, EMATs work only with ferrous metal samples. They have been used extensively, however, for pipe and rod inspection where the geometry allows for the efficient excitation of guided waves.

Laser Generation

This is another fully non-contact method of Lamb Wave excitation [23], [24], [25]. It uses periodical heating of the sample surface with some kind of radiation. Because of its low cost and high power density, laser radiation is the most popular in the area of photoacoustics. Energy from the chopped, or Q-switched laser beam is partially absorbed by the substance, producing periodical heating of a chosen surface area, thus generating thermal waves penetrating the sample to a certain frequency-dependent depth. Harmonic heat expansion and shrinking occurs in the target region and gives rise to ultrasonic waves. Using several laser beams it is possible to select both the desired mode and the direction of the resulting Lamb Wave in a way similar to contact periodic arrays. Although very elegant, clean, and non-contact, the laser generation

Reproduced with permission of the copyright owner. Further reproduction prohibited without permission.

method has several significant drawbacks. One of these is the low excitation efficiency due to several physical processes involved. Besides, the high-density laser radiation can cause permanent damage to the sample. In addition, signal detection with lasers requires very elaborate equipment such as optical interferometers.

Discussion

In tomographic experiments, Lamb waves originating from the same transmitter are allowed to propagate through the target area in as many directions as possible. This limits the applicability of resonant techniques depending on the transmitter-receiver orientation. Laser-based methods seem attractive because a single scanned laser transmitter can be substituted for a whole perimeter array of piezoelectric transducers, but the receiving part of the equipment would be costly to design and implement. The currently available air-coupled transducers are cost-prohibitive if thought of as parts of a multi-element array. EMATs work only with magnetic materials, not with aluminum or organic composites. The two choices left are the Hertzian contact, and water-coupled contact piezoelectric transducers. In fact, the only differences between these are the area of the contact between the delay line and the surface, and the delay line shape. Either of them can be used depending on the application, i.e. surface insulation, desired mode symmetry etc. At low values of the frequency-thickness product the Hertzian transducers excite the A_0 mode more efficiently than the S_0 mode.

Reproduced with permission of the copyright owner. Further reproduction prohibited without permission.

1.1.3 Application to NDE problems

Corrosion detection

Detection of hidden corrosion in plates and pipes is a very important industrial problem because very often only one side of the object is open for the inspection. The pulse-echo thickness measurement technique with bulk waves is tedious and inaccurate, especially in corroded areas with rough surfaces. The frequency-thickness dependence of the velocity of the ultrasonic guided waves, as well as their long propagation distance and global character have attracted serious attention of the research community. Corrosion results in an effective thinning of the sample in affected areas. If a particular guided mode propagates in the sample, interaction with thinned region will increase or decrease its speed depending on the current position on the mode's dispersion curve. The arrival time will change accordingly, making it possible to judge the size and degree of the corrosion damage. This change of the arrival time has been experimentally observed and studied by many authors including Rose et al. [26], Chahbaz et al. [27], Sun and Johnson [28], etc. Reference [26] contains a systematic experimental investigation of guided wave interaction with artificial thinning defects. In addition to changing the arrival time (phase or group velocity), corrosion also affects the amplitudes of reflected and transmitted signals, and filters out some modes which may have been initially present in the signal, but have an $f \cdot d$ product in the corroded region below their cut-off frequency. The authors also suggest a very accurate method of thickness measurement called a frequency compensation technique which is based on the mode cut-off phenomenon. According to this technique, the cut-off mode would not disappear after passing through the corroded region of

Reproduced with permission of the copyright owner. Further reproduction prohibited without permission.

the unknown thickness d^* if its frequency were different (f^*). After adjusting the frequency according to

$$f \cdot d = f^* \cdot d^*$$

so that the former cut-off mode again appears in the received signal, it is possible to estimate the effective thickness d^*.

For mode cut-off experiments the initial pulse should be broadband enough to excite several modes. For arrival time and amplitude measurements the mode should be properly selected using the wedge or another resonant method.

Fatigue evaluation

Advanced composite materials have been widely adopted in aerospace, automotive and other industries because of their high strength-to-weight ratio and because their properties can be tailored to specific requirements. Controlling structural integrity of the composite structures is often a very difficult problem because of their complex anisotropy. One important measure of the current state of the composite material is its fatigue which shows up as a gradual degradation of its elastic moduli. Since Lamb wave velocity in the material explicitly depends on its elastic constants, an effective method was proposed by Seale et al. [29], [30] to assess fatigue damage in composites by monitoring guided wave speed. The method uses long Lamb waves to excite S_0 and A_0 modes in graphite-epoxy composites. Long waves are less sensitive to the structure of material and the composite can be treated as isotropic. In addition, at low frequencies the S_0 mode has weak dispersion thus simplifying the measurement process. The longer waves provide more global information of the ma-

Reproduced with permission of the copyright owner. Further reproduction prohibited without permission.

terial properties. The method provides more insight into the state of the entire plate region than currently used local strain gauges.

Disbond detection

Sun and Johnston [28] experimentally studied interaction of Lamb waves with adhesively bonded lap splice and doubler joints in aluminum sheets with and without rivets. The authors monitored the amplitude of the S_0 mode while scanning a pair of contact water-coupled piezoelectric transducers along and across the joint. For the doublers, disbonds showed up as the amplitude maxima, for the lap joints they corresponded to the amplitude minima. The rivet rows were reported to produce amplitude minima. These observations qualitatively agree with theoretical expectations and demonstrate the possibility of accurate disbond detection and location. Mustafa et al. in [31] reviewed various existing techniques of disbond detection and pointed out that Lamb waves offer a fast and effective alternative. Using the wedge method to select particular modes and thus improve sensitivity, the authors were able to locate disbonds in doubler and lap joints with confidence and accuracy. Summarizing various Lamb wave inspection applications Rose [15] emphasized that sometimes only very little or no energy can propagate through the lap joint. The problem can be solved by choosing the appropriate angle in the wedge method to find the mode that forces the energy across the joint.

Other applications

Among other inspection problems that can be solved with Lamb waves are:

- Assessment of thermal damage to composite structures based on the sensitivity of Lamb wave velocity to changes of elastic moduli in affected area (Seale and

Reproduced with permission of the copyright owner. Further reproduction prohibited without permission.

Smith [32]).

- Detection of ice accumulation on airplane wings or shipboards [9], [15]. Such detection is possible since some guided modes at specific points of the dispersion curve exhibit mainly in-plane surface vibrations. Such a motion does not couple to substances not supporting shear stresses, such as air or water, and the corresponding guided wave is not a leaky one under normal conditions. However, if icing occurs, the energy leaks into the ice layer will reduce the amplitude or completely cut-off the sensitive mode.

- Finding defects in the pulse-echo mode. Interaction of guided waves with defects is a very complicated mechanism involving scattering (McKeon and Hinders [33]) and mode conversion. In a conventional measurement scheme the observer only detects the results of this interaction by placing ultrasonic transducers far enough from the defect location. In a pulse-echo setup the reflected (or scattered back) signal can be detected with the time of flight of a particular mode being a good measure of the defect location. This method was successfully employed for pipe inspection by Rose [15]. To get satisfactory results and avoid side reflections, guided waves were forced to propagate in a pre-determined direction using the comb excitation method. Some Lamb wave modes, such as the backward region (Liu et al. [34]) of the S_1 mode in aluminum, exist in a very narrow frequency-thickness region. Any defect will cause such a mode to reflect back since it cannot pass through the defect.

- Inspecting for structural defects in anisotropic materials, such as thin steel

Reproduced with permission of the copyright owner. Further reproduction prohibited without permission.

sheets, based on the sensitivity of the Lamb wave velocity to the direction of propagation [35], [36], [37].

Discussion

The above review of Lamb wave applications demonstrates that they are sensitive to all defects that can possibly exist in plate- or pipe-like structures. However, today's industrial inspection routines are still based on tedious point-by-point or line-by-line measurements. The goal of this research is the development of Lamb wave tomography as a fully automated inspection technique which is robust enough to rapidly assess large areas, and represent the defect information in a form, convenient for visual interpretation.

1.2 Tomography

According to Natterer [38] computerized tomography (CT) is defined as the reconstruction of a function from the set of its line or plane integrals. In practice the integrals can be measured only for a finite number of lines. Their arrangement, usually referred to as a scanning geometry, is determined by the design of the scanner. The reconstruction procedure and the accuracy of the results strongly depend on the scanning geometry.

Scanning geometries

Fig. 1.7 shows three typical scanning geometries. In the parallel scheme (Fig. 1.7a.), employed in the first generation of medical CAT-scanners (Webb [39]), a single transmitter and a single receiver step in tandem to complete one projection. The sample, or apparatus, then rotates to take another projection and the whole process is repeated

Reproduced with permission of the copyright owner. Further reproduction prohibited without permission.

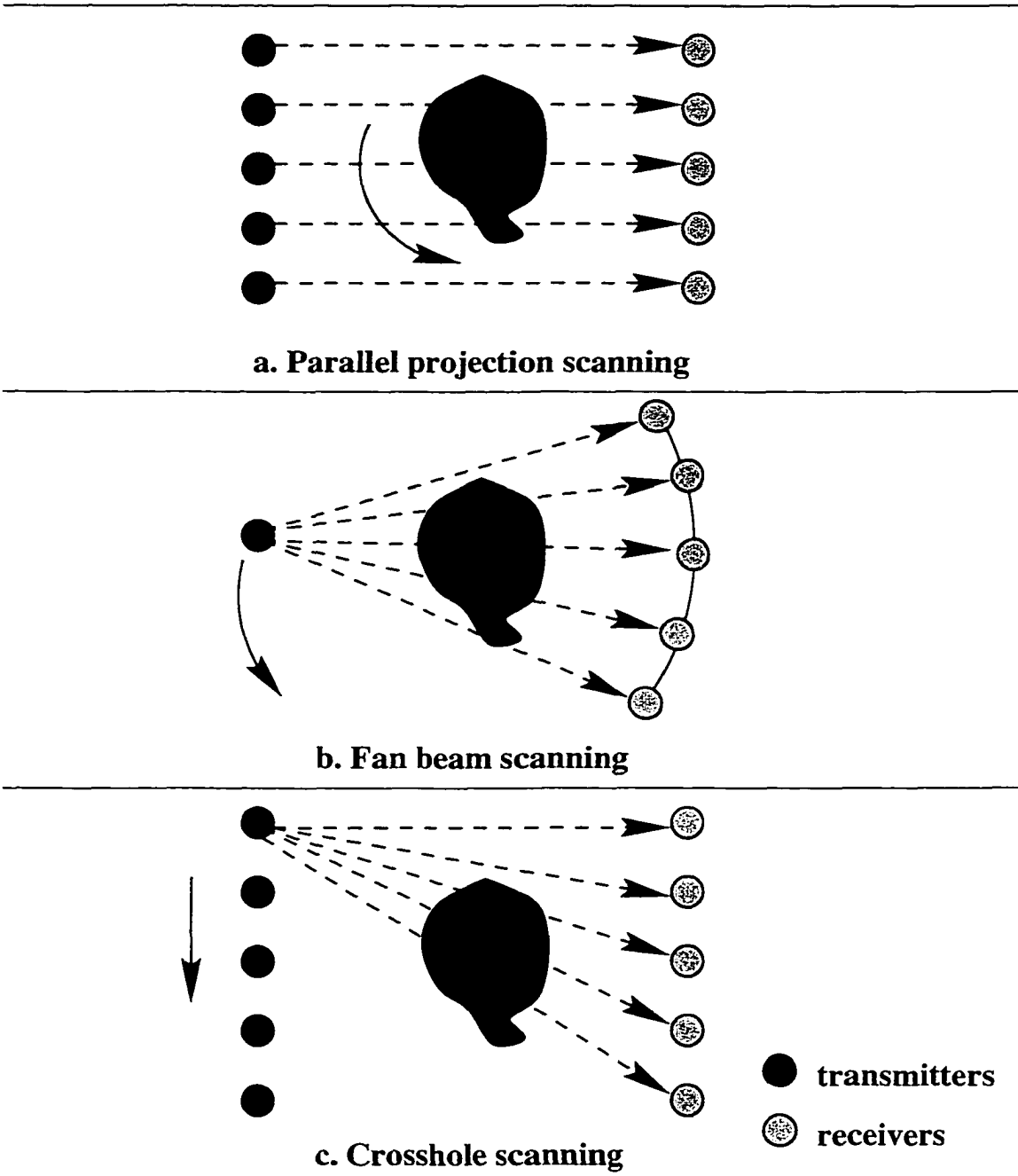

Figure 1.7: Three tomographic geometries used in the scope of this work. Dashed arrows indicate ray paths, curved arrows indicate sample (or source-receiver assembly) rotation after completion of the current projection.

Reproduced with permission of the copyright owner. Further reproduction prohibited without permission.

until projection angles cover the interval $(0, 2\pi)$. A more efficient fan beam geometry (Fig. 1.7b.) implemented in third generation CAT scanners, contains one transmitter and an array of receivers distributed uniformly along a circular arc. This scheme is much faster since rotation of the sample is the only mechanical motion involved. Fig. 1.7c. introduces the so called crosshole geometry [40], [41], widely employed in geophysics and seismology, where two linear arrays of transmitters and receivers are placed into boreholes and then all possible combinations of rays are recorded by the principle "one send all receive".

Sampling and resolution

For all scanning geometries, the accuracy of any reconstruction method strongly depends on the spatial density of the "rays" penetrating the object. In general, higher image quality is observed in well-covered central regions while poorly illuminated peripheral areas suffer from noise and reconstruction artifacts. In addition, the task of tomography can be reduced to the reconstruction of the object from its Fourier spectrum, and the latter should not be under-sampled. In other words, the directions of wave vectors should cover the range $(0, 2\pi)$ as densely and as uniformly as possible. However, these two requirements hold together only for the parallel projection geometry where the ray density and the wave vector directivity pattern are uniform. Also while the wave vector coverage for the fan beam scheme is complete in a global sense, both the local directivity pattern and the ray density are nonuniform throughout the region. Dickens and Winbow [42] noticed that for the crosshole experiment even the global wave vector coverage is rather poor and limited by the minimum and maximum possible ray angles. Moreover, even well covered regions (Bregman [40]) may have

Reproduced with permission of the copyright owner. Further reproduction prohibited without permission.

rays with a very limited range of angles, resulting in very poor resolution of structures that are oriented perpendicular to the raypaths. This lack of local angular coverage qualitatively changes the situation from a well-constrained imaging problem to one where there is no unique solution even if an infinite amount of perfectly noise-free data with an infinitely small sampling interval were available.

Reflection and transmission tomography

The parallel projection and the fan beam geometries were originally designed for X-ray transmission tomography where attenuation is the only measured quality. Unlike X-rays, ultrasonic waves do not penetrate voids or strongly scattering objects which create shadow zones. The critical angle phenomenon also prevents them from penetrating areas densely populated with multiple scatterers. In such cases transmission tomography produces an image, similar to a shadowgram (Gomm and Mauseth [43]). A cluster, blocking the transmission, will appear as a single blurred feature (Fig. 1.8b). In such cases reflection tomography [44] may be of help because it reconstructs the outline of the cluster, which sometimes is more useful (Fig. 1.8c). Reflection tomography uses the backscattered field to reconstruct the object. It can be implemented both in a pulse-echo and in a pitch-catch mode. Hall et al. [45] combined the results of the transmission and reflection tomography using image fusion. Because of the complementary nature of these two techniques, a significant increase in the amount of detail present in the image was reported.

Straight ray and diffraction tomography

Originally, all tomographic reconstruction algorithms were based on the assumption of straight rays connecting the transmitter and receiver positions. This

Reproduced with permission of the copyright owner. Further reproduction prohibited without permission.

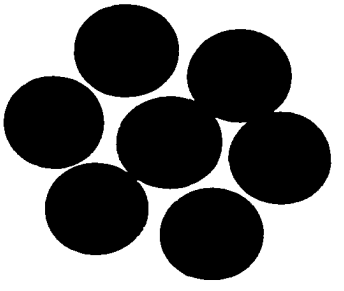

a. Original cluster defect

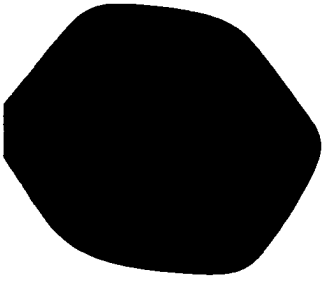

b. Result of transmission tomography

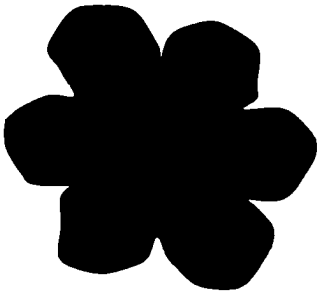

c. Result of reflection tomography

Figure 1.8: Limitations of ultrasonic transmission and reflection tomography: unlike X-rays, ultrasound cannot penetrate densely packed clusters of strong scatterers. In such cases reflection tomography is more informative about the internal structure of the defect.

Reproduced with permission of the copyright owner. Further reproduction prohibited without permission.

assumption is valid for X-rays propagating in biological tissues and can, in principle, hold for ultrasound in non-refractive media. However, the majority of interesting defects do scatter ultrasound and reconstruction is properly done via diffraction tomography. Weak spatial variations in the index of refraction result in bending of ray paths, thus calling for ray tracing algorithms to describe their complex behavior. Reconstruction of strong scatterers requires inversion of the wave equation that can, in general, only be approximated.

Discussion

One of the tasks of the present work is to find the combination of a scanning geometry and a reconstruction algorithm to optimally suit the needs of Lamb wave tomography for aging aircraft structures. We limited our search to the transmission mode methods since the vast majority of sample aluminum plates with manufactured defects in our laboratory were of small size, and reflections from the edges would complicate the measurement process in the pulse-echo mode. However, if plate size is not a limiting factor, reflection tomography can provide useful supplementary information to correct transmission-mode images, especially for the cluster-type multiple defects.

1.3 Initial state of the problem

This work is a logical continuation of the preceding efforts of Hinders, McKeon and Sun [28,33,46–48] to lay the foundations of the Lamb Wave Tomography for plate NDT. Sun studied the interaction of Lamb waves with delaminations in doubler and lap joints and utilized the Pulsed Phase Lock Loop (P_2L_2) for accurate measurement

Reproduced with permission of the copyright owner. Further reproduction prohibited without permission.

of the subtle changes in the Lamb Wave velocity.

McKeon and Hinders built the Parallel Projection Tomographic Scanner controlled by the LabView software running on a $Macintosh^{TM}$ computer. The P_2L_2 output was recorded as a measure of change in the arrival time. Hinders wrote a $Mathematica^{TM}$ image reconstruction program based on the convolution-backprojection algorithm. McKeon designed and built the Crosshole Tomographic Scanner, adapted the Algebraic Reconstruction Technique (ART) for the crosshole Lamb Wave Tomography, and studied the scattering of Lamb waves from cylindrical defects in plates.

This work started by exploring the advantages and limitations of the available parallel projection and crosshole tomographic techniques. Typical results of this exploration are presented in the following two subsections.

1.3.1 Parallel Projection Lamb Wave Tomography

The performance of the Parallel Projection tomography was studied on four samples with manufactured defects. The first two samples were cut from a 2.3 mm-thick aluminum plate. They had a 15 mm-diameter through hole and a 1"-diameter 50% thickness reduction circular flat bottom hole machined near the center of the scanned area. The second pair of samples were manufactured from 2 mm-thick stitched graphite-epoxy composite featuring a 1"-diameter through hole and an impact damage in the center of the scanned region.

In order to speed up the experiment all the motion control, data acquisition and reconstruction software were rewritten in "C" language and ported to the Red Hat Linux-5.0 operating system. With these enhancements the typical scanning

Reproduced with permission of the copyright owner. Further reproduction prohibited without permission.

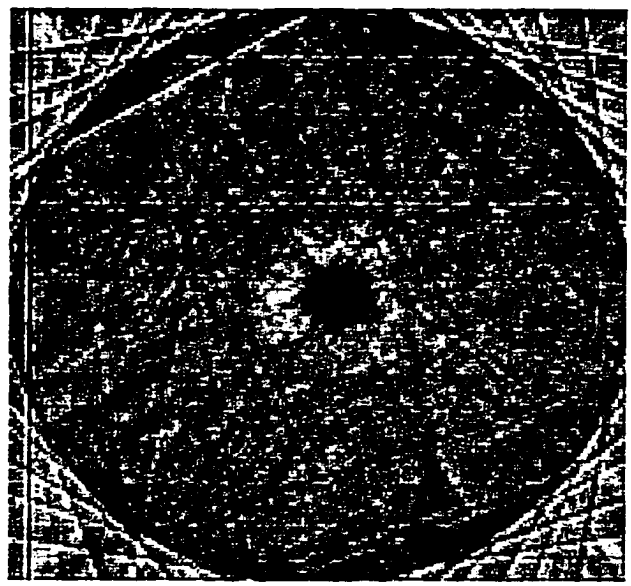

Figure 1.9: Reconstruction of a 15 mm-diameter through hole in aluminum plate with parallel projection Lamb wave tomography: 18 projections, 160 steps. The size of the reconstructed area is 160 × 160mm.

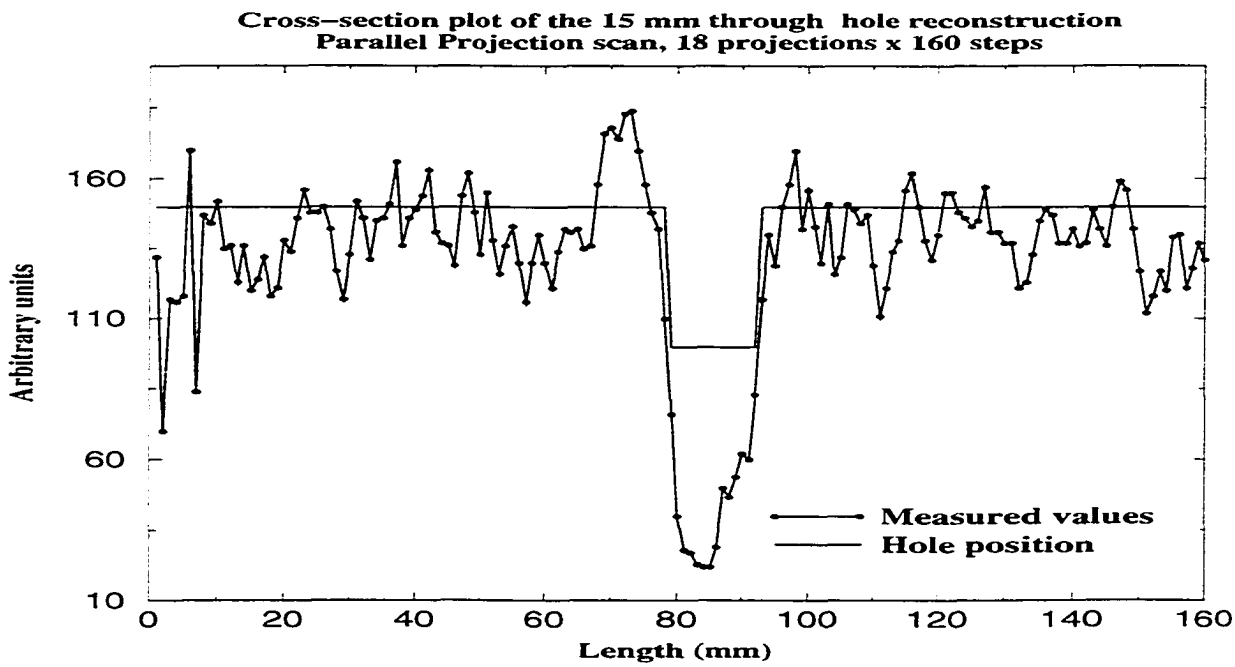

Figure 1.10: Horizontal profile of the image (Fig. 1.9), taken at half-height, and schematic hole position.

Reproduced with permission of the copyright owner. Further reproduction prohibited without permission.

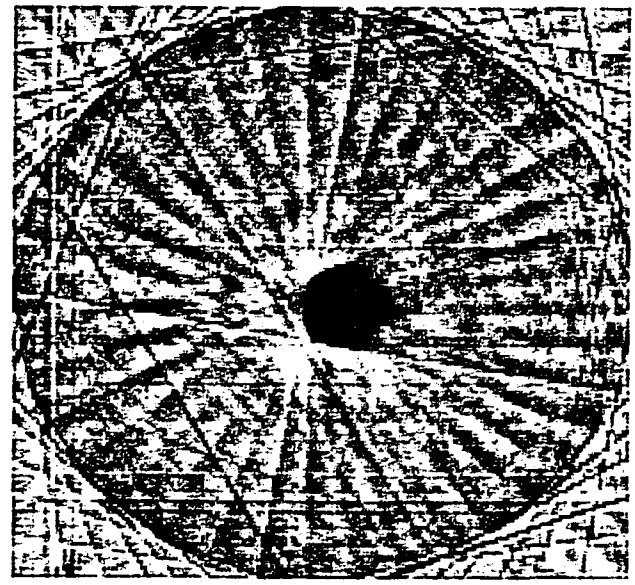

Figure 1.11: Reconstruction of a 25.4 mm-diameter circular flat-bottom hole in aluminum plate with parallel projection Lamb wave tomography: 18 projections, 160 steps. The size of the reconstructed area is 160 × 160mm.

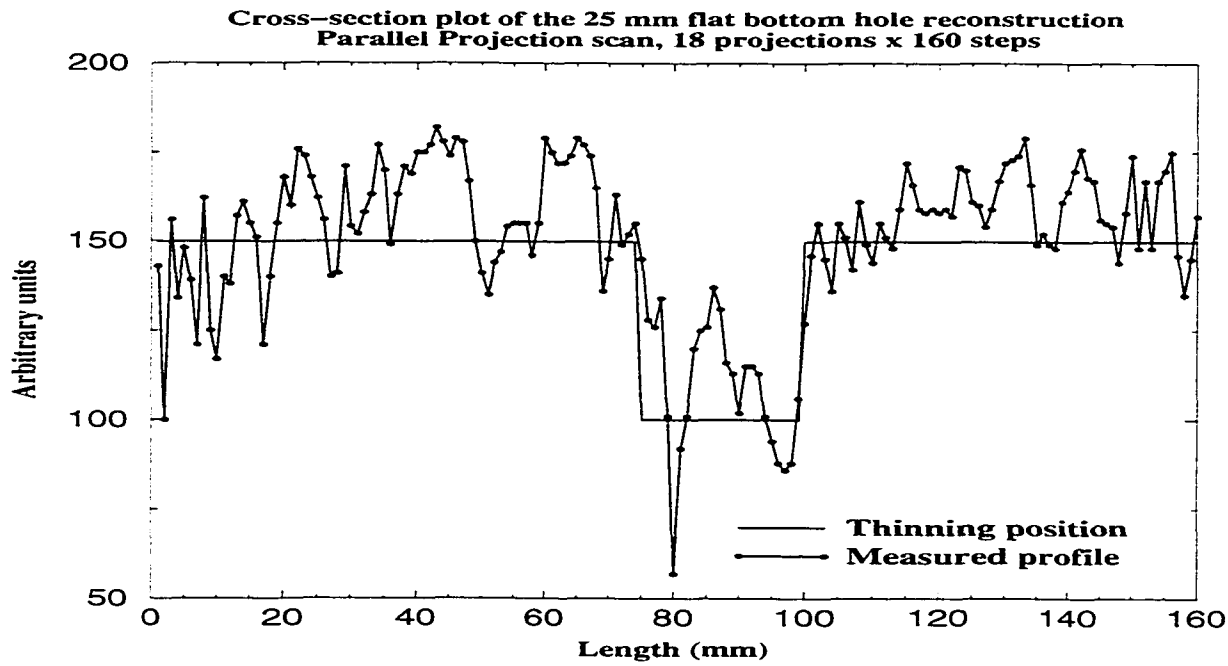

Figure 1.12: Horizontal profile of the image (Fig. 1.11), taken at half-height, and schematic defect position.

Reproduced with permission of the copyright owner. Further reproduction prohibited without permission.

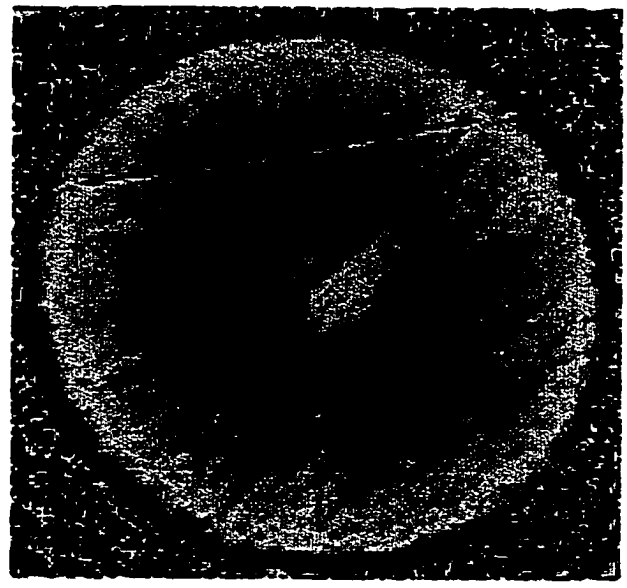

Figure 1.13: Reconstruction of a 25.4 mm-diameter through hole in a stitched graphite-epoxy composite plate with parallel projection Lamb wave tomography: 18 projections, 160 steps. The size of the reconstructed area is 160 × 160mm.

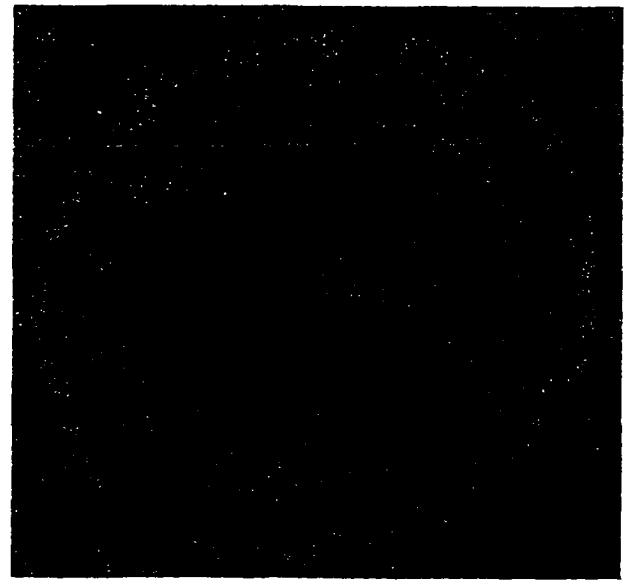

Figure 1.14: Reconstruction of an impact damage in a stitched graphite-epoxy composite plate with parallel projection Lamb wave tomography: 18 projections, 160 steps. The size of the reconstructed area is 160 × 160mm.

Reproduced with permission of the copyright owner. Further reproduction prohibited without permission.

time reduced to a couple of minutes and the reconstruction with the convolution-backprojection algorithm turned out to be almost real time on a $PentiumPro^{TM}$ – 200.

Identical Parallel Projection scans of all four samples were taken with 18 projection angles and 160 1-mm-long steps per projection. Although we worked in a pitch-catch mode and were interested in recording the time of flight of the S_0 mode, the equipment instead recorded the output of the P_2L_2. As explained in the P_2L_2 manual and in [28], this output is proportional to the phase difference between the current signal and the reference signal on which the P_2L_2 was initially locked. While rather small, this difference is directly related to a change in the signal phase velocity. In the Parallel Projection mode the distance between transmitter and receiver is constant and the P_2L_2 is capable of tracking phase changes with great precision.

Figures 1.9 and 1.11 present the unprocessed reconstructions of the first two samples. The quality of these images is high, the dimensions of the defects are realistic. It is even possible to visually distinguish between a through hole and a flat bottom recess by the reconstructed intensity of their inner areas. Figures 1.10 and 1.12 show horizontal profiles of the images taken at the half-height. These profiles allow for quantitative assessment of the algorithm performance. Figures 1.13 and 1.14 show reconstructions of the defects in composite plates. The defects are clearly observable, but mainly due to their privileged position near the geometrical center of the scanned area. These relatively poor results can be explained by the anisotropy of the composite plates making Lamb wave velocity depend on the direction of propagation. Some correction for this dependence should be introduced into the reconstruction algorithm,

Reproduced with permission of the copyright owner. Further reproduction prohibited without permission.

or the wavelength has to be made much larger than the characteristic size of a stitch. In the case of the S_0 mode, long waves are less dispersive and will less effectively interact with defects.

Since isotropic materials (aluminum) are of primary interest within this work we can conclude that the performance of the Parallel Projection Lamb wave tomography with P_2L_2 is very high. The method provides good accuracy, low level of artifacts, and near real time reconstruction with a mature convolution-backprojection algorithm. The ray density and directivity pattern are almost uniform within the reconstruction circle ensuring the uniformity of the image quality in the region.

However, the parallel projection scheme has a serious drawback: it cannot be implemented in an array of transducers without mechanically moving parts. In this work the parallel projection images will serve mainly as a standard against which the performance of other methods is measured.

1.3.2 Single Projection Crosshole Lamb Wave Tomography

As with the Parallel Projection Tomography, all of the motion control and data acquisition software were rewritten in "C" language and ported to the Red Hat Linux-5.0 operating system, running on a $PentiumPro^{TM} - 200$ machine. This sped up the data acquisition process and we were able to use more scanning steps to increase ray density. We used the original code for the Algebraic Reconstruction Technique (ART) written by McKeon, and his pattern matching software to extract arrival times of the S_0 mode and build the Single Projection Crosshole images on a 40×40 sampling grid. With a step size of 5 mm the scanning region is a 200×200 mm square.

Reproduced with permission of the copyright owner. Further reproduction prohibited without permission.

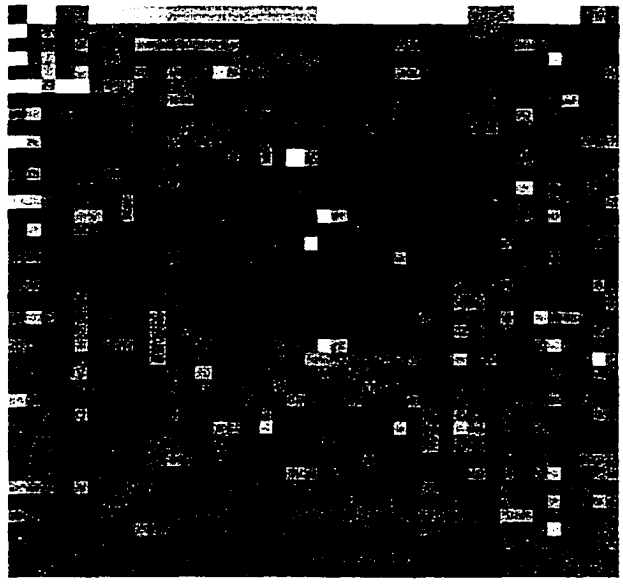

Figure 1.15: Reconstruction of a 25.4 mm-diameter through hole in aluminum plate with a single projection crosshole Lamb wave tomography: 40 × 40 steps, step size = 5mm. The size of the reconstructed area is 200 × 200mm.

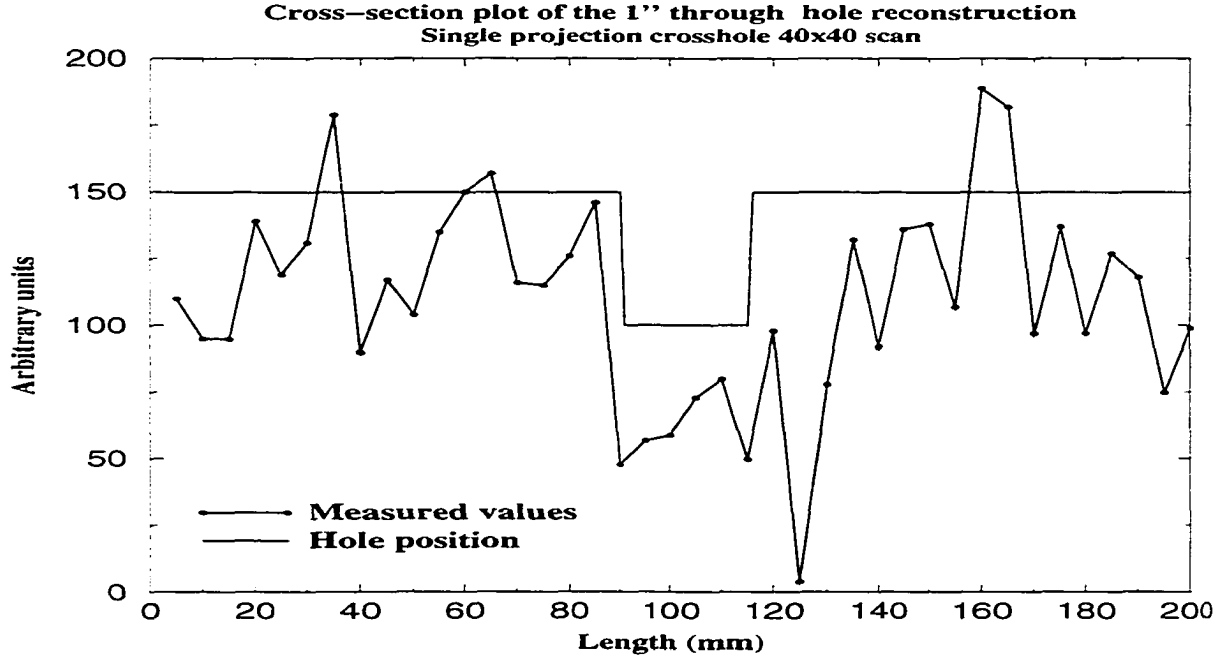

Figure 1.16: Horizontal profile of the image (Fig. 1.15), taken at half-hight, and schematic hole position.

Reproduced with permission of the copyright owner. Further reproduction prohibited without permission.

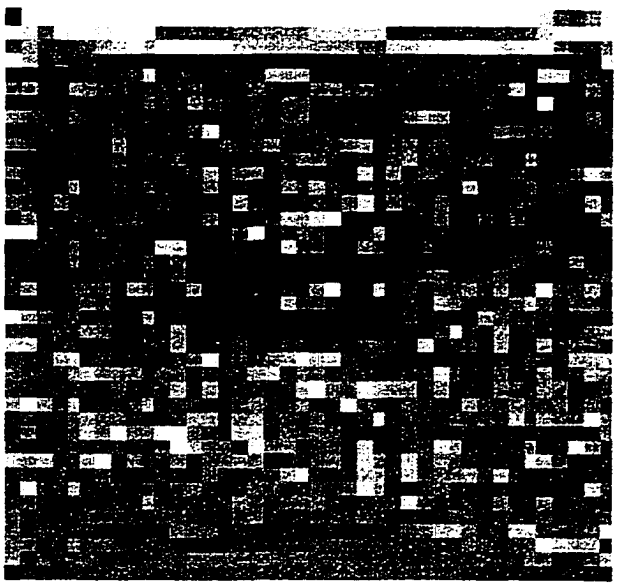

Figure 1.17: Reconstruction of a 25.4 mm-diameter circular flat-bottom hole in aluminum plate with parallel projection Lamb wave tomography: 40×40 steps, step size = 5mm. The size of the reconstructed area is 200×200mm.

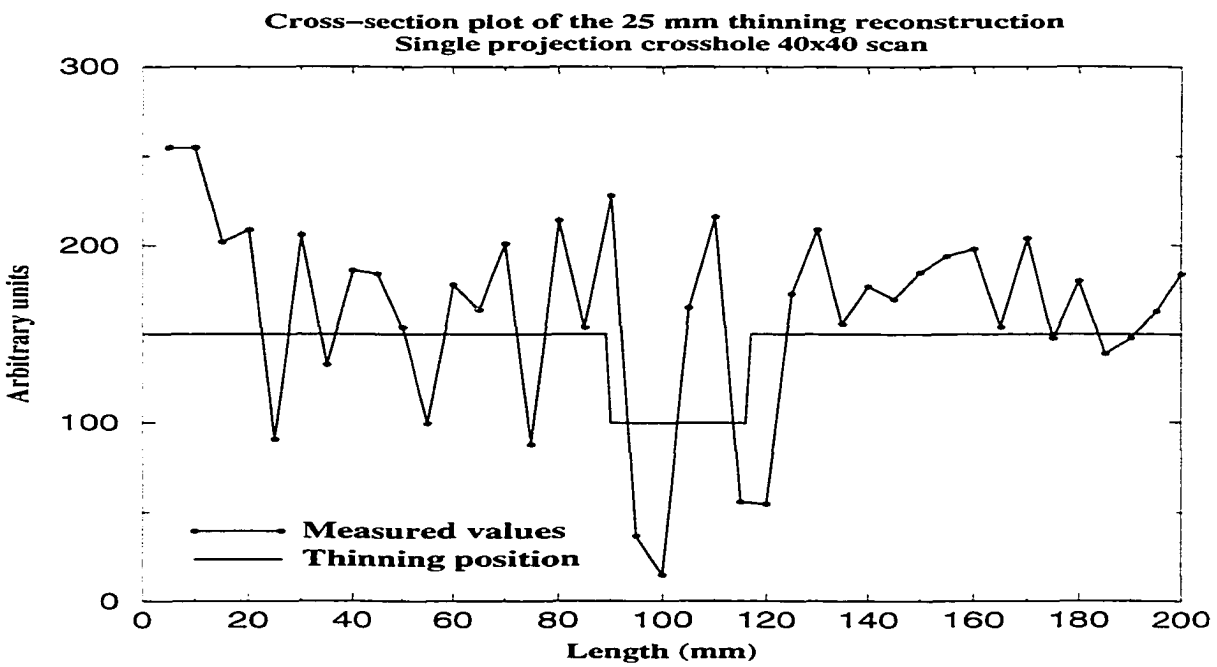

Figure 1.18: Horizontal profile of the image (Fig. 1.17), taken at half-height, and schematic defect position.

Reproduced with permission of the copyright owner. Further reproduction prohibited without permission.

Figures 1.15 and 1.17 show the unprocessed ART reconstructions of a through hole and of a flat bottom hole in 2.3 mm-thick aluminum plates. Although defects are visible, both images suffer from the "salt and pepper noise" and diagonal artifacts, peculiar to the ART reconstruction. The poor resolution, especially near the upper and lower image boundaries, is due to the extremely low ray density in those areas. In addition, both defects seem elongated in the horizontal direction. As discussed earlier, this happens because the wave vectors of the rays, penetrating the central area, have a limited number of directions and the accurate inversion is not simply possible. Figures 1.16 and 1.18 show horizontal profiles of the images taken at the half-height. They clearly demonstrate the defect sizing errors and the level of the salt-and-pepper noise, especially when compared to the corresponding profiles in Parallel Projection reconstruction (Figures 1.10 and 1.12).

Discussion

The images created with Parallel Projection and a Single Projection Crosshole Lamb Wave Tomography serve as a starting point of this work. Our goal is to find a tomographic technique that can be implemented without mechanically moving parts and produces a resolution comparable to that of the Parallel Projection method.

Reproduced with permission of the copyright owner. Further reproduction prohibited without permission.

Chapter 2

Estimation of arrival times

2.1 Important concepts

The two most important scalar quantities used in conventional ultrasonic tomography are the amplitude (attenuation) and the arrival time of a signal. If no diffraction or dispersion is present in the system, monitoring one of these quantities is often enough to uniquely characterize its relevant elastic properties.

In the immersion tank experiments, when the object is completely surrounded by liquid and the acoustic coupling is uniform, signal attenuation can be used to reliably monitor various medium properties. The attenuation of Lamb waves is no exception and can be effectively used in conjunction with theoretical dispersion curves to monitor a wide variety of plate defects. Uniform coupling remains the most important, but very severe, requirement for reliable amplitude measurements. Uniform coupling can be established in experiments with leaky Lamb waves when the whole sample and transducers are immersed into a liquid bath, and acoustic energy is trans-

Reproduced with permission of the copyright owner. Further reproduction prohibited without permission.

formed into guided waves leaking their energy back into the liquid. The current advances in air-coupled transducer technology [21] have made it possible to excite and detect Lamb waves directly from the air. Such an approach eliminates coupling variation problems and makes amplitude measurements applicable to the Lamb wave inspection. The primary limitation of this technique is the high insertion loss of the air coupled transducers which can be compensated for only by very sensitive receiving electronics and high-power input amplifiers. On the other hand, conventional water layer coupling of contact transducers is position-dependent and often does not allow for accurate enough amplitude measurements with multiple transducers, or one moving transmitter-receiver pair, as is the case for Lamb wave tomography.

The arrival time of a signal is essentially independent of coupling and allows for tomographic reconstruction if the distance between transmitter and receiver is known. The problem therefore reduces to signal detection and its arrival time estimation, which are discussed below.

2.1.1 Noise reduction issues

In the context of the present work the term "signal" will refer to the digitized time history of the amplified voltage in a receiving piezoelectric transducer placed on the surface of an elastic plate. Digitization in our experiments was performed via an A-D converter built into either digital LeCroy 9310 oscilloscope or GAGE CompuScope 8012A computer plug-in board. In both cases we used 50 or 100 MegaSamples/s temporal sampling rate. For our operating frequencies of 1.0 and 2.25 MHz these sampling rates were far beyond the Nyquist frequencies of 2.0 and 5.0 MHz corre-

Reproduced with permission of the copyright owner. Further reproduction prohibited without permission.

spondingly.

The noise in our signal came from several different sources:

1. Ultrasonic preamplifier noise - white
2. Resonant vibrations of the finite plate - colored
3. Electrical cross-influence noise - colored
4. Other sources - white

In addition, our broadband piezoelectric transducers excited undesirable plate modes at frequencies up to 5MHz and down to 300 kHz. Some of those propagating modes are faster than the S_0 mode of interest and their early arrivals make the detection problem even more challenging. The input energy distribution between different modes is also a rather complicated process, especially when mode conversion occurs near defects and inhomogeneities of interest. This can result in a significant drop-off or increase of the S_0 amplitude compared to that of the second and later arrivals. The raw signal with all the above noise components is shown in Fig. 2.1.

To eliminate electrical cross-influence noise we used thorough grounding of the equipment and coaxial cables wherever possible. Despite our efforts, however, there always is some leak of the pulser energy into receiving channel. This leak shows up as an indication of the excitation tone burst in the beginning of the received trace.

To emphasize the desired frequency region we used an analog band-pass filter cutting a narrow band around the input tone burst carrier frequency. This helped exclude higher and lower frequency guided modes from the received signal and made

Reproduced with permission of the copyright owner. Further reproduction prohibited without permission.

S_0 appear first in a homogeneous test sample. Such a treatment significantly improved the signal quality, as shown in Fig. 2.2.

In the ideal noise-free case the amplitude should be zero all the time between the trailing edge of the tone-burst and the arrival of the fastest guided mode (the region $10 - 70\mu s$ in Fig. 2.2). However, even after filtering this time interval is apparently filled with a strong colored noise component. We identified this particular noise as a resonant standing elastic wave generated in the finite plate. We easily damped these oscillations with a strip of modeling clay at the edge of the plate. The resulting signal of better quality is shown in Fig. 2.3.

The initial tone burst with a variable number of harmonic cycles is generated by the HP8116A function generator or by the Matec TB-1000 tone burst computer plug-in board. This type of excitation signal is relatively narrow-band compared to common ultrasonic acoustics single spike excitation. It allows to avoid excitation of plate modes at frequencies other than the operating frequency, and the input energy is used more efficiently.

At our operating frequency-thickness region only two lowest order modes can exist in the plate (Fig. 1.4), and the S_0 mode always has higher phase velocity than the A_0. The first arrival (Fig. 2.3) is an S_0 mode, followed by the A_0 mode and numerous reflections of the plate edges.

2.1.2 Estimation of arrival time in dispersive medium

The preceding analysis demonstrates that we solved the noise problem and isolated the S_0 mode as the fastest part of the received signal. It therefore can be

Reproduced with permission of the copyright owner. Further reproduction prohibited without permission.

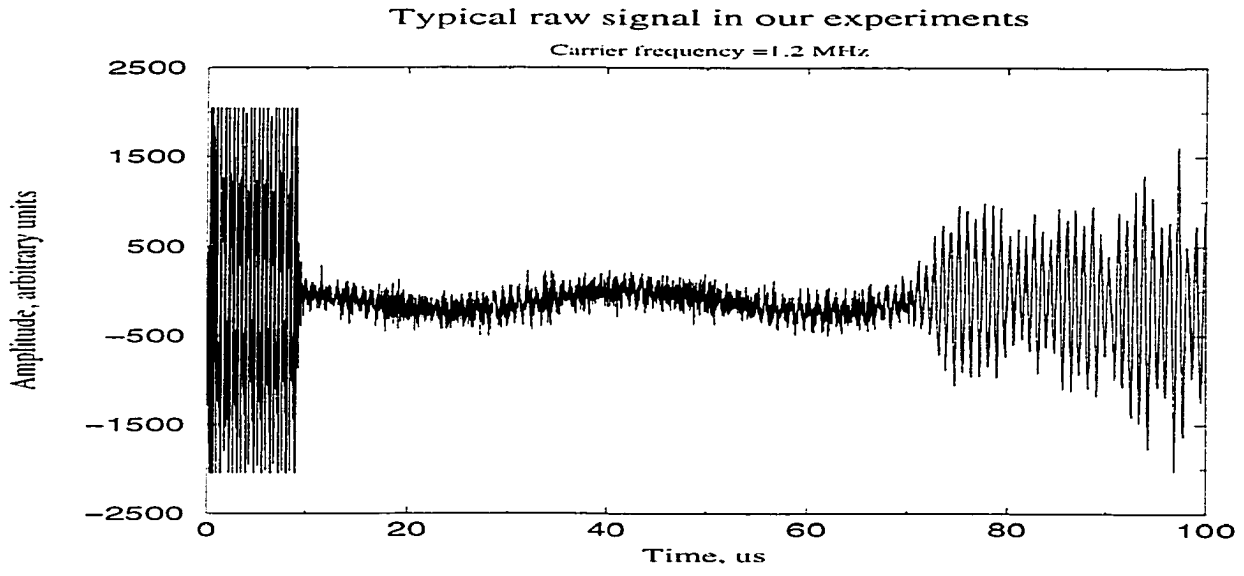

Figure 2.1: Raw signal typical for our experiments. Note the presence of the excitation tone burst between 0 and 10 μs due to the electrical cross-influence.

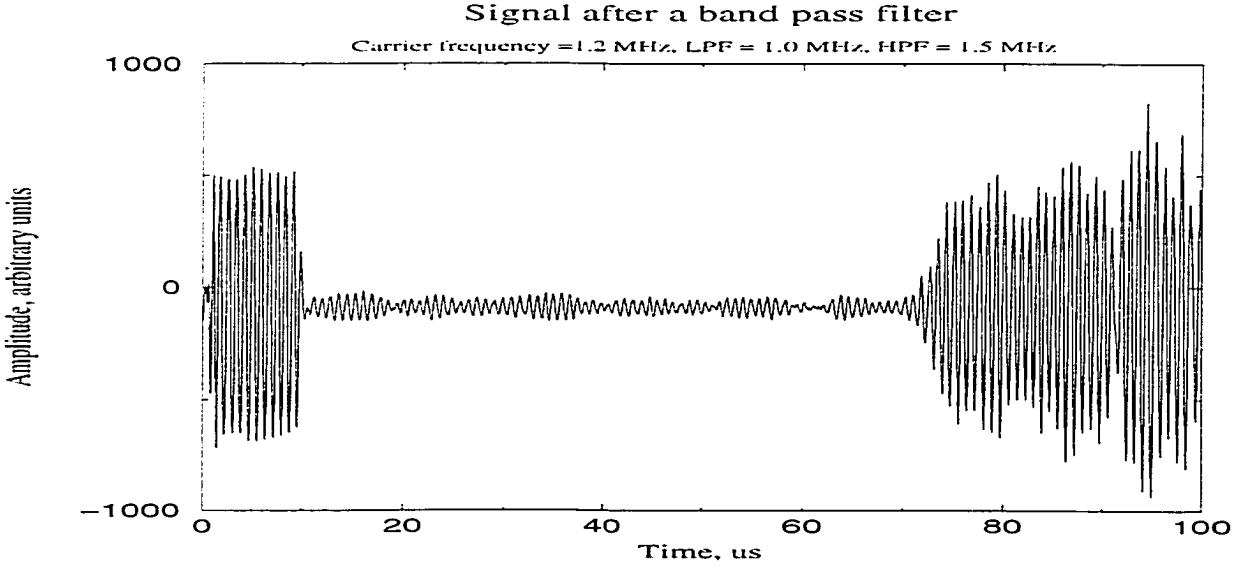

Figure 2.2: Band-pass filtered signal. The colored noise left in the region 10-70 μs is produced by standing waves in the finite plate.

Reproduced with permission of the copyright owner. Further reproduction prohibited without permission.

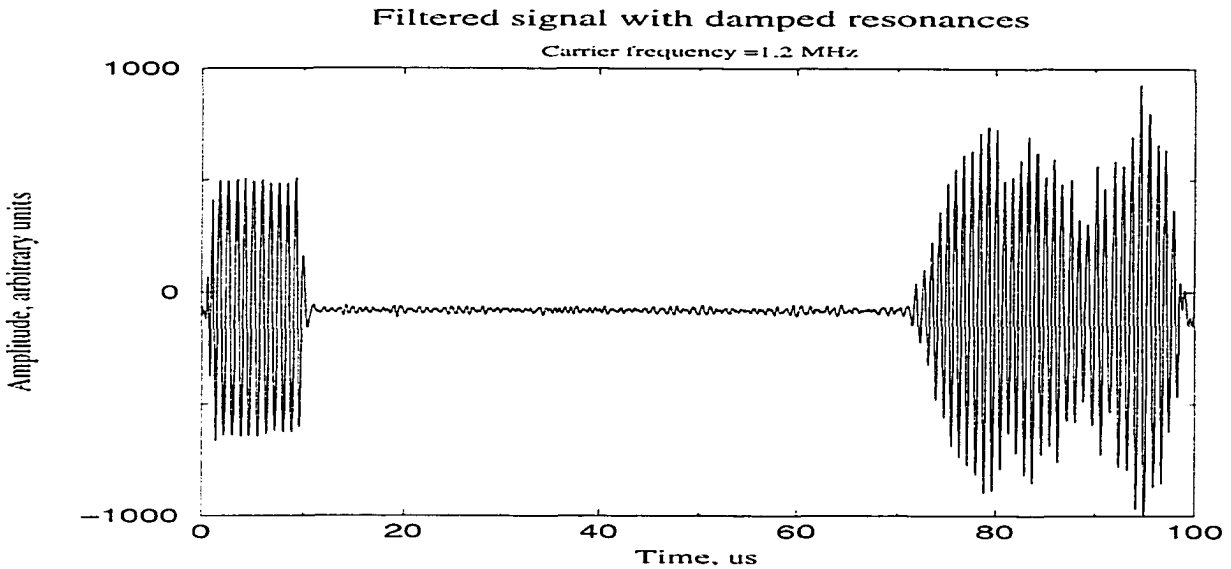

Figure 2.3: Band-pass filtered signal, standing plate waves were damped with clay.

extracted from the rest of the signal and analyzed in order to determine its arrival time. However, Lamb waves are inherently dispersive and finding their arrival time is more of a problem than in the bulk wave case. Fig. 2.4 demonstrates a typical bulk wave reflection from a water-aluminum interface and Fig. 2.5 shows a Lamb wave recorded in our experiments. In the non-dispersive acoustic case (Fig. 2.4) the shape of the excitation pulse is preserved even after multiple reflections from water-aluminum interface, and finding the arrival time of a particular echo is simply a matter of finding the position of its sharp front edge.

Dispersion, on the other hand, means that the propagation velocity of elastic disturbance depends on its frequency. Because of the finite size of the excitation pulse, its spectrum always contains frequencies within some band of varying width. The traveling elastic disturbance can be treated as a superposition of harmonic waves of different frequencies. Due to dispersion these waves propagate with different ve-

Reproduced with permission of the copyright owner. Further reproduction prohibited without permission.

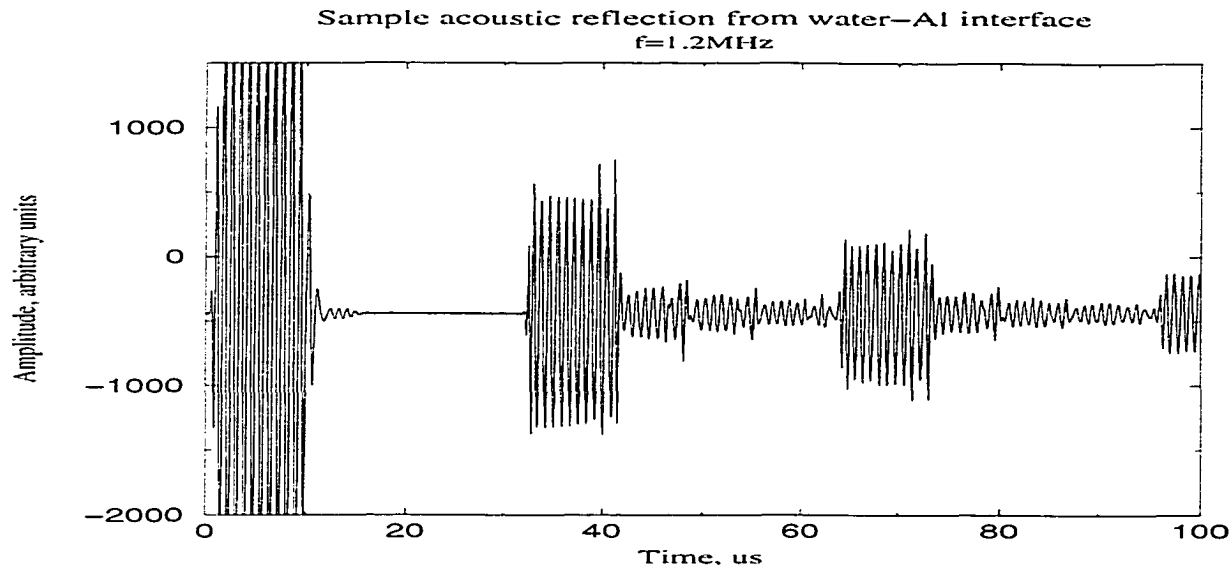

Figure 2.4: Tone burst reflection from the water-aluminum interface. Wave packets do not spread in this nondispersive case. Arrival time is easy to find even after multiple reflections.

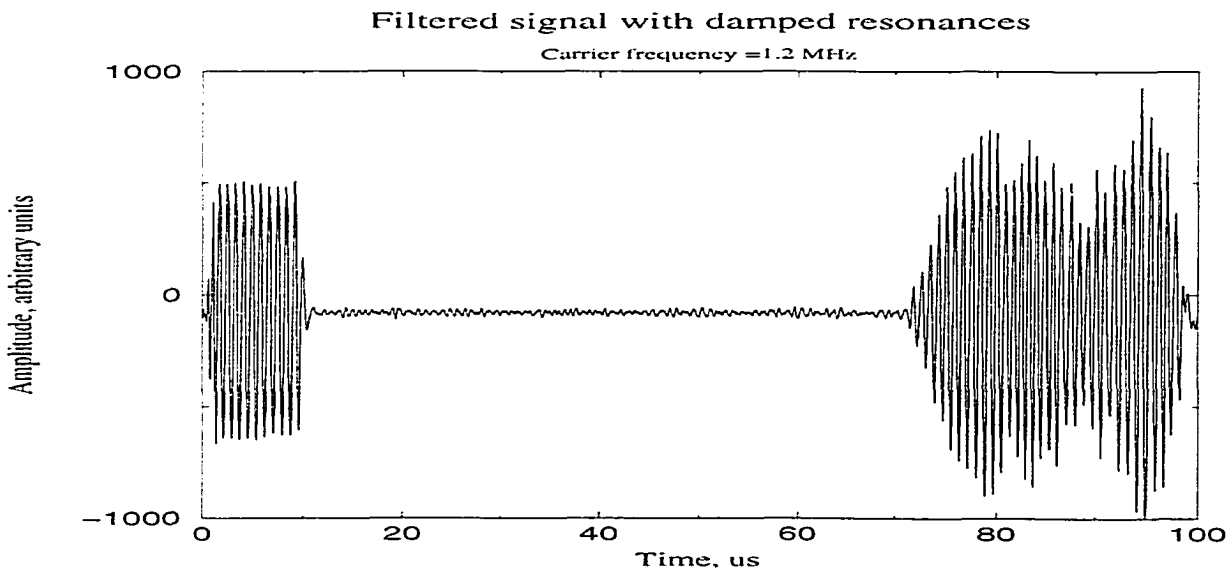

Figure 2.5: Lamb waves: Rectangular envelope of the original tone burst spreads due to dispersion. The arrival time problem is no longer straightforward.

Reproduced with permission of the copyright owner. Further reproduction prohibited without permission.

locities, and the resulting wave packet gets blurred with time. Its shape and length constantly evolve, and determining the arrival time is no longer a straightforward problem, especially for practical tomographic geometries where the ray lengths vary considerably.

However, if the frequency spectrum of the disturbance is nonzero within only a narrow range, the wave packet, once blurred to a certain extent, will later preserve its shape and move as a whole with a group velocity. The latter is a key concept of the guided wave propagation and has been extensively discussed in literature (Brekhovskikh [7], Rose [9], Tohyama and Koike [49], Achenbach [5], Graff [6], Grinchenko and Meleshko [8], Medwin and Clay [50]). Below we summarize several important properties of the group velocity to get more insight into the problem of arrival time estimation.

Group velocity concept

Following the discussion of Brekhovskikh [7], the narrow-band disturbances with spatial spectrum $\hat{f}(k)$ being nonzero only in a small vicinity near some k_0 can be represented as modulated harmonic waves

$$f(x,t) = F(x,t)\exp\left[i(k_0 x - \omega_0 t)\right] \tag{2.1}$$

where $\omega_0 \equiv \omega(k_0)$ and the envelope $F(x,t)$ changes slowly in space and time compared with $\exp\left[i(k_0 x - \omega_0 t)\right]$.

At the initial instance $t = 0$

Reproduced with permission of the copyright owner. Further reproduction prohibited without permission.

$$f(x,0) = \int_{-\infty}^{\infty} \hat{f}(k) \exp(ikx) dk = F_0(x) \exp(ik_0 x)$$

where $\hat{f}(k) \simeq 0$ with $\|k - k_0\| > \Delta k$, $\Delta k \ll k_0$. Setting $k = k_0 + \varepsilon$ we can write:

$$F_0(x) = \int_{-\infty}^{\infty} \hat{f}(k_0 + \varepsilon) \exp(i\varepsilon x) d\varepsilon \tag{2.2}$$

To obtain the disturbance $f(x,t)$ from (2.1) at an arbitrary time t we can assume that $k = k_0 + \varepsilon$ and expand $\omega(k)$ in a Taylor series in the vicinity of k_0:

$$f(x,t) = \int_{-\infty}^{\infty} \hat{f}(k) \exp\{i[k_0 x + \varepsilon x - \omega_0 t - (d\omega/dk)_{k_0} \varepsilon t - \ldots]\} d\varepsilon \tag{2.3}$$

Now we use our assumption of small ε and not very large t and retain only linear term in the expansion (2.3):

$$f(x,t) \simeq \exp\left[i(k_0 x - \omega_0 t)\right] \int_{-\infty}^{\infty} \hat{f}(k_0 + \varepsilon) \exp\{i\varepsilon[x - (d\omega/dk)_{k_0} t]\} d\varepsilon$$

The derivative $d\omega/dk = v_g$ is called the group velocity of the wave because the narrow-band disturbance resembles the modulated harmonic wave:

$$f(x,t) = F_0(x - v_g t) \exp[i(k_0 x - \omega_0 t)] \tag{2.4}$$

with the envelope $F_0(x - v_g t)$ propagating at the group velocity v_g without changing its form. The density of wave energy is concentrated in the area where $F_0(x - v_g t)$ is

Reproduced with permission of the copyright owner. Further reproduction prohibited without permission.

not small, i.e., the energy also moves with the group velocity. The strict mathematical derivation of this fact, based on variational Hamilton's principle, can be found in [5].

It is very important to note that both kinematic and dynamic derivations of velocity assume small changes of the wavenumber and the associated small changes of frequency. If the observation time is also not too large then the next omitted term in the frequency expansion yields a small correction to the phase:

$$\left|\frac{d^2\omega}{dk^2}\right| \frac{\Delta k^2 t}{2} \ll \pi$$

In our experiments Lamb waves are excited with a tone burst composed of several harmonic cycles at the carrier frequency. The frequency bandwidth of this disturbance decreases with increasing number of cycles in the burst and therefore can be made small enough to define the group velocity. Fig. 2.6 demonstrates our typical 13-cycle tone burst at frequency $f = 1.2$ MHz, and Fig. 2.7 shows the typical 5-cycle tone burst at the same frequency. Fig. 2.8 compares Fourier power spectra of the above tone bursts. It is evident that the bandwidth of the input signal can be efficiently controlled by varying the number of harmonic cycles in it. There exists, however, an upper limit to that number due to the tradeoff between transducer separation and pulse length.

The envelope of the initial disturbance is roughly rectangular but after traveling some distance in the plate it generally splits into several envelopes corresponding to different modes that exist in the plate at a given frequency. Later on, if the above conditions are met, all envelopes become relatively stable and propagate with group velocities corresponding to their modes. The modulated carrier wave splits

Reproduced with permission of the copyright owner. Further reproduction prohibited without permission.

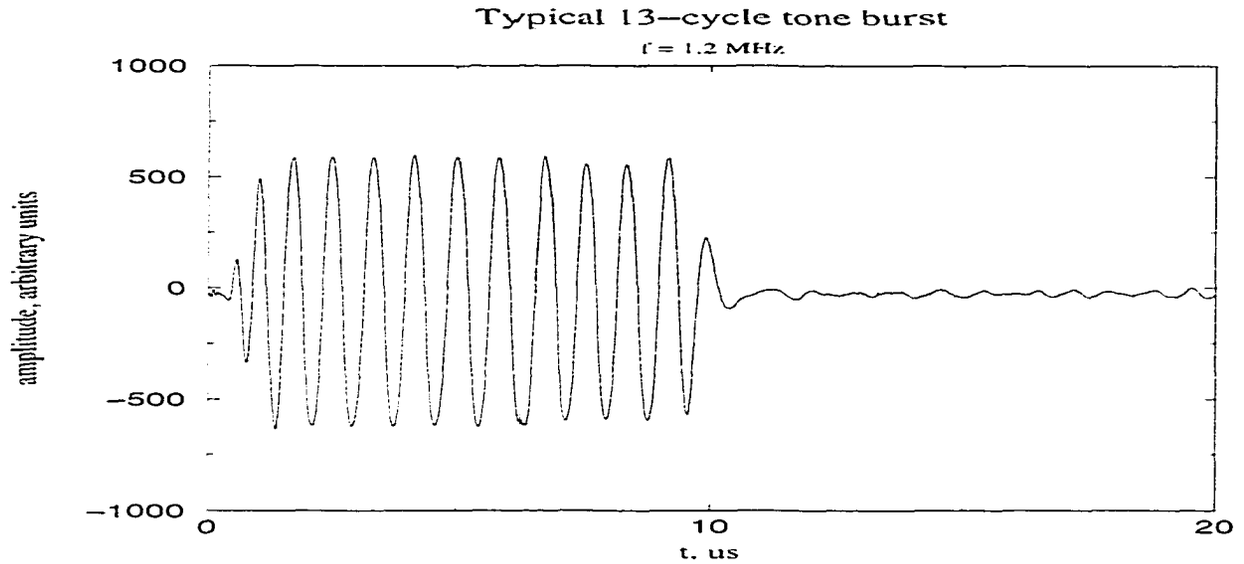

Figure 2.6: Typical tone burst used for Lamb wave excitation. Carrier frequency – 1.2 MHz. number of cycles – 13.

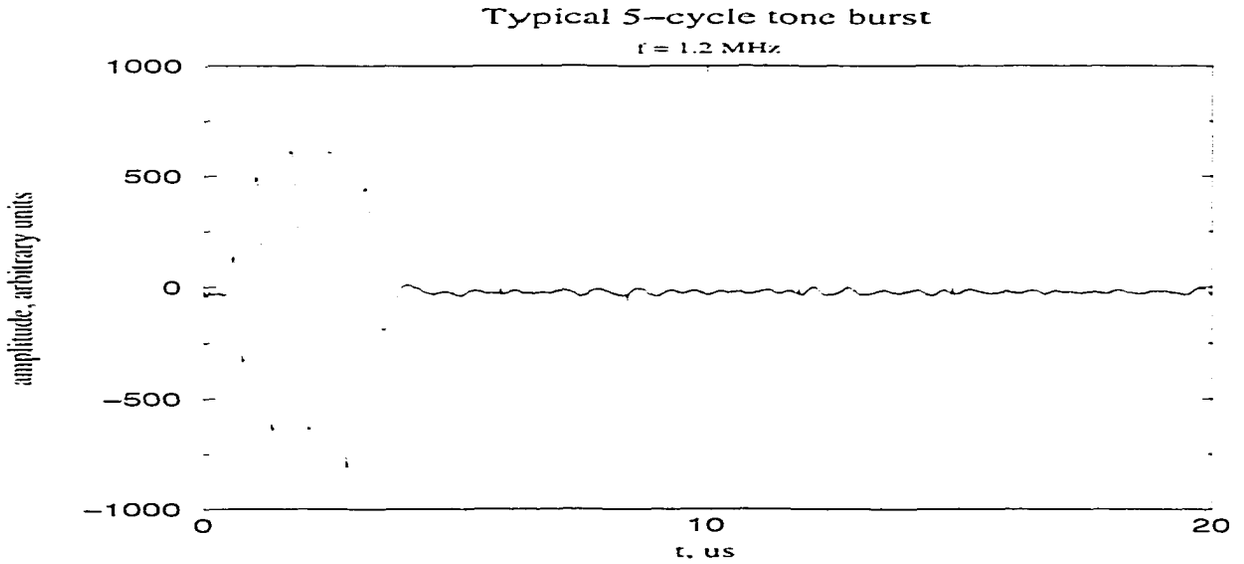

Figure 2.7: Typical tone burst used for Lamb wave excitation. Carrier frequency – 1.2 MHz. number of cycles – 5.

Reproduced with permission of the copyright owner. Further reproduction prohibited without permission.

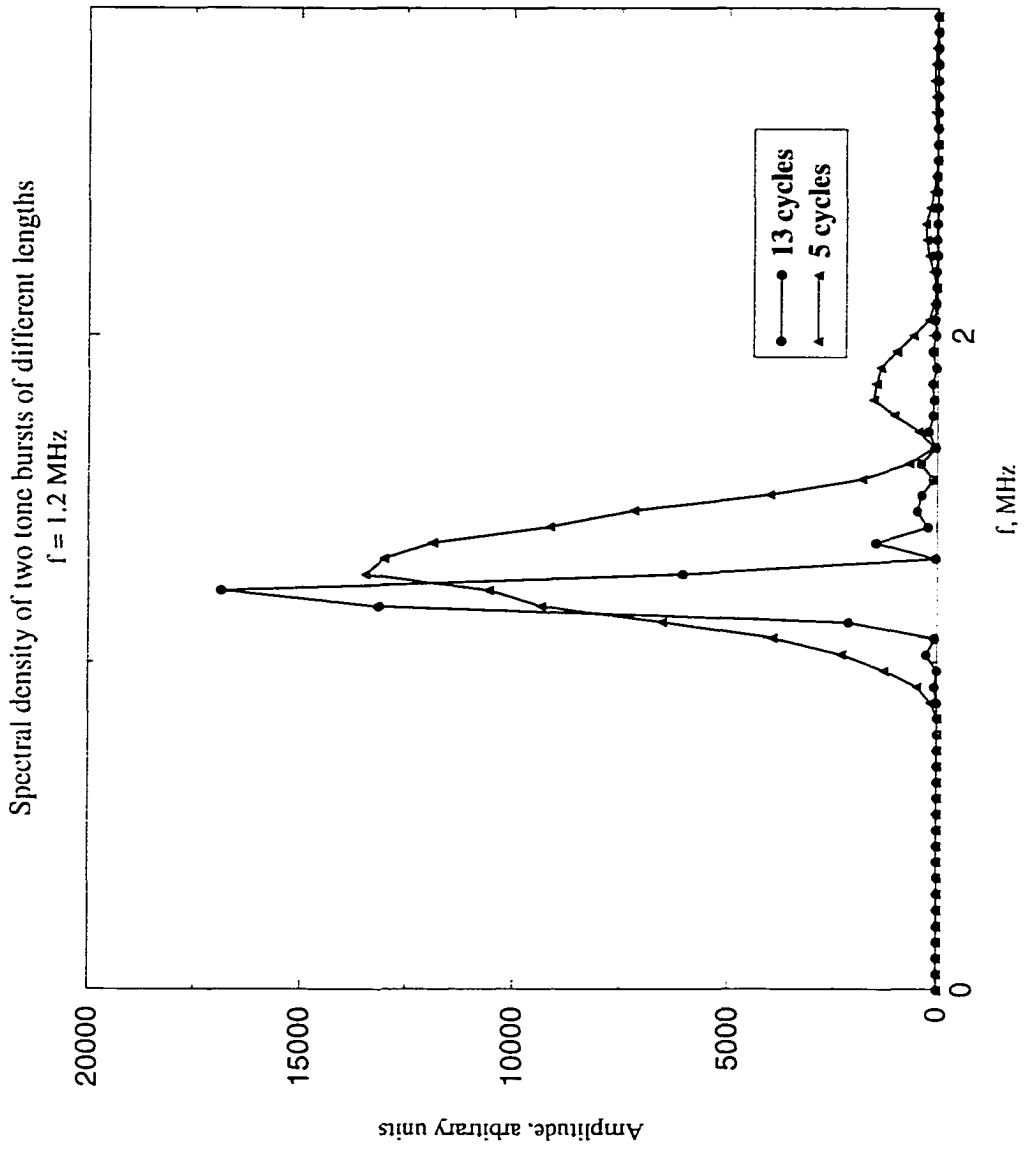

Figure 2.8: Fourier power spectra of two tone bursts of different duration (Figs 2.6 and 2.6). Bandwidth can be effectively controlled by changing the number of cycles in the tone burst.

Reproduced with permission of the copyright owner. Further reproduction prohibited without permission.

into several wavelets each surrounded by its own envelope. In the intersections, i.e. between the S_0 and the A_0 modes, the carrier wave in general undergoes abrupt phase shifts. The physics of such shifts is outlined by Tohyama and Koike [49]; a discussion of signal representation by its envelope and phase can be found in [51].

In the case of broad-band disturbances [6], the larger range of frequencies present in the signal will lead to a larger range of velocities of corresponding harmonic waves in a dispersive medium. Their phases will no longer agree in general, but there will be positions and times at which a number of waves have nearly the same phase. These harmonics will reinforce one another and produce the predominant part of the disturbance. This part again will travel with a group velocity and consist of the dominant frequency ω_0, at which the phase spectrum has a stationary point. Other propagation details will depend on the properties of the amplitude and phase spectra of the disturbance.

It is evident from the above analysis that even in the simplest case of a narrow-band disturbance in a dispersive medium, one must distinguish between the phase and the group arrival times. The former is related to the phase velocity v_{ph} of a particular harmonic, known from the dispersion equation, and can be measured as $t_{ph} = \Delta x / v_{ph}$. Here Δx is a distance between two selected points where the phase of that harmonic is the same. To explain the measurement process, recall that the phase of a one dimensional harmonic wave with frequency ω is given by $\phi = \omega t - kx$. The phases in two points x_1 and x_2 will be equal if

$$\omega t_1 - k x_1 = \omega t_2 - k x_2$$

Reproduced with permission of the copyright owner. Further reproduction prohibited without permission.

or

$$\Delta t = \frac{k}{\omega}\Delta x = \frac{\Delta x}{v_{ph}}$$

The practical measurement scheme is summarized in the Table 2.1:

Phase delay measurement
1. Record the signal in two different locations
2. Find any two points with the phases shifted equally from beginnings
3. Measure the time delay between them

Table 2.1: Phase delay measurement algorithm. Requires signal recording in two different locations.

In the non-dispersive case such a measurement would be a very accurate estimate of the phase velocity. In the dispersive case there are two main obstacles in computing it:

1. It is difficult to locate the beginning of the wave packet with accuracy less than one wavelength since the envelope function grows exponentially from below the noise level and the amplitude of the carrier wave in that region is smaller or comparable to noise;

2. The phase of the carrier wave in general is discontinuous at the intersections of adjacent envelopes and, so far, it has been impossible to accurately keep track of these changes.

Due to these reasons we found it impractical to measure phase arrival times in our experiments and resorted to other alternatives such as the group velocity and the

Reproduced with permission of the copyright owner. Further reproduction prohibited without permission.

associated group delay. Since the shape of a narrow-band disturbance is relatively stable once it develops, it is possible to measure the velocity of the disturbance as a whole by measuring the envelope delay. We formulate the measurement process in the algorithmic form:

Group delay measurement
1. Record the signal in two different locations
2. Determine envelopes of the acquired waveforms
3. Stretch the envelopes to the same scale
4. Find the time delay between their corresponding points

Table 2.2: Group delay measurement algorithm.

The arrival time identification problem is the key concept of the Lamb tomography since the accuracy of its solution very strongly affects all subsequent steps of the inversion process. A significant portion of our work has therefore been devoted to finding a robust and accurate method for time delay estimation. Below we describe the advantages of several signal processing techniques customized for this particular problem. All discussed methods belong to either time-domain (pattern matching, neural networks, heuristic search) or time-frequency domain (time-frequency analysis, wavelet transform analysis, generalized traveltime method) families. The neural networks and pattern matching methods are very general and also can be used in the time-frequency space. In this work, however, they were used only in time-domain context.

Fig. 2.9 shows theoretical arrival times computed as a ratio of the transmitter-receiver distance to the velocity of the S_0 mode in the defect-free plate. The velocity

Reproduced with permission of the copyright owner. Further reproduction prohibited without permission.

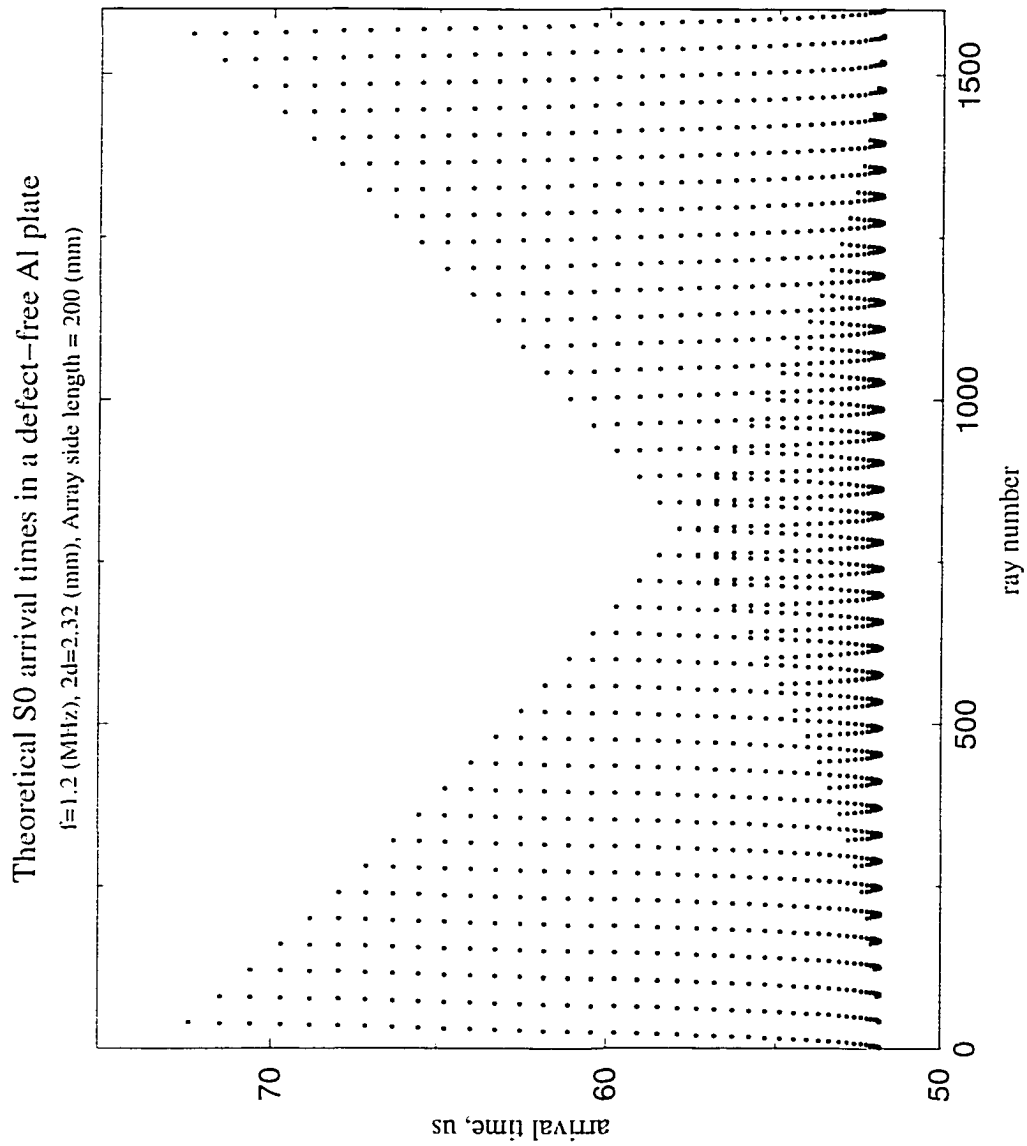

Figure 2.9: Theoretical arrival times of the S_0 mode in a defect-free aluminum plate. To generate this pattern the source-receiver distance was changed the same way as in our crosshole scanner.

Reproduced with permission of the copyright owner. Further reproduction prohibited without permission.

was experimentally estimated to 3.86 $mm/\mu s$. The pattern on Fig. 2.9 is specific to the crosshole geometry and to the chosen scanning method with 40×40 transmitter-receiver positions.

To compare the output of various time delay estimation methods we performed two typical measurement sets on two aluminum plates. One plate was defect-free and the other had a 25.4 mm-diameter 50% thickness reduction flat-bottom-hole in the middle. The data were acquired in a tomographic crosshole experiments with 40 transmitter and receiver positions. For each plate we recorded total of 1600 waveforms resulting from all possible transmitter-receiver positions on a 2.23 mm - thick aluminum plate at a frequency of 1.2 MHz. The transducer step size was 5 mm, and the distance between transmitter and receiver lines was 200 mm.

Each of the time delay estimation algorithms, described in the following sections, was applied to these two experimental data sets. We then computed mean square errors between 1600-point sequences of experimental and theoretical arrival times in defect-free aluminum plate. The value of the mean square error served as an independent measure of the performance of each algorithm.

2.2 Pattern matching techniques

One of the powerful time-domain detection methods is pattern matching. Given some signal-like pattern one can match it point by point against parts of the signal until a specified accuracy (or minimum error) is reached. Two common error measures are mean square error and absolute deviation. Using this technique some acceptable results were obtained by McKeon and Hinders [46–48]. Another popular way of

Reproduced with permission of the copyright owner. Further reproduction prohibited without permission.

finding similarities in different traces is to search for peaks of their cross correlation functions [52]. To determine the arrival time of the S_0 Lamb wave mode we used the procedure given in Table 2.3.

Pattern matching algorithm
1. Record several sample signals.
2. Identify and extract signal portions corresponding to the S_0 mode.
3. Study the properties of extracted wave packets.
4. Generate a pattern mimicking the shape of the packet.
5. Move the pattern step by step along the measured signal.
6. At each step compare the pattern against the portion of the signal.
7. If match occurs, compute the arrival time from pattern position.

Table 2.3: Pattern matching algorithm.

An exact match between the pattern and a part of a measured signal is a very improbable event. A less restrictive method for estimating the difference between two discrete data sets $\{S_i\}$ and $\{P_i\}$, $i = (0 \ldots N-1)$ is measuring the mean square (MS) error:

$$\delta_{ms} = \frac{1}{N} \sum_{i=0}^{N-1} (S_i - P_i)^2 \tag{2.5}$$

or the absolute error:

$$\delta_{abs} = \frac{1}{N} \sum_{i=0}^{N-1} |S_i - P_i| \tag{2.6}$$

After moving the pattern along the signal and measuring corresponding error (steps 5,6) we identify the step where δ_{ms} or δ_{abs} reaches its minimum and declare that a match. Step 7 then computes the arrival time sought.

Reproduced with permission of the copyright owner. Further reproduction prohibited without permission.

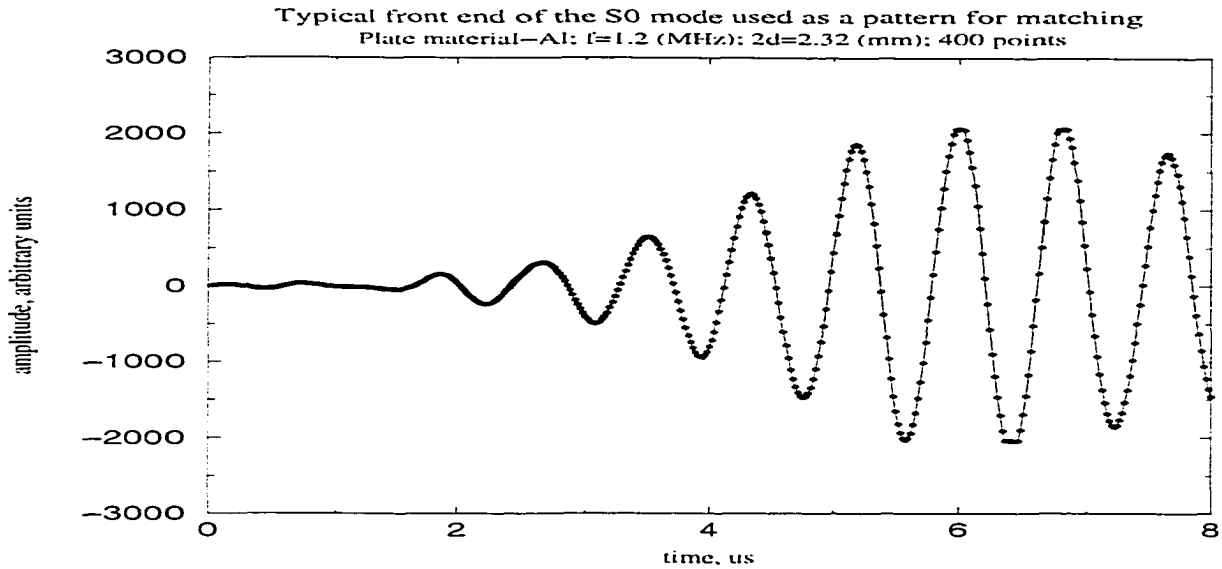

Figure 2.10: Typical shape of the leading edge of the fastest mode. It is difficult to accurately find the beginning of the wave packet.

It is worth noting that the minimum MS or absolute error by itself does not guarantee the perfect match, but only the best among tested cases. The resemblance between the pattern and the corresponding section of a signal may be very poor, in which case the above algorithm fails. Thoughtful pattern design is therefore a key point of the MS-error matching algorithm.

Fig. 2.10 represents a typical shape of the first arrival in our experiments. A simple and rather good approximation to it could be a sine wave modulated by Gaussian or other bell-shaped function. The envelope of the first arrival may change significantly depending on the travel distance and presence of defects, but the model can be adjusted accordingly by changing the Gaussian parameters. However, in tomographic experiments we record thousands of rays traveling through unknown media and we don't know *apriori* the shape of the next signal.

Reproduced with permission of the copyright owner. Further reproduction prohibited without permission.

As a first approximation we applied this method to experimental data sets using several static patterns, such as several cycles of sine wave modulated linearly, with Gaussian or with other functions. As expected, matching produced reasonably good results for the defect-free plate, when the shape of the first arrival is relatively stable. In the presence of defects, matching results were often unpredictable and arrival times determined with this method, can be used only for qualitative statements about the presence/absence of defects.

After a series of experiments with static patterns we realized that the matching pattern should be adapted to the changes in the shape and amplitude of the part of the signal of interest. To accomplish this, either a challenging forward modeling problem must be solved, or some empirical knowledge has to be utilized. The forward problem could be solved by numerically propagating Lamb waves in the region of interest using finite difference method [53], boundary element method [83] or other numerical propagator, such as the one proposed by Pan and Wang [54]. Then the shape of the S_0 mode could be calculated and used as a matching pattern to measure the real times. As a drawback, this method requires some *a priori* information about defect distribution in the scanned region. This knowledge would be impossible to obtain while rapidly inspecting large areas of unknown objects.

An alternative method would use the signals recorded in previous experiments to compare against the current signal. The library would contain a great variety of sample waveforms together with calculated arrival times. Matching against the current signal could be either done one by one, and then finding a global minimum MS error to declare success, or using a trained neural network. The latter method

Reproduced with permission of the copyright owner. Further reproduction prohibited without permission.

will be discussed later.

Tomographic resolution improves with increasing the number of measurements per projection. For large numbers of steps the transducer position increment becomes rather small. In the approximation of continuous defects without sharp edges, the difference between signals, acquired in two successive measurements, would also be small. We therefore can use part of the previously processed signal as a pattern to match against the current one (target tracking). Although not so comprehensive, this way is much faster and more elegant than building a database of all possible signals. The stability of this algorithm strongly depends on the accuracy of previous steps, structure of the signal and pattern width. To avoid mistakes we should start matching in the vicinity of the signal start (unknown). This can be done via making scan steps small (signal changes smoothly) or using theoretical prediction of the arrival time. The first case provides high accuracy until random errors make it unstable. To improve stability one should incorporate additional knowledge about temporal properties of the signal (wavelength and zero crossings) into the algorithm. The second case is always stable but each step has errors that show up after image reconstruction. As a drawback, the first arrival time for each measurement set should be extracted manually.

The last procedure is summarized in the Table 2.4:

Reproduced with permission of the copyright owner. Further reproduction prohibited without permission.

Adaptive pattern matching algorithm
1. Manually extract the S_0 arrival time t_1 from the first waveform in a dataset.
2. Select a desired number of points from vicinity of t_1 as a matching pattern.
3. Apply matching algorithm to the next waveform and extract the arrival time.
4. Choose the next pattern from the current waveform as in 2.
5. Repeat from 3. for all waveforms.

Table 2.4: Adaptive pattern matching algorithm.

Fig. 2.11 shows the result of application of adaptive pattern matching algorithm to the test tomographic data set acquired on a defect-free aluminum plate. The pattern length N in this case was chosen to be 400 points. Comparison with theoretical arrival times (Fig. 2.9) shows an MS error of 2.74. Although the method shows good potential in tracking the arrival time of successive signals, it can be seen that its results often differ from their expected values by several wavelengths. Such failures occur from time to time because the MS-error matching criterion is very weak and should probably be substituted by another more accurate measure. Yet another cause of failure is that different signals are digitized at different points. To accurately compare them one must first interpolate and artificially oversample them to reduce the quantization discrepancies.

Fig. 2.12 shows the result of application of adaptive pattern matching algorithm to the test tomographic data set acquired on an aluminum plate with a 25.4 mm-diameter circular 50% thickness reduction flat bottom hole. Visual analysis of the plot reveals the same quality problems as with a defect-free plate.

We can conclude that the adaptive pattern matching is capable of tracking arrival times but needs further enhancements such as:

- Choosing a match criterion more restrictive than δ_{ms} or δ_{abs};

Reproduced with permission of the copyright owner. Further reproduction prohibited without permission.

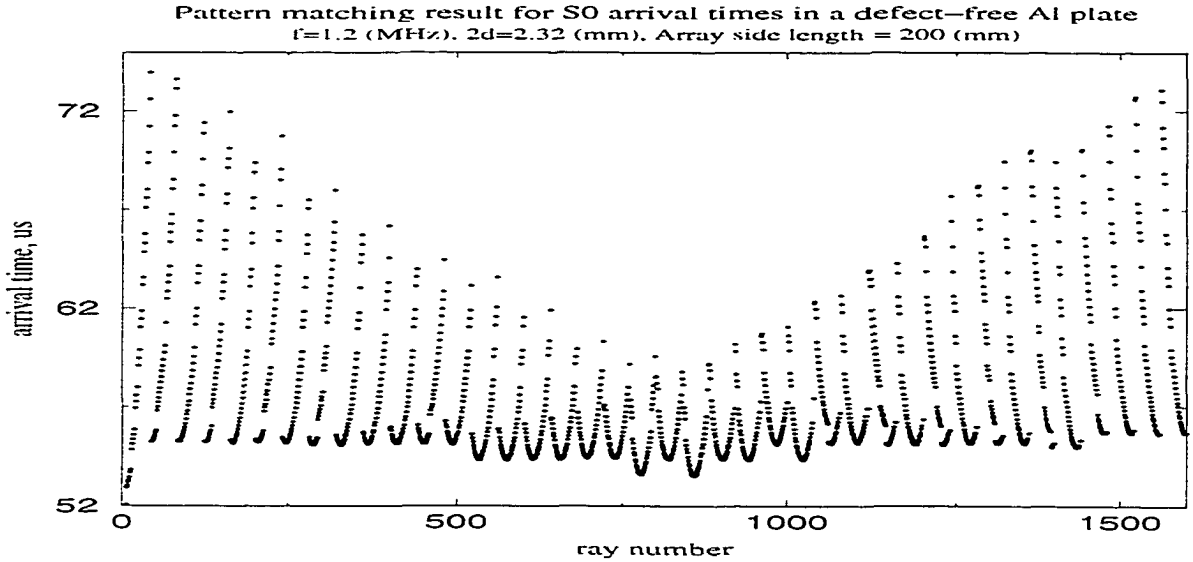

Figure 2.11: Arrival times in a defect-free aluminum plate, obtained with adaptive pattern matching method. Comparison with theoretical times (Fig. 2.9) yields MS error $\delta_{ms} = 2.74$.

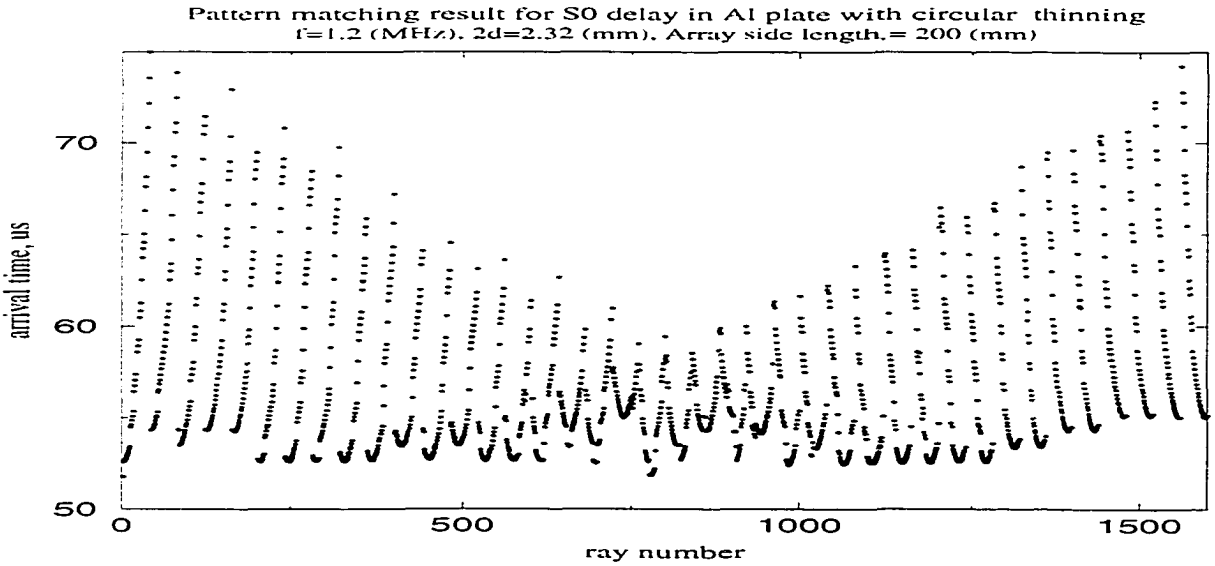

Figure 2.12: Arrival times in aluminum plate with 25.4 mm-diameter flat-bottom hole in the center, obtained with adaptive pattern matching method.

Reproduced with permission of the copyright owner. Further reproduction prohibited without permission.

- Using AD converters with higher vertical quantization rate;
- Optimizing pattern length and the size of time search window.

2.3 Neural network approach

In the previous section we found that the pattern matching approach is potentially capable of solving the arrival time problem for the Lamb wave tomography. However, the mean square error is a very rough resemblance measure and using it as the only matching criterion does not guarantee a fail-safe performance. We believe that a match should be declared only when several independent conditions hold simultaneously. The Artificial Neural Network (ANN) method is an example of such an approach.

K. Leonard ([55]) studied the performance of the ANN with a backpropagation training algorithm applied to the S_0 arrival time problem. To train the network he used sets of waveforms captured in tomographic experiments. When 1600 whole waveforms were used for training, comparison of the output arrival times to theoretical ones yielded an MS error $\delta_{ms} = 1.1$. Even better performance was observed when only portions of waveforms, surrounding first arrivals, were used for training. These portions can be easily extracted by means of some lower-resolution method such as one of the time-frequency algorithms discussed below. Using 400-sample portions the network yielded an MS-error $\delta_{ms} = 0.882$ which is significantly better than that for the pure time-frequency algorithm. One of the results reported in [55] is the ability of the ANN to smooth the original time-frequency data, partially eliminating the

Reproduced with permission of the copyright owner. Further reproduction prohibited without permission.

systematic uncertainty in the arrival times. This is due to the more comprehensive matching criteria used in ANN.

As a general conclusion of [55], the backpropagation training algorithm was unable to successfully recognize both the signal (the S_0 mode) and its arrival time. This problem is much more complicated that just recognizing the pattern of the S_0 mode and needs either some preprocessing of the input or a different topology. A time delay neural network used to recognize specific structures occurring in consecutive frames of speech is listed as a more appropriate alternative.

2.4 Time-frequency analysis

The time domain pattern matching approach requires a great deal of empirical knowledge about the signal of interest. For instance, to start the adaptive pattern matching algorithm the operator must supply the hand-picked arrival time of the first signal in the set and use some theoretically calculated arrival times to outline the search zone. The neural network approach needs even more information in the form of the signal database necessary for training the network, which can be quite different for different materials, etc.

Software for an industrial tomographic inspection system should be able to work in autonomous mode with little or no input from the operator. The operator would, if needed, input the operating frequency, material parameters and DAQ sampling rate to set up the measurement equipment. It is desirable, however, to let a software expert system do the rest of the work. We considered the time-frequency approach as a promising substitute to the pure time domain methods.

Reproduced with permission of the copyright owner. Further reproduction prohibited without permission.

The idea behind time-frequency analysis is that the energy density spectrum tells us which frequencies existed during the whole duration of the signal and no indication as to when they existed (Cohen [56]). A great variety of more or less successful methods have been developed to combine the time and frequency domains of the signal into a more powerful and informative representation. The advantage of a joint time-frequency representation would be the simultaneous knowledge about the presence of particular frequencies in the signal and times at which those frequencies occur. So far no universal distribution, capable of handling different signals with equally good resolution has been constructed. All existing successful transforms are tailored to particular signals and our purpose was to find one yielding enough resolution both in time and frequency domains for accurate extraction of the features of interest from the recorded Lamb wave signals. Such a distribution would combine the most useful information in both domains and simplify detection of the arrival time of the event at particular frequency.

In our tomographic experiments we excite Lamb waves with a narrow-band tone burst and the first received arrival is a wave packet composed of the amplitude-modulated central carrier frequency. The spectrum of such a packet has a sharp maximum at the carrier frequency. The part of the signal before the first arrival would not contain that frequency. We believe that using appropriate time-frequency algorithm it is possible to determine the time when the carrier frequency enters the signal spectrum - i.e. the signal arrival time.

The simplest time-frequency representation can be constructed by means of a moving-window Fourier transform. The window of a fixed size moves along the signal

Reproduced with permission of the copyright owner. Further reproduction prohibited without permission.

and at each step its content is Fourier transformed to determine which frequencies existed in that time interval. Narrowing the window to a certain extent increases the resolution in time but for very short windows the spectrum becomes meaningless because of the increasing bandwidth of the short signals.

More generally, an uncertainty principle can be formulated which states that the signal with both arbitrarily small bandwidth and duration can not exist. To formulate the uncertainty principle we will follow the discussion from [56] and define the measures of signal duration σ_t and of the bandwidth σ_ω analytically:

$$\sigma_t^2 = \overline{t^2} - \overline{t}^2 = \int (t - \overline{t})^2 |s(t)|^2 dt \tag{2.7}$$

$$\sigma_\omega^2 = \int (\omega - \overline{\omega})^2 |S(\omega)|^2 d\omega \tag{2.8}$$

where σ_t and σ_ω are standard deviations of signal $s(t)$ and its spectrum $S(\omega)$. The signal density $|s(t)|^2$ is concentrated mainly in the interval of width $2\sigma_t$, and its spectral power density $|S(\omega)|^2$ is confined within a band of width $2\sigma_\omega$.

We also define the covariance of a signal as:

$$Cov_{t\omega} = \int t\phi'(t)|s(t)|^2 dt - \overline{t}\overline{\omega} = \overline{t\phi'(t)} - \overline{t}\overline{\omega} \tag{2.9}$$

where $\phi(t)$ is the phase of a signal and $\phi'(t)$ is the instantaneous frequency at time t. The covariance, as defined above, is a good measure of how time is correlated with instantaneous frequency.

Reproduced with permission of the copyright owner. Further reproduction prohibited without permission.

The uncertainty principle, proof of which is based on the Cauchy-Schwartz inequality, states that

$$\sigma_t \sigma_\omega \geq \frac{1}{2}\sqrt{1 + 4Cov_{t\omega}^2} \tag{2.10}$$

(2.10) means that the bandwidth and duration of any signal cannot be arbitrarily small at the same time. Moreover, the minimum value for their product depends on the properties of a particular signal and by no means can be less than $\frac{1}{2}$ (when $Cov_{t\omega} = 0$).

This shows that the window size in the moving-window Fourier transform cannot be made arbitrarily small without affecting the bandwidth of the corresponding part of the signal. The time resolution limit of a spectrogram will therefore be equal to the size of the smallest window capable of reliably detecting the carrier frequency. Such a detection is possible only when the part of signal within the window includes at least one complete period at a carrier frequency. At 1 MHz such a period T will be:

$$T = \frac{1}{f} = 1\mu s$$

A typical value for the phase velocity of the S_0 mode in aluminum in our experiments is $v_{ph} = 3.8mm/\mu s$. Hence, if the distance between transmitter and receiver changes by 0.26 mm, the phase of the wave shifts 2π or one period. The best temporal resolution of the spectrogram in our case is equivalent to that when the transmitter-receiver distance randomly changes by $\pm 0.26mm$. Of course, for better frequency resolution the real window must be wider than just one temporal period.

Reproduced with permission of the copyright owner. Further reproduction prohibited without permission.

The low temporal resolution of a spectrogram forced us to look for alternative distributions, which would be capable of handling our signals. The Wigner distribution [56] is the prototype of distributions that are qualitatively different from the spectrogram. It can be defined both in terms of the signal $s(t)$ or its spectrum $S(\omega)$:

$$W(t,\omega) = \frac{1}{2\pi}\int s^*(t-\frac{\tau}{2})s(t+\frac{\tau}{2})e^{-i\omega\tau}d\tau = \frac{1}{2\pi}\int S^*(\omega-\frac{\theta}{2})S(\omega+\frac{\theta}{2})e^{-it\theta}d\theta \tag{2.11}$$

This distribution can be readily applied to signals without any special preparation. To study its resolution and computational efficiency we implemented it numerically using our multipurpose FFT routine.

The Wigner distribution does not belong to a class of positive distributions because it is not positive throughout the time-frequency plane. In addition, it is not necessarily zero when the signal is zero and at frequencies that do not exist in the signal spectrum. These phenomena are called interference or "cross terms" and lead to numerous artifacts in the resulting two dimensional representation. Fig. 2.13 demonstrates the signal (b) typical for our experiments, its Fourier power spectrum (c) and the corresponding Wigner transform (a). The cross term artifacts show up at frequencies higher than the peak frequency on the signal power spectrum. These artifacts complicate traversing the time frequency plane while looking for the signal arrival time. However, such a search can be implemented if we start it from the left side and go to the right along the horizontal line corresponding to the frequency of interest. Visual comparison shows good correlation between the signal start and the beginning of the red line at the carrier frequency. It would be desirable, however,

Reproduced with permission of the copyright owner. Further reproduction prohibited without permission.

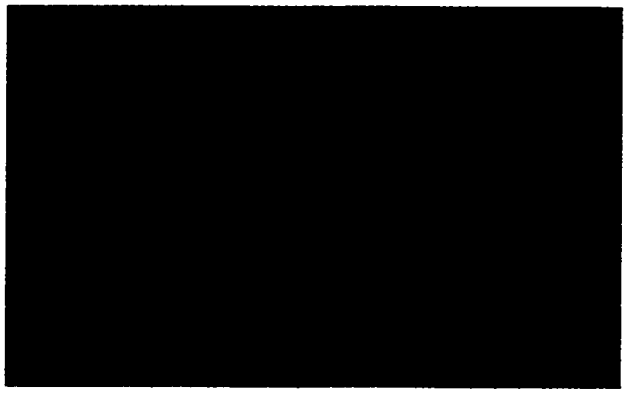

a. Wigner transform.

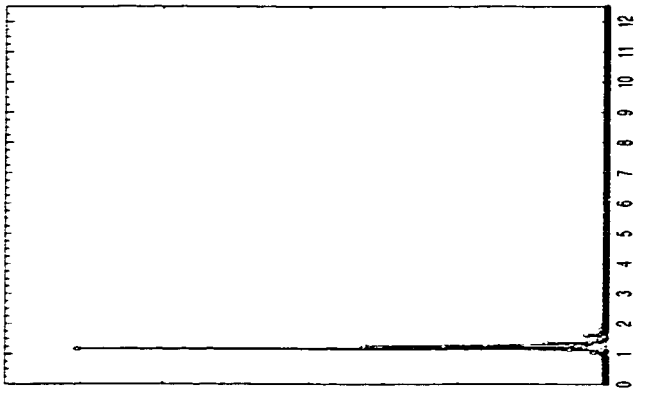

b. Power spectrum.

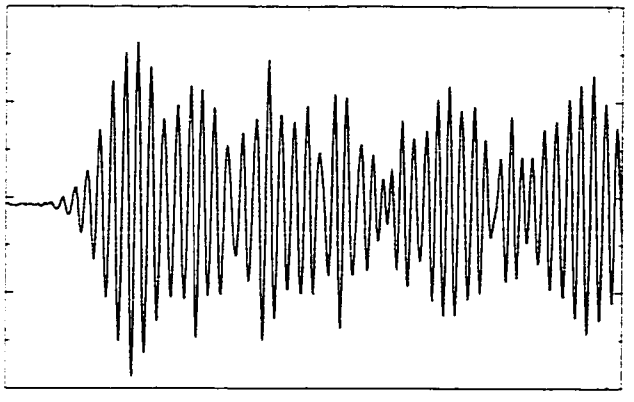

c. Original signal.

Figure 2.13: (a) – Wigner transform of the signal (c). The power spectrum is shown in (b). The Wigner distribution was computed according to (2.11), note severe artifacts at frequencies above the carrier frequency (peak frequency on the power spectrum (b)).

Reproduced with permission of the copyright owner. Further reproduction prohibited without permission.

to reduce the level of cross term artifacts and to speed up the computation process. Straightforward numerical computation of the Wigner distribution of an N-point signal requires N Fourier transforms. Although rather fast for one signal, this process becomes the major bottleneck if many (tens of thousands) of signals are involved. In addition, the Wigner transform needs higher sampling rate than the conventional DFT to avoid aliasing, its frequency resolution is reported to be only a quarter of that obtained by DFT [29].

A successful attempt to adapt Wigner distribution to study the dispersion of Lamb waves is described in [29]. This approach involves calculation of so called Wigner-Ville distribution which is a Wigner distribution of the analytic signal. The analytic signal is a complex signal where the real component is the original signal and the imaginary component is its Hilbert transform. The Wigner-Ville transform reduces the sampling requirement to that of the Nyquist criteria. To minimize the cross term interference the Wigner-Ville distribution is convolved with a Gaussian window function $G(t, \omega)$. The resulting pseudo Wigner-Ville distribution is positive and much less noisy than its predecessors. It was effectively employed in [29] for the arrival time estimation and building Lamb wave dispersion curves. Although the results with experimental data were less accurate than those with simulated waveforms, the method is stated to be quite useful for the dispersion curve calculation purposes.

Even though pseudo Wigner-Ville distribution has many advantages over the Wigner distribution, by definition it is even more time consuming. In the case of Lamb wave tomography this fact is very restrictive and we decided to look for other existing time-frequency transforms.

Reproduced with permission of the copyright owner. Further reproduction prohibited without permission.

As pointed out in [56] the joint time-frequency density $P(t,\omega)$ should satisfy two obvious requirements called marginal conditions. They state that summing up the energy distribution for all frequencies at a particular time should give the instantaneous energy and summing up over all times at a particular frequency should give the energy density spectrum:

$$\int P(t,\omega)d\omega = |s(t)|^2 \tag{2.12}$$

$$\int P(t,\omega)dt = |S(\omega)|^2 \tag{2.13}$$

where $|s(t)|^2$ is intensity per unit time at time t and $|S(\omega)|^2$ is intensity per unit frequency ω. The distribution based on the short time Fourier transform (the spectrogram) generally does not satisfy these conditions because windowing introduces effects unrelated to the properties of the original signal. The Wigner distribution satisfies both marginals (2.12) and (2.13) but is not positive. Wigner showed [56] that manifestly positive bilinear distributions satisfying the time and frequency marginals do not exist.

However, there exists a class of positive distributions satisfying the marginal requirements and not bilinear in the signal:

$$P(t,\omega) = |S(\omega)|^2|s(t)|^2\Omega(u,v) \tag{2.14}$$

where

Reproduced with permission of the copyright owner. Further reproduction prohibited without permission.

$$\int_0^1 \Omega(u,v)du = 1 \quad ; \quad \int_0^1 \Omega(u,v)dv = 1 \tag{2.15}$$

Variables $u(t)$ and $v(\omega)$ can be defined as accumulating signal (spectral) energy from the beginning of the signal (spectrum) to the points t (ω) correspondingly.

We decided to use distributions (2.14) to estimate arrival time of the S_0 mode in the Lamb Wave tomographic experiment. The form of the appropriate function $P(t,\omega)$ is determined by the behavior of $\Omega(u,v)$. For simplicity and to satisfy (2.15) we chose

$$\Omega(u,v) \equiv 1 \quad and \quad P(t,\omega) = |S(\omega)|^2|s(t)|^2 \tag{2.16}$$

So defined, the distribution 2.16 is obviously positive (non-negative). Whenever the signal at certain time or the spectrum at a certain frequency is zero, the distribution is also zero – the property called strong finite support. The marginals (2.12) and (2.13) can in general be satisfied only for special signals with unit integral spectrum. However, this is not a problem for our purposes. In addition, mathematical simplicity of 2.16 yields very low computational requirements. To be calculated numerically for the signal of length N (2.16) needs only one Fourier transform of order N, which is N times faster than the Wigner transform.

The results of application of (2.16) to the same signal as in Fig. 2.13 are shown in Fig. 2.14a. The interference and any other types of artifacts are completely absent in the image. The carrier frequency can be easily identified and corresponds to the maximum of the Fourier power spectrum (Fig. 2.14b). The arrival time can also be

Reproduced with permission of the copyright owner. Further reproduction prohibited without permission.

a. Positive transform.

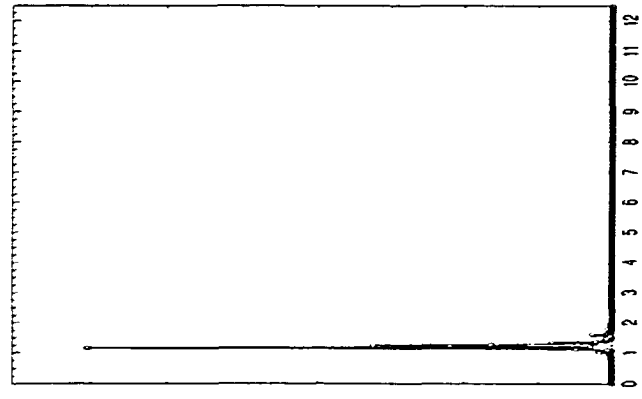

b. Power spectrum.

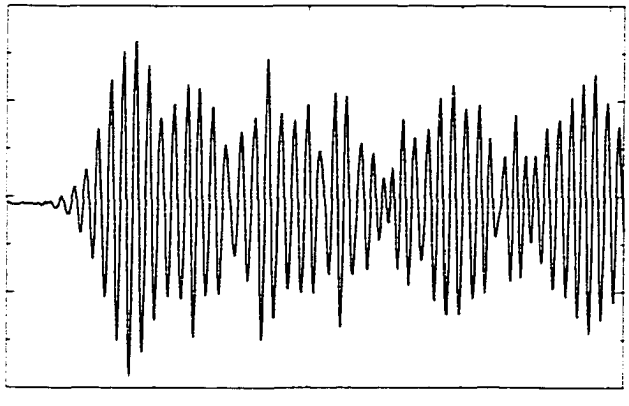

c. Original signal.

Figure 2.14: (a) – custom positive transform of the signal (c). The power spectrum is shown in (b). The time frequency distribution is based on the equation (2.16), note the absence of artifacts on the image.

Reproduced with permission of the copyright owner. Further reproduction prohibited without permission.

found via traversing the image. The accuracy, however, depends on several factors including the uncertainty principle, which holds for this particular distribution, and the way we process the image.

The application of the positive time-frequency distribution (2.16) can be summarized into Table 2.5:

Measuring arrival time with Positive distribution
1. Compute FFT of the current zero-mean waveform
2. Determine the carrier frequency f
3. Construct distribution 2.16 and build the image
4. Traverse the image in the vicinity of f to get the arrival time

Table 2.5: Measuring arrival time with Positive distribution

This algorithm is computationally efficient and capable of working in the autonomous mode. Indeed, to start it one must supply only the carrier frequency and such general parameters as the signal sampling rate and the number of points in the waveform. Below we discuss the results of its practical usage.

Figures 2.15 and 2.16 demonstrate results of the application of the arrival time location algorithm to the test data sets described earlier. Even visually the overall quality of the data is far superior to that obtained with the adaptive pattern matching algorithm (Fig. 2.11 and 2.12). Comparison of Fig. 2.15 to the theoretical set of arrival times for the defect-free aluminum plate (Fig. 2.9) demonstrates an MS-error of $\delta^2_{ms} = 2.188$ which is much better than that of the adaptive pattern matching ($\delta^2_{ms} = 2.74$). The arrival time pattern in Fig. 2.16 reveals the presence of a defect in the middle of the scanned area. This shows up as a relative slowing down

Reproduced with permission of the copyright owner. Further reproduction prohibited without permission.

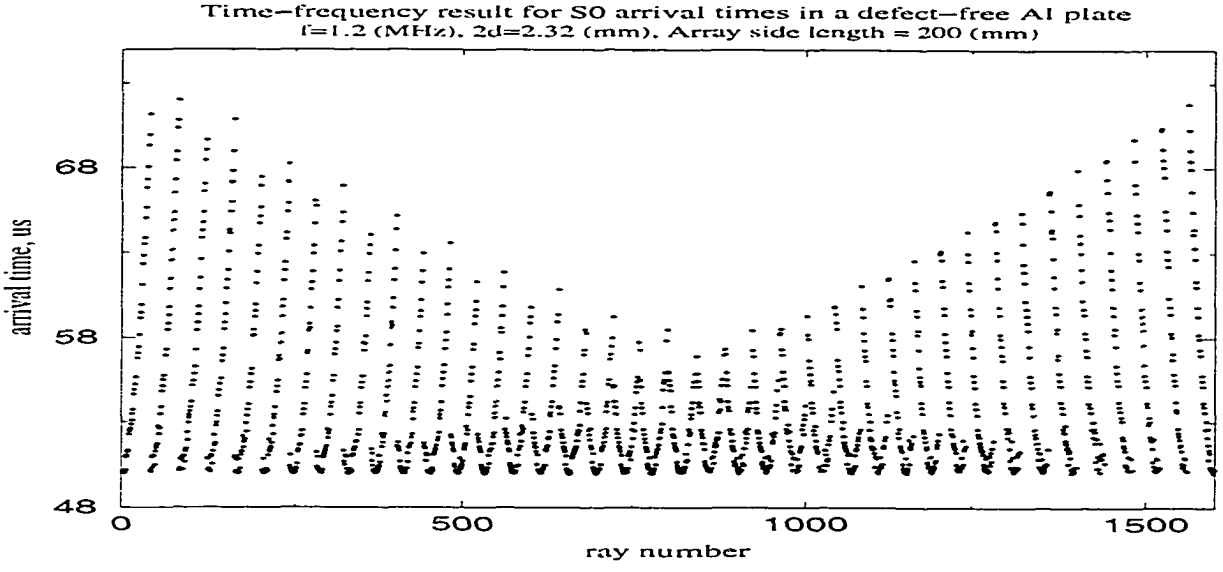

Figure 2.15: Arrival times in a defect-free aluminum plate obtained with a time-frequency algorithm based on a positive distribution (2.16). Comparison with theoretical times (Fig. 2.9) yields MS error $\delta_{ms} = 2.188$.

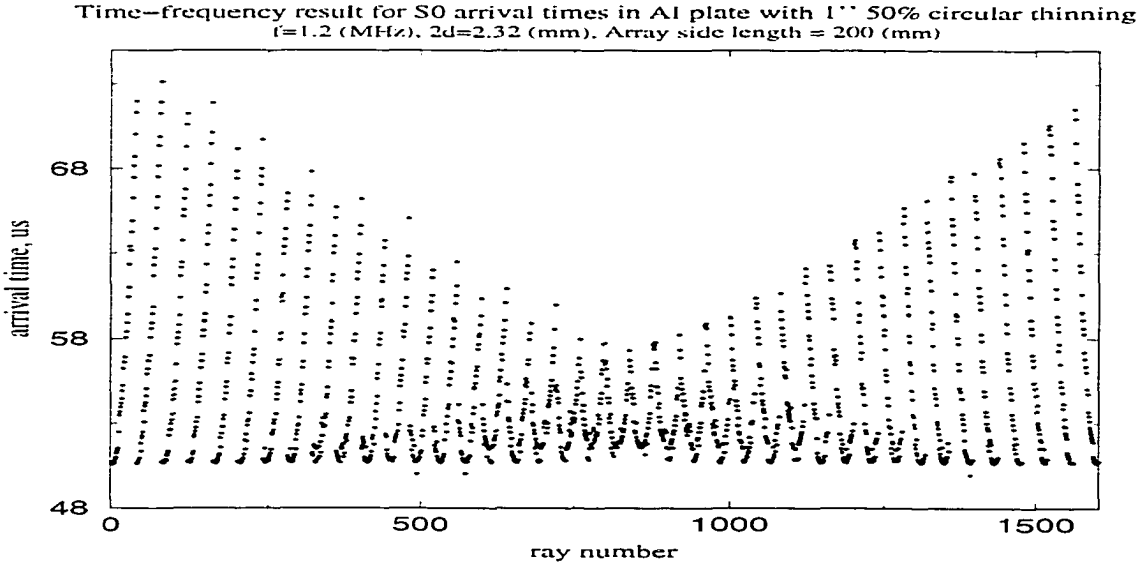

Figure 2.16: Arrival times in aluminum plate with 25.4 mm-diameter flat-bottom hole in the center obtained with a time-frequency algorithm based on a custom positive distribution.

Reproduced with permission of the copyright owner. Further reproduction prohibited without permission.

in the central part of the lower boundary of the arrival times. In other words, the accuracy of the time-frequency method is high enough to resolve a flat bottom hole with confidence. It is worth noting that the adaptive pattern matching algorithm also resolved it, but the error level was much higher. However, theoretical arrival times change strictly in accordance with the transmitter-receiver distance while the output of time-frequency algorithm displays intervals of regular change intermingled with comparably long jumps. The common order of magnitude of these jumps is one or two periods (wavelengths) of the Lamb wave. The reason for this lies in the nature of the time-frequency analysis. The uncertainty principle (Eq. 2.10), which holds for the positive distribution used, prohibits simultaneous exact knowledge of time and frequency of the event. Since the current image traversing scheme uses only one frequency (the carrier) to search for the arrival time, the latter can be found with uncertainty of the order of $1-2$ wave periods. The recommended solution would be to look for the arrival time within a broader frequency band thus improving temporal accuracy.

The results of this section can be summarized as follows:

- The spectrogram and the Wigner family of time-frequency distributions can potentially be used to determine signal arrival times but are computationally-intensive and suffer from interference or aliasing artifacts, complicating the search procedure.

- We found a distribution (2.16) that has strong finite support, obeys the uncertainty principle and is physically intuitive and mathematically simple. It can be computed much faster than the above distributions and does not create any

Reproduced with permission of the copyright owner. Further reproduction prohibited without permission.

artifacts. In addition, it is applicable to our particular signals. When applied to the test data set, this distribution produces rather (in MS-sense) results and can be used for efficient arrival time extraction in an autonomous mode.

- Systematic errors in time computation due to the uncertainty principle could potentially be reduced if Fourier Transform were substituted with a custom wavelet transform.

2.5 Wavelet transform analysis

Wavelet transform-based methods constitute a strong alternative to the common Fourier analysis when resolution in both time and frequency is an issue. Harmonic waves are not the only family of functions that form orthogonal bases on the finite interval. There exist a great variety of such families each allowing for signal expansion into an infinite sum of wavelets with corresponding coefficients. All wavelets in a chosen family can be derived from the so called mother wavelet. The main idea behind the wavelet transform is that the choice of the mother wavelet affects the number of terms in the series expansion of the signal. In other words, the closer the mother wavelet resembles the signal, the fewer significant terms (frequencies) will be present in the series expansion. Unlike harmonic waves, infinite in time, most of the commonly used wavelets are localized both in time and frequency domains. This property makes them potentially very useful for the much more accurate estimation of arrival times than that of the Fourier-based time-frequency methods [57], [58].

The wavelet transform method has been successfully implemented by Legendre

Reproduced with permission of the copyright owner. Further reproduction prohibited without permission.

et al. [59] for the problem of detection of arrival times of certain Lamb Wave modes, generated by EMAT transducers in the metallic walls of hydrogen reservoirs. Also, even after 64-time averaging the signals in [59] were rather noisy, but the authors successfully detected the peak value of the wave packet of the desired mode.

Since the typical low-noise Lamb wave signal (Fig. 2.3) in our experiments consists of a single carrier frequency, modulated by slowly changing envelopes, choosing the mother wavelet as a modulated piece of a sine wave at a carrier frequency would be both simple and effective. The only potential problem could be the constantly changing shape of the signal leading to the corresponding changes in its spectrum. The time-frequency search for the arrival time could be performed similarly to that in Fourier-based methods, except frequency will have different meaning and should be interpreted in a different way.

2.6 Time-domain search

The positive distribution-based time-frequency method for temporal localization of the first arrivals in the Lamb wave tomographic experiment produces results yielding satisfactory image quality after reconstruction. However, these results suffer from significant systematic errors related to the uncertainty principle. Although we already discussed some existing ways of minimizing this error, it was still very appealing to design a simple alternative time domain algorithm using accumulated empirical knowledge about the signal.

We constructed several empirical algorithms utilizing such signal properties as carrier frequency, temporal sampling rate and vertical quantization rate. All of them

Reproduced with permission of the copyright owner. Further reproduction prohibited without permission.

search for a certain event associated with the first arrival, provided the signal-to-noise ratio is high and the noise can be effectively neglected. As is clear from Fig. 2.3, our typical signal satisfies the above requirement after analog band-pass filtering and damping standing ultrasonic waves.

The first approach we used was related to the phase velocity of the signal. We stacked all received waveforms into a square array (a procedure commonly used in medical imaging [43]) and tried to shift each of them to be in phase in the area of the first arrival. Shift values measured with respect to the first waveform served as a common reference with known arrival time determined manually. The arrival time of a particular signal in the stack could then be easily determined. The results of phase alignment could be easily viewed as an image with black and white stripes corresponding to positive and negative areas of the signal. However, the best results obtained with this method showed regular phase disagreement of $\pm$ one period in the area of the first arrival. This phenomenon can be explained by the continuous phase drift within the modulation envelope and our inability to handle low-amplitude front end of the S_0 mode. This was our last attempt to measure phase delay in a multi-signal Lamb wave tomographic experiment.

The second approach is related to the group velocity of the signal. It completely ignores the phase information and focuses on tracking the envelope of the first arrival. Such a tracking can be accomplished in many ways but the one we chose has proved to be very fast and more accurate than all other methods including the time-frequency algorithm. To be efficient, however, the method requires a very narrow-band signal with high SNR. The algorithm is summarized in Table 2.6.

Reproduced with permission of the copyright owner. Further reproduction prohibited without permission.

Time domain Group Delay measurement
1. Acquire a series of narrow-banded signals with high SNR.
2. Make them zero-mean.
3. Empirically determine envelopes of the S_0 mode in each signal.
4. Optionally rescale all envelopes to the same range.
5. Set some suitable amplitude threshold.
6. Find the crossing of the envelope and the horizontal threshold line using interpolation.
7. Output the temporal coordinate of the crossing.

Table 2.6: Time domain Group Delay measurement

The algorithm measures group delay as the arrival time of a chosen point on the leading edge of the S_0 mode. This is not in accordance with theory and cannot be accurate since the envelope's shape constantly evolves with time. The more accurate approach, following the definition of the group velocity, would search for the delay of a center of gravity of the envelope. However, in our experiments the S_0 mode is most of the time followed by either A_0 mode or reflections from the plate boundaries. Its trailing edge is always distorted and separation of the S_0 is impossible without numerical methods introducing additional artifacts. It should be emphasized that for large inspection areas edge reflections will not be a problem. Using high input power will allow for longer transmitter-receiver distances and for satisfactory temporal separation of the S_0 and A_0 modes. In that case the algorithm can be easily modified to look for the center of gravity of the first-coming wave packet.

Notwithstanding slight inaccuracies in its underlying assumptions, the above time domain group delay measurement algorithm produces very good output. Fig. 2.17 is the result of its application to a test set of waveforms acquired on a defect-free aluminum plate. Comparison to theoretical arrival times (Fig. 2.9) yields an MS error

Reproduced with permission of the copyright owner. Further reproduction prohibited without permission.

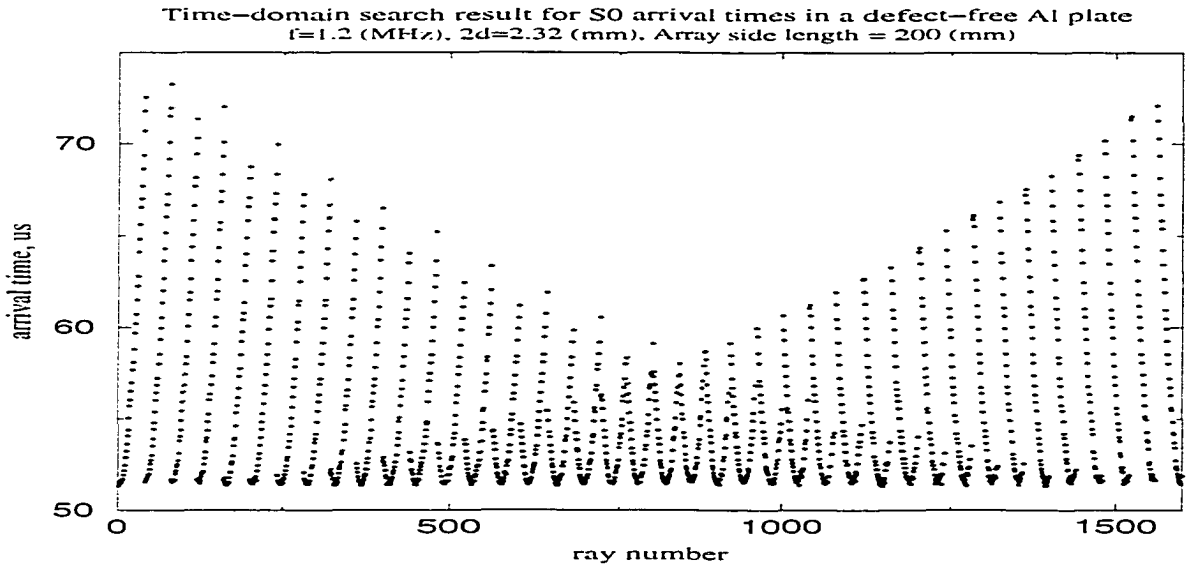

Figure 2.17: Arrival times in a defect-free aluminum plate obtained with a time-domain group delay measurement algorithm (Table 2.6). Comparison with theoretical times (Fig. 2.9) yields MS error $\delta_{ms} = 0.213$.

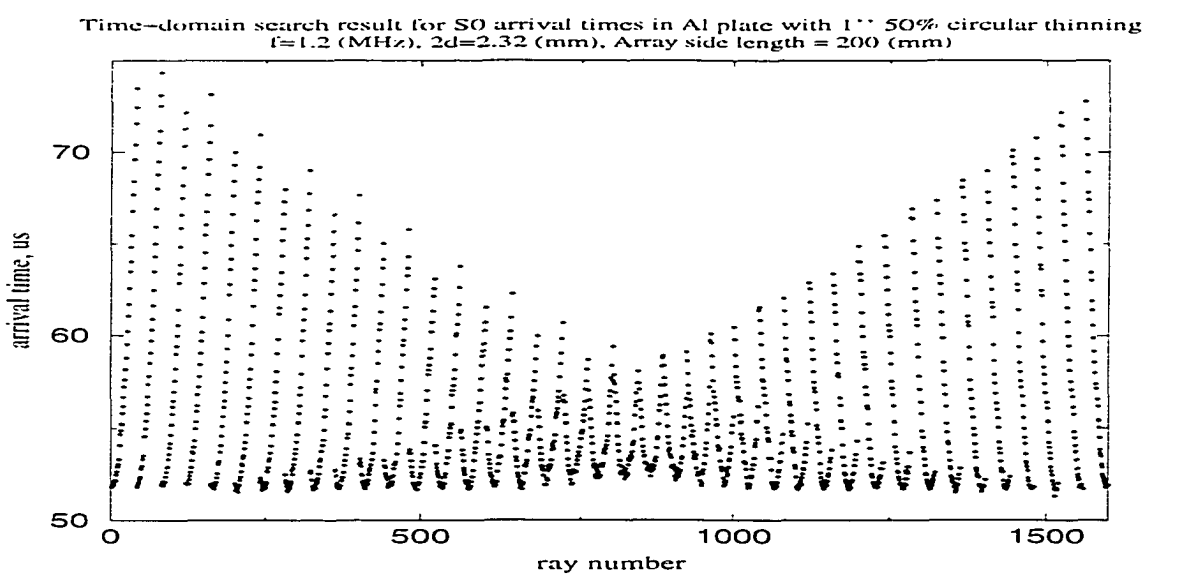

Figure 2.18: Arrival times in aluminum plate with 25.4 mm-diameter flat-bottom hole in the center obtained with a time-domain group delay measurement algorithm. The defect shows up as a slowdown on the bottom line $t = 52\mu s$ around the ray 800.

Reproduced with permission of the copyright owner. Further reproduction prohibited without permission.

$\delta_{ms} = 0.213$ which is much better than that for the time-frequency algorithm. Visual inspection reveals that arrival times are distributed rather smoothly, without sharp jumps characteristic of the time-frequency method. Fig. 2.18 shows the arrival times of signals acquired over the 25.4 mm-diameter 50% thinning flat bottom hole in aluminum plate. The defect in the middle of the scanned area is clearly outlined as a relative slowing down in the central part of the lower boundary of the arrival time pattern. The accuracy of the group delay measurement method is the highest among the methods discussed in this work.

The following remarks summarize this section:

- All attempts to automatically determine the phase delay of the S_0 mode resulted in accuracy not higher than a wave period at carrier frequency.
- The proposed time domain group delay measurement algorithm demonstrated high accuracy and superiority to all methods implemented in the scope of this work.
- In the absence of plate edges and at larger transmitter-receiver distances the wave packet of the S_0 mode would be separated from the slower modes, simplifying computation of its center of gravity. The algorithm could then be modified to compute group delay strictly in accordance with its physical definition, thus potentially improving both accuracy and agreement with group velocity dispersion theory.

Reproduced with permission of the copyright owner. Further reproduction prohibited without permission.

2.7 Generalized traveltime method

A very general and accurate delay estimation method for dispersive media was proposed by Herman [60], tested by Goudswaard et al [61], and further developed by Ernst and Herman [62]. The method called generalized traveltimes is based on an error norm, related to the phase of the wavefield. To avoid the cumbersome step of interpreting arrivals it computes phase "traveltime" as a logarithm of the Fourier transform of the signal part cut around a theoretically guessed time of flight, simplifying the task and making it almost automatic.

The authors of [62] comment that no single traveltime can be associated with the direct guided wave due to its dispersive nature. Since each frequency travels with a different phase velocity, the traveltime of a certain event also varies with frequency, leading to a dispersive $\tau(\omega)$. The generalized traveltimes in [62] are defined as follows:

$$\tau^{GT}(d,\omega) = t_{min} - \frac{d}{d\omega}\Im\left[\log\left\{\sum_i e^{-(\alpha+j\omega)(t_i-t_{min})}\hat{d}(t_i)\right\}\right] \tag{2.17}$$

where t_{min} and t_{max} are the start and end of a time window surrounding the arrival of the direct guided wave, $t_{min} < t_i < t_{max}$, α is a real positive damping constant, $\hat{d}$ is a windowed and tapered version of the input data, and $\Im$ stands for the imaginary part of the complex number.

It is clear that generalized traveltimes (2.17) reduce to the group delay. Originally traveltimes were defined as a phase delay [60], but the authors noticed the impossibility of unwrapping the phase with the accuracy less than $2\pi n$, which was a serious obstacle. This uncertainty in phase occurs because low frequencies are missing in the data due to filtering effects of hardware and the waveguide itself. The phase of

Reproduced with permission of the copyright owner. Further reproduction prohibited without permission.

the dispersive wave can only be defined up to a constant – this statement from [62] fully agrees with our extensive experience and inability to accurately calculate phase delay.

Using the properties of the Fourier transform (2.17) can be rewritten in the following form, which is more convenient for numerical computations:

$$\tau^{GT}(d,\omega) = t_{min} + \Re\frac{-iF\{te^{-\alpha t}d(t)\}}{F\{e^{-\alpha t}d(t)\}} \tag{2.18}$$

Here F denotes the Fourier transform and $\Re$ is the real part of a complex signal. This representation explains the need for a damping factor α when the spectral magnitude of the data is zero and generalized time (2.18) is not defined.

The definition of generalized traveltimes (2.17) is both an intuitive and physically correct approach to the complicated concept of the group velocity in dispersive media. We adapted it to the Lamb wave tomography and studied its performance on the two test data sets.

Fig. 2.19 demonstrates the result of application of the generalized traveltimes algorithm to a test data set acquired on a defect-free aluminum plate. For each signal we first determined the theoretical value of the arrival time, then cut a 512-sample portion of the signal, centered at that value and applied (2.18) to that portion. As recommended in [62], we prepared the window by subtracting the mean and padding with many enough zeros to ensure smooth behavior at the window sides. Although the MS error is rather large ($\delta_{ms} = 7.625$), it is mainly due to the constant offset of the resulting arrival times with respect to the theoretical ones. The overall quality, however, is rather high and can be compared only to that of the time domain envelope

Reproduced with permission of the copyright owner. Further reproduction prohibited without permission.

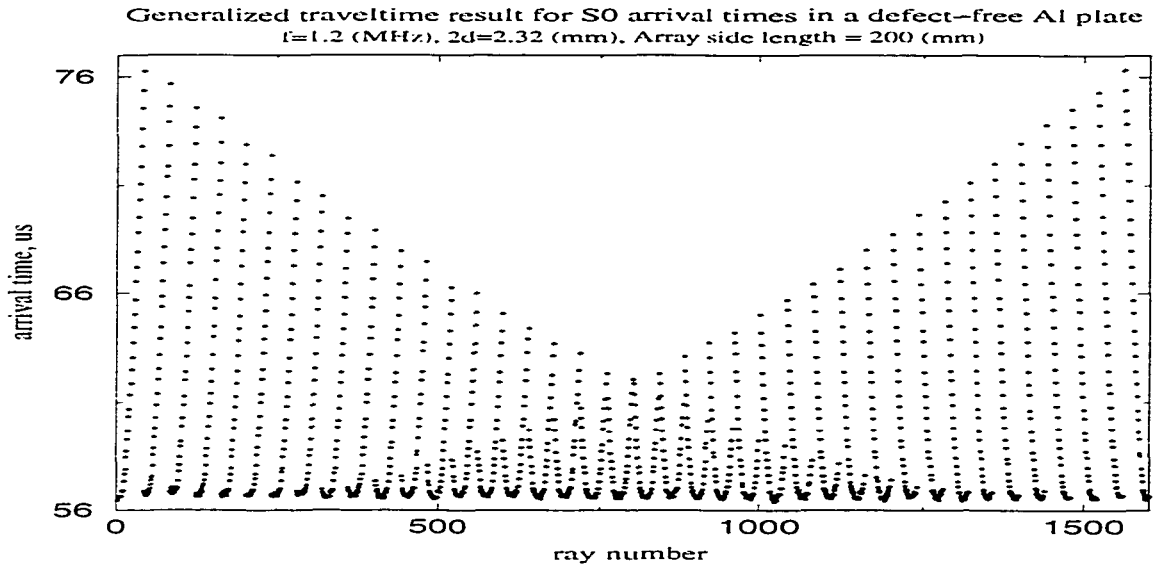

Figure 2.19: Arrival times in a defect-free aluminum plate obtained with a method of generalized traveltimes. Comparison with theoretical times (Fig. 2.9) yields MS error $\delta_{ms} = 7.625$.

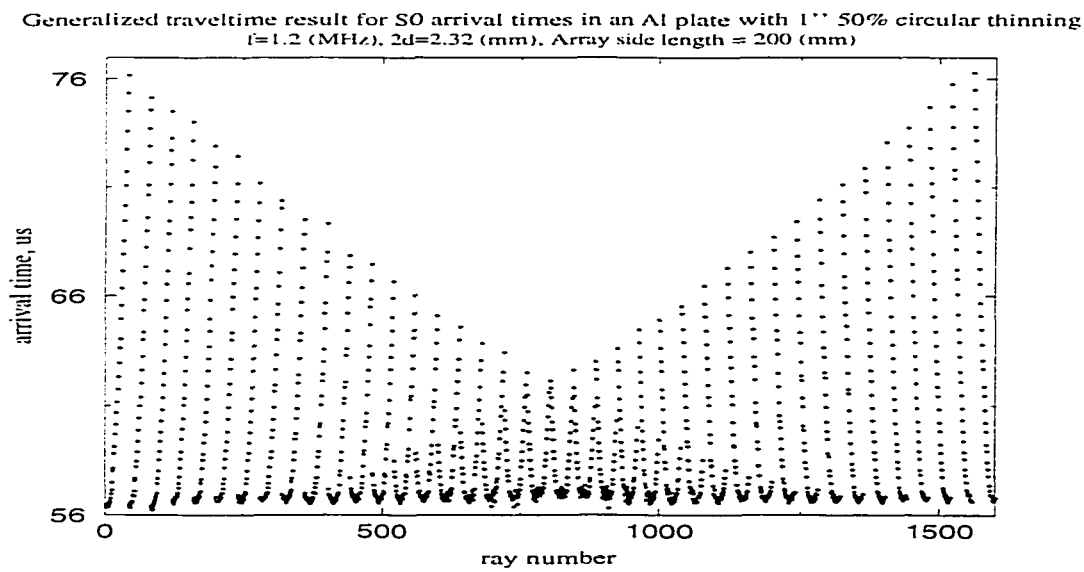

Figure 2.20: Arrival times in aluminum plate with 25.4 mm-diameter flat-bottom hole in the center obtained with a method of generalized traveltimes.

Reproduced with permission of the copyright owner. Further reproduction prohibited without permission.

delay algorithm. To test the generalized traveltimes ability to reveal plate defects we applied the same algorithm to the signal set acquired over the 25.4 mm-diameter 50% thinning flat bottom hole in aluminum plate. The defect in the middle of the scanned area can be noticed but the resolution is lower than that of the time-frequency and the time domain envelope delay algorithms.

2.8 Discussion

- We observed relatively low performance of the methods relying on phase velocity measurements since the absolute phase of the guided wave can only be measured with the accuracy not more than several wavelengths. Accurate results can be achieved only with relative phase delay measurements of the same signal in two spatially separated points. The last algorithm can be used only in defect-free plates and is not applicable to our tasks.

- After testing the performance of the majority of the techniques discussed in this chapter we reached maximum accuracy and speed with time domain group delay estimation method. In its current realization the method determines the time delay of the leading edge of the envelope of the fastest mode and requires well-filtered signals with distinctive first arrivals. The arrival times extracted with the method yield the lowest MS error when compared to the theoretical ones. Another success criterion is the quality of the tomographic reconstruction. Most of the results of this work were obtained with time domain group delay estimation methods, very efficiently handling Lamb wave signals typical to our

Reproduced with permission of the copyright owner. Further reproduction prohibited without permission.

experiments.

- Time-frequency analysis based on a custom-built positive distribution is a robust autonomous method, although less accurate than the group delay method. It cannot compute time delay with enough precision because of the uncertainty principle. However, it provides a reliable first estimate of the arrival time that can be used for as an input to more accurate algorithms if theoretical prediction is a problem. The method is fast, highly insensitive to signal quality, and works practically without human intervention. Using wavelet transform instead of conventional DFT may improve time localization accuracy.

- The method of generalized traveltime is automatic, fast and based on the deep insight into the nature of guided waves and the concept of group velocity. Preliminary results obtained with the method were promising, although not free from the DFT-specific uncertainty.

- Both pattern matching and neural network approaches have been explored extensively within this work. Although the results for some samples were quite satisfactory, we were unable to reach the reliability and accuracy of our more successful methods.

Reproduced with permission of the copyright owner. Further reproduction prohibited without permission.

Chapter 3

Fan beam tomography

This chapter summarizes our attempts to build the data acquisition and image reconstruction procedure for the Lamb wave fan beam tomography. It begins with an explanation of the Fan Beam tomographic reconstruction algorithm as it is introduced in the literature. Some results of its application to reconstruction of simulated two dimensional objects (circles and ellipses) are presented, and then the feasibility of the technique for application to Lamb wave tomography of aircraft skins is studied. Further development of the subject is based on the conclusions and recommendations drawn from this theoretical study.

The experimental section describes the use of the Fan Beam scanner manufactured for Lamb wave tomography, and the application of the developed reconstruction algorithm to the inversion of real traveltime data measured in several different ways. Finally, we assess the feasibility of the Lamb Wave tomography based on the Fan Beam data acquisition geometry and convolution-backprojection inversion scheme.

Reproduced with permission of the copyright owner. Further reproduction prohibited without permission.

3.1 General discussion of the method

The convolution-backprojection algorithm has proved to be successful in reconstructing plate defects from the projections acquired with the Parallel Projection scanning technique. To generate such projections in the case of Lamb waves, a source-receiver pair linearly scans over the length of a projection, then rotates and scans the next projection until the entire circle is covered. The method requires rotation of either the sample or the transmitter-receiver assembly, which is slow and cumbersome. Both are hard to realize in field conditions when large objects are being scanned, with near real-time requirements for the data acquisition process. Using transducer arrays does not solve the problem because in the parallel projection case we cannot completely exclude mechanical motion in the system.

A fast and practical alternative to the parallel projection scheme is the so called "fan-beam" scheme, widely used in medical imaging [39]. A study of its resolution, conducted by Natterer, can be found in [63]. In this case the projections are generated by a single transducer emanating a fan-like beam which is recorded by a bank of receivers. One can arrange the receivers in different ways, with each configuration having a different reconstruction algorithm. Usually the receivers are located either along the arc centered at the transmitter at equiangular intervals, or are equally spaced along a straight line. The transmitter-detector assembly is rotated to measure projections at corresponding angles. The data-collection procedure is much faster than in the parallel case, but mechanically moving parts are still present in the system.

Fig. 3.1 illustrates the main components of the fan beam scanning geometry. The current transmitter is located at O and γ is the current projection angle. M is

Reproduced with permission of the copyright owner. Further reproduction prohibited without permission.

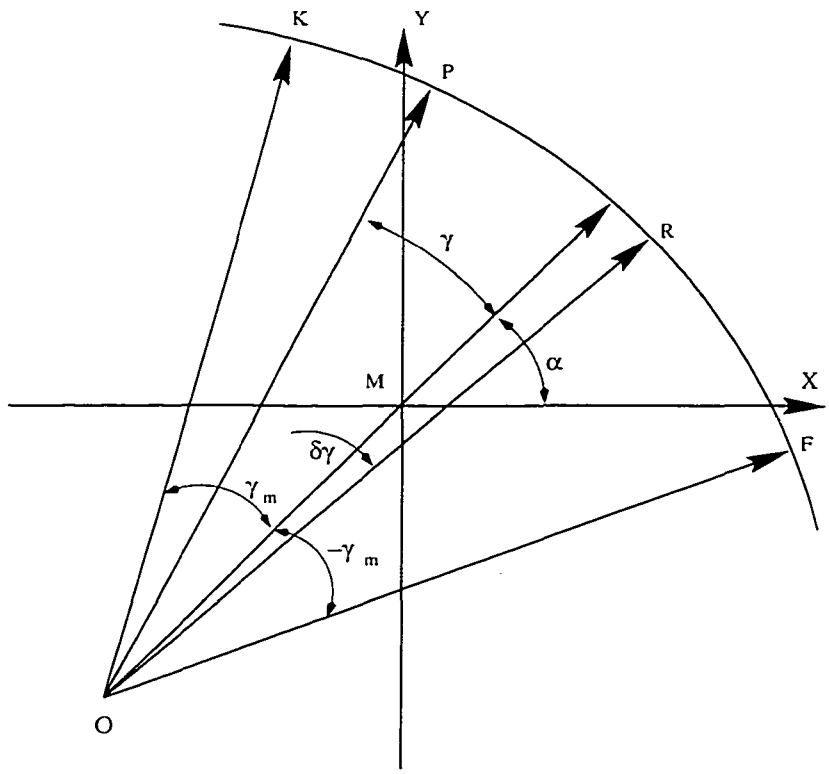

Figure 3.1: The Fan Beam geometry: M - geometrical center of the system; O - transmitter; $\pm\gamma_m$ - range of the fan beam; $\delta\gamma$ - angular distance between receivers; α - current projection angle; γ - current receiver angle.

Reproduced with permission of the copyright owner. Further reproduction prohibited without permission.

the rotation center of the system and it also serves as a Cartesian origin. Receivers are spread along the arc $\widehat{FK}$ symmetrically about the middle ray OM. The receiver spacing being considered is equiangular with the angle increment $\delta\gamma$. The current receiver angle α is measured with respect to the central ray and ranges from $-\gamma_m$ to γ_m. It is useful to keep the number of receivers odd so that all the algorithms are symmetric about the central ray ($\alpha = 0$).

The next projection is taken when the whole system has been rotated about M by incrementing the projection angle γ. In the most straightforward implementation γ covers the complete range $(0, 2\pi)$.

Image reconstruction from fan beam projections is very similar to that from parallel projections, except for some small changes in the algebra. The whole reconstruction algorithm is described by Kak and Slaney in [64]. Here we outline the three basic steps of the algorithm and explain some details of its computer implementation.

The filtered backprojection formula is as follows:

$$f(x,y) = \int_0^{2\pi} \frac{1}{L^2} Q_\alpha(\gamma') d\alpha \tag{3.1}$$

where L is the distance $|MP|$ from the point P with coordinates (x, y) to the transmitter O for the current projection (Fig. 3.2). The $Q_\alpha(\gamma')$ is the filtered projection data along the line $\gamma = \gamma'$ for the current projection.

Below is the practical realization of the above formula [64]:

1. Assume that each projection $R_\alpha(\gamma)$ has N data points (N is odd) sampled at interval $\delta\gamma$, where α is the projection angle (Fig. 3.1). Angle γ varies in the range $(-\gamma_m, \gamma_m)$ and takes N values $n \cdot \delta\gamma, n \in (-\frac{(N-1)}{2}, \frac{(N-1)}{2})$. First we modify

Reproduced with permission of the copyright owner. Further reproduction prohibited without permission.

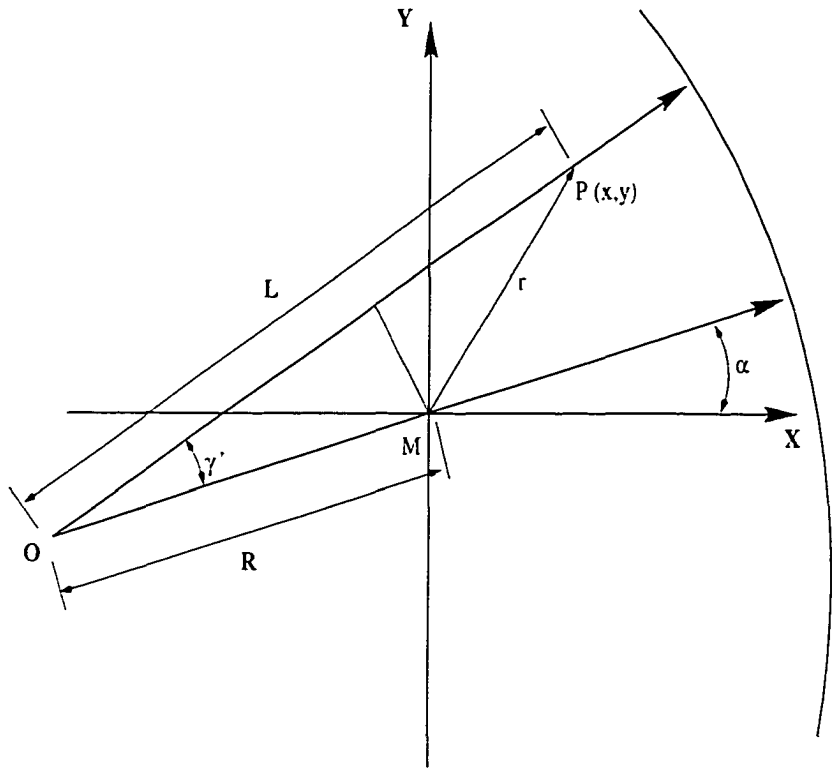

Figure 3.2: Illustration of the fan beam reconstruction algorithm: α - current projection angle; image point P with coordinates (x, y); γ' - angle between the central ray OM and the direction on the point P being reconstructed.

Reproduced with permission of the copyright owner. Further reproduction prohibited without permission.

the projection data and build intermediate values

$$R'_\alpha(n \cdot \delta\gamma) = R_\alpha(n \cdot \delta\gamma) \cdot R \cdot \cos(n \cdot \delta\gamma)$$

Here $n = 0$ corresponds to the ray passing through the center of projection.

2. Convolve each modified projection $R'_\alpha(n \cdot \delta\gamma)$ with the impulse response filter $g(\gamma)$, samples of which are given by

$$g(n \cdot \delta\gamma) = \frac{1}{2}\left(\frac{n \cdot \delta\gamma}{\sin(n \cdot \delta\gamma)}\right)^2 \cdot h(n \cdot \delta\gamma)$$

to get the corresponding filtered projection $Q_\alpha(n \cdot \delta\gamma)$:

$$Q_\alpha(n \cdot \delta\gamma) = R'_\alpha(n \cdot \delta\gamma) * g(n \cdot \delta\gamma). \tag{3.2}$$

With samples of $h(n \cdot \delta\gamma)$ given by

$$h(n \cdot \delta\gamma) = \begin{cases} \frac{1}{4(\delta\gamma)^2} & n = 0 \\ 0 & n \text{ even} \\ -\frac{1}{(n\pi \cdot \delta\gamma)^2} & n \text{ odd} \end{cases}$$

samples of g become:

$$g(n \cdot \delta\gamma) = \begin{cases} \frac{1}{8(\delta\gamma)^2} & n = 0 \\ 0 & n \text{ even} \\ -0.5 \cdot \frac{1}{(\pi \cdot \sin(n \cdot \delta\gamma))^2} & n \text{ odd} \end{cases}$$

Kak and Slaney [64] also recommend to convolve the result with an additional smoothing filter to enhance the reconstruction quality. The Hamming window could be a good candidate for such a filter.

Reproduced with permission of the copyright owner. Further reproduction prohibited without permission.

3. Perform a weighted back-projection of each filtered projection (3.2) along the fan.

$$f(x,y) \approx \Delta\alpha \sum_{i=1}^{M} \frac{1}{L^2(x,y,\alpha_i)} Q_\alpha(n \cdot \delta\gamma') \tag{3.3}$$

Here γ' is the angle of the fan beam ray that passes through the point (x, y) and $\Delta\alpha = \frac{2\pi}{M}$ where M is the number of projections. The value of γ' in general does not correspond to one of the $(n \cdot \delta\alpha)$s for which the filtered projection $Q_\alpha(n \cdot \delta\gamma)$ is known. We therefore perform a cubic spline interpolation (sometimes a simple linear one is enough) to calculate (3.3). L in (3.3) is the distance from the transmitter to the current point (x, y).

3.2 Reconstruction of simulated defects

The above described Fan Beam reconstruction algorithm was implemented in a software routine written in the "C" programming language. The realization is very similar to that of a Parallel Projection method. The only changes made were generation of the modified projection $R'_\alpha(n \cdot \delta\gamma)$, some filter adjustment and calculation of the distance L between transmitter and point (x, y). Attention was also paid to the numerous purely geometrical questions such as ray numbering and angle calculation.

We tested the performance of the reconstruction algorithm on a number of two-dimensional simulated defects of circular and elliptical shape. Both simulation and reconstruction programs had the same geometrical parameters. Changing parameters such as rotation radius R, number of projections, number of receivers per projection,

Reproduced with permission of the copyright owner. Further reproduction prohibited without permission.

and angular interval between receivers, allowed us to optimize the settings of the real Lamb wave Fan Beam scanner.

Analysis of Fig. 3.3 reveals that if the transmitter rotating around M covers the big circle with radius $|OM| = R$, and if the fan beam opening angle is $2 \cdot \gamma_m$, then the most effectively covered area where all the fan beams intersect is the smaller circle of radius $r = R \cdot \sin(\gamma_m)$. We can therefore conclude that the bigger the opening angle of a fan beam, the better is the effective area coverage. On the other hand, to increase γ_m we need either more rays per beam (more receivers) or wider angular spacing $\delta\gamma$. In the first more desirable case we are physically restricted by the number of receivers available in the array or by the time necessary for stepping a single receiver along the arc. In the second case we lose information by decreasing the ray density (which can also be improved by increasing the number of projections). The problem therefore reduces to the joint optimization of the number of receivers, projections and receiver angular spacing.

Since the scanning geometry is symmetrical about the origin O (Fig. 3.3) it seems reasonable to make the reconstruction region to be a square with side $a = R \cdot \sqrt{2}$. This square is embedded into the big circle and cannot be made bigger since we cannot provide information for pixels outside the big circle. The number of pixels in this image can be chosen arbitrarily but making it much bigger than the number of rays in a fan beam is senseless because it won't bring any new information but will only increase the reconstruction time due to extensive use of interpolation.

Furthermore, we can choose the optimal fan beam opening angle to be 90° (see Fig.3.4), so that the best-covered area of radius $r = 0.5a$ is exactly embedded

Reproduced with permission of the copyright owner. Further reproduction prohibited without permission.

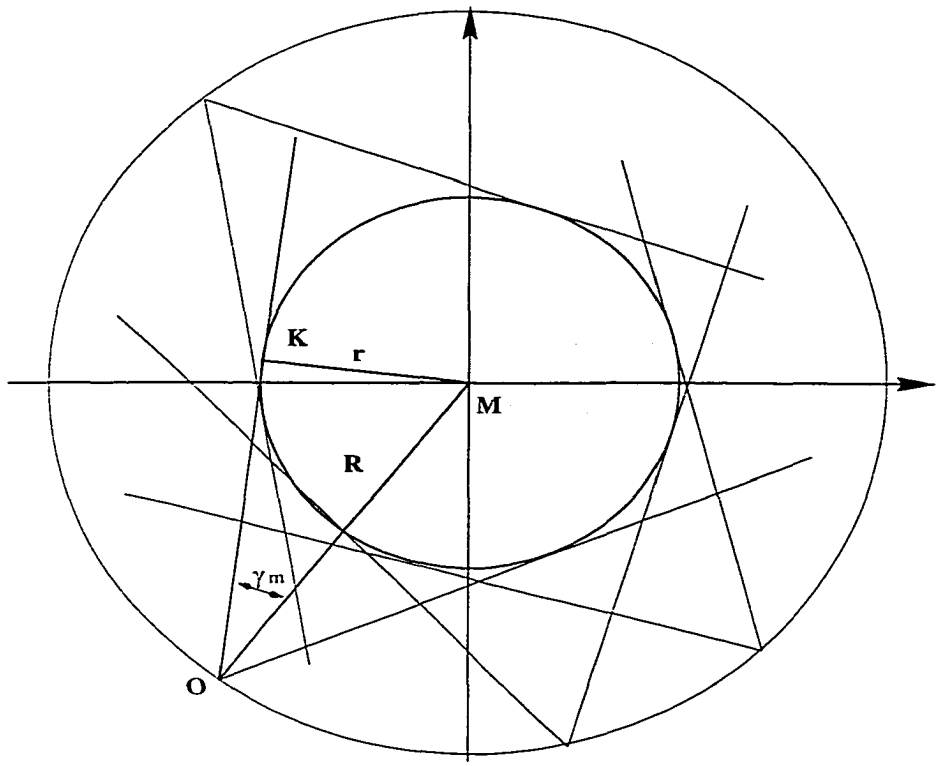

Figure 3.3: Area coverage of the circular fan beam geometry: $\pm\gamma_m$ – fan beam opening angle; R – radius of the perimeter transducer array; r – radius of the most densely covered area where all fan beams intersect.

Reproduced with permission of the copyright owner. Further reproduction prohibited without permission.

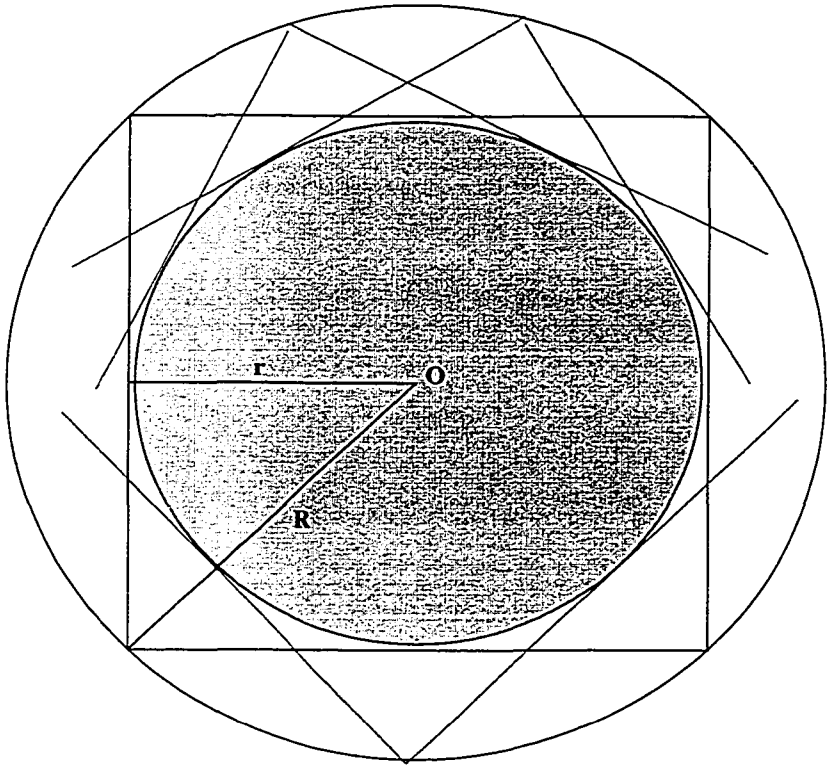

Figure 3.4: Dependence of the size of the reconstructed image on the fan beam opening angle: r – radius of the best-covered area; R – radius of the circular perimeter array of transducers; square - region displayed on the image.

Reproduced with permission of the copyright owner. Further reproduction prohibited without permission.

into the image square. We also note that some reconstruction artifacts such as the circle surrounding the best covered area can be almost completely removed by the appropriate choice of padding values in Step 2 of the algorithm. Then the whole image area (see Figs. 3.5, 3.6) will be useful for data interpretation (not forgetting that the ray density outside the best covered circle is smaller than inside).

With fixed fan beam opening angle $\frac{\pi}{2}$ we are now left with only two parameters to consider: number of projections and number of rays per projection. We ran the reconstruction program with different values of the above two parameters and show the resulting images in the table of figures below (Figs. 3.7 – 3.10). All reconstructions are done for a simulated elliptical defect with major axes 32 and 72 mm long. The transmitter rotation radius $R = 100$ mm, number of pixels per row is 300. It can be clearly seen from the table that 21 rays per beam produce blurred images independent of the numbers of projections. This is because we make a 300×300 pixel image instead of a 20×20 one, and, therefore, overuse interpolation. With the number of pixels corresponding to the number of rays in a fan beam we can remove blurring. Increasing the number of projections brightens the image and hides typical artifacts as the background structure gets finer.

Reproduced with permission of the copyright owner. Further reproduction prohibited without permission.

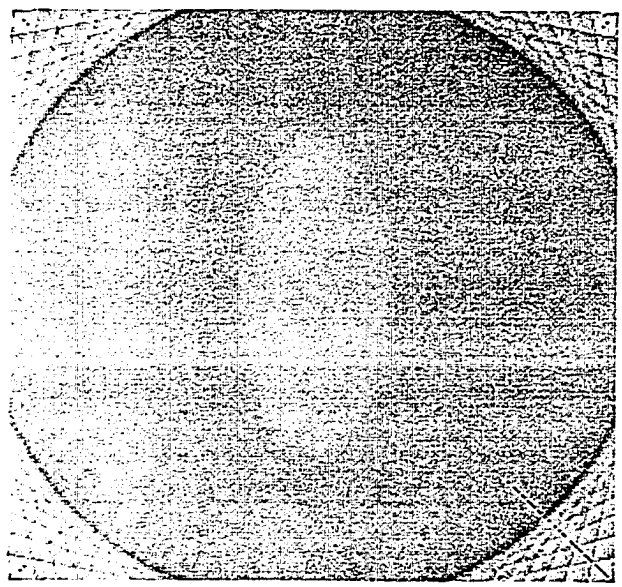

Figure 3.5: Simulated ellipse reconstruction from fan beam projections with convolution-backprojection algorithm: 64 projections, 101 ray, padding with maximum. Note the artifacts and blurring.

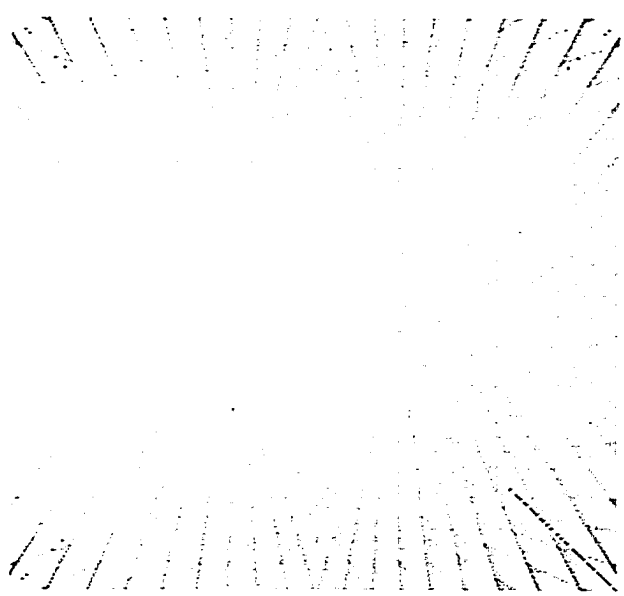

Figure 3.6: Simulated ellipse reconstruction from fan beam projections with convolution-backprojection algorithm: 64 projections, 101 ray, padding with zeroes.

Reproduced with permission of the copyright owner. Further reproduction prohibited without permission.

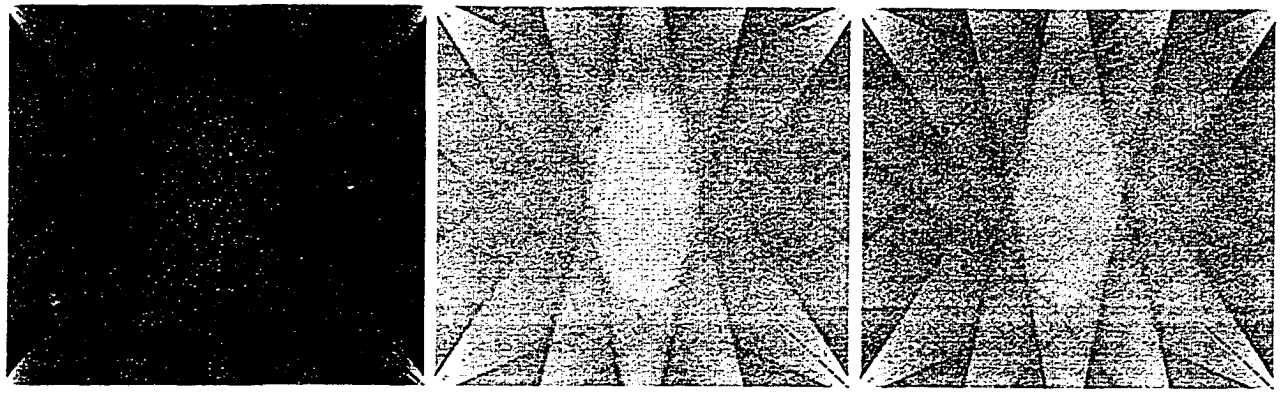

16 projections, 21 rays | 16 projections, 51 rays | 16 projections, 101 rays

Figure 3.7: Simulated ellipse reconstructions from fan beam projections with convolution-backprojection algorithm: 16 projections. Resolution increases with the number of rays per projection.

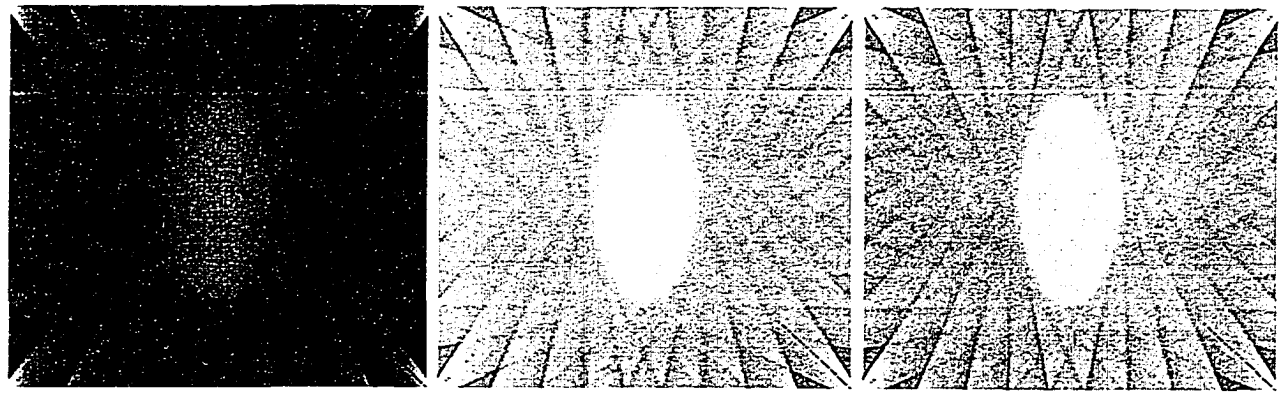

32 projections, 21 rays | 32 projections, 51 rays | 32 projections, 101 rays

Figure 3.8: Simulated ellipse reconstructions from fan beam projections with convolution-backprojection algorithm: 32 projections. Resolution increases with the number of rays per projection.

Reproduced with permission of the copyright owner. Further reproduction prohibited without permission.

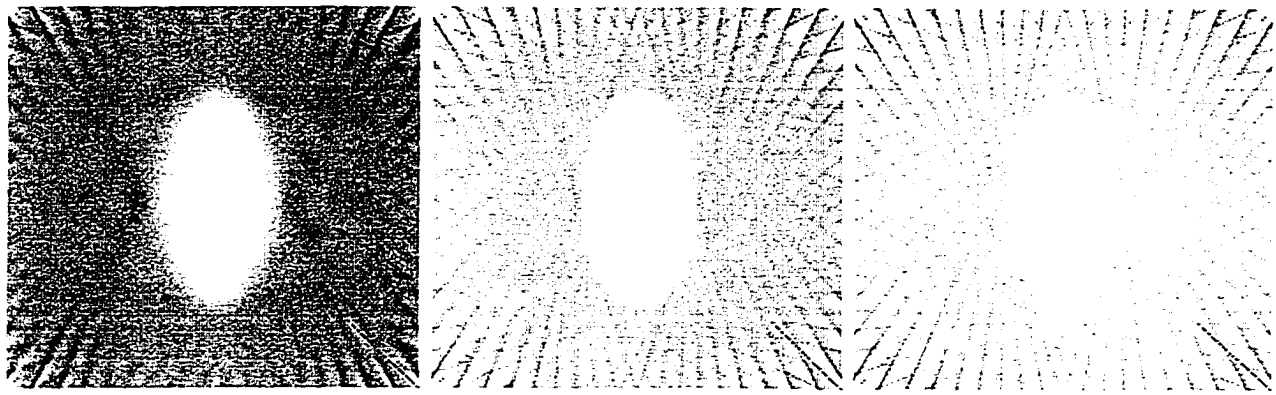

64 projections, 21 rays | 64 projections, 51 rays | 64 projections, 101 rays

Figure 3.9: Simulated ellipse reconstructions from fan beam projections with convolution-backprojection algorithm: 64 projections. Resolution increases with the number of rays per projection.

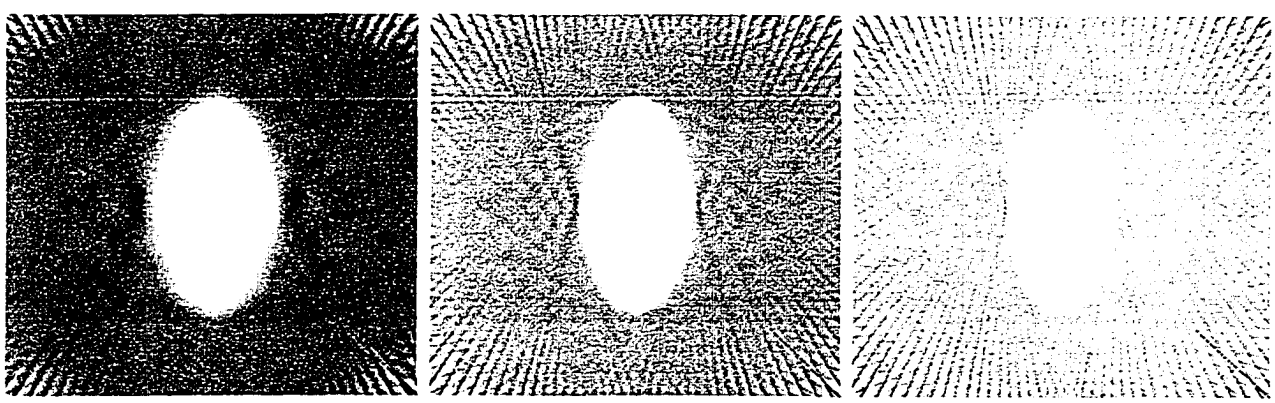

128 projections, 21 rays | 128 projections, 51 rays | 128 projections, 101 rays

Figure 3.10: Simulated ellipse reconstructions from fan beam projections with convolution-backprojection algorithm: 128 projections. Resolution increases with the number of rays per projection.

Reproduced with permission of the copyright owner. Further reproduction prohibited without permission.

3.2.1 Circular array implementation

We started working on fan beam tomography because of the possibility of using a circular perimeter array of transducers capable of both transmitting and receiving ultrasound. In this arrangement transducers are equally spaced along a big circle with angular increment $\delta\epsilon$ (Fig. 3.11). This scheme is free from mechanically moving parts and can be implemented for scanning large areas with Lamb waves. Fortunately, we can still use the reconstruction algorithm for equiangular receiver spacing. This is because the angular increment $\delta\gamma$ used in the reconstruction procedure still remains constant $\delta\gamma = 0.5\delta\epsilon$ and $\delta\epsilon$ is constant.

However, there is an important difference between this and original equiangular fan beam geometry (Fig. 3.11): now rays within a fan beam have different lengths. This is not a major problem in medical scanners where the target is concentrated essentially near the geometrical center of the area, surrounded by sources and receivers, and outside the object the waves travel in air. Therefore it doesn't matter whether the receivers are placed along the arc $\widehat{BC}$ (original version) or along the arc $\widehat{PM}$ (current version). In our experiments Lamb waves spend all their time in the material, and when the sources and receivers are placed on the same circle we have to take into account the variation in ray lengths and minimize its influence on the quality of measured arrival times. Subtle changes in the time delay of the first arrival caused by interaction with defects can be masked easily by bigger changes due to the variation in ray lengths. As discussed below, this fact became a major issue limiting the usefulness of P_2L_2 as a time-extraction device and imposing requirements of high precision on the mechanical scanner used for the fan beam tomography.

Reproduced with permission of the copyright owner. Further reproduction prohibited without permission.

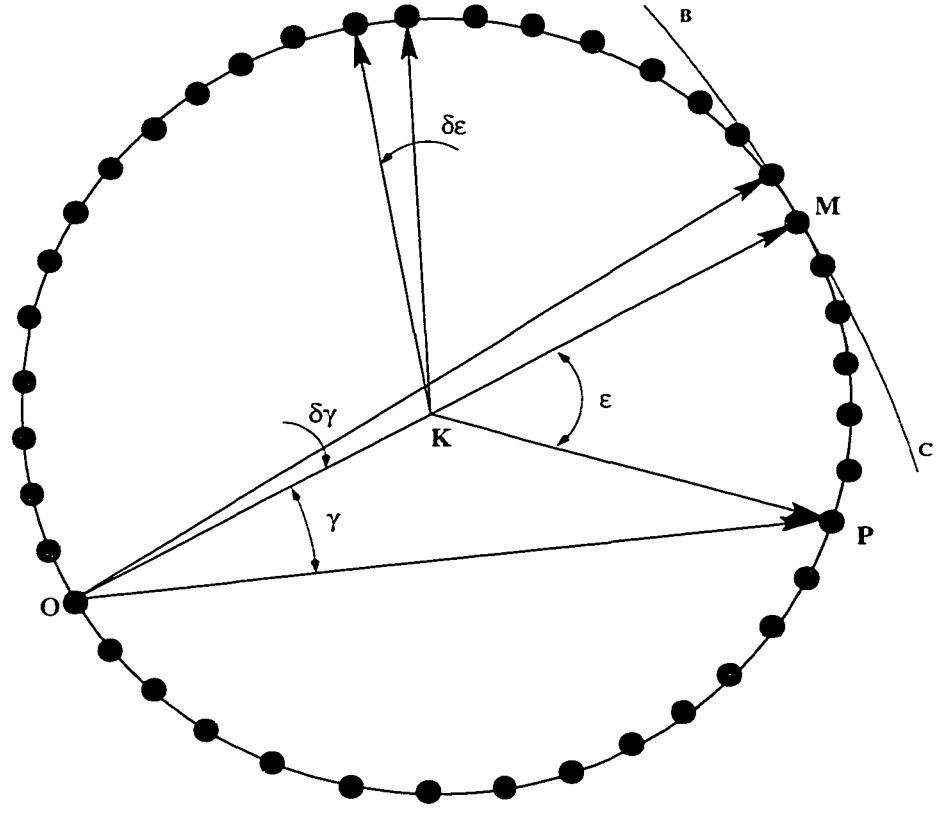

Figure 3.11: Adapting fan beam geometry to a circular perimeter array of transducers: original configuration is described in terms of γ and $\delta\gamma$; new configuration uses ϵ and $\delta\epsilon$; note that $\delta\epsilon = 2\delta\gamma$.

Reproduced with permission of the copyright owner. Further reproduction prohibited without permission.

3.3 Practical implementation and experimental results

3.3.1 Adaptation to the new geometry

The main difference between the traditional fan beam approach in medical applications and Lamb Wave tomography is the variable distance between transducers. In medical imaging the target where the actual attenuation of X-rays occurs is located near the geometrical center of the equipment, so rays travel most of their way in air without attenuation, and actual ray lengths can be different without affecting the reconstruction algorithm which assumes them to be the same. In the Lamb wave case the waves spend all of their time in the material, and when the sources and receivers are located along the same circle this naturally implies different ray lengths which we have to take into account.

Since the arrival time changes not only due to the presence of defects but also due to geometrical differences in ray lengths, it was necessary to find some quantity independent on the latter. We found the average wave velocity $\overline{V}$ to satisfy this requirement. For each ray $\overline{V}$ can be easily calculated as

$$\overline{V} = \frac{L}{t}$$

where L is the length of the current ray, t is the measured arrival time for that ray.

In the experimental setup (Fig. 3.12) the receiving transducer R moves along the circular arc of radius r centered at O. The line OR is actually a rigid arm geared to a stepper motor. The scanning angle $\gamma = \angle ROK$ is the angle between the central

Reproduced with permission of the copyright owner. Further reproduction prohibited without permission.

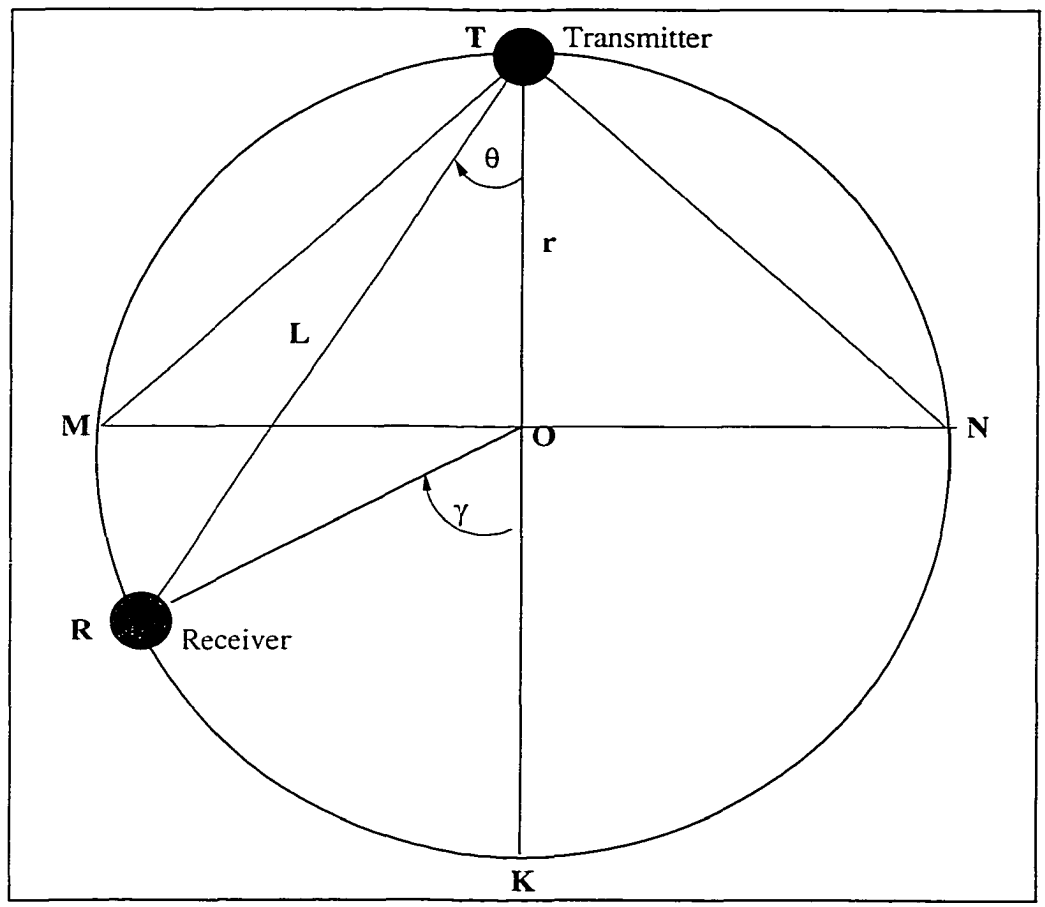

Figure 3.12: Ray length calculation for the experimental fan beam geometry.

Reproduced with permission of the copyright owner. Further reproduction prohibited without permission.

ray TK of the fan beam and the current direction of the arm OR. The actual ray angle $\theta = \angle RTO$ used by the reconstruction algorithm is $\theta = \frac{\gamma}{2}$. It is desirable to make the opening angle of the fan beam $\angle MTN = 90°$ having the holder arm OR sweep the whole 180°. In this case the best-covered area, or the circle formed as an intersection of all fan beams, will be exactly embedded into the image square with side $a = |OR| \cdot \sqrt{2}$. This image will also have biggest possible size because it is, in turn, embedded into the transducer array circle.

Since we ignore both ray bending and diffraction effects and use a straight ray assumption for image reconstruction, the ray length can be determined as the distance $L = |TR|$ between transmitting and receiving transducers. Both transducers have footprint of radius $\approx 7mm$ (Fig. 3.13). The distance between their centers may serve as a first approximation of the ray length.

$$L = 2 \cdot r \cdot \cos(\theta) = 2 \cdot r \cdot \cos(\frac{\gamma}{2}) \tag{3.4}$$

We use (3.4) in the program that corrects experimental data for changing ray lengths.

3.3.2 Data collection procedure

Since a circular array of transducers was not available at the time, we mimicked its behavior using a single transmitter-receiver pair. This idea was implemented in a custom fan beam scanner made by modifying our parallel projection scheme (Fig. 3.15). The scanner (Fig. 3.14, top view) is mounted on a support bar and consists of a static arm and a motor-controlled swing arm rotating about the geometrical center. The source and receive transducers are mounted on both arms at equal distances from the center of rotation. The transducers are equipped with small

Reproduced with permission of the copyright owner. Further reproduction prohibited without permission.

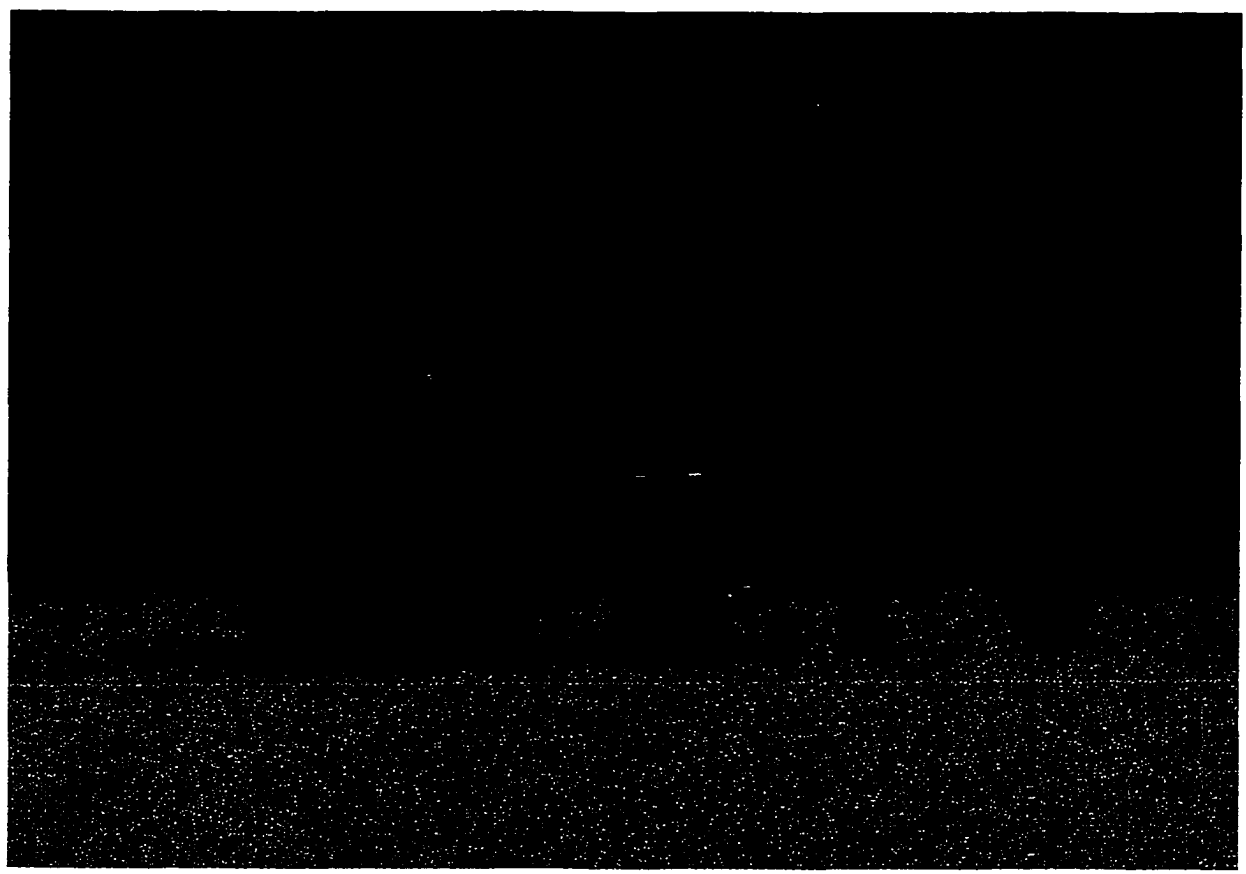

Figure 3.13: Transducers with cone-shaped delay lines used for Lamb wave excitation at various frequencies. From left to right: 100 KHz $ValpeyFisher^{TM}$ transducer; 1.0 MHz and 2.25 MHz $Panametrics^{TM}$ transducers.

Reproduced with permission of the copyright owner. Further reproduction prohibited without permission.

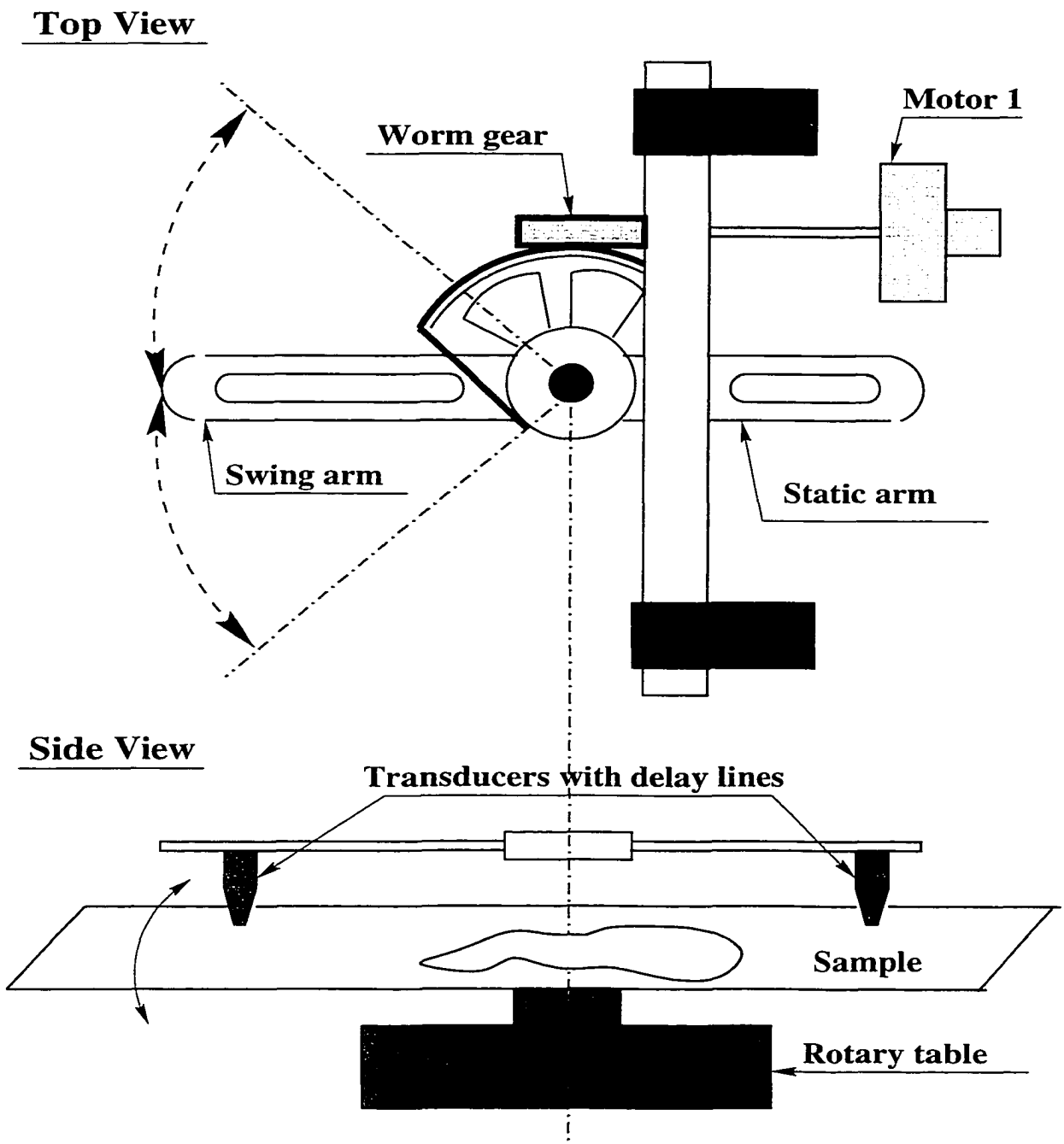

Figure 3.14: Schematic of the fan beam scanner.

Reproduced with permission of the copyright owner. Further reproduction prohibited without permission.

Figure 3.15: Photo of the fan beam scanner in $W\&M$ NDE lab.

Reproduced with permission of the copyright owner. Further reproduction prohibited without permission.

footprint delay lines and are spring-loaded to ensure good coupling with the sample plate. The latter is placed on the rotary table under the arm assembly (Fig. 3.14, side view). The swing arm is worm-geared to a stepper motor and can sweep through an arc of specified opening angle to complete a single fan beam projection. Additional projections can be acquired after turning the sample on the rotary table.

We used three different ways to collect fan beam projection data for tomographic reconstruction. The first two methods used a Pulsed Phase Lock Loop (P_2L_2) – a device that proved to be extremely helpful in Parallel Projection Tomography. The third method, borrowed from the Cross Borehole Tomography, uses the software expert system, described in Chapter 2, to retrieve arrival times from digitized waveforms. All three methods are described below.

Method 1: Data acquisition using the P_2L_2

A block diagram of the first method is shown in Fig. 3.16. The P_2L_2 sends a tone burst typically containing 3–10 cycles of a sine wave to the transmitter T. which in our case is a longitudinal contact $Panametrics^{TM}$ piezoelectric transducer with resonant frequency of 1.0 or 2.25 MHz. The receiving transducer R of the same type as T is positioned on the moving holder arm OR (Fig. 3.12). Both transducers are equipped with cone-shaped delay lines to reduce footprint (Fig. 3.13). Delay lines are coupled to transducers with an ultrasonic gel and to the plate with a thin layer of water. The amplified and filtered signal from R feeds the input of the P_2L_2, which is synchronized with the LeCroy oscilloscope. The P_2L_2 also generates the spike indicating the chosen sampling point on the signal in CH1 of the oscilloscope. The spike is displayed in CH2. The actual data is retrieved from the "Ref" socket of

Reproduced with permission of the copyright owner. Further reproduction prohibited without permission.

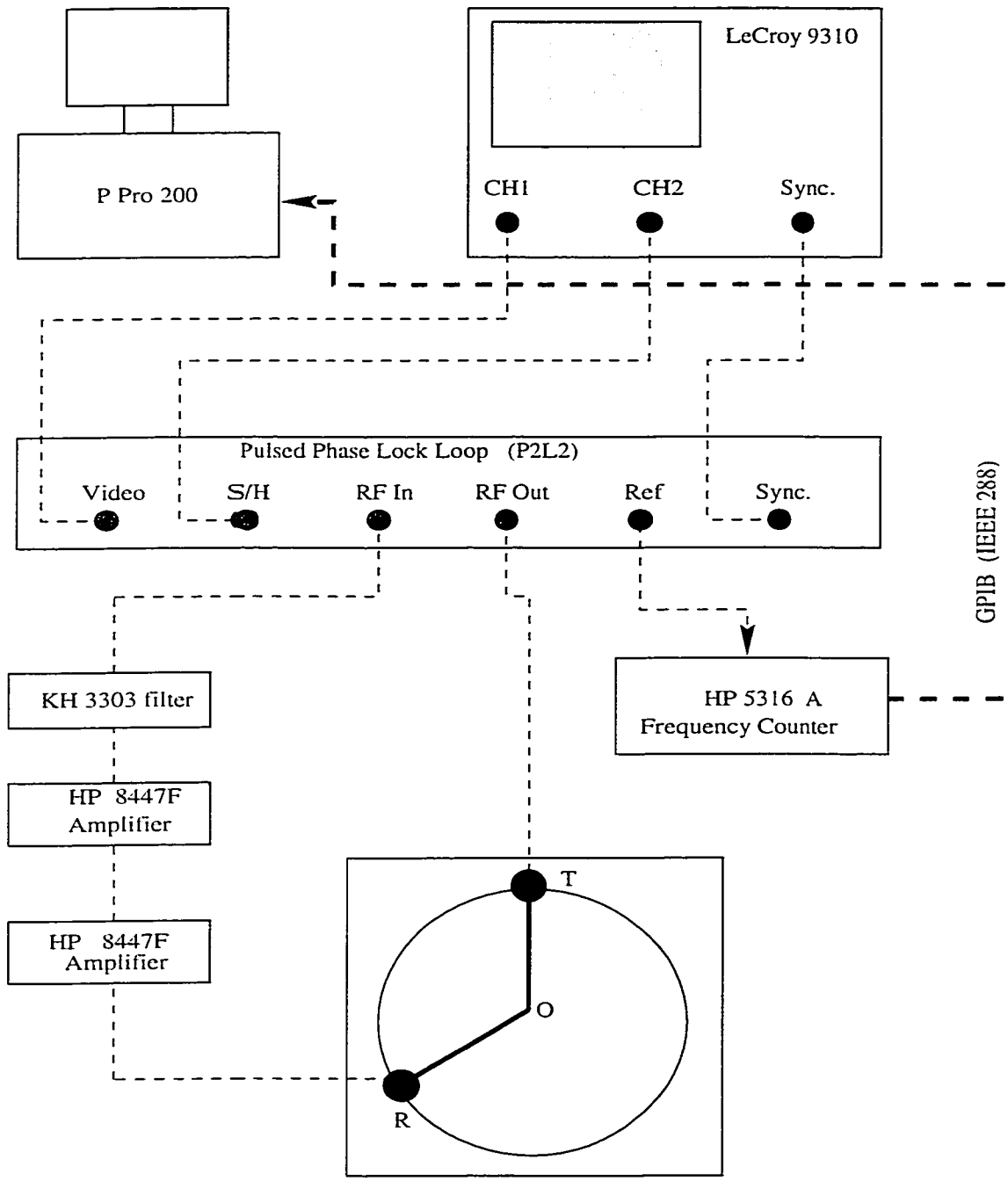

Figure 3.16: Fan beam measurement setup with P_2L_2. T and R are transmitting and receiving transducers.

Reproduced with permission of the copyright owner. Further reproduction prohibited without permission.

the P_2L_2 and is proportional to the phase shift of the reference point on the signal if the Loop is locked. The data from the frequency counter is transferred to the computer via GPIB IEEE 288. The mechanical motion of the holder arm OR and rotary table, as well as data acquisition, is controlled by a computer. The receiving transducer makes a specified number of steps sweeping a fan beam, and the data is retrieved after each step thus forming a single tomographic projection. The rotary table then turns the sample and the next projection is acquired. Both the step size and the speed of the rotary table should be small enough for the P_2L_2 not to lose the reference point. This is an inherent limitation of the method. Besides this, the total range of ray lengths within a fan beam should be rather narrow, otherwise the P_2L_2 also loses the reference point. This happens because the length increment for the adjacent rays varies within the fan beam, and it gets bigger at the edges. The wider the fan beam the more different are the lengths of adjacent rays and the P_2L_2 eventually cannot follow these fast changes in arrival times from one ray to the next.

On the other hand, if the above conditions are met, the method provides very accurate and repeatable data which can easily be transformed into the real arrival times of the reference points. If ray lengths are constant as in the Parallel Projection case, using the P_2L_2 is quite satisfactory. One cannot use it at all for Cross Borehole Tomography because ray lengths there change over a wide range. Fan Beam Tomography is an intermediate case and the goal of this portion of the work was to determine experimentally whether or not the P_2L_2 would be useful.

The P_2L_2 output has always been believed to be a linear function of the signal arrival time. To make sure of this we manually calibrated the device in the frequency

Reproduced with permission of the copyright owner. Further reproduction prohibited without permission.

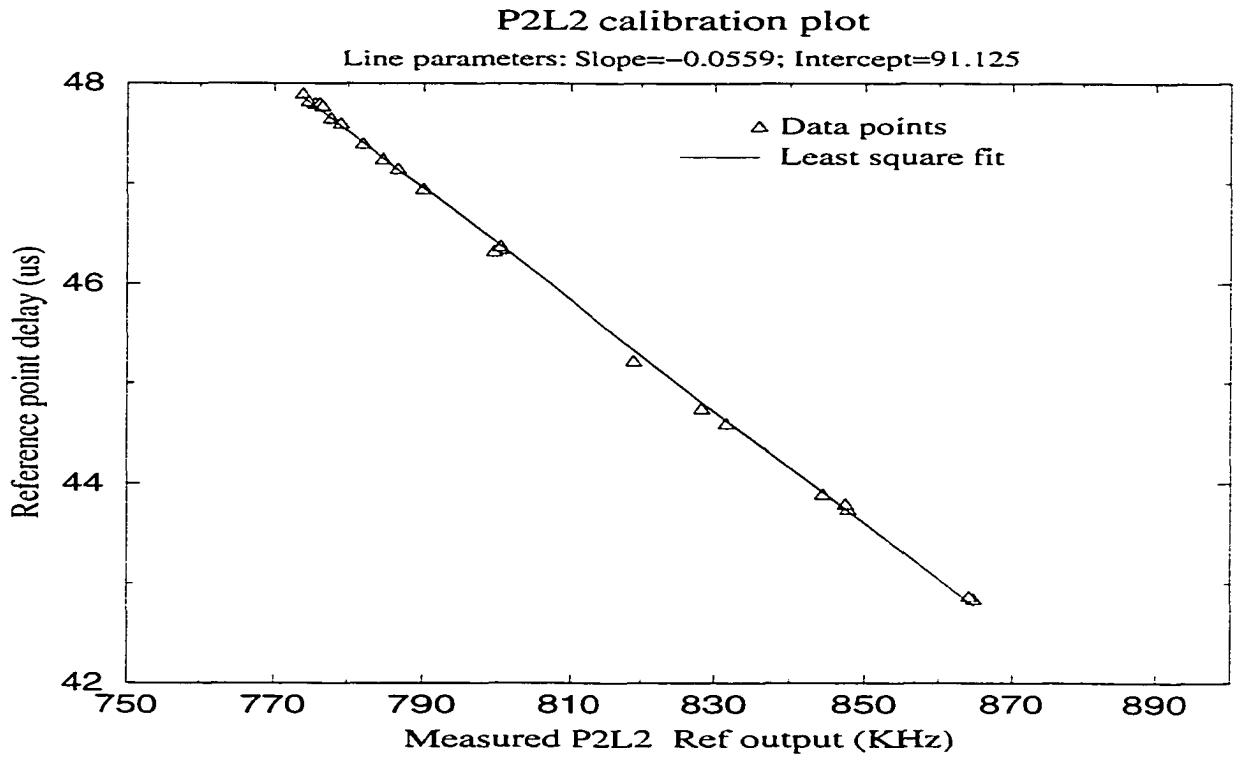

Figure 3.17: P_2L_2 calibration plot.

Reproduced with permission of the copyright owner. Further reproduction prohibited without permission.

range around 750 kHz. The results are represented on (Fig. 3.17). They demonstrate good linearity of the output and can be used in the P_2L_2 data interpretation software.

In order to take data with the P_2L_2 we modified the program driving the fan beam scanning apparatus so that the step size is small (0.5°) and the holder arm returns to the starting position slowly. It is worth mentioning that in the case of the circular array such a small step size is hardly affordable because of the increased number of transducer elements (720 to cover the whole circle in the last case). Nevertheless, we performed the experiment for the sake of completeness. We scanned aluminum samples with and without machined defects at frequencies of 0.75 and 1.1 MHz, and then processed the data to visualize the defects. The quality of all reconstructed images was unacceptably poor. Below we mention several possible reasons of the failure:

1. We were unable to get a straight horizontal line for the velocity plot of a single fan beam projection of a clean sample; instead we obtained a more or less strong parabolic residual trend (Fig. 3.18) depending on the data treatment method used;

2. We suspected the following conditions causing this trend:

a) The P_2L_2 output was hard to interpret;

b) Large transducer footprint made ray lengths uncertain;

c) The P_2L_2 output frequency changed slightly while the locked device was tracking the reference point.

To answer a) we modified the data collection procedure (see the second method below). To answer b) we prepared special cone-shaped delay lines with a small foot-

Reproduced with permission of the copyright owner. Further reproduction prohibited without permission.

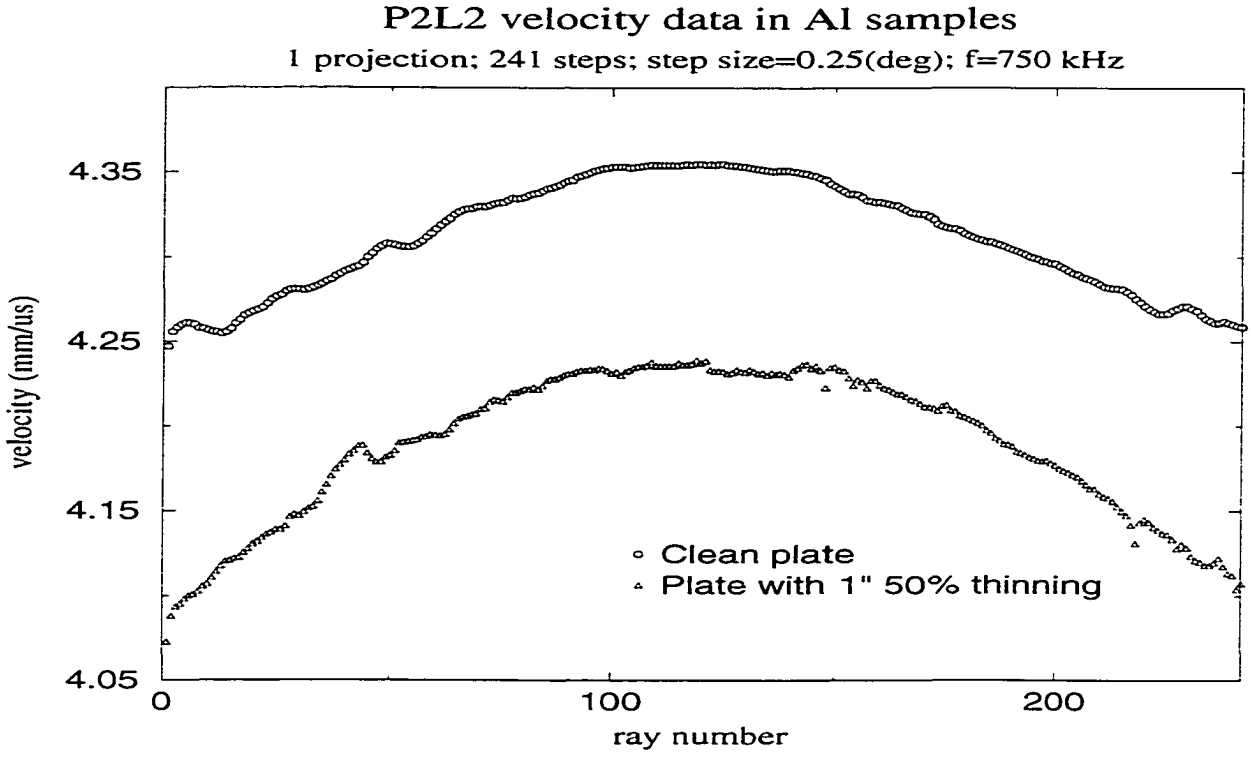

Figure 3.18: Parabolic trends on velocity data obtained with P_2L_2.

Reproduced with permission of the copyright owner. Further reproduction prohibited without permission.

prints (see the discussion below).

Method 2: Measuring P_2L_2 spike arrival time

A block diagram for the second method (Fig. 3.19) is the same as described above except that now we directly retrieve the time delay of the reference point in the signal. To do this we lock the P_2L_2 as in the first method and read the signal from CH2 of the oscilloscope via the GPIB interface into the computer. This signal is merely the spike generated by the P_2L_2 and following the reference point of the signal. The position of the spike's sharp maximum indicates the delay time of the reference point and can be easily found in software. This method allowed us to accurately determine the delay of the signal point with the same phase. It is much more intuitive than the first method which provides the same data but requires P_2L_2 calibration and is more difficult to interpret and correct.

This method was applied to a defect-free aluminum plate and to an aluminum plate with 25.4 mm- diameter 50% thickness reduction flat-bottom hole in its center. The projection of radius 108 mm taken at 1.1 MHz consisted of 241 steps taken at a constant central angle increment of 0.25°, so the total fan beam opening angle was 60°.

The raw data comparison plot is presented in Fig. 3.20. It is clear that due to the difference in ray lengths the raw arrival times have a trend which should be removed. To remove the trend we wrote a correction routine based on (3.4). This routine reads the raw arrival times, converts them into real ones using sampling rate (100 MHz) and artificial delay (23.0 μs) parameters, and then divides the theoretical ray lengths (3.4) by the arrival times. It, therefore, outputs average velocities

Reproduced with permission of the copyright owner. Further reproduction prohibited without permission.

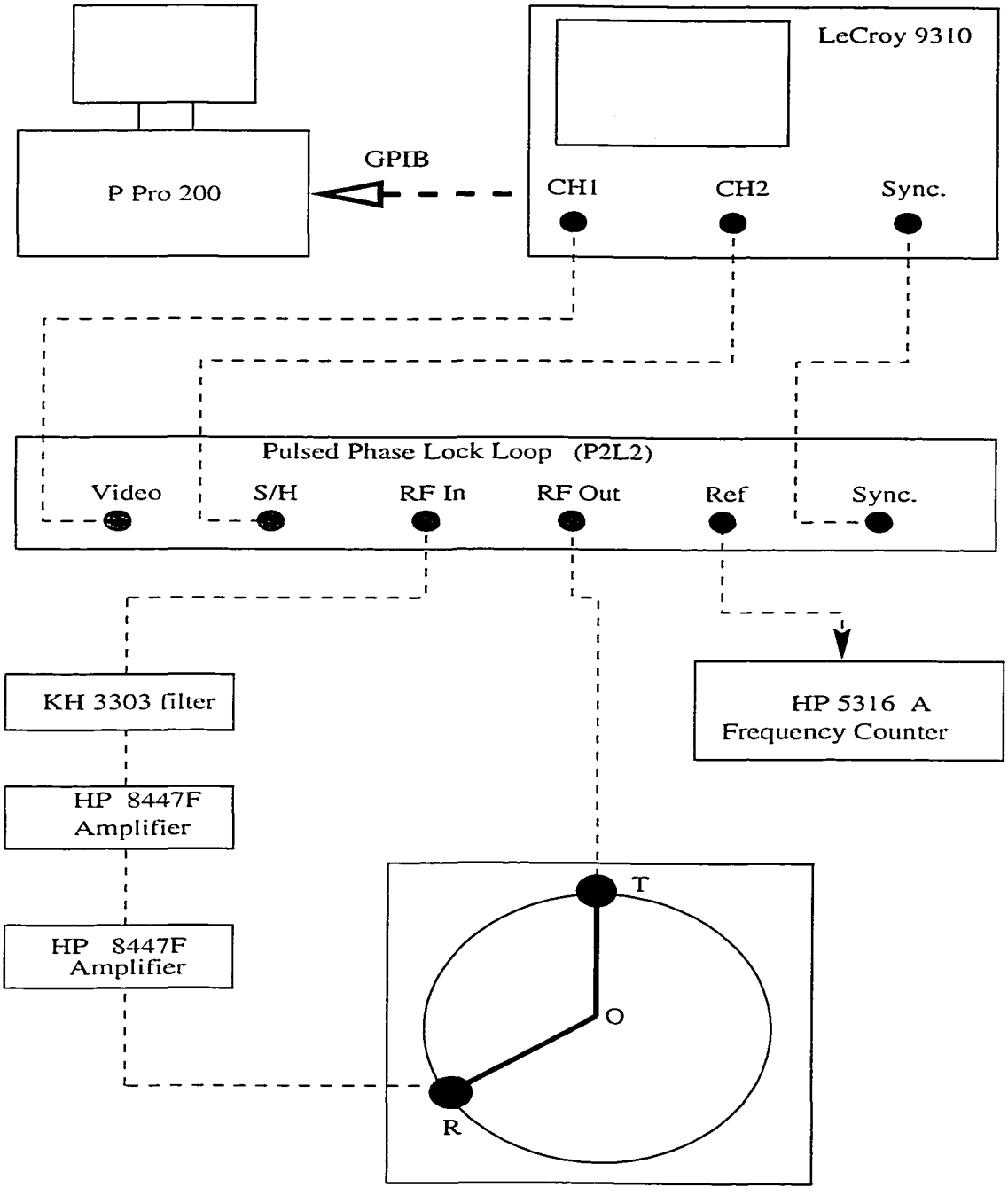

Figure 3.19: Fan beam setup for P_2L_2 spike position measurement.

Reproduced with permission of the copyright owner. Further reproduction prohibited without permission.

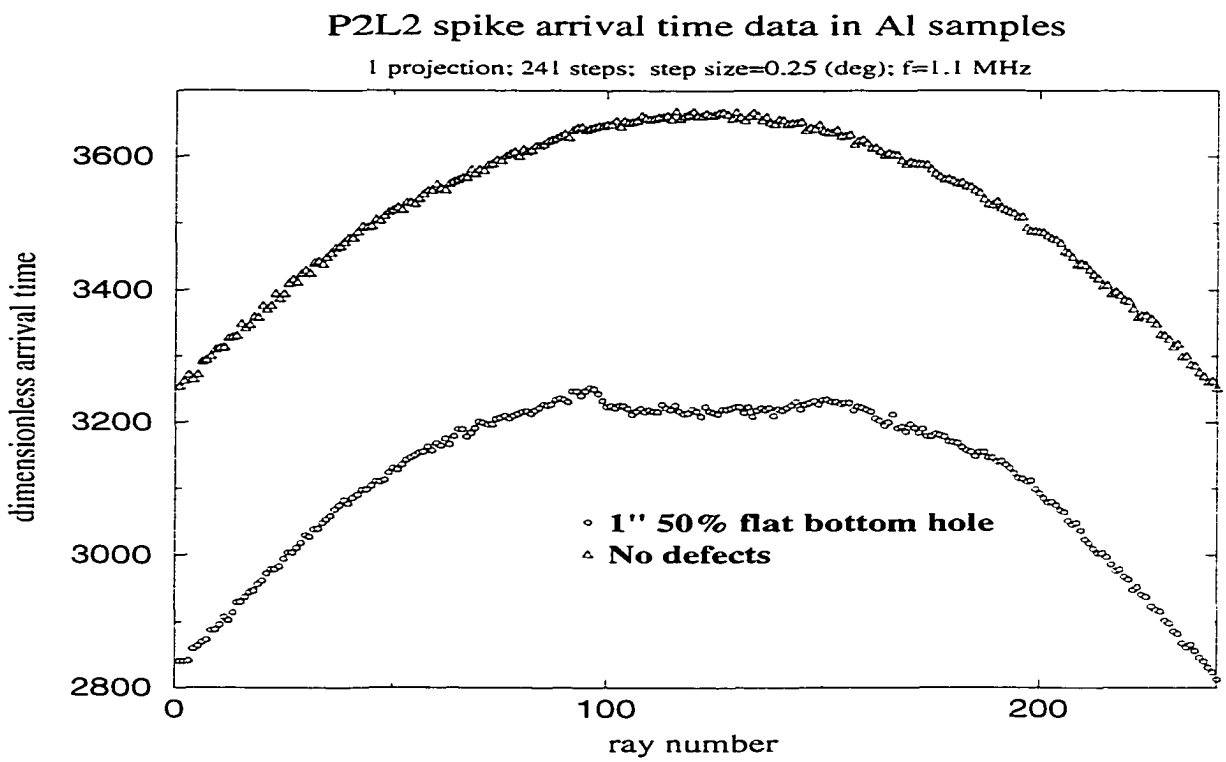

Figure 3.20: Comparison of projection data for defect-free aluminum plate and for a plate with 25.4 mm-diameter flat-bottom hole. Data represent position of the P_2L_2 spike in a fan beam tomographic experiment.

Reproduced with permission of the copyright owner. Further reproduction prohibited without permission.

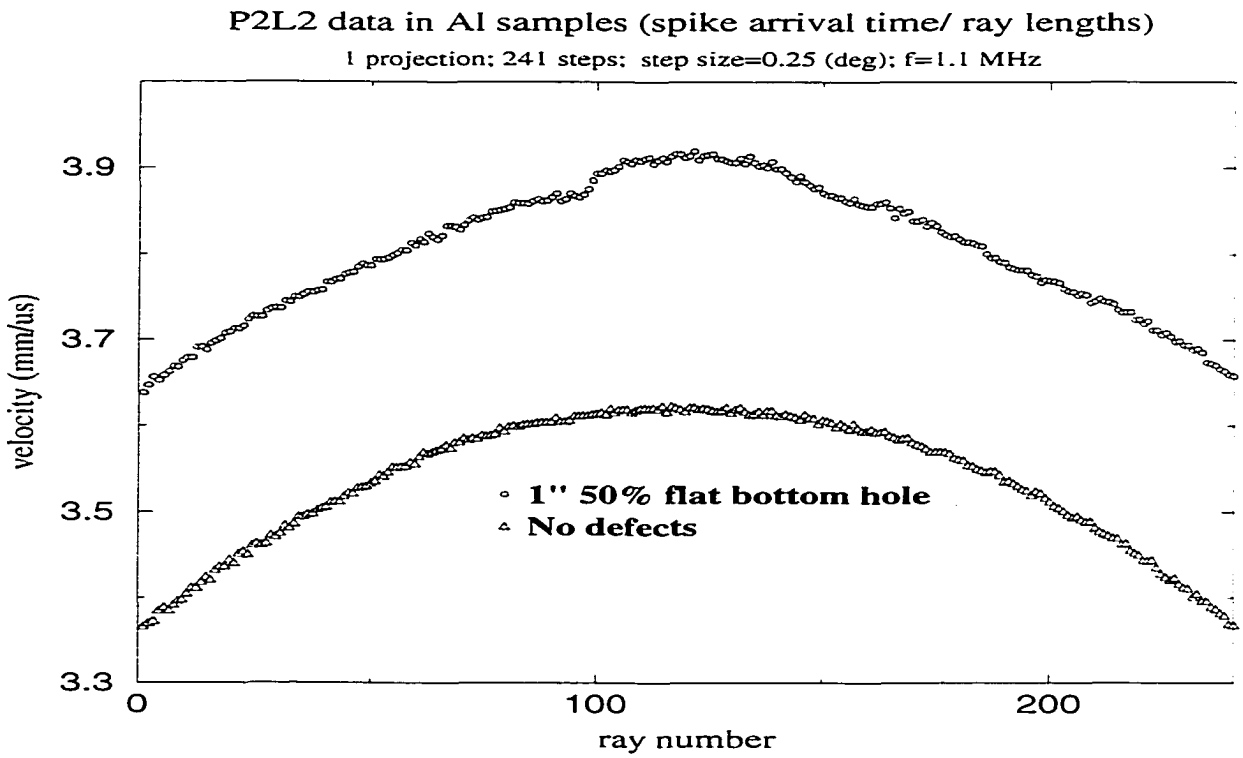

Figure 3.21: Residual parabolic trends on velocity data obtained with P_2L_2 spike position measurement. Velocities were computed from the arrival times in Fig. 3.20

Reproduced with permission of the copyright owner. Further reproduction prohibited without permission.

(mm/μs) of the signal. Theoretically this action should remove the above trend so the velocity plot in the absence of defects should be a horizontal straight line. Unfortunately, this doesn't happen in practice (Fig. 3.21) and some residual trends ar still present for both samples. However, the defect shows up much better now as a hump in the center. This is in agreement with theory because thickness reduction in this frequency region (1.1 MHz) results in growth of the S_0 mode velocity.

The remaining bias cannot be easily removed by scaling data or tuning the equipment. The physical nature of this bias is still unclear: possibly the P_2L_2 changes its output frequency while tracking the signal. This change in frequency results in a velocity change and makes accurate measurements much more complicated.

One way to solve the problem is to make a reference measurement on a defect-free plate and then subtract the reference data from real data. The drawback is that it is not always possible to get a "calibration standard"clean plate of the same material as the sample when field testing. We have, however, tried to do this with our laboratory samples (Fig. 3.22). As a result the defect in the center gets more emphasized but the "wings" on both sides still make interpretation difficult.

Numerous attempts to make use of the P_2L_2 in Fan Beam Tomography have failed. The device was initially intended to serve as a reference standard of "good" data compared to relatively low quality data from the expert system. However, we could not acquire usable fan beam data with it and decided to concentrate on the expert system development, which is summarized below.

Reproduced with permission of the copyright owner. Further reproduction prohibited without permission.

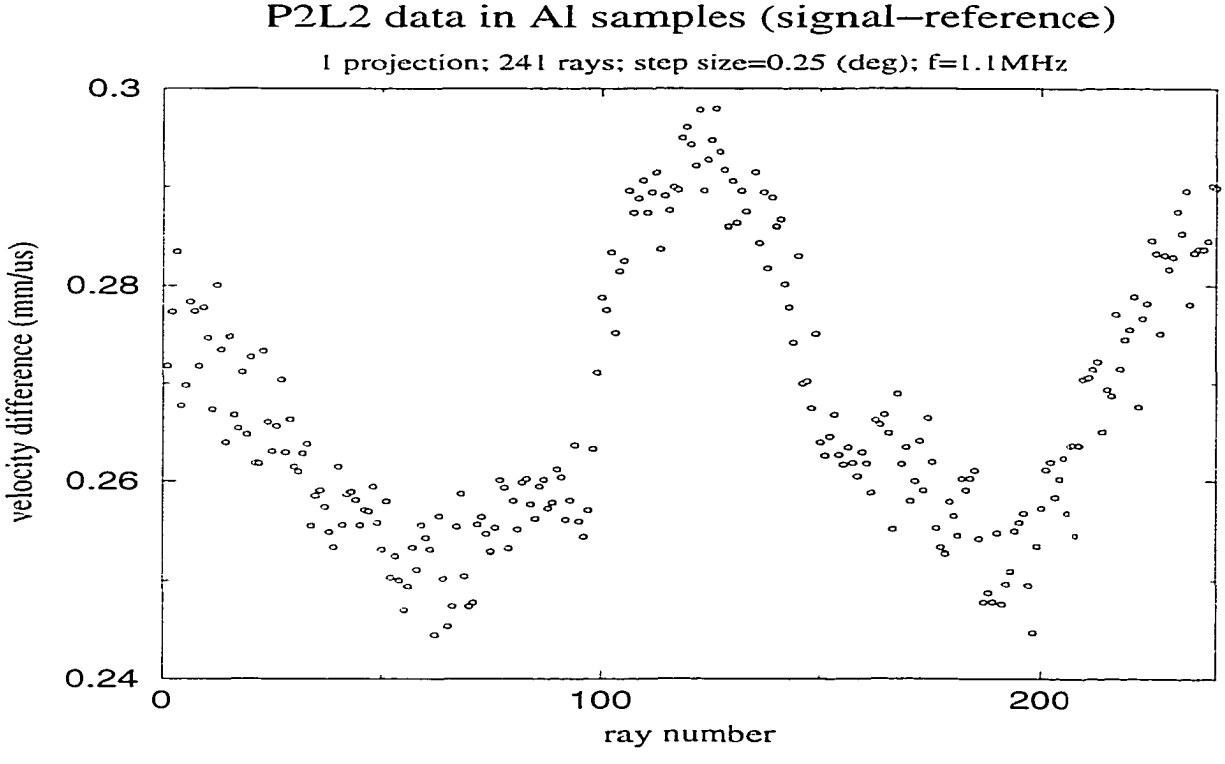

Figure 3.22: Difference plot obtained as a result of subtraction of the plots in Fig. 3.21. Central hump represents the defect. Note the artifacts on both sides of the image.

Reproduced with permission of the copyright owner. Further reproduction prohibited without permission.

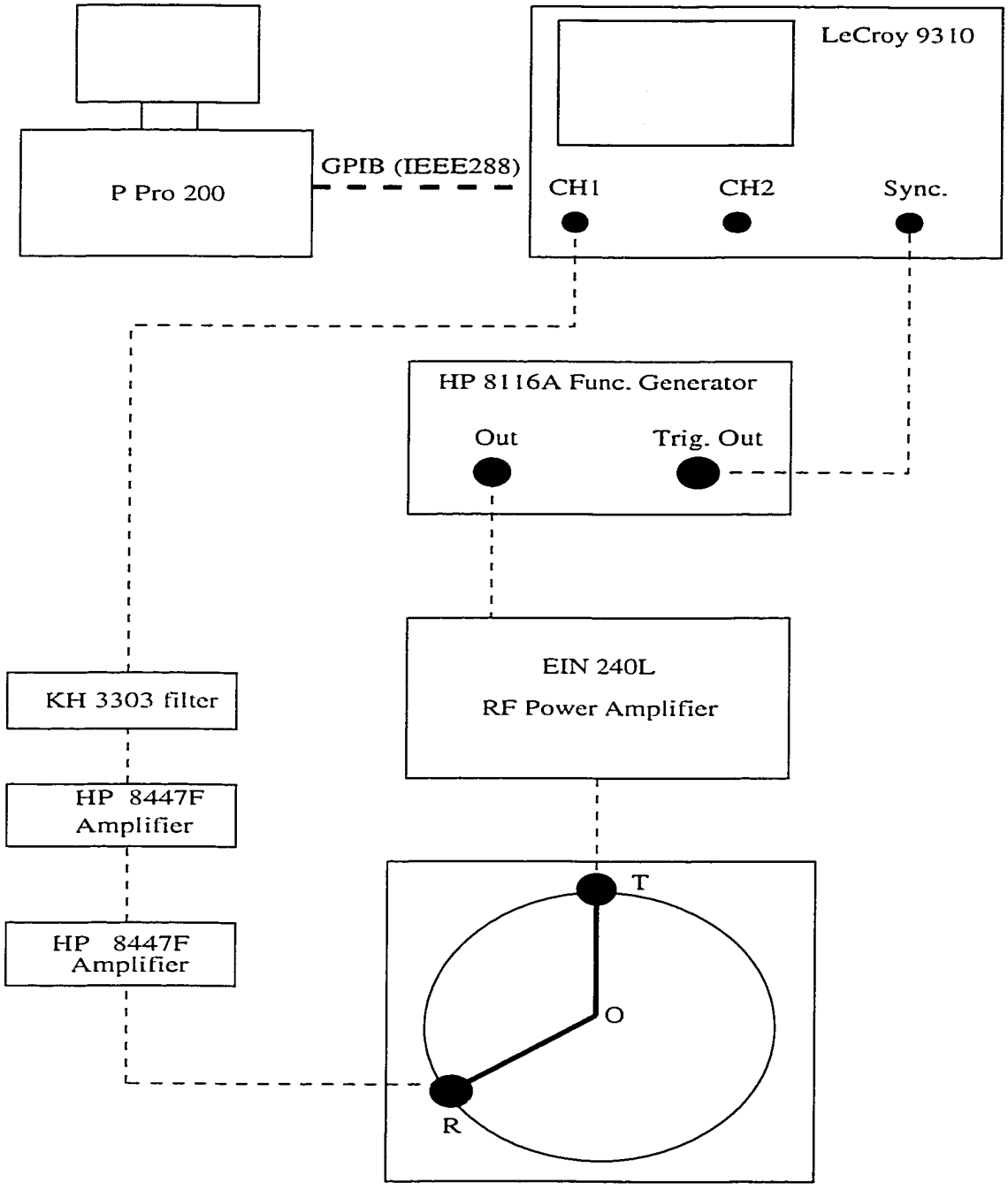

Figure 3.23: Fan beam setup in waveform capture mode.

Reproduced with permission of the copyright owner. Further reproduction prohibited without permission.

Method 3: Using expert system to find arrival times

The third method of data acquisition (Fig. 3.23) does not rely on any additional hardware to solve the arrival time problem. Instead it saves the entire digitized waveform from the LeCroy oscilloscope at each scanning step and then extracts the parameters of interest in software. We use an HP8116A function generator to generate a tone burst similar to that in the first and second methods. We also use ENI 240L (or 3100L) RF power amplifier to drive the transmitting transducer. As a result, the method produces a long file of stacked 5000-point waveforms that is analyzed by custom software programs.

The most important parameter to be extracted from the digitized waveforms is the arrival time of the fastest mode. This time depends upon the presence of any defects and, obviously, upon the distance between transmitter and receiver. We therefore need to detect the rather small variations in arrival time which carry the information about defects. It means that the measurement error should be smaller than the effect itself. We also have to remove the regular trend associated with the change in ray lengths during the scan. This is done by applying (3.4) to all the rays and then calculating the average velocities. The real measurement and scaling process is shown in (Fig. 3.24-3.29).

Fig. 3.24 represents the raw output of the program that analyses saved waveforms and estimates the arrival times of the fastest Lamb wave mode (mode S_0 in our case) excited at 1.1 MHz. The sample was 2.3 mm-thick aluminum plate with a 25.4 mm-diameter 50% thickness reduction flat-bottom hole in the center. This defect shows up as a minor distortion on the top of the curve which itself is a bias

Reproduced with permission of the copyright owner. Further reproduction prohibited without permission.

resulting from the regular change of ray lengths during the scan. For comparison we also show the data for another sample – 2.3 mm-thick aluminum plate with five 15 mm-diameter through holes drilled along a straight line and spaced at 43 mm from each other (Fig. 3.25). The fan beam shown covers only 3 holes. Again, their effect on the arrival times shows up as a slight distortion superimposed onto the regular bias.

Figs. 3.26 and 3.27 are the results of division of the theoretically calculated ray lengths by the arrival times. In other words, these are the average velocity plots. Now the defects are clearly seen as deep valleys with rough bottom structure. It is worth noting that all the software arrival time extraction algorithms used in this work determine the group delay rather than the phase delay. The dispersion of the group velocity of the S_0 mode in the 2.3 mm-thick aluminum plate at a frequency of 1.1 MHz is positive and any plate thinning slows the mode down. The through hole would also show up as slow region since rays bend around it and become longer. The shape of the valleys can be explained using only diffraction and scattering theories since the defect size is comparable to the wavelength of the Lamb waves [33].

It can be seen from both plots that there are some errors in determining the arrival time. This noise in the data can be further reduced by improving the corresponding time-finding software and the signal quality, but it cannot be eliminated completely. Another problem is the small linear bias present in the velocity data. Its nature is unknown at the moment, but most likely it occurs due to the mechanical imprecision of the equipment. The bias can be eliminated by subtracting reference data taken on a clean sample from the current data. The arrival time noise can be

Reproduced with permission of the copyright owner. Further reproduction prohibited without permission.

filtered out using the simplest moving-average filter of low order. The results of such filtering (moving average filter of order 10) of the above data are shown in Fig. 3.28 and 3.29. The mentioned bias is still present in filtered data. These plots justify the use of the low order moving average filters. They remove high spatial frequency random noise leaving regular features almost untouched. On the other hand, increasing the order of such a filter can eliminate some useful information.

Since the fan beam velocity data are consistent for both single thinning and multiple-hole samples we have completed their 18-projection scans taking 241 steps per projection at every 0.25°. The distance $|OR|$ (Fig. 3.12) was equal to 108 mm. The opening angle of the fan beam was thus equal to 60°. At that time this was the largest physically possible opening angle for the existing apparatus, and the best covered area could not be greater than the circle of radius $r = |OR| \cdot \sin(30°) = 56mm$. Later we broadened the opening angle up to 90° increasing the radius of the best covered area up to $r = |OR| \cdot \sin(45°) \approx 76mm$.

We then applied the fan beam reconstruction algorithm to the data. The image reconstructed from the raw data for the plate with the single 25.4 mm-diameter flat bottom hole is shown in Fig. 3.30 and the reconstruction from the data filtered with a moving average filter of the order 10 is shown in Fig. 3.31. The inner circle radius (best covered area) in both figures is 56 mm. In the first image the defect is much broader than it is in reality. This is caused by the high sensitivity of the reconstruction algorithm to the noise in data. The second image shows very good quantitative correspondence with the defect size.

We were unable to obtain a satisfactory reconstruction image for the Al plate

Reproduced with permission of the copyright owner. Further reproduction prohibited without permission.

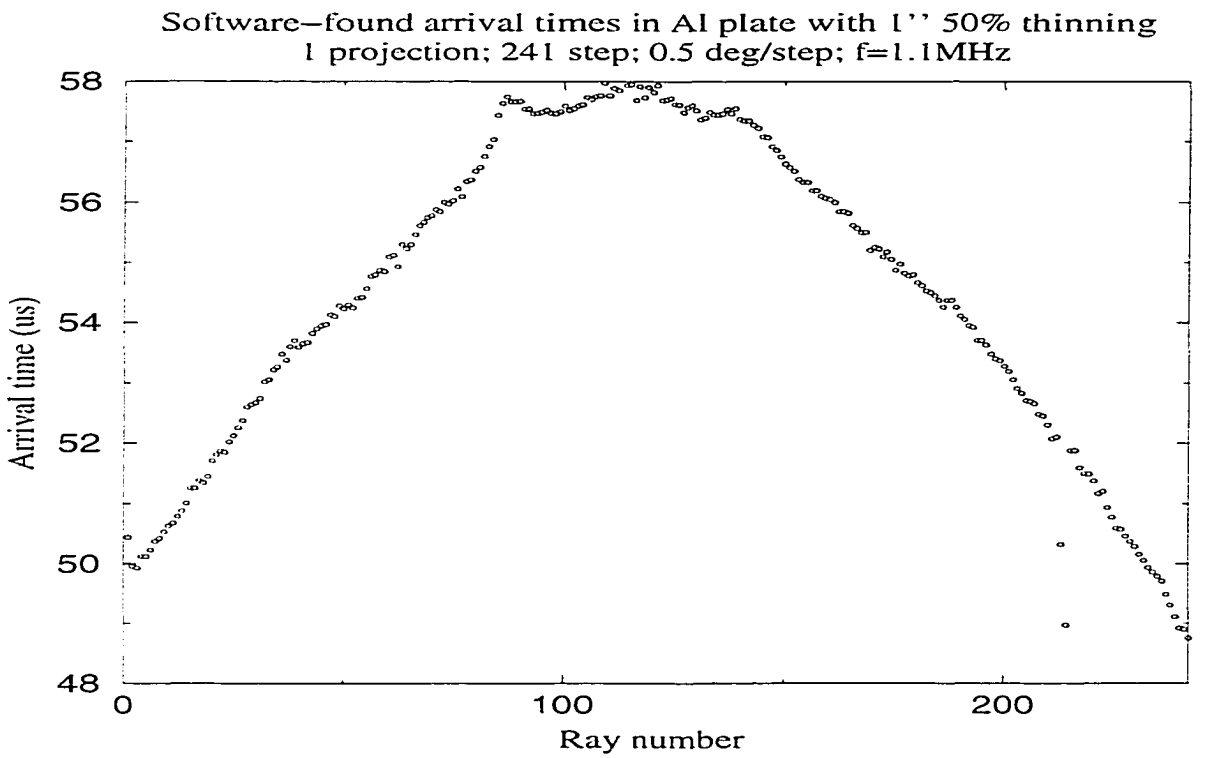

Figure 3.24: Software-extracted raw arrival times in aluminum plate with 25.4 mm-diameter flat-bottom hole.

Reproduced with permission of the copyright owner. Further reproduction prohibited without permission.

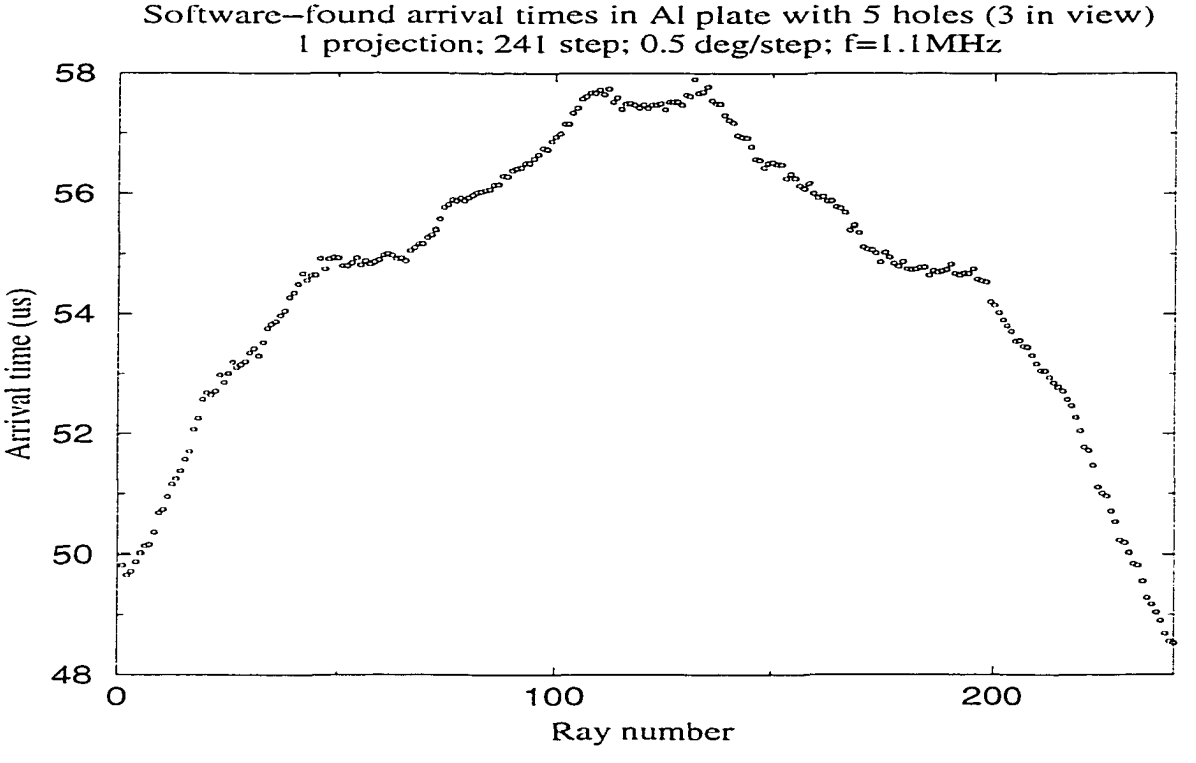

Figure 3.25: Software-extracted raw arrival times in aluminum plate with five 15 mm-diameter through holes.

Reproduced with permission of the copyright owner. Further reproduction prohibited without permission.

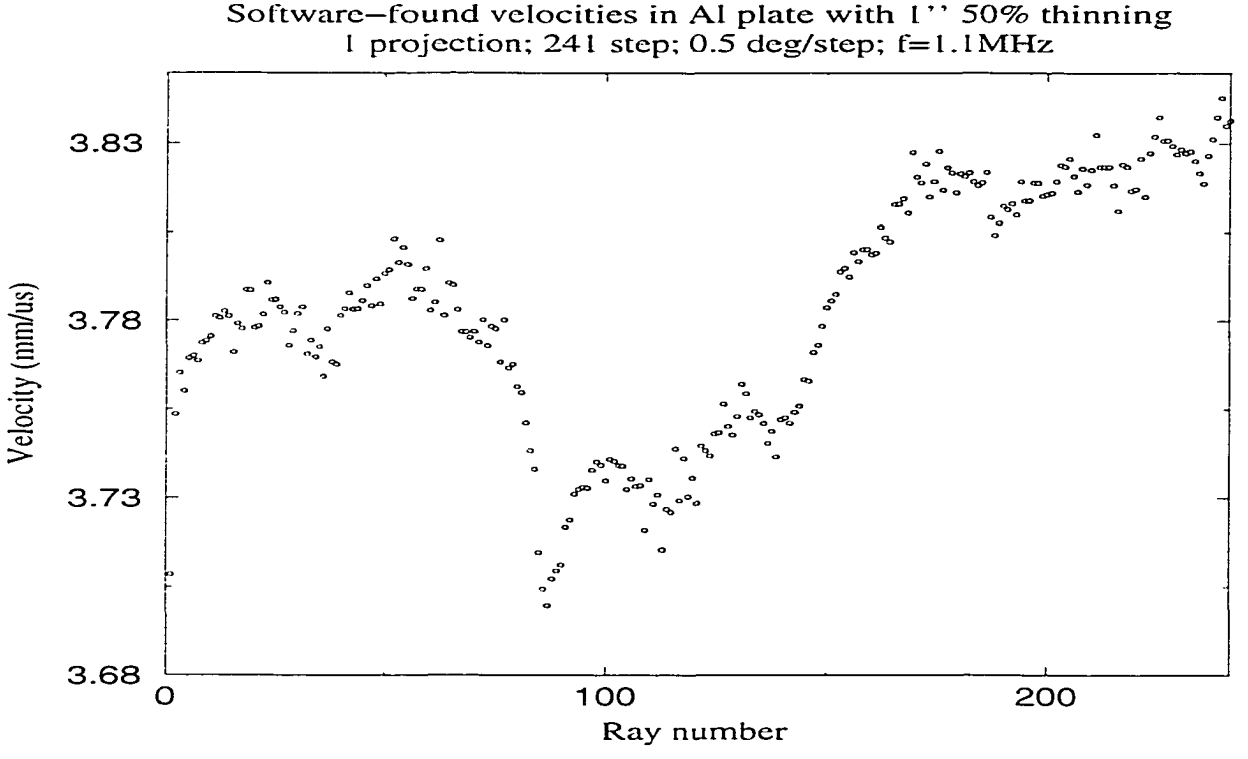

Figure 3.26: Raw velocities in aluminum plate with 25.4 mm-diameter flat-bottom hole. Velocities were calculated from the arrival times in Fig. 3.24.

Reproduced with permission of the copyright owner. Further reproduction prohibited without permission.

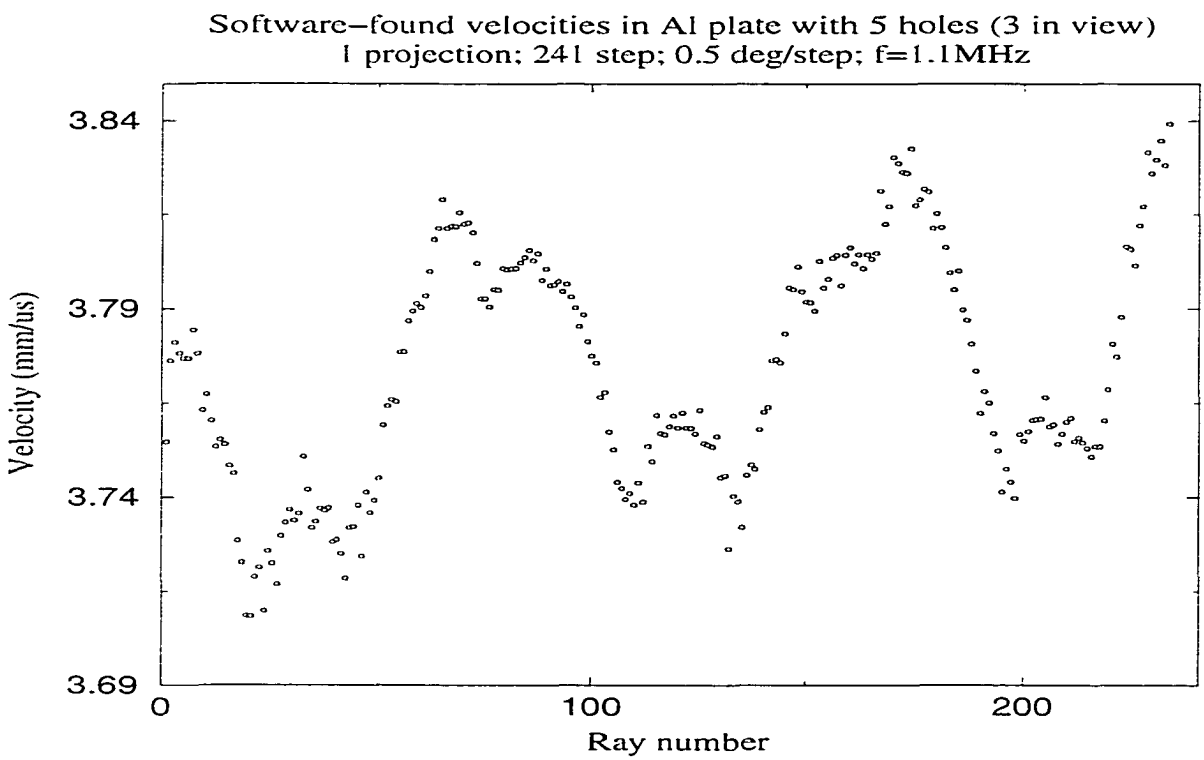

Figure 3.27: Raw velocities in aluminum plate with five 15 mm-diameter through holes. Velocities were calculated from the arrival times in Fig. 3.25.

Reproduced with permission of the copyright owner. Further reproduction prohibited without permission.

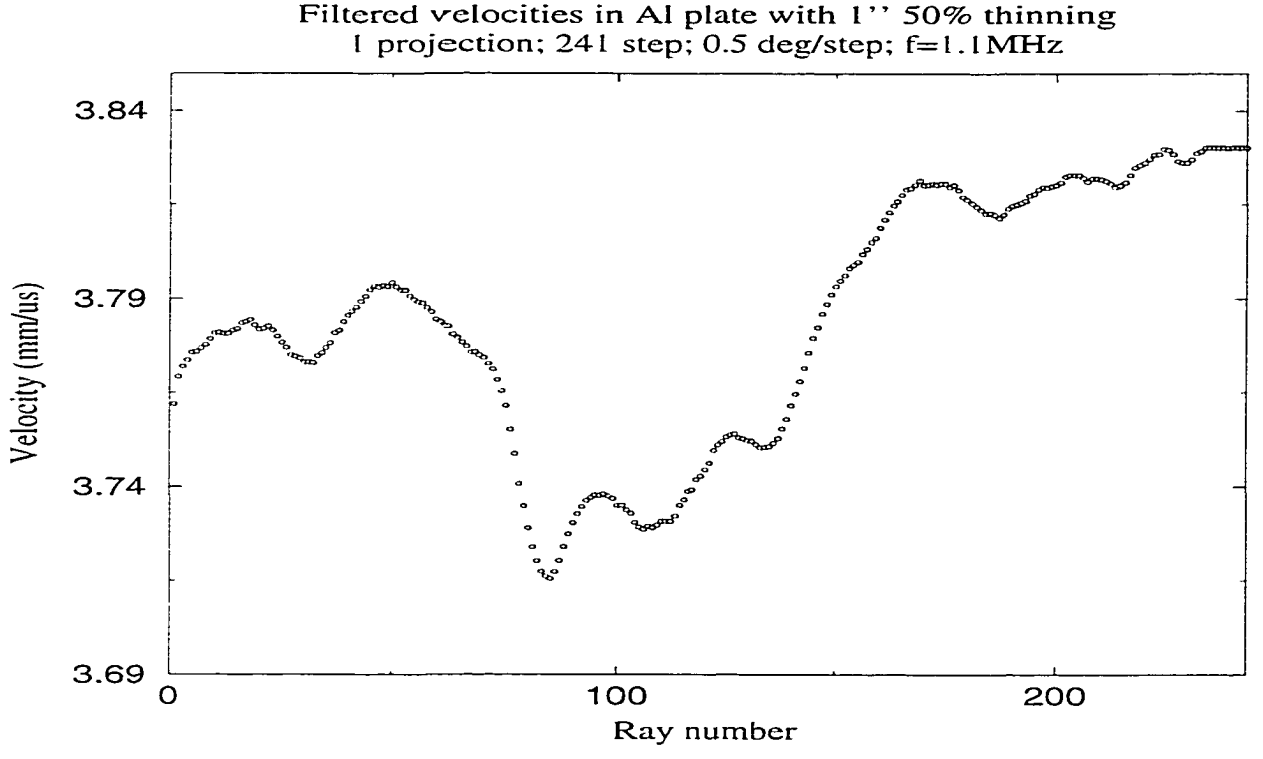

Figure 3.28: Smoothed velocities in aluminum plate with 25.4 mm-diameter flat-bottom hole. Velocities were obtained by smoothing data in Fig. 3.26 with a moving average filter of order 10.

Reproduced with permission of the copyright owner. Further reproduction prohibited without permission.

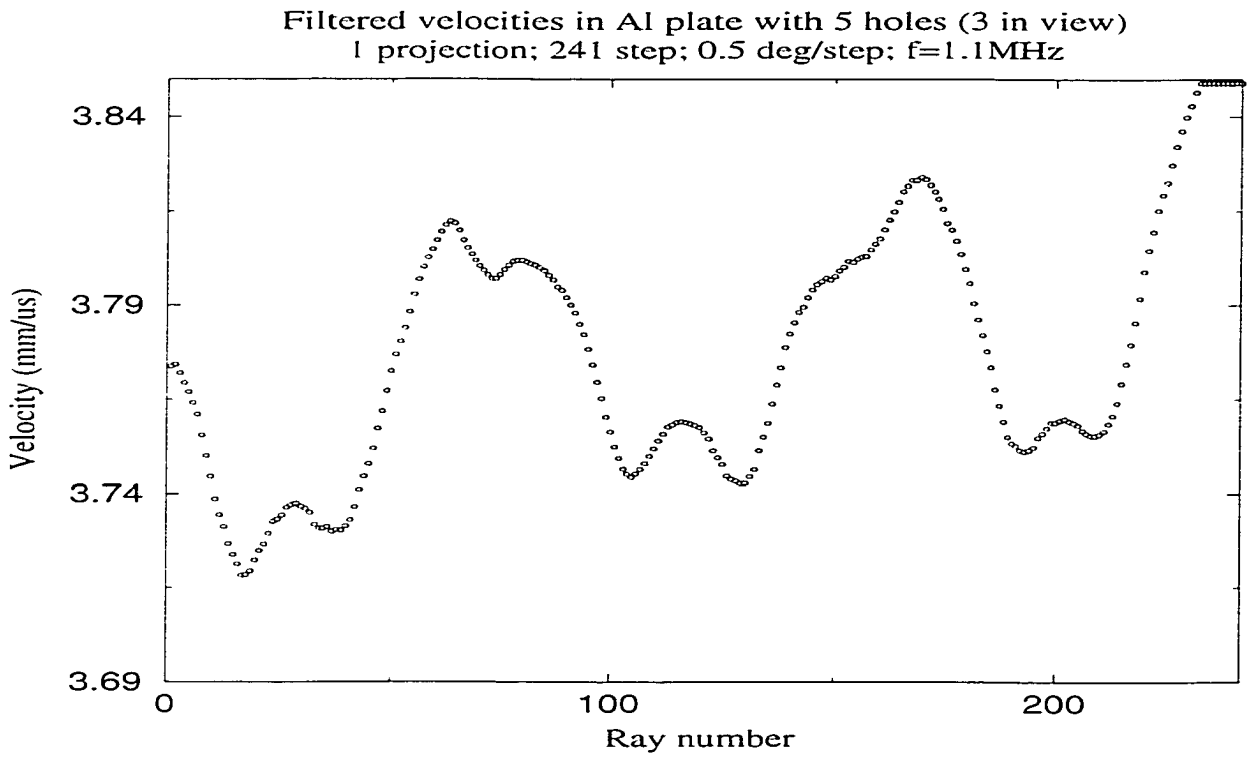

Figure 3.29: Smoothed velocities in aluminum plate with five 15 mm-diameter through holes. Velocities were obtained by smoothing data in Fig. 3.27 with a moving average filter of order 10.

Reproduced with permission of the copyright owner. Further reproduction prohibited without permission.

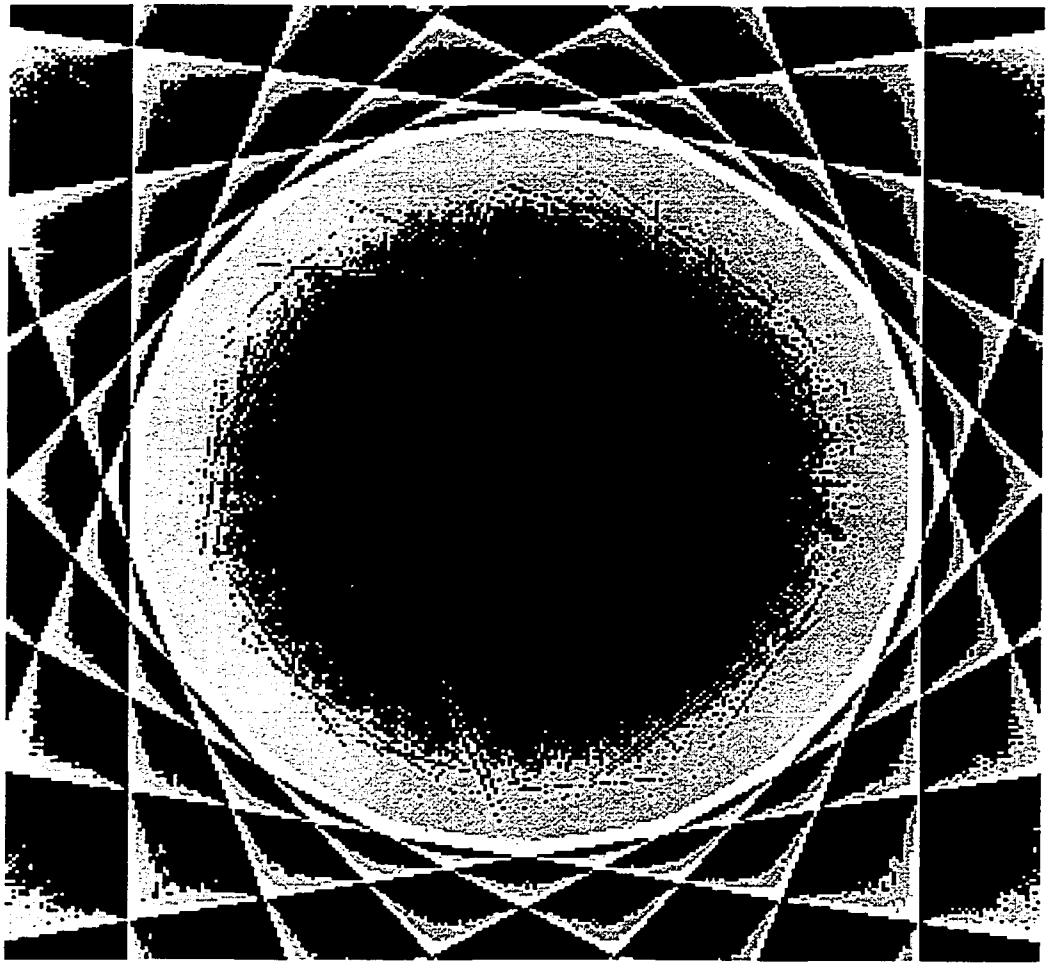

Figure 3.30: Fan beam reconstruction of single 25.4 mm-diameter flat-bottom hole in aluminum plate from raw (unfiltered) velocity data. The radius of the artifact-free circular area is 56 mm. The reconstructed defect is unrealistically large.

Reproduced with permission of the copyright owner. Further reproduction prohibited without permission.

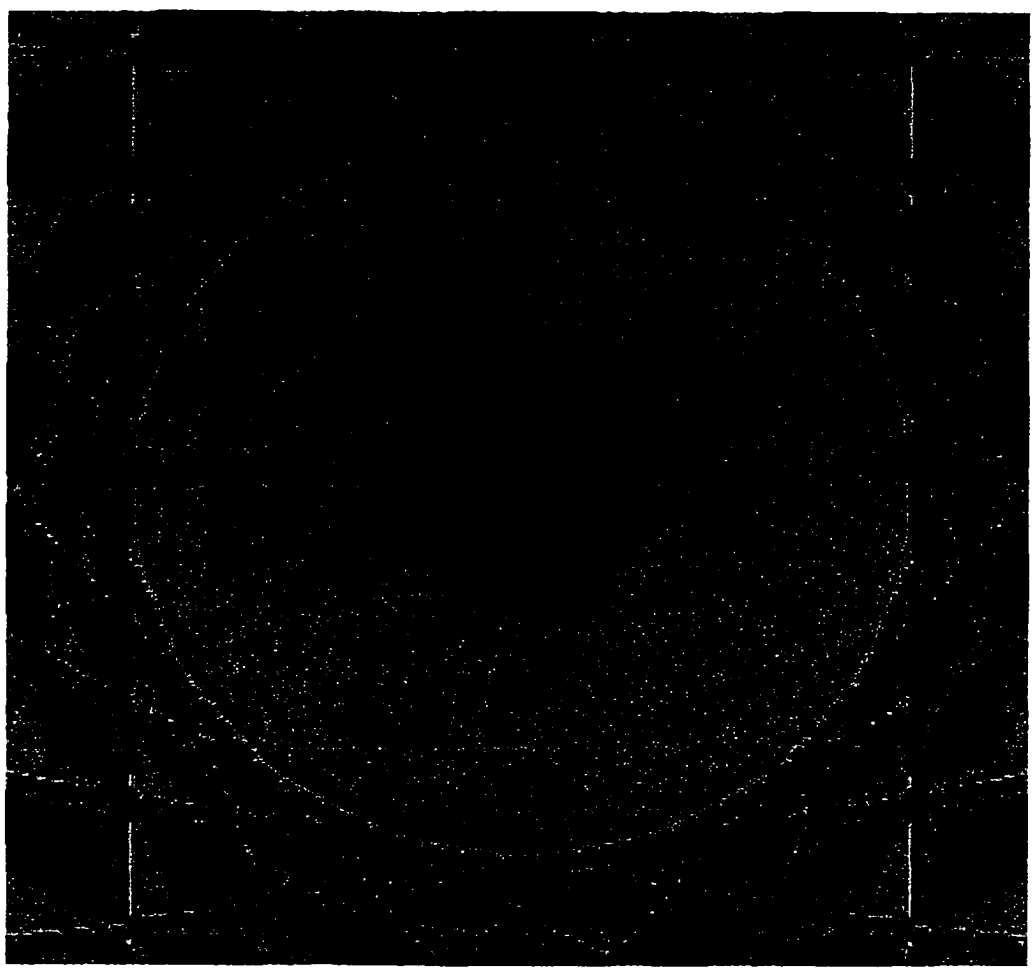

Figure 3.31: Fan beam reconstruction of single 25.4 mm-diameter flat-bottom hole in aluminum plate from smoothed velocity data. The radius of the artifact-free circular area is 56 mm. The size of the reconstructed defect is much closer to the reality than that in Fig. 3.30.

Reproduced with permission of the copyright owner. Further reproduction prohibited without permission.

with 5 through holes. According to the single projection data we should have been able to get a satisfactory result at least for the filtered data. But instead of three separate holes we get a large dark spot covering almost the entire image area. The first possible reason for this is that the systematic linear bias present in all the projections distorts the reconstruction. The second reason could be an inability of the current version of the reconstruction program to resolve more than one spatially separated defect, i.e. the assumption of straight rays breaks down.

In order to check the second reason we have numerically modeled the fan beam projections of two elliptic defects placed in various positions within the scanned area. The reconstruction program was then applied to the simulated data and the results are shown in Figs. 3.32 and 3.33. The separate objects obviously can be resolved by the reconstruction program. There are two remaining possible reasons for the inability to reconstruct multiple defects. The first reason is the poor quality of the projection data, mainly the systematic bias present in Figs. 3.28 and 3.29. It is probably related to the mechanical properties of the scanner such as dragging the transducer behind and accumulating position error due to the loose gear thread. The second reason is the Lamb wave scattering on multiple defects which complicates interpretation of signals received at certain "critical" directions.

It seems reasonable to eliminate existing uncertainty in ray length determination by using contact transducers with smaller footprint area. To accomplish this we chose 7 mm diameter 2.25 MHz *Panametrics*^{TM} transducers and fabricated cone-shaped acrylic resin delay lines for them. The lower ends of delay lines contact the sample and have a diameter of 2mm. The delay time of compressional elastic waves

Reproduced with permission of the copyright owner. Further reproduction prohibited without permission.

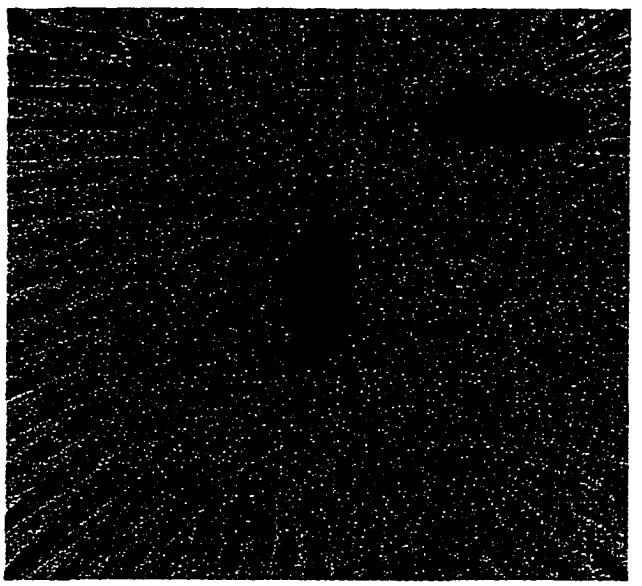

Figure 3.32: Resolution of the fan beam tomography: two simulated small ellipses.

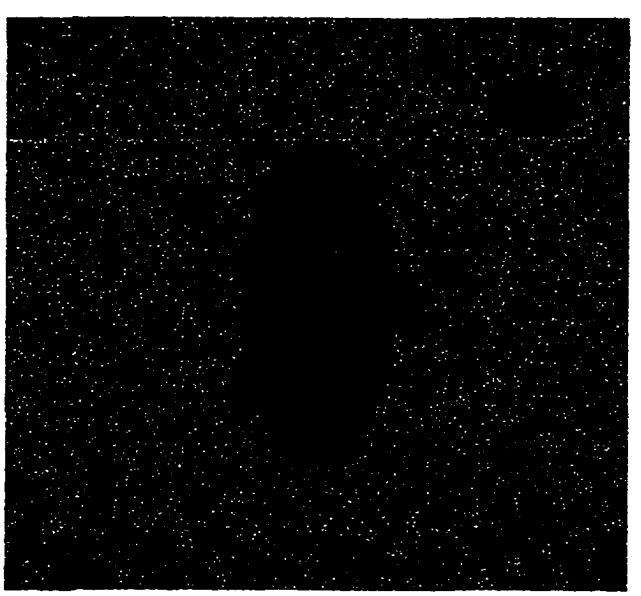

Figure 3.33: Resolution of the fan beam tomography: two simulated ellipses of different size.

Reproduced with permission of the copyright owner. Further reproduction prohibited without permission.

penetrating both delay lines is measured to be 12.1 μs. The drawback of this footprint reduction is the loss of received energy and therefore the need to amplify the signal. Since standard HP 8447F amplifiers are rather broad band, they amplify noise at all frequencies (white noise) including the operating band. The most appealing way to reduce this kind of noise is signal averaging that can be performed digitally in the hardware (LeCroy oscilloscope) or software. We have chosen the latter due to its flexibility. Another way to improve the Signal to Noise Ratio (SNR) is by using more input power or applying time delayed amplification. These methods could be used in a later version of the instrument, but the appropriate hardware is not currently available at $W\&M$.

Figs. 3.34 and 3.35 show the results of signal averaging done by reading several number of waveforms at the same scanning position from the oscilloscope, adding them point by point and then dividing by the number of reads.

It can be easily seen that averaging indeed helps reducing white noise and the level of reduction is proportional to the rate of averaging. However, averaging requires multiple reads from the digital oscilloscope thus slowing down the experiment. For laboratory research purposes the rate of 5 seems acceptable from both SNR and scanning time points of view. Modern data acquisition cards with faster data transfer mechanisms allow for higher averaging rates without significant drop in speed.

3.3.3 Discussion

The results of this chapter provide insight into aspects of Lamb Wave Tomography based on the combination of the Fan Beam data acquisition geometry and the

Reproduced with permission of the copyright owner. Further reproduction prohibited without permission.

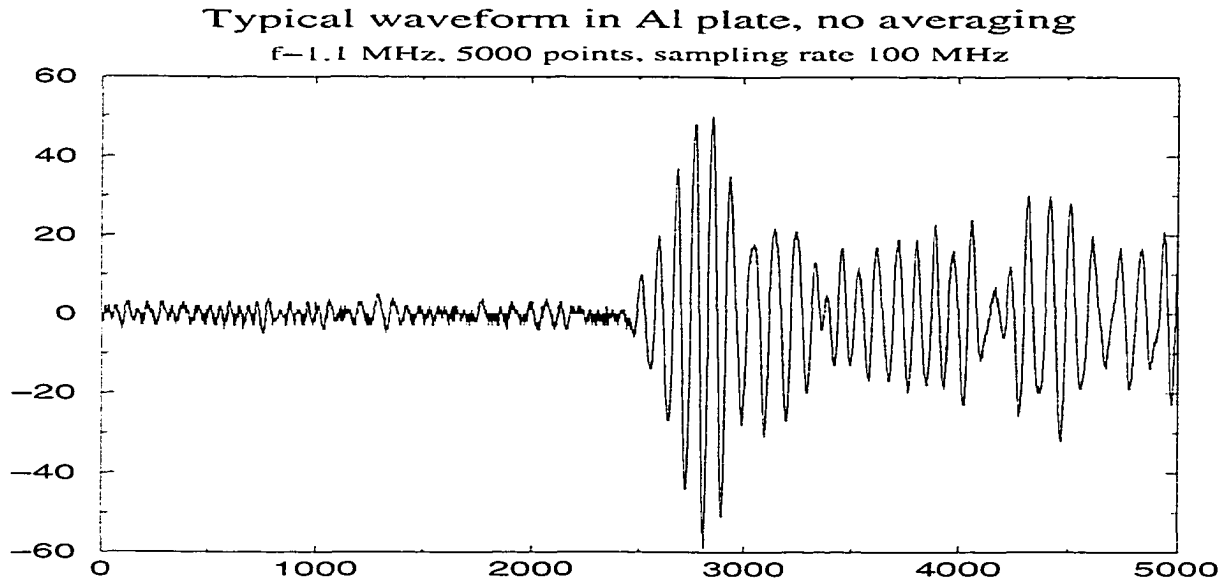

Figure 3.34: Noise reduction by averaging: A typical raw signal.

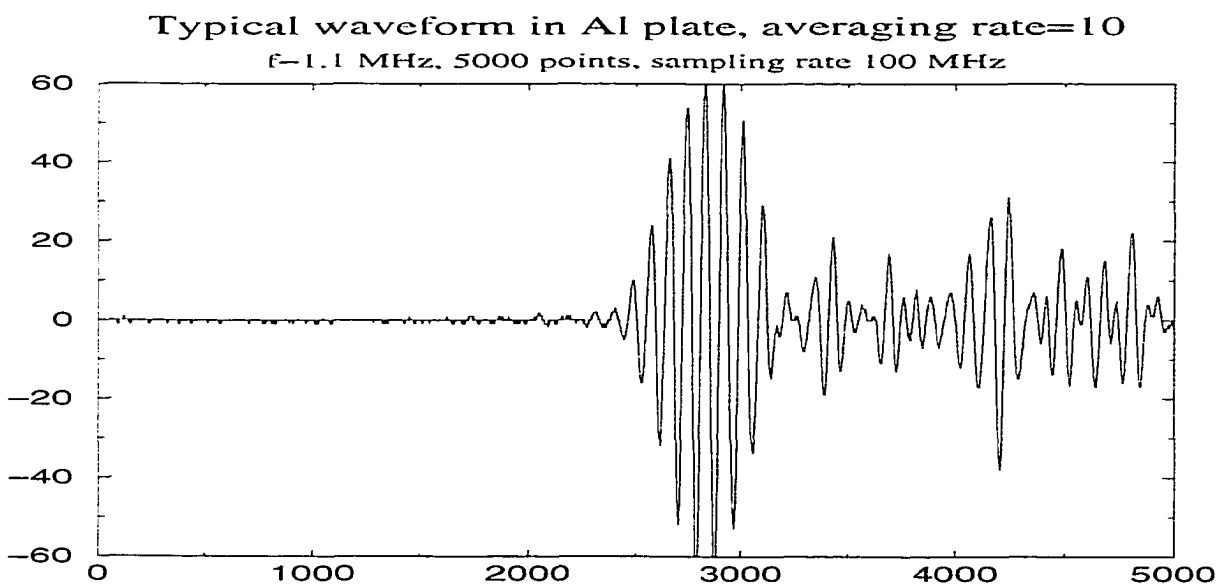

Figure 3.35: Noise reduction by averaging: Signal from Fig. 3.34 averaged 10 times.

Reproduced with permission of the copyright owner. Further reproduction prohibited without permission.

convolution-backprojection reconstruction algorithm. They can be summarized as follows:

- The convolution-backprojection algorithm was adapted for the circular array geometry and tested on simulated data. Its resolution strongly depends on the number of projections as well as on the number of rays per projection. These and the total number of transducers in the array can be easily optimized by simulating the defects. The image quality can be further enhanced by equipping the algorithm with appropriate software filters.

- A serious drawback of the circular array fan beam geometry is that the ray density is not uniform within the big circle. The most densely covered is the inner circle with a radius which depends on the fan beam opening angle. We found that the maximum size for practical use is reached when the opening angle is 90^{circ}. At that time the best covered area has the radius of $r = R/\sqrt{2}$ and is half as small as the total scanned area. This is very inefficient for large-scale applications such as aircraft skins or ship hulls.

- For the success of the Lamb wave traveltime tomography the distance between transducers should be measured with high accuracy. This was not the case with our current version of the scanner apparatus. As a result, projection data were biased causing the reconstruction algorithm to perform poorly.

- All attempts to use P_2L_2 to track signal phase changes failed because its output always contained an inexplicable parabolic trend. The best-guess explanation for this trend is that the P_2L_2 frequency changes constantly thus making the

Reproduced with permission of the copyright owner. Further reproduction prohibited without permission.

velocity of dispersive Lamb waves change accordingly.

- The arrival time extraction software was accurate enough to spatially resolve several defects. However, the inversion algorithm failed to reconstruct even a single defect. When the associated noise was successfully filtered with simple averaging filters the reconstruction quality significantly improved. This illustrates the unforgiving nature of the convolution-backprojection algorithm and highlights the problems with its application to inherently noisy Lamb wave tomography.

- The tomographic apparatus can be implemented as a circular array of transducers thus fully excluding mechanical motion from the system. An array-based equipment will be fast and provide unbiased data since the ray lengths will be accurately determined once and forever. This will eliminate many of the problems described above except the poor area coverage and sensitivity to noise.

Although many of the problems, associated with the Lamb Wave Fan Beam Tomography based on the convolution-backprojection algorithm can, in principle, be solved, the remaining ones convinced us to switch to a more promising alternative - the Lamb Wave Crosshole Tomography based on the Algebraic Reconstruction Algorithm. This technique is discussed in the next chapter.

Reproduced with permission of the copyright owner. Further reproduction prohibited without permission.

Chapter 4

Double crosshole Lamb wave tomography

This chapter focuses on the development of double crosshole Lamb wave tomography based on the Algebraic Reconstruction Algorithm. First, the theory is discussed briefly, followed by implementation details and simulated results for various scanning geometries. In the experimental part we describe the scanning technique, the data collection procedure, and include several images, reconstructed from the manufactured defects in aluminum plates. Finally we compare all the tomographic methods and algorithms used in the present work and discuss needed directions of further development.

Reproduced with permission of the copyright owner. Further reproduction prohibited without permission.

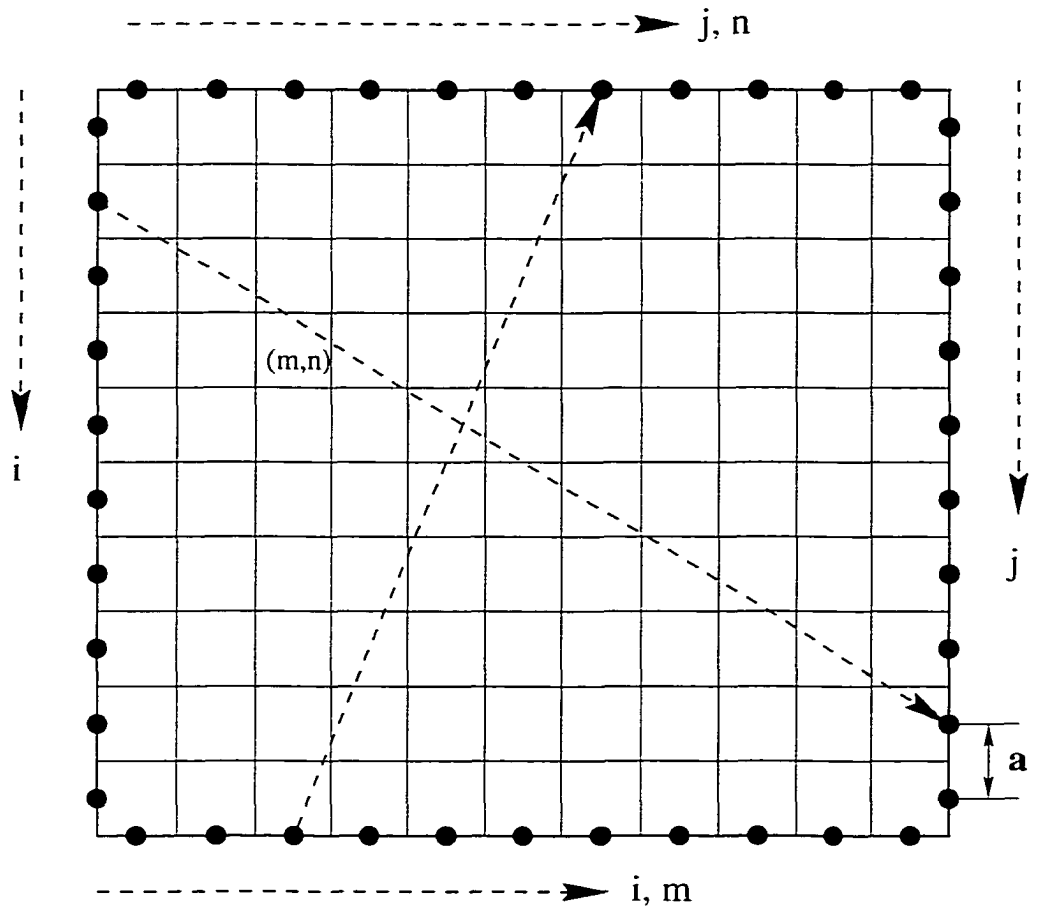

Figure 4.1: Explanation of the ART algorithm for the double crosshole geometry: a - distance between transducers; pixels (m, n) are indexed as shown; ray enumeration order (i, j) is different for different projections.

Reproduced with permission of the copyright owner. Further reproduction prohibited without permission.

4.1 The Algebraic Reconstruction Algorithm

The Algebraic Reconstruction Technique (ART) serves the same purpose as the previously described Parallel Projection and Fan Beam reconstruction algorithms, namely, it provides solutions for the problem of recovering an object from its projections. What makes it useful for Lamb wave tomography is its iterative nature and its great flexibility which allows practically any scanning geometry and incomplete data sets. On the contrary, Parallel Projection and Fan Beam algorithms both belong to the convolution-back projection family, which requires strictly determined scanning configurations and is very sensitive to any incompleteness or noise in the experimental data.

For the sake of clarity we will briefly describe the Four-Legged Crosshole geometry ART algorithm for our particular scanning setup as shown in (Fig. 4.1). Circles are the transducer positions which can all be occupied by transducers in the case of a square array of transducers. In the current implementation only two positions are occupied at a time since we use a single transmitter-receiver pair. Both transducers are attached to linear slider screws and can be moved back and forth using two stepper motors controlled by the computer. The transmitting transducer steps along the lower edge from left to right incrementing i from 0 to $N-1$. The receiving transducer slides along the upper edge sweeping all N available j-positions for a fixed i. For each relative position the whole wave train is recorded and stacked into a data file. After N^2 measurements, the first cross-hole projection is complete. We then move the transmitter down from the upper left corner and move the receiver up and down along the right side. Again, N^2 measurements complete the second projection. The

Reproduced with permission of the copyright owner. Further reproduction prohibited without permission.

increased number of crosshole projections is the only difference between the double- and the single-projection crosshole geometries.

The ray density is critical to the reconstruction quality. It can be increased by increasing the number of transducer locations per side, which can be rather expensive in the case of an array. Alternatively, one may try to measure additional data using the available setup. For example, two more crosshole projections can easily be obtained by swapping transmitting and receiving transducers. Furthermore, transmitting from one and receiving on the other three sides of the rectangle would provide additional valuable information and also increase ray density. The most desired solution is to be able to take data in both directions along the rays connecting any two points on the square (Fig. 4.1). This can easily be accomplished by having a perimeter array of multiplexed transducers, but is much harder to realize when the perimeter is covered by moving transducers mechanically. We, therefore, limited ourselves to acquiring only two mutually orthogonal crosshole projections.

As we have seen (Fig. 4.1), each ray can be assigned two coordinates i, j. For each projection $i, j \in [0, N)$. The resulting square image can be divided into cells (pixels) in an arbitrary fashion, but the most reasonable decision is to make the square pixel side length equal to the transducer step size a. This will preserve all the information contained in the data. We have drawn pixels so that transducer positions are in the middle of the edge pixel sides. Each pixel in the resulting matrix has unique coordinates $m, n \in [0, N)$ starting from the lower left corner. Each $ray[i, j]$ crosses a certain number of pixels on its way from transmitter to receiver. The term "ray" actually stands for the path the Lamb wave travels in the medium (plate). These

Reproduced with permission of the copyright owner. Further reproduction prohibited without permission.

paths are straight lines if the plate is made of isotropic homogeneous material. If some anisotropy or defects are present the paths will differ from straight lines and generally will be curved in some complex fashion. It is obvious that in the latter case the arrival time of a particular Lamb wave mode and the pixels it travels through will differ from those in the straight ray assumption. To take the ray bending effects into account and thus to improve the resolution of reconstruction methods, Lamb wave diffraction tomography is needed.

In the scope of the present chapter we primarily concentrate on the straight ray assumption. Even when the defects are so severe as through holes and we don't expect the geometrical approach to work, it is still very important to check the limits of the method's applicability. Diffraction tomography is currently under active development in the literature even for the simplest acoustic case. There is no reliable universal algorithm yet, but many existing algorithms need a straight ray ART for the initial estimation of the velocity pattern in the sample. That is why even in the case of failure to reconstruct severe scatterers we still need a tested, working version of the straight ray ART code.

Let's now assume all the rays to be straight lines connecting transmitters and receivers. Each $ray[i,j]$ will cross certain pixels on its way. In other words, the wave will travel some time within each of those pixels. We assume the velocity to be constant for each pixel and denote it as $v[m,n]$ where m,n are the pixel's coordinates starting from the bottom left corner. The time the wave spends crossing the pixel will then be $t[i,j,m,n] = \frac{\delta[i,j;m,n]}{v[m,n]}$, where $\delta[i,j;m,n]$ is the length of a segment that $pixel[m,n]$ cuts from the $ray[i,j]$. To get the experimentally measured arrival time for

Reproduced with permission of the copyright owner. Further reproduction prohibited without permission.

a given $ray[i,j]$ we need to sum all partial times $t[i,j;m,n]$ over the pixels involved:

$$T[i,j] = \sum_{m,n \in ray[i,j]} t[i,j;m,n] = \sum_{m,n \in ray[i,j]} \frac{\delta[i,j;m,n]}{v[m,n]} \tag{4.1}$$

(4.1) is a system of linear equations with unknown slownesses $\frac{1}{v[m,n]}$. We can calculate the segment lengths $\delta[i,j;m,n]$ theoretically and measure $T[i,j]$ experimentally. Solving the matrix equation will yield the velocity pattern of a given Lamb wave mode throughout the square region. Since the operating frequency is known we can easily transform the velocity map into a thickness map. We can also use the velocity map as an input for various iterative diffraction tomography methods.

For the chosen scanning geometry the total number of equations in a single crosshole projection equals N^2 where N is the number of transmitter positions. In our experiments, for example, we often use $N = 100$. To avoid the direct inversion of such a large matrix the less computationally intensive iterative Algebraic Reconstruction Technique is commonly used. When applied to our case it leads to the following sequence of operations:

1. Determine the segment lengths $\delta[i,j;m,n]$, then estimate pixel velocities (an initial guess) and calculate estimated values for the arrival time of each ray:

$$T^0[i,j] = \sum_{m,n \in ray[i,j]} \frac{\delta[i,j;m,n]}{v^0[m,n]} \tag{4.2}$$

2. For each ray calculate velocity updates in the cells containing that ray:

$$\triangle \frac{1}{v_{m,n \in ray[i,j]}[m,n]} = \frac{T[i,j] - T^0[i,j]}{L[i,j]} \tag{4.3}$$

Reproduced with permission of the copyright owner. Further reproduction prohibited without permission.

where $L[i,j]$ is the length of $ray[i,j]$ and $T[i,j]$ is the experimentally measured arrival time for $ray[i,j]$.

3. Add the update to the current $\frac{1}{v[m,n]}$ values for that ray thus completing the first iteration:

$$\frac{1}{v^1[m,n]} = \triangle \frac{1}{v[m,n]} + \frac{1}{v^0[m,n]}; m,n \in ray[i,j] \tag{4.4}$$

4. The values $v^1[m,n]$ can be used as an input for the second iteration. Steps (4.2) – (4.4) are repeated until the required accuracy is reached.

The above algorithm updates pixel velocities ray-by-ray leading to the so called "salt and pepper" noise [64] in the resulting image. To eliminate it, at each iteration one can first calculate the updates for all the rays and only then update all the pixel velocities simultaneously. The modified method is called SIRT (Simultaneous Iterative Reconstruction Technique) and is also used further in this chapter.

4.2 Reconstruction of simulated defects

When this work started we already had a crosshole scanner built by Hinders and McKeon, but it was only suitable for the two-legged tomography, described in the introduction. In other words, we could only measure a single crosshole projection with it. Nascent Technology Solutions, LLC provided a custom support jig for the sliders making it possible to take two mutually perpendicular sets of crosshole projections. Before modifying the apparatus we needed to make sure that adding one more projection will really improve the quality of the reconstructed image. We also

Reproduced with permission of the copyright owner. Further reproduction prohibited without permission.

needed to change the existing reconstruction program to accommodate it to various scanning geometries. One effective way to accomplish these tasks is by working with simulated objects. We decided again to simulate one or two elliptical defects within the region of interest and reconstruct them with the ART algorithm. Varying the number of crosshole projections and the number of rays in each projection gave us the information about image quality and resolution to help us decide whether we would need to modify the existing crosshole scanner.

We modified the existing straight ray ART program created by Jim McKeon so that it became easily adaptable to practically any scanning geometry. The new version could handle up to four single 100×100 crosshole projections simultaneously instead of just one. The preprocessing step involves computation of all geometry-related parameters and storing them in the memory, then the program performs the reconstruction itself. It is likely that in field conditions geometry will be defined only once which can save up to 75% of the time for repetitive tasks. Currently it runs $\approx 10sec.$ on our Pentium-Pro 200, and 75% of this time is used for geometry processing.

Simulations were performed over a 100×100 mm square having 20, 50 and 100 transducer positions per side. Corresponding distances between adjacent transducers were 5.0, 2.0 and 1.0 mm.

We have grouped our simulated results into horizontal triples. Images within a triple have the same number of pixels (i.e. transducers in the array) and differ only by a number of crosshole projections. One projection means conventional crosshole geometry when the line of sources is parallel to the line of receivers. (We do not

Reproduced with permission of the copyright owner. Further reproduction prohibited without permission.

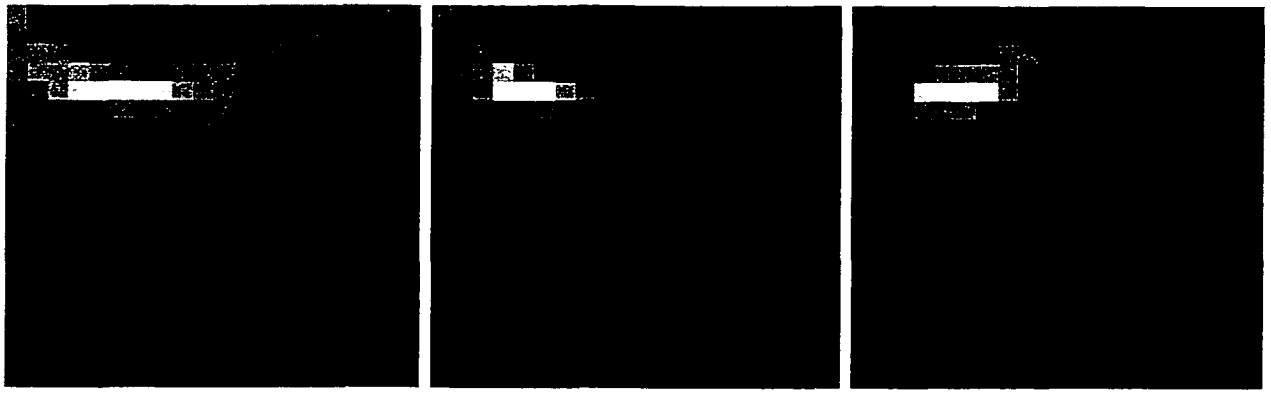

1 projection, 20 × 20 | 2 projections, 20 × 20 | 3 projections, 20 × 20

Figure 4.2: Simulated elliptical defect reconstructions from 1,2 and 3 crosshole projections with sequential ART algorithm: 20 × 20 pixels.

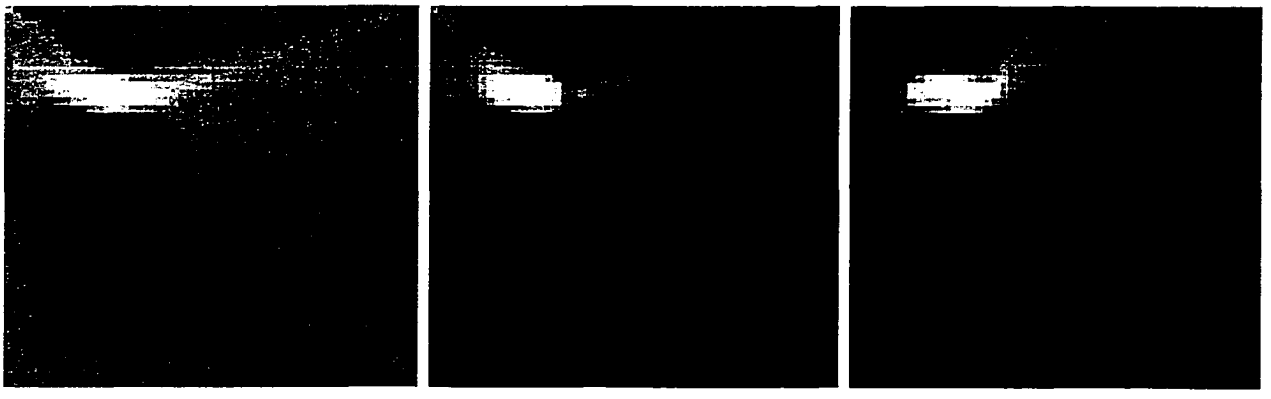

1 projection, 50 × 50 | 2 projections, 50 × 50 | 3 projections, 50 × 50

Figure 4.3: Simulated elliptical defect reconstructions from 1,2 and 3 crosshole projections with sequential ART algorithm: 50 × 50 pixels.

Reproduced with permission of the copyright owner. Further reproduction prohibited without permission.

1 projection, 100 × 100 2 projections, 100 × 100 3 projections, 100 × 100

Figure 4.4: Simulated elliptical defect reconstructions from 1,2 and 3 crosshole projections with sequential ART algorithm: 100 × 100 pixels.

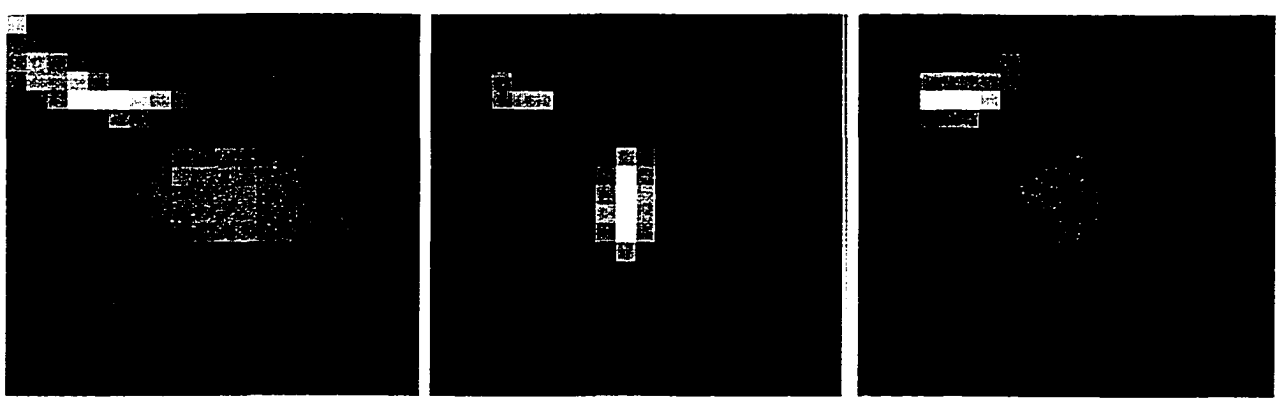

1 projection, 20 × 20 2 projections, 20 × 20 3 projections, 20 × 20

Figure 4.5: Sequential ART reconstructions of two simulated elliptical defects from 1,2 and 3 crosshole projections: 20 × 20 pixels.

Reproduced with permission of the copyright owner. Further reproduction prohibited without permission.

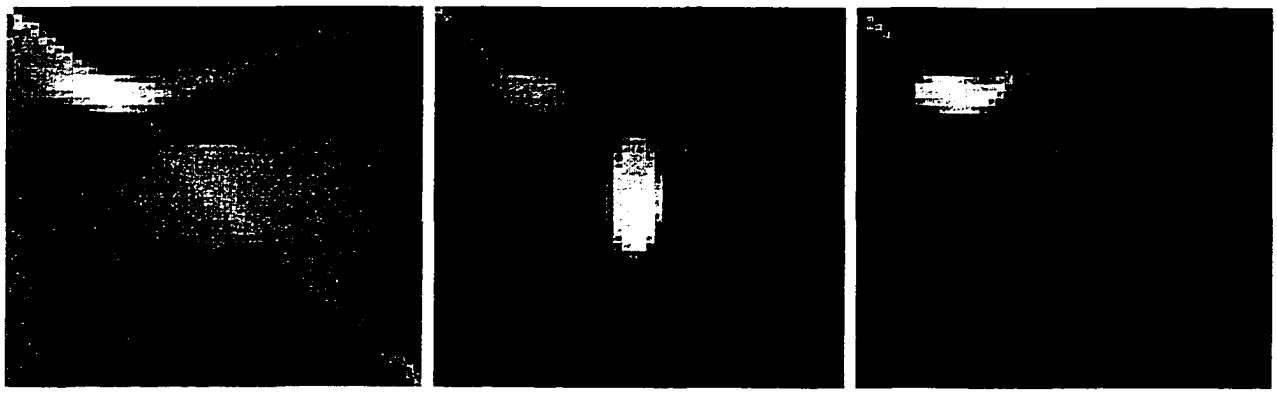

1 projection, 50 × 50 | 2 projections, 50 × 50 | 3 projections, 50 × 50

Figure 4.6: Sequential ART reconstructions of two simulated elliptical defects from 1,2 and 3 crosshole projections: 50 × 50 pixels.

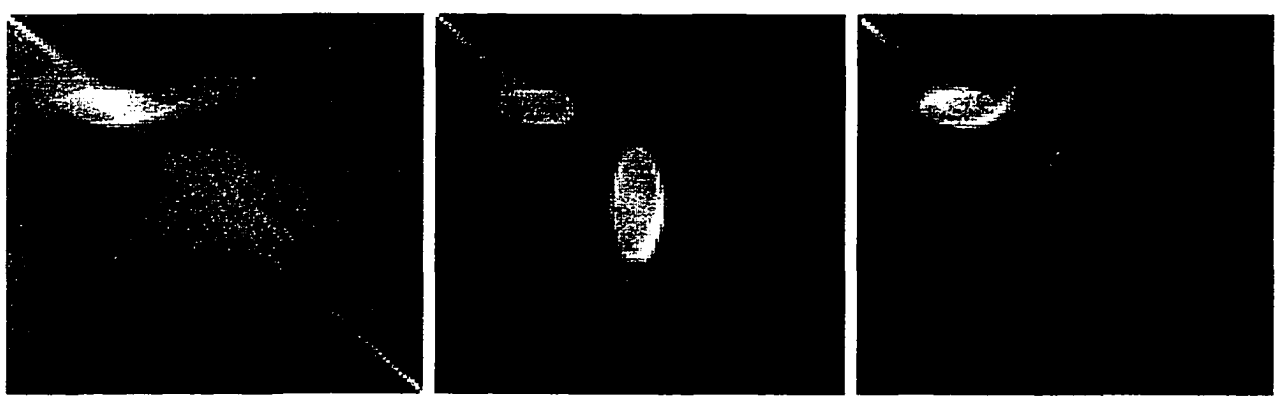

1 projection, 100 × 100 | 2 projections, 100 × 100 | 3 projections, 100 × 100

Figure 4.7: Sequential ART reconstructions of two simulated elliptical defects from 1,2 and 3 crosshole projections: 100 × 100 pixels.

Reproduced with permission of the copyright owner. Further reproduction prohibited without permission.

exchange sources and receivers). Two projections crossed at 90° give us the second image in a triple. Three projections are made when the sources remain in place and receivers are put along the other three sides of the square. Certainly, the ray density in the last geometry lacks symmetry but this is not a problem with a real transducer array when we can easily make four such experiments transmitting subsequently from the all four sides.

The first three triples show reconstructions of a single simulated ellipse with horizontal semi-axis of 10 mm and vertical semi-axis of 6 mm. The reconstructions from 2 and 3 crosshole projections are clearly superior to the reconstruction from 1 projection. Images obtained with 50 transducers per side are of acceptable quality and doubling the number of transducers per side makes the resolution even better. This result partially answers the question about the number of real transducers in an array to be built in the subsequent work. It probably will not exceed 200 (50 transducers per square side), although better spatial resolution requirements or cheaper price may stimulate us to use more transducers, such as 512 or even 1024 per side.

The next three triples show reconstructions of two simulated ellipses one of which is the same as previously and another one is drawn in the center and has horizontal semi-axis of 6 mm and vertical semi-axis of 15 mm. We added the second ellipse to make sure the algorithm handles multiple objects and to choose the best geometry for the laboratory experiments. It is clear that for all numbers of transducers per side the reconstructions from 2 crosshole projections are superior to those from one and three projections. And again, the number of 50 transducers per side seems to be big enough to capture the shape, orientation and spatial separation of the two

Reproduced with permission of the copyright owner. Further reproduction prohibited without permission.

objects.

The results of the above simulation helped us configure the laboratory scanning experiment. To save physical labor, computational time and disk space it is reasonable not to exchange transmitters and receivers because the reconstruction quality is good enough without it. An acceptable quality can be achieved with 2 crosshole projections having 50 or 100 transducer positions per square side. Single projection images lack resolution and suffer from tomographic artifacts. Moreover, the limited number of ray angles creates the situation where the imaging problem may not have a unique solution even if all the data were perfectly consistent and noiseless [40]. And finally, one should avoid data acquisition geometries that lack symmetry, such as a single or a triple crosshole schemes. Incompleteness in scanning symmetry results in a nonuniform spatial resolution of the reconstructed images.

4.3 Double crosshole experiment

4.3.1 Double crosshole scanner

The block diagram of data acquisition equipment for crosshole tomography is presented in Fig. 4.8. The HP8116A function generator is used to generate a tone burst containing 4-10 harmonic voltage cycles. After amplification, the tone burst feeds the transmitting transducer, which excites Lamb waves in the sample. The received signal is amplified, filtered and recorded by a computer. The same computer also controls motion of both transmitting and receiving transducers. Fig. 4.10 shows the detailed view of the crosshole scanner.

Reproduced with permission of the copyright owner. Further reproduction prohibited without permission.

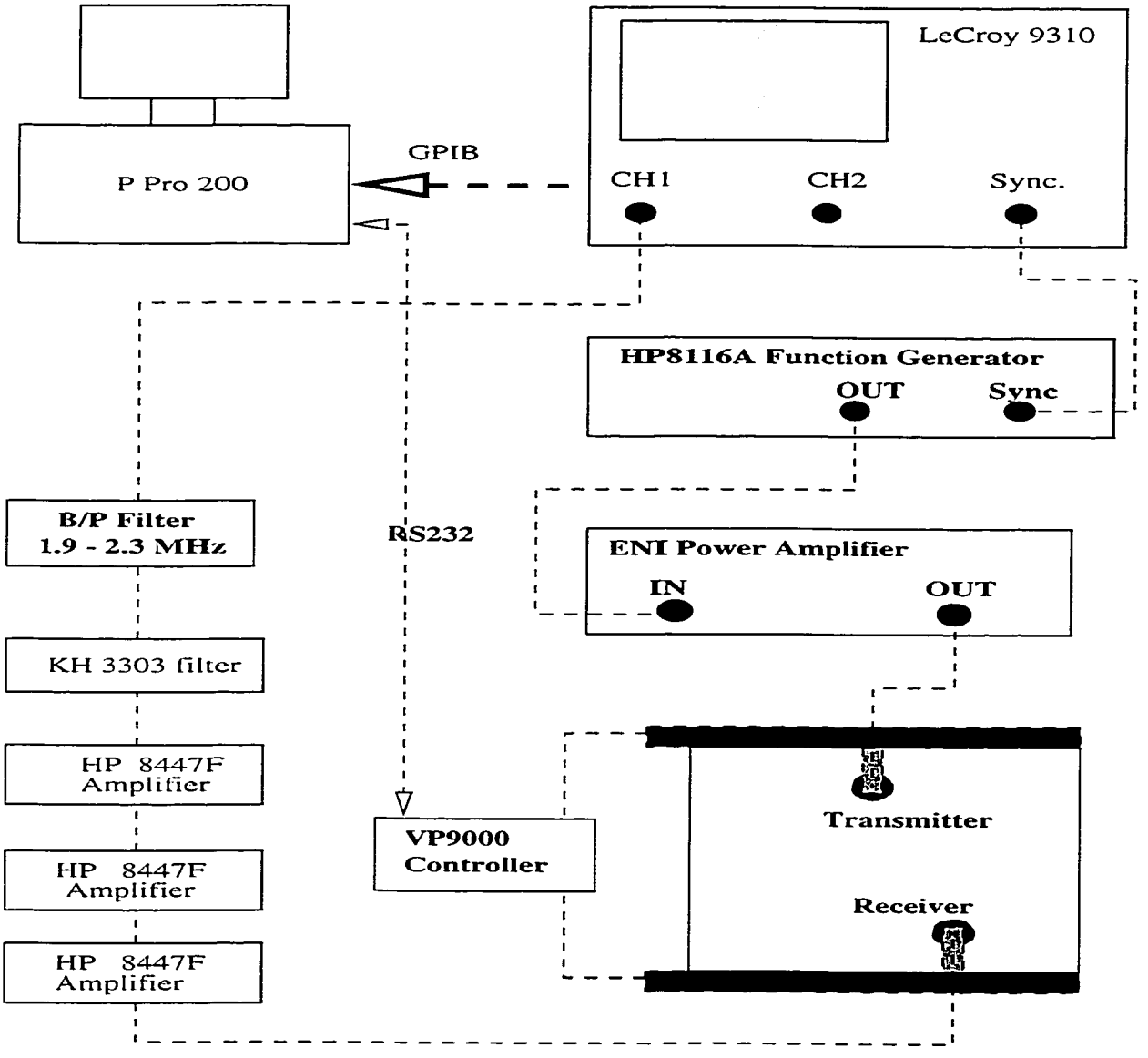

Figure 4.8: Block diagram of the data acquisition equipment for crosshole tomography.

Reproduced with permission of the copyright owner. Further reproduction prohibited without permission.

Figure 4.9: Photo of the crosshole scanner in our lab.

Reproduced with permission of the copyright owner. Further reproduction prohibited without permission.

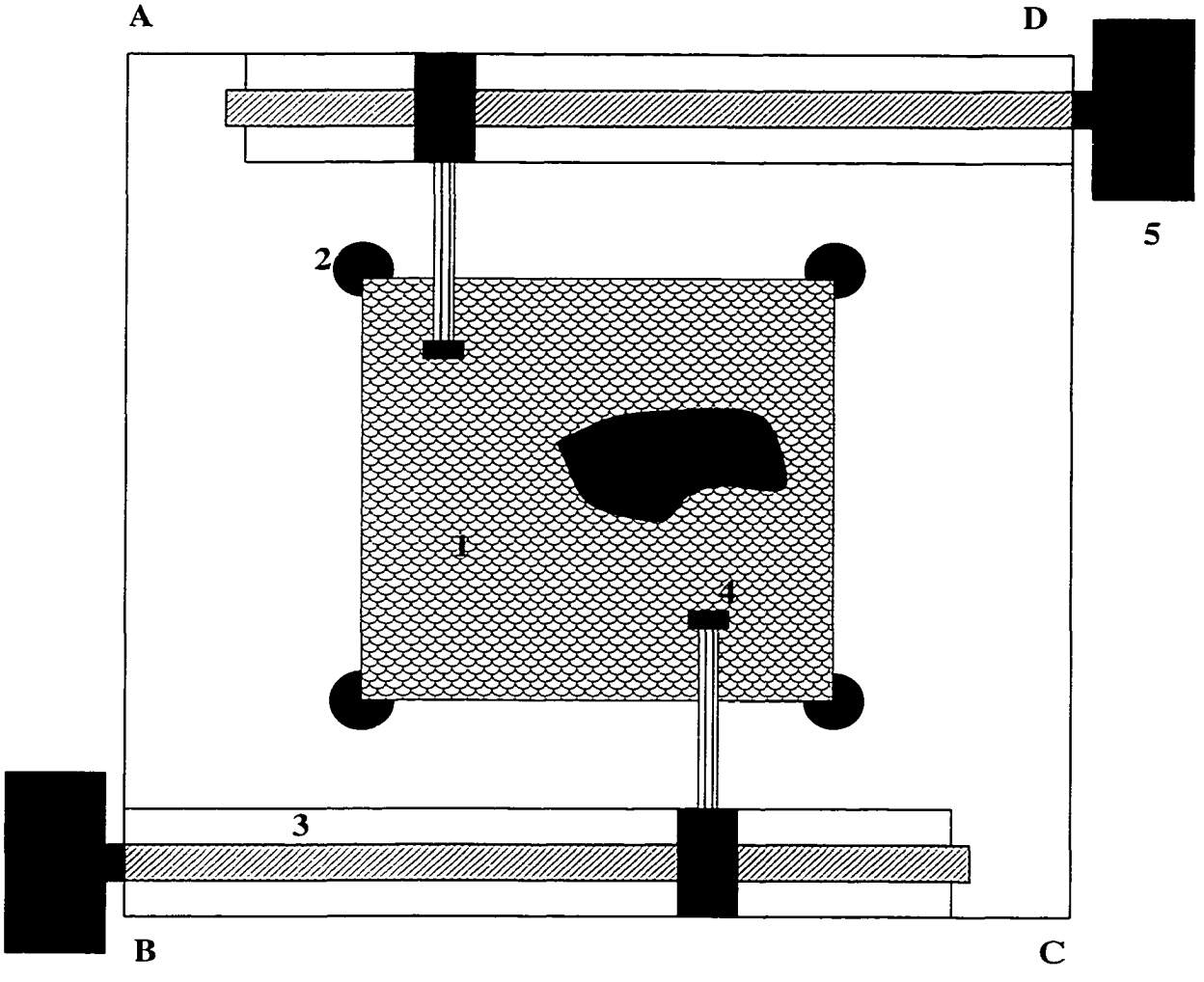

1-sample; 2- rubber holder; 3-slider
4-transducer; 5-stepper motor

Figure 4.10: Schematic of the crosshole scanner.

Reproduced with permission of the copyright owner. Further reproduction prohibited without permission.

Since one of our follow-on goals is the development of array-based Lamb wave tomographic equipment and the array itself is a cost-consuming part of it, we mimic the array behavior with a pair of mechanically moved transducers. They step along the two linear sliders placed parallel to each other. It is relatively easy to take one crosshole projection this way, but it is much harder to take additional projections because the sample must stay in place while we move and align the sliders.

In order to simplify the task Nascent Technology Solutions, LLC provided a rigid frame $ABCD$ for the sliders (Figs. 4.10, 4.9) made of thick plywood. Each of the sliders, (3), can be mounted along any of the four sides without moving the sample, (1), which is secured in place by means of four rubber clamps equipped with screws. After measuring the first set of crosshole projections as shown in Fig. 4.10 we place the sliders along the sides AB and CD and record the second set of projections. Some adjustment of the transducer starting position is always necessary to make sure that both projections cover exactly the same area.

Each crosshole experiment results in a stack of N^2 5000-point wave trains which needs to be processed in order to extract one or several values of interest from every wave train. Currently we extract only one value – the arrival time of the fastest Lamb wave mode. At our operating frequency this is usually S_0 - the first symmetric mode. Although fairly robust, our time extraction algorithms are still produce various estimation errors ranging from fractions of the quarter-wavelength to complete failure to detect signal. Fortunately, the percentage of severe errors is small enough ($\sim 1\%$), so that the entire data set is not fatally distorted. In addition, we correct the above failures by substituting out-of-range data points with values of

Reproduced with permission of the copyright owner. Further reproduction prohibited without permission.

their closest neighbors. However, the ART algorithm runs well on experimental data and produces satisfactory images, which are presented below.

4.3.2 Experimental Results

Figures 4.11 – 4.20 are the images reconstructed from experimental data sets using both the sequential ART (ART) and the Simultaneous Iterative ART (SIRT) algorithms. The samples studied were:

Fig. 4.11 and Fig. 4.15: 2.29 mm-thick Al plate with two 10% circular thinnings with diameters of 29 and 25 mm. Distance between centers – 53 mm, scanning frequency – 1.2 MHz, scanning geometry 100 × 100, step size – 2 mm, number of crosshole projections – 2;

Fig. 4.12 and Fig. 4.16: 2.29 mm-thick Al plate with 5 circular through holes with diameters of 14 mm. Distance between centers – 45 mm, scanning frequency – 1.2 MHz, scanning geometry 100 × 100, step size - 2 mm, number of crosshole projections – 2;

Fig. 4.13 and Fig. 4.17: 1.274 mm-thick Al plate with 10% thinning rectangular defect. Defect size – 52 × 26 mm, rounded corners, scanning frequency – 2.2 MHz, scanning geometry 100 × 100, step size – 2 mm, number of crosshole projections – 2;

Fig. 4.14 and Fig. 4.18: 2.29 mm-thick Al plate with 30% thinning oblong defect. Defect size – 110 × 26 mm, rounded corners, scanning frequency – 1.2MHz, scanning geometry 100 × 100, step size – 2 mm, number of crosshole projections – 2;

Fig. 4.19 and Fig. 4.20: lap joint imitation. An 1.274 mm-thick Al plate with a 72 mm – wide stripe of the same material glued to it. Scanning frequency – 1.5MHz,

Reproduced with permission of the copyright owner. Further reproduction prohibited without permission.

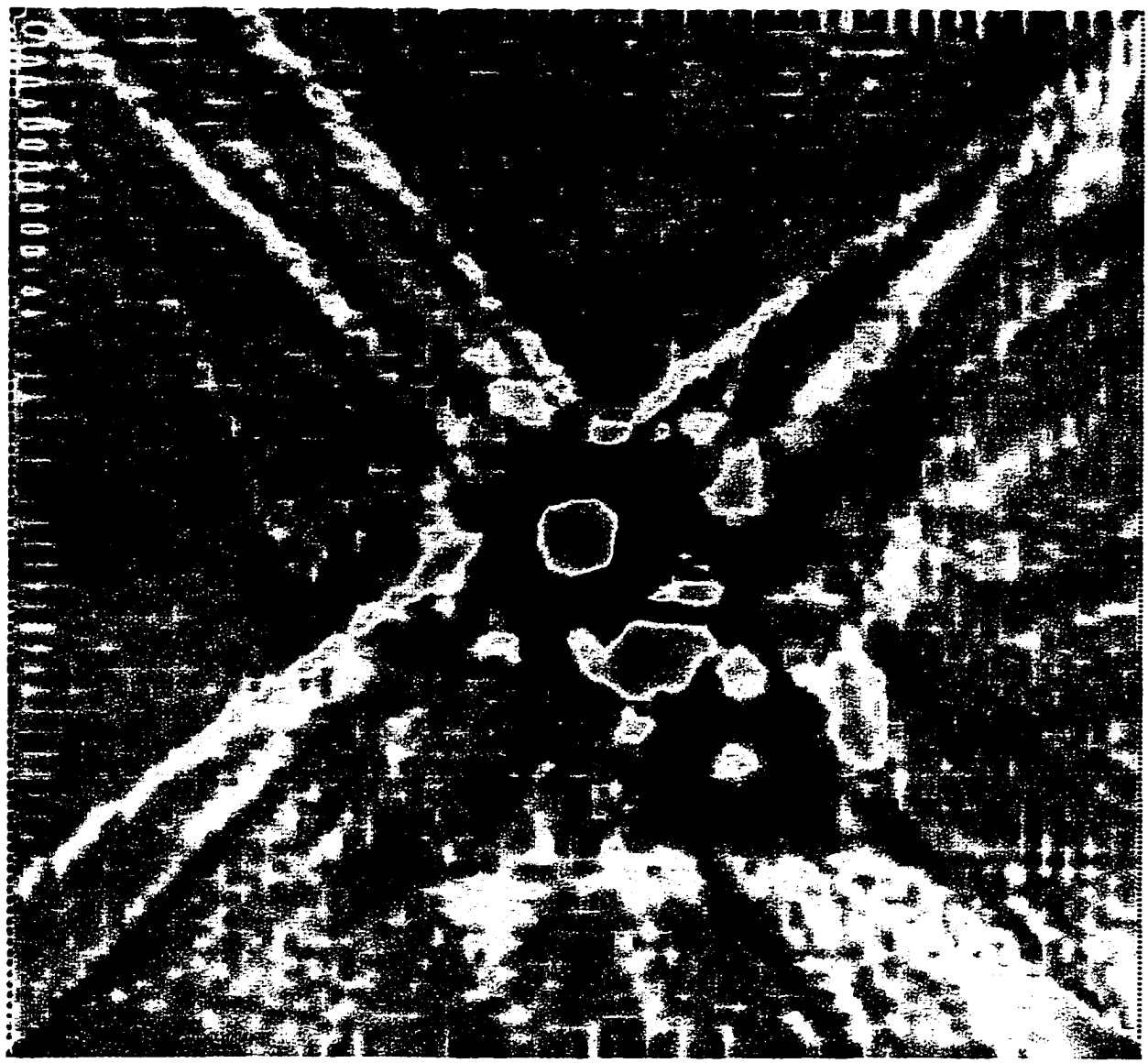

Figure 4.11: Sequential ART reconstruction of two circular flat-bottom holes in aluminum plate. Defect diameters: 29 and 25 mm. Distance between centers: 53 mm. Image size: 200 × 200 mm. $f = 1.2$ MHz. Note the level of "salt and pepper noise" throughout the image.

Reproduced with permission of the copyright owner. Further reproduction prohibited without permission.

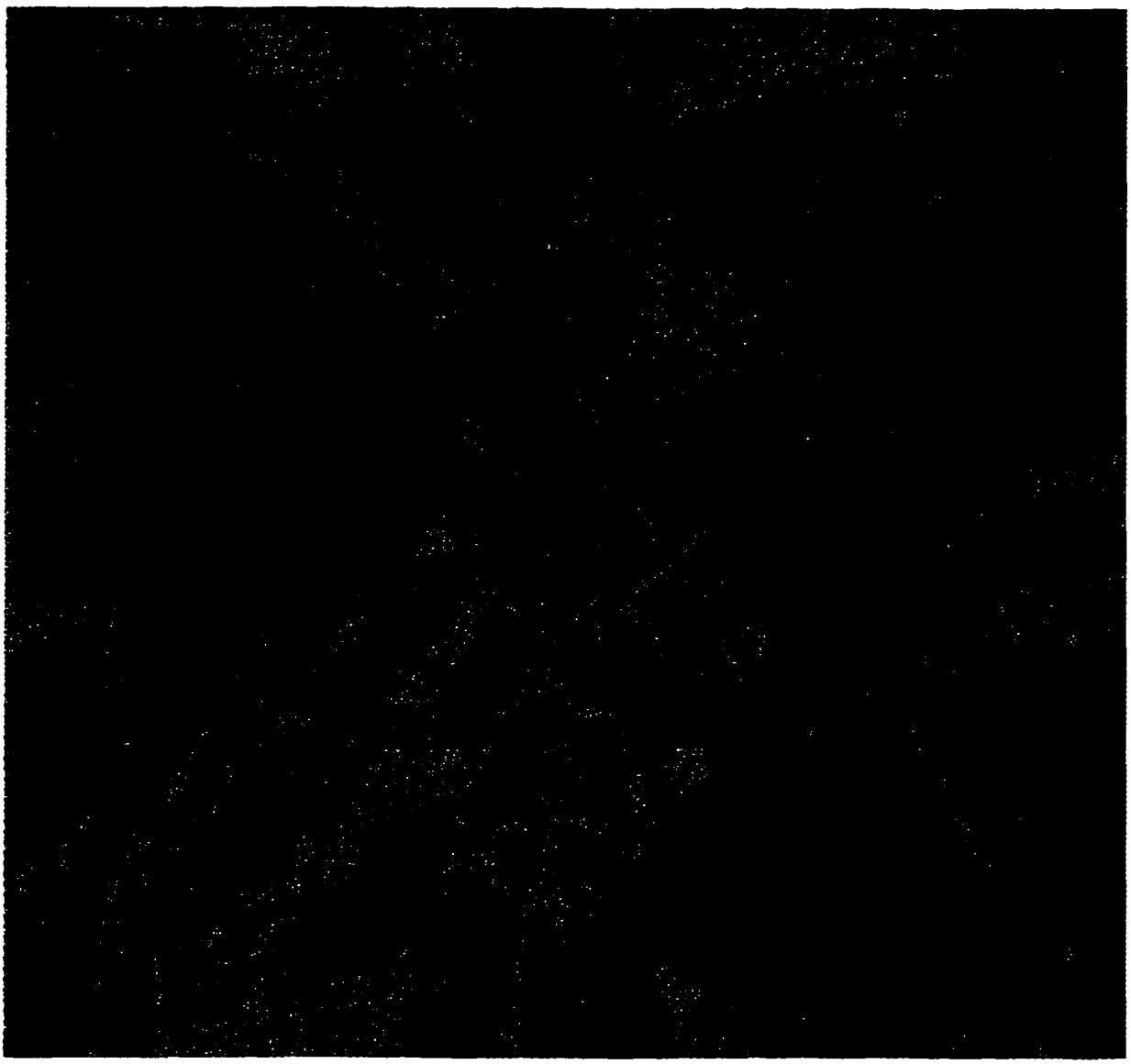

Figure 4.12: Sequential ART reconstruction of five equally spaced 15 mm-diameter through holes in aluminum plate. Image size: 200 × 200 mm. $f = 1.2$ MHz. Note the level of "salt and pepper noise" and distorted shape of the holes near the edges.

Reproduced with permission of the copyright owner. Further reproduction prohibited without permission.

Figure 4.13: Sequential ART reconstruction of a rectangular thinning region in aluminum plate. Image size: 200 × 200 mm. $f = 2.2$ MHz. Note the level of "salt and pepper noise".

Reproduced with permission of the copyright owner. Further reproduction prohibited without permission.

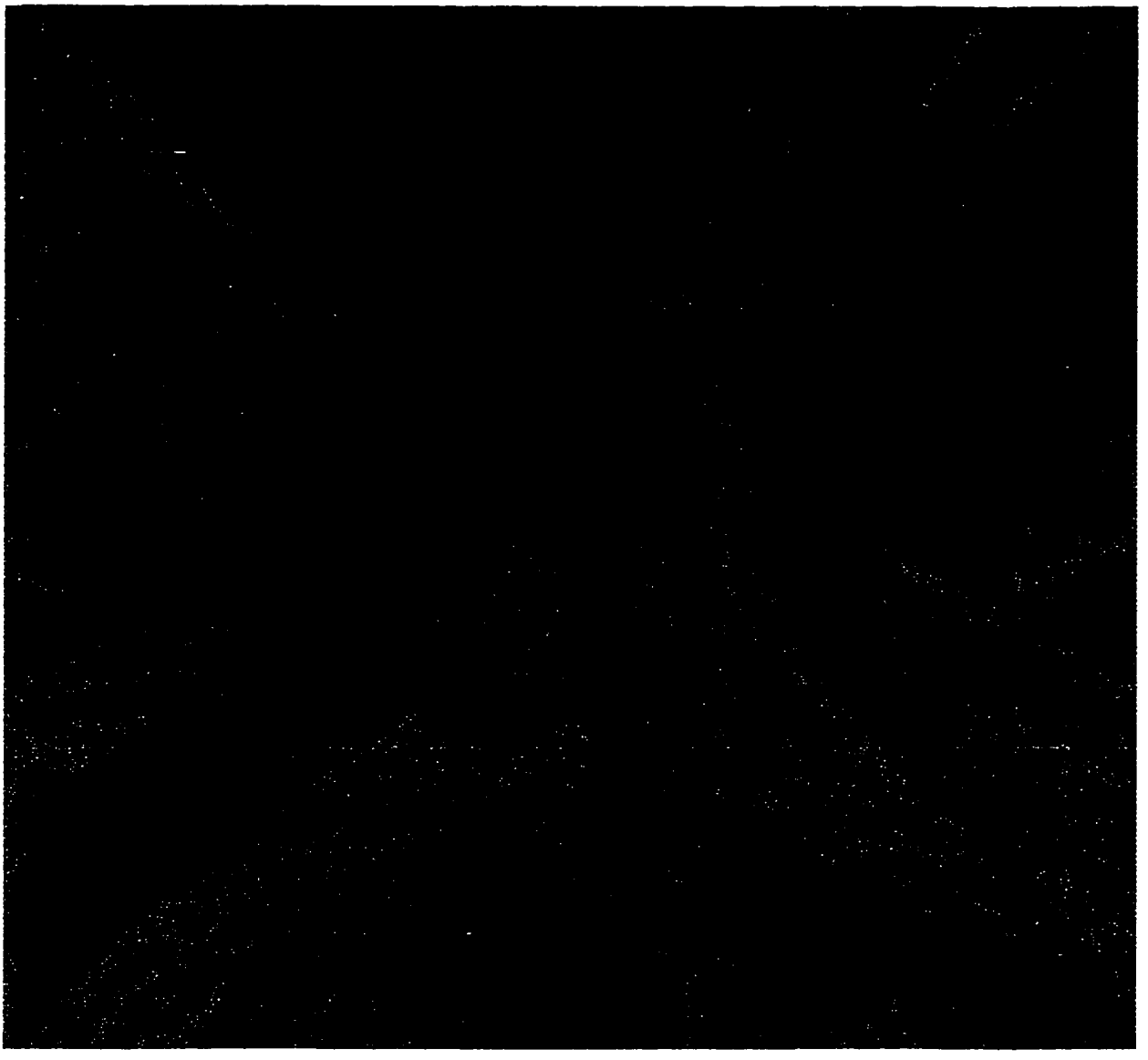

Figure 4.14: Sequential ART reconstruction of an oblong thinning region in aluminum plate. Image size: 200 × 200 mm. $f = 1.2$ MHz. Note the level of "salt and pepper noise".

Reproduced with permission of the copyright owner. Further reproduction prohibited without permission.

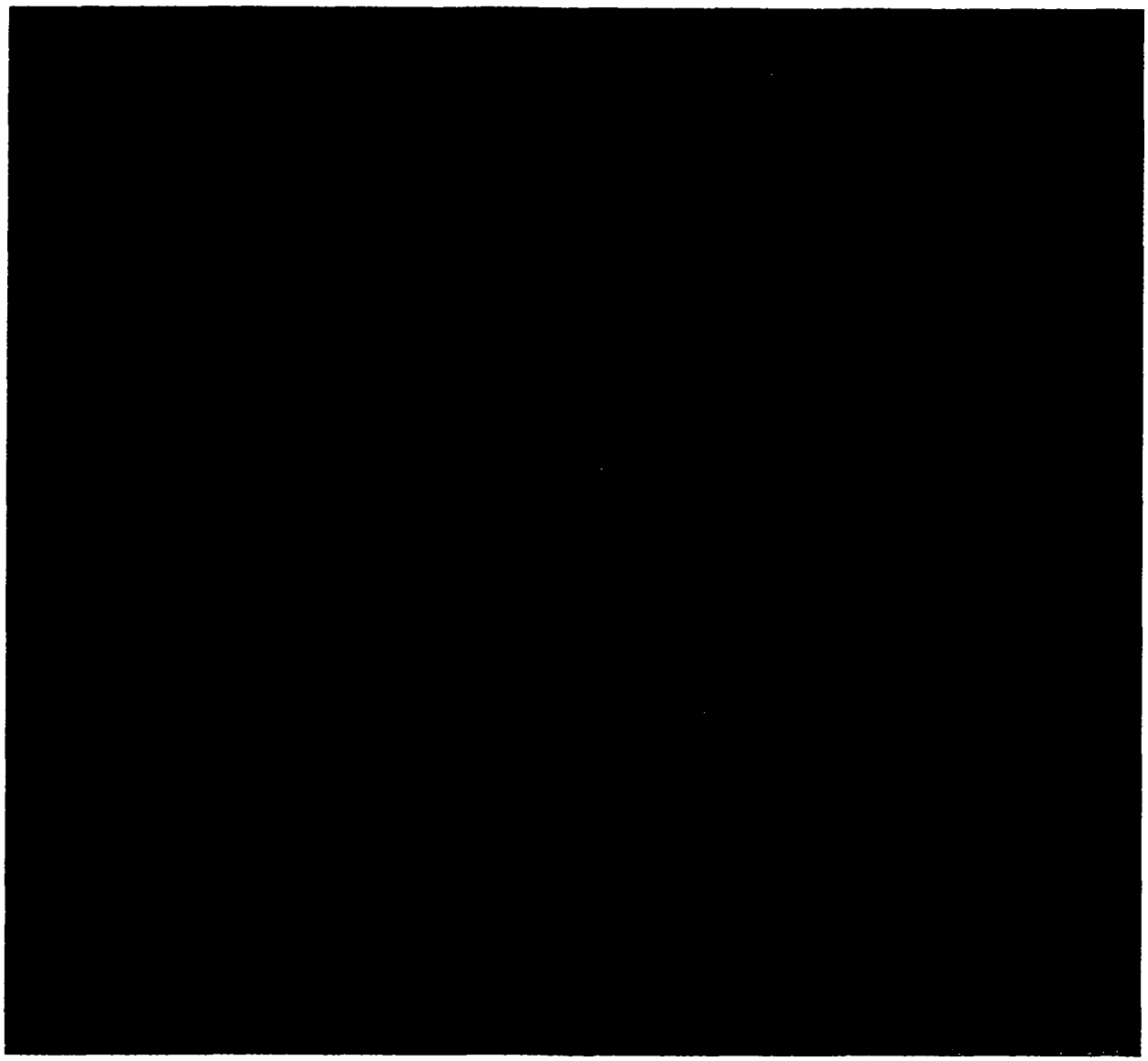

Figure 4.15: SIRT reconstruction of two flat bottom holes. Image size: 200 × 200 mm.

Reproduced with permission of the copyright owner. Further reproduction prohibited without permission.

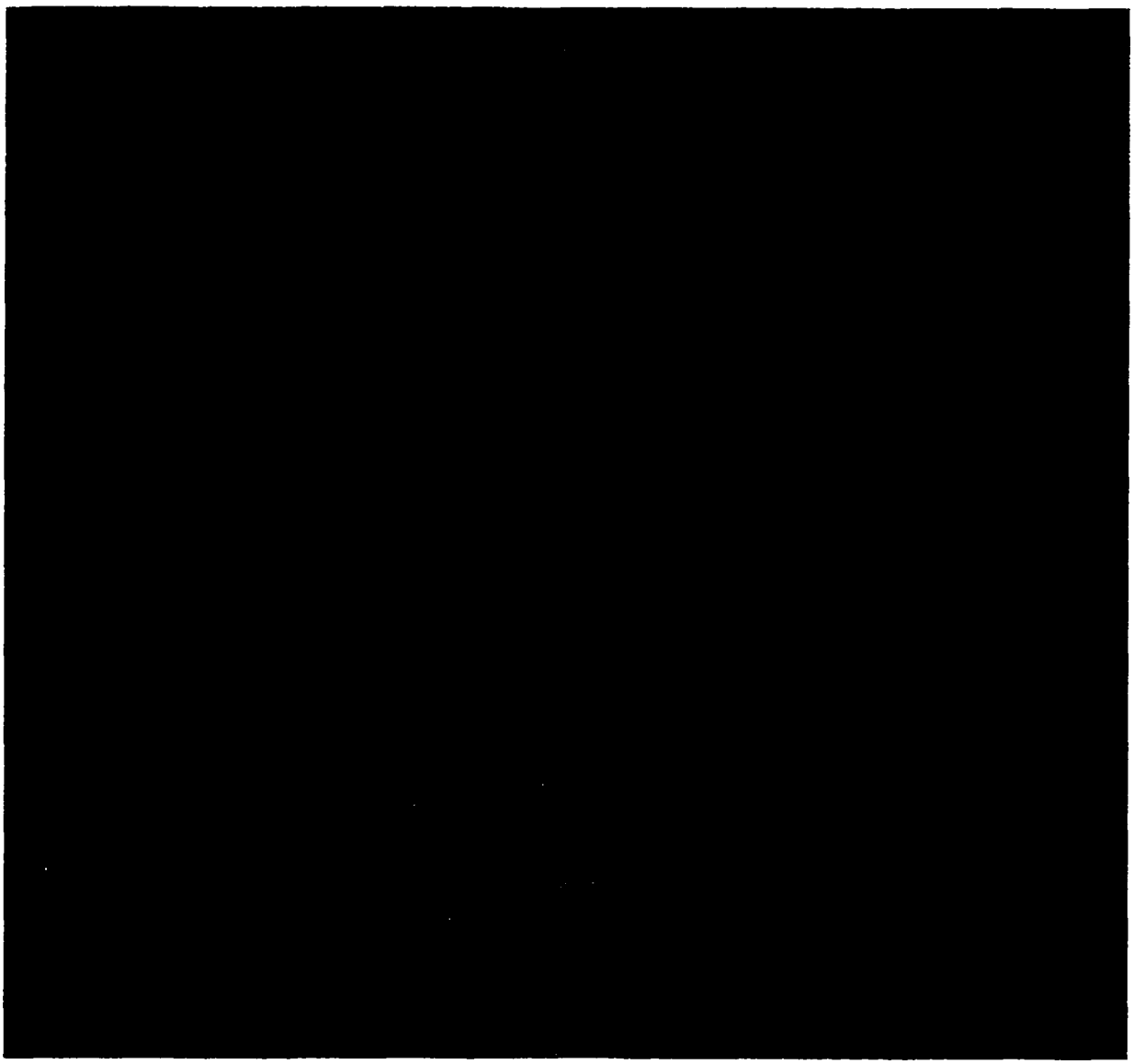

Figure 4.16: SIRT reconstruction of five through holes. Image size: 200 × 200 mm.

Reproduced with permission of the copyright owner. Further reproduction prohibited without permission.

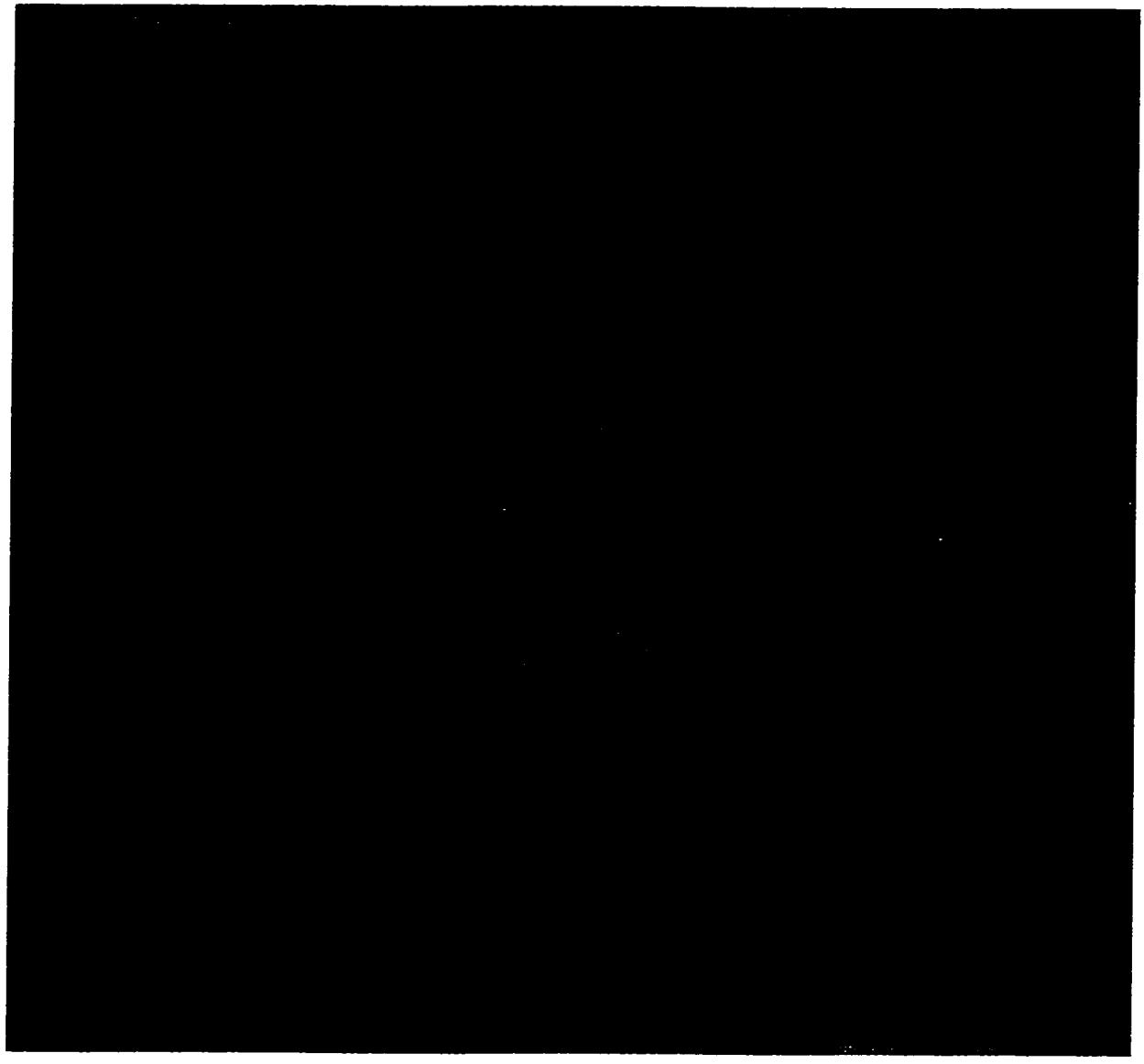

Figure 4.17: SIRT reconstruction of a rectangular thinning region. Image size: 200 × 200 mm.

Reproduced with permission of the copyright owner. Further reproduction prohibited without permission.

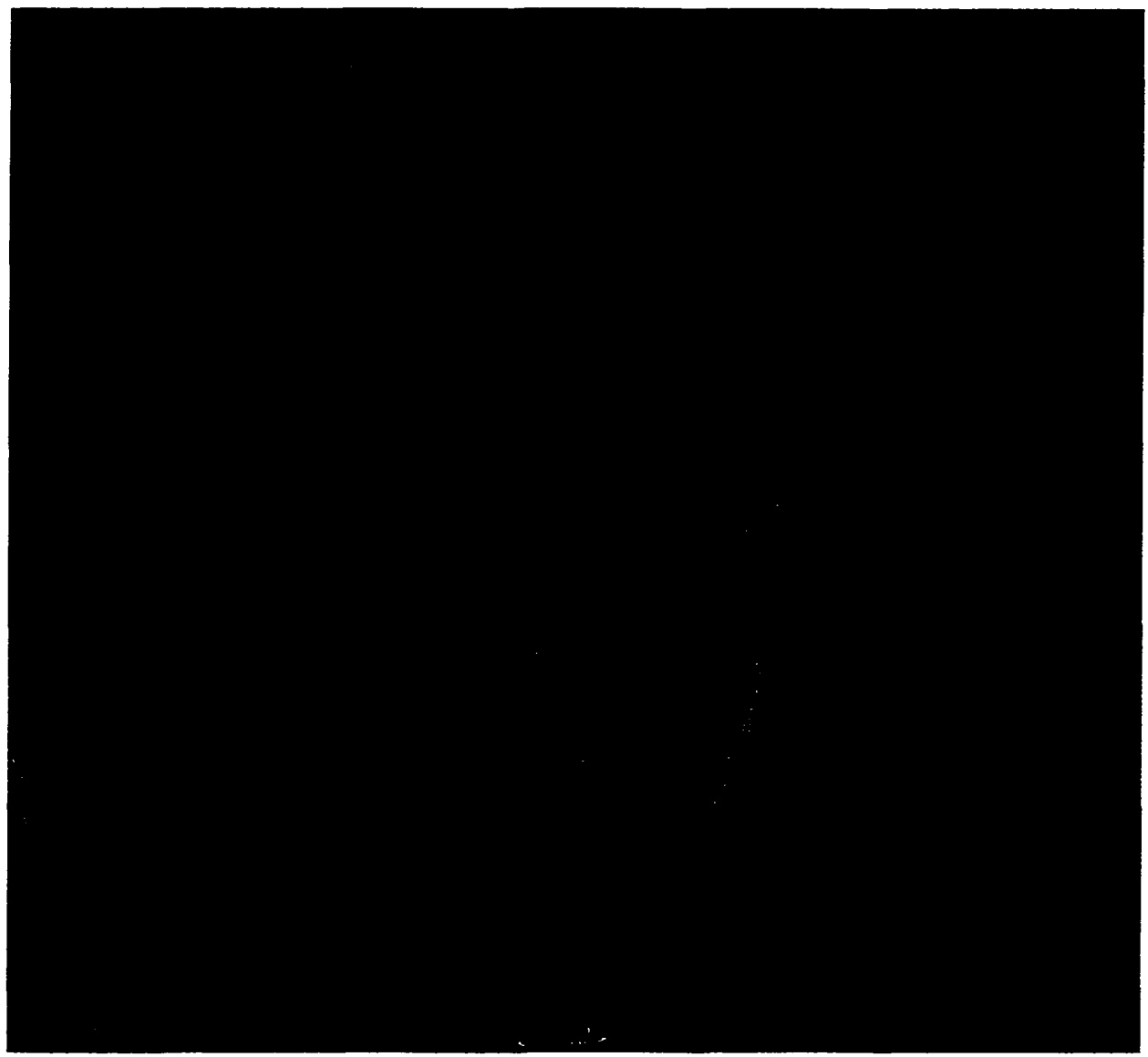

Figure 4.18: SIRT reconstruction of an oblong thinning region. Image size: 200×200 mm.

Reproduced with permission of the copyright owner. Further reproduction prohibited without permission.

Figure 4.19: SIRT reconstruction of adhesively bonded doubler in aluminum plate, 1 iteration. Different colors indicate: red – no adhesive; green - poor bond quality, adhesive sticks to only one side; blue – good bond quality.

Reproduced with permission of the copyright owner. Further reproduction prohibited without permission.

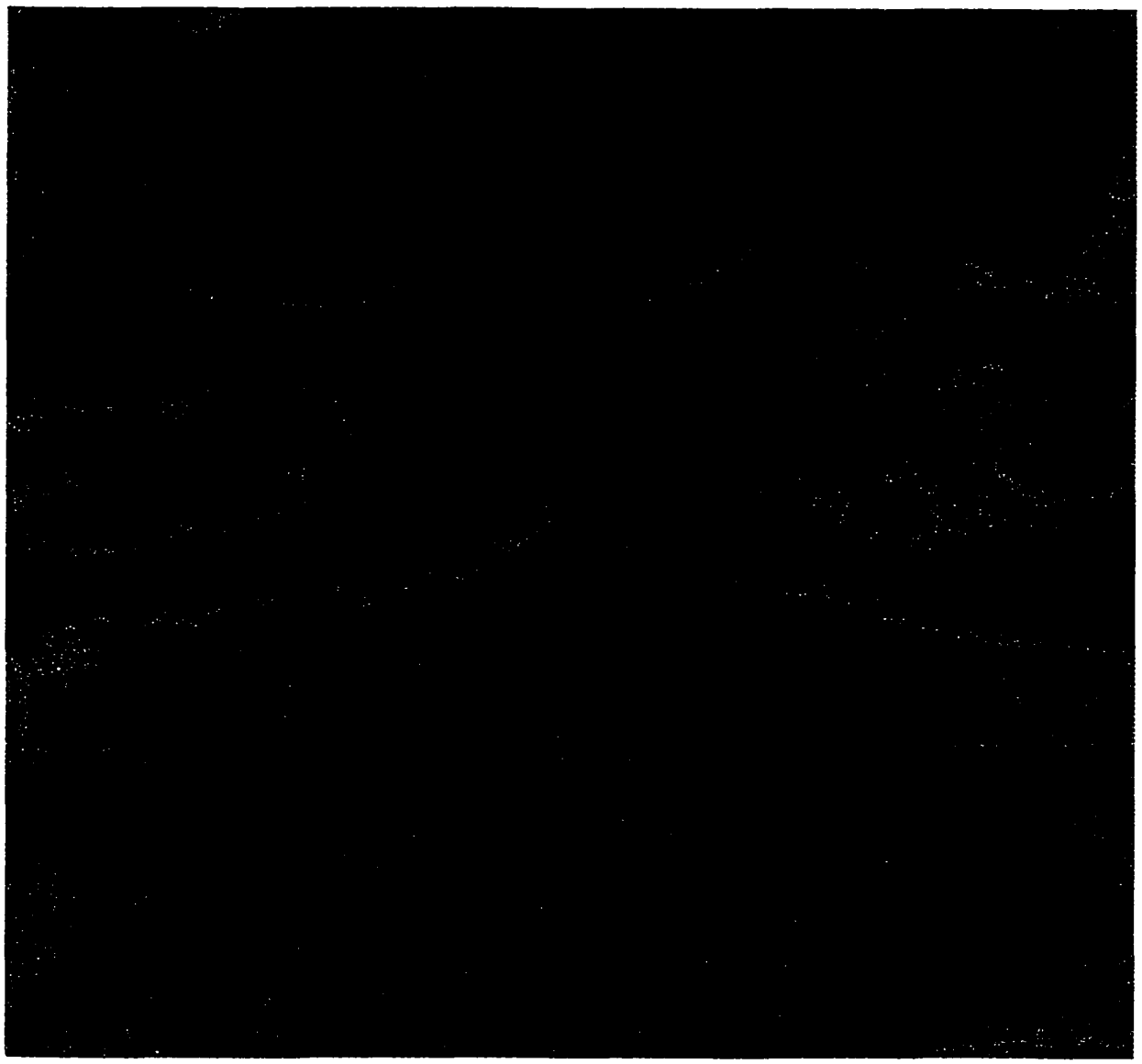

Figure 4.20: SIRT reconstruction of adhesively bonded doubler in aluminum plate, 10 iterations. Different colors indicate: red – no adhesive; green – poor bond quality, adhesive sticks to only one side; blue – good bond quality.

Reproduced with permission of the copyright owner. Further reproduction prohibited without permission.

scanning geometry 100 × 100, step size – 2 mm, number of crosshole projections – 2;

In all cases we used a thin layer of water for coupling purposes. The transducers were equipped with cone-shaped delay lines made of acrylic resin. The footprint diameter of the delay line was 2 mm.

4.4 Analysis of the results

It was surprising to us that the straight ray assumption, used in both reconstruction algorithms, worked well even for the through holes. Lamb waves definitely refract around the hole, and their arrival time increases. Assuming straight paths, the reconstruction algorithm interprets that increase as a wave slowdown and assigns smaller velocity values to some (often wrong) pixels. As a result, the shape and the exact size of the defect may be distorted upon reconstruction and the image cannot always serve as a velocity map. A method is needed that naturally incorporates ray bending effects into the reconstruction process. Diffraction tomography, discussed in the following chapter, is one such method.

Visual comparison of the reconstruction quality of the ART algorithm versus SIRT shows that the latter always yields much smoother picture and shows fewer artifacts than the former. The "salt-and-pepper" noise, specific for the ART, is completely absent on the SIRT images. The run time and memory usage are approximately the same for both algorithms. Therefore, it seems practical to use SIRT and its derivatives as a primary reconstruction algorithm in subsequent imaging tasks. The ART algorithm can also be utilized for revealing reconstruction artifacts and using this information, improve the images, obtained with SIRT.

Reproduced with permission of the copyright owner. Further reproduction prohibited without permission.

The spatial resolution of both methods is good enough to ensure subjective visual separation of all the defects studied. In the the case of two flat bottom holes the imaging artifact slightly complicates visual separation. Several realistic ways to improve the image quality are suggested below.

Scanning the simulated lap joint sample, we encountered its "filtering" property meaning that the layered zone transmits Lamb waves selectively. We were unable to receive a good signal at our usual frequency of 2.2 MHz for a 1.274 mm - thick plate. The optimal signal quality was achievable only at 1.5 MHz. At this frequency the S_0-mode is less dispersive in the plate than at 2.2 MHz. And it is also less dispersive in the lap joint region than at 1.1 MHz. Nevertheless, it was possible to detect the areas where the adhesive is missing. The sample has been disassembled and carefully compared against the image. Qualitative agreement between the spots of missing glue and red areas on the image was observed.

4.5 Discussion

- The Algebraic Reconstruction Technique allows for a good quality of reconstruction even from noisy, corrupted and incomplete data, such as the Lamb wave arrival times, estimated with custom software. It also works for practically any scanning geometry. The SIRT algorithm preserves all the advantages of the conventional ART; in addition it produces less noise and fewer artifacts.

- The resolution and image quality of the double crosshole technique are both far superior to those of the single crosshole tomography. This is mainly because of

Reproduced with permission of the copyright owner. Further reproduction prohibited without permission.

the doubled coverage in wave vector space and higher ray density. However, both ray density and directivity patterns are still nonuniform throughout the image. This results in a lower resolution and image quality in the peripheral areas. The only way to improve the coverage is to add more crosshole projections, such as four "corner" projections discussed in the following chapter. With all six possible crosshole projections the ray density will be high all over the square area and the fill-factor of the crosshole geometry will be equal to 100% instead of 50% in the fan beam case. However, the data acquisition geometry should have the highest possible symmetry to avoid extra reconstruction artifacts.

- The 100×100 square transducer array provides an acceptable quality of the reconstruction from the two mutually perpendicular crosshole projections for the area of 20×20 cm. For larger areas, or for a better resolution, more transducers may be needed, up to 512×512.

- Lamb wave diffraction tomography will help reach a quantitative agreement of defect size and shape with observation and to turn the image into a precise thickness map of the sample.

Reproduced with permission of the copyright owner. Further reproduction prohibited without permission.

Chapter 5

Diffraction Tomography

This chapter summarizes the application of a ray tracing method to the problem of image reconstruction in Lamb wave tomography. It covers theory, discussion of possible approaches, computer implementation of the chosen technique, simulated results and reconstructions from experimental data.

5.1 Review of the current state of Diffraction Tomography

The main task of tomography is characterization of the structure and properties of an unknown medium. To accomplish this task it is common to penetrate the medium with an appropriate type of radiation along many different directions, then to extract information about a specific property from the scattered, reflected or transmitted field, and finally to build a cross-sectional map of this property using tomographic reconstruction algorithms. To simplify and speed up the reconstruction

Reproduced with permission of the copyright owner. Further reproduction prohibited without permission.

process, the majority of X-ray transmission tomography applications assume rays traveling in along straight lines. This assumption yields satisfactory results as long as the wavelength is much smaller than the size of the defect being imaged. However, the straight ray assumption is not always valid for optical, elastic and other types of waves in inhomogeneous media. In such cases diffraction tomography (DT) is an important alternative to conventional (straight ray) tomography (CT).

According to Kak and Slaney [64] the accuracy of tomography using the straight ray assumption suffers from the effects of refraction/diffraction, causing each projection to not represent integrals along straight lines. When the sizes of defects in the object become comparable to, or smaller than, a wavelength, geometric ray theory fails, and one must resort directly to wave propagation and diffraction based analyses.

The mathematical complexity and the reconstruction time of a chosen DT algorithm depend on how closely it models reality. Different assumptions, used by various authors to simplify the model, produce different families of algorithms, optimized for particular kinds of problems. The goal of the current work is to improve the resolution of Lamb wave tomography.

Below we review the current state of development in the field of diffraction tomography by summarizing several successful algorithms and their basic assumptions. The selected methods include: traveltime tomography (Bregman et al. [40], Pratt [41], Andersen [65], Wang and Kline [66]); generalized Fourier slice theorem - based algorithm (Gelius et al. [67, 68]); layered diffraction tomography algorithm (Pai [69], Dickens [42, 70]); generalized ART algorithm (Ladas [71, 72], Almquist et

Reproduced with permission of the copyright owner. Further reproduction prohibited without permission.

al. [73]). The accuracy of the first Born and the first Rytov approximations is discussed by Chen [74]. The reviewed papers do not completely represent the literature but reveal existing trends well enough to stimulate new ideas appropriate to our work.

5.1.1 Traveltime tomography

Traveltime tomography uses sets of arrival times collected over the perimeter of some area to reconstruct certain material properties throughout the area. In the simplest case of a straight-ray approximation a tomographic iterative or non-iterative inversion of arrival times is used to estimate the Lamb wave velocity map. The next level of resolution can be reached with the help of acoustic ray theory, assuming that rays propagate according to Fermat's principle. Ray tracing is usually used to calculate curved ray paths in the medium with varying refractive index. Geometrical acoustics assumes that the wavelength is much smaller than the size of a scatterer. The following papers represent different attempts to enhance the resolution of traveltime tomography.

Bregman et al. [40] presented an iterative inversion technique based on two-dimensional ray tracing. These authors noted that the lack of complete angular coverage and ray path dependence on the background velocity make geological crosshole imaging problems substantially more complicated than those of X-ray tomography. They proposed a sequence of ray tracing and linear inversions as a scheme to image either compressional or shear wave velocity patterns between coplanar boreholes. At each iteration, the traveltimes and their derivatives were calculated for the current estimate of the velocity structure, and then velocity perturbations were computed as

Reproduced with permission of the copyright owner. Further reproduction prohibited without permission.

an inverse step. The iterations continue until the model traveltimes match the data traveltimes or until no improvement in the fit is observed.

Their algorithm was tested both on a simple analytical model and on extensive field data sets, yielding accurate velocity models agreeing well with independent geologic evidence. This demonstrated that incorporation of ray path curvature into crosshole tomography is both desirable and numerically feasible.

Another imaging method in the area of traveltime tomography was proposed by Pratt and Goulty [41]. The authors made use of the complementary nature of conventional traveltime tomography and wave equation imaging. They suggested using conventional velocity tomograms as an input to wave-theoretical imaging. As an additional input, the algorithm requires statistical estimates of the scattered field and the source time function. Both procedures are rather complicated and computationally intensive.

The input velocity calculation can be accomplished using ray tracers as described in [40]. The quality of the velocity pattern has a crucial impact on the algorithm's performance. Wave-equation imaging is then applied to the data using frequency domain finite difference modeling. Images can be enhanced by stacking the results from several frequency components. This algorithm was tested on simulated data and proved to yield high resolution.

A review of digital ray tracing algorithms in the two-dimensional refractive index media was presented by Andersen and Kak [65]. This review summarized acoustical ray theory and stressed the role of Fermat's principle in ray tracing. It described and discussed ray tracing by a second-order numerical algorithm, by the

Reproduced with permission of the copyright owner. Further reproduction prohibited without permission.

method of characteristics and by computing the angular displacement. The authors pointed out the problems arising from discrete representation of the refractive index field and emphasized the role of interpolation in its solution. In addition, the review covers ray linking and the accuracy issues, as well as ray propagation through phantoms for tomographic imaging.

Wang and Kline [66] adapted Fermat's principle for ray tracing in anisotropic media where the phase and group velocity vectors are not collinear. The authors developed a complex iterative reconstruction scheme using straight ray ART reconstructions as a background model for their generalized ray tracing algorithm. The background model was then updated using subsequent reconstructions with curved ray ART. The method was tested on simulated and experimental data showing overall improvement in the image quality.

5.1.2 Non-iterative DT methods

Non-iterative inversion of tomographic projection data became possible mainly due to the existence of the Fourier slice theorem relating the Fourier transform of a projection to the Fourier transform of the object along a single radial. A generalized version of the theorem, which makes DT possible, relates the one-dimensional spatial Fourier transform of the measured data to the two-dimensional spatial Fourier transform of the object along a portion of a circle in the object's Fourier space. Practical implementations of the algorithm usually assume a uniform background medium, far-field illumination, and the first Born or Rytov approximation. The following articles introduce several recent non-iterative DT algorithms.

Reproduced with permission of the copyright owner. Further reproduction prohibited without permission.

Gelius et al. [67] presented and discussed a DT method based on the generalized projection slice theorem and working with line or point source data and general acquisition geometries without assuming far-field illumination and paraxial approximations. The method can also handle irregularly spaced data and nonuniform background models. It is non-iterative and belongs to the backpropagation family of algorithms. The model assumes weak scattering and so makes use of either Born or Rytov approximations. Dynamic ray tracing and uniform asymptotic methods are used to handle edge and caustic diffractions in the background model. The algorithm was applied to the reconstruction of an agar cylinder in a water tank with a fan-beam method. Quantitative agreement with the object's shape and sound velocity was obtained, but the algorithm is computationally intensive since it relies on numerical integrations.

In his subsequent paper Gelius [68] developed a noniterative DT algorithm suited for imaging transmission mode seismic data. As an input the method takes a background model obtained with curved ray traveltime tomography. Unlike most existing DT methods, the new algorithm can handle irregularly spaced data, general background models, and general acquisition geometries. Both of its main steps – data filtering and back-propagation – employ paraxial ray-tracing techniques. This method was shown to be a high-resolution technique, well suited for imaging complicated geological models with nonuniform background.

Pai [69] introduced the concept of vertical eigenstates separating the wave equation in crosshole applications. The technique is computationally faster than alternatives using horizontal eigenstates. Even though horizontal eigenstates are

Reproduced with permission of the copyright owner. Further reproduction prohibited without permission.

known analytically, the corresponding approach requires solving N ordinary differential equations for each transmitter. The vertical eigenstate formalism, however, involves solving N differential equations for the whole array of transmitters. This essential advantage is natural since vertical arrays demand vertical basis functions.

Pai also considered possible applications of the new technique to the problems of modeling, continuation, and inversion. He discussed the behavior of vertical eigenstates on the two sides of a fault layer in a 2-D model as well as their application to the forward modeling of arbitrarily (but weakly) varying media using the Born approximation. He proposed an effective inversion algorithm for diffraction tomography and compared it to the existing algorithms which use horizontal eigenstates.

Mast et al. [75–77] developed and tested another inverse scattering method employing the focusing properties of certain acoustic fields obtained by using eigenfunctions of scattering operators as incident-wave patterns. The method was reported considerably more efficient than filtered backpropagation and comparable in efficiency to Fourier inversion.

A single mode (P-wave) diffraction tomography algorithm for models that can be approximated as sets of horizontal layers, proposed by Pai, was examined by Dickens [70]. Dickens distinguishes crosshole diffraction tomography from reflection imaging and traveltime tomography. The resolution of the latter is determined by the size of the Fresnel zone associated with the wavelength used to collect the data. On the other hand, diffraction tomography uses transmitted, reflected, and diffracted events to provide velocity information with sub-wavelength resolution.

As an input, the algorithm requires a layered model of the subsurface, which

Reproduced with permission of the copyright owner. Further reproduction prohibited without permission.

can be constructed from well log data or from traveltime tomography. Layered diffraction tomography then computes corrections to this model. The algorithm is based on the expansion of layered Green's functions in vertical (for crosshole tomography) or horizontal (for surface seismic geometries) eigenstates. The first Born approximation is used, so "the true model must be representable by weak-scattering perturbations about the layered background medium." The Rytov approximation [64] can be used as well.

This algorithm was tested on complex geologically-realistic models and proved to be $O(N^4)$ computationally intensive. It outperformed both the backpropagation technique and traveltime tomography, which it uses as an input. The quality of the reconstruction can be improved if more *a priori* information is incorporated into the initial model. It was also shown that to maintain its spatial resolution, diffraction tomography does not necessarily require the use of complete wavetrains. In fact, Dickens demonstrated satisfactory reconstruction quality using small wavetrain portions surrounding the first arrivals. Those short pieces can still contain reflected components with large wavenumbers, unlike zero-momentum-transfer first arrivals used in traveltime tomography.

Dickens and Winbow [42] attempted to quantify the resolution of diffraction tomography and studied its capability to image simple targets from limited-view-angle data. They summarized the current state of development in the field of diffraction tomography as the ability to image an arbitrary defect immersed in a uniform medium when the background velocity varies slowly and the defect is much smaller than the wavelength. According to the authors, the method constructs an image for each

Reproduced with permission of the copyright owner. Further reproduction prohibited without permission.

separate frequency and the resulting image corresponds to inverting full time-domain data. In contrast to reflection imaging, traveltime tomography and crosshole logging, diffraction tomography treats reflections, refractions and diffractions equally.

The authors recommended using traveltime tomography to provide the initial velocity estimate for wave equation-based diffraction tomography. Traveltime tomography, yielding lower spatial resolution, is insensitive to the starting model and diffraction tomography can improve the resolution on the basis of good input velocity information. Wave vector coverage is a very important characteristic of imaging geometry that limits the reconstruction capability. Among the ways to extend this coverage the authors suggest using several frequencies and adding data obtained from different source-receiver configurations. The spatial resolution was studied as the ability to reconstruct a point target for various scanning geometries. The range of validity of the first Born approximation was tested using several disk targets and layered models.

5.1.3 Iterative DT methods

The iterative inversion method presented in this section is a rare example of applying iterative Algebraic Reconstruction Technique (ART) to diffraction tomography. The ART method works well in conventional tomography and is less sensitive to the limited view and the noise problems than most non-iterative algorithms.

Almquist et al. [73] used ART and filtered backprojection algorithms for the tomographic reconstruction of the nearfield pressure map of piezoelectric transducers. They found ART reconstructions to be less noisy without the need of averaging projection data or smoothing the resulting image. This observation agrees with our

Reproduced with permission of the copyright owner. Further reproduction prohibited without permission.

findings about the performance of a filtered backprojection algorithm applied to noisy data (see chapter 3). The authors also attempted to quantify the spatial resolution of the ART method used with parallel projection geometry.

The iterative solution to the reconstruction problem in diffraction tomography was constructed by Ladas and Devaney [71]. The authors noted that diffraction tomography is not a simple extension of conventional tomography because the interaction of coherent waves with an object is a very complex problem. However, when Born and/or Rytov approximations hold, the generalized projection-slice theorem can be employed, and diffraction tomography becomes very similar to conventional tomography.

The authors compared iterative and non-iterative categories of tomographic reconstruction algorithms and found that backpropagation methods are inefficient when applied to a limited-view problem, which dictates the need for an Algebraic Reconstruction (ART) algorithm in diffraction tomography. The proposed algorithm yields superior reconstructions to the filtered backpropagation technique when the number of views is relatively small and projection angles are unevenly spaced. It is a generalization of the conventional ART algorithm since it reduces to the latter in the zero-wavelength limit. The analysis presented assumes the Rytov approximation, plane wave illumination and planar measurement surfaces. The extension to the Born approximation and to other plane wave geometries is straightforward. It is not trivial to extend the algorithm to other incident wave fields because of the absence of a projection slice theorem for those fields.

In [72] the same authors demonstrated the performance of their DT ART al-

Reproduced with permission of the copyright owner. Further reproduction prohibited without permission.

gorithm in a fan beam tomographic experiment with only 26 view angles. They described the measurement and reconstruction procedure in great detail, covering both backpropagation and phase unwrapping steps and explaining the iteration process for the DT case. The better reconstruction quality of the DT ART algorithm, compared to the filtered backpropagation algorithm is due to the fact that the former returns the minimum norm solution to the reconstruction problem, while the latter guarantees the same only in the case of a continuum of view angles, which was not the case in many typical experiments.

5.1.4 Performance evaluation

The ranges of validity of the first Born and the first Rytov approximations, employed widely in diffraction tomography [78, 79], were examined by Chen and Stamnes [74]. The study was motivated by the absence of agreement in the current tomographic literature on the issue of relative merits and disadvantages of the two most popular approximations. The authors compared both approximations with the exact solution to the problem of plane wave scattering on the infinite circular cylinder. They used a filtered backpropagation algorithm for object reconstruction and chose the average percent error of the reconstructed refractive index as a criterion.

As a result, they obtained an empirical relation for the range of validity as a product of the radius of the cylinder and the refractive index difference between the cylinder and the surrounding medium. In these terms, the validity of the FBP algorithm based on the first Born approximation was found to be 3 times less than that of the hybrid FBP algorithm based on the first Rytov approximation. The

Reproduced with permission of the copyright owner. Further reproduction prohibited without permission.

authors point out that better phase-unwrapping methods can improve the resolution of the FBP based on the first Rytov approximation.

5.2 Choosing further direction

The above review demonstrates that all refraction/diffraction tomographic algorithms yield better resolution than conventional methods using the straight-ray assumption. The problem, however, remained of choosing an algorithm appropriate for the Lamb wave tomography. In previous chapters we discussed the applicability of conventional parallel projection, fan beam and crosshole data collection geometries used together with filtered backprojection or algebraic reconstruction (ART) techniques to the image reconstruction from travel times of Lamb waves in plates. We found the double crosshole geometry combined with simultaneous iterative reconstruction technique (SIRT) the most appropriate technique for Lamb wave tomography since it can be implemented in a square perimeter array of transducers, yields the best possible area coverage and is rather insensitive to experimental noise and uncertainties in arrival times. The most reasonable choice then is to retain the merits of this data acquisition procedure and algebraic reconstruction algorithm while improving its resolution by means of DT.

After detailed analysis of existing DT methods and taking into account all advantages of double crosshole technique we decided to develop an iterative reconstruction procedure similar to that proposed by Wang and Kline [66]. The output image from the present straight ray algorithm would serve as an input background for the ray tracing routine. The curved ray ART would then reconstruct the updated

Reproduced with permission of the copyright owner. Further reproduction prohibited without permission.

image and feed the next iteration until the desired quality or asymptotic behavior is observed. Andersen [80] analyzed existing methods of iterative reconstruction along curved rays and made useful recommendations about their practical implementation. One significant difficulty, however, lies in the fact that all existing DT methods were developed for bulk waves, which obey much simpler propagation rules than guided waves. Lamb waves are combinations of shear and longitudinal waves constantly interacting with plate boundaries, and it is difficult to formulate Snell's law for them. Mode conversions frequently occur on defect boundaries, and dispersion makes all the quantities frequency dependent. Nevertheless, we decided to use ray tracing since it is the most natural extension of the straight ray approach to inhomogeneous media.

The limits of applicability of the ray acoustic approximation can be estimated directly from the governing equations [81]. The Helmholtz equation in Cartesian coordinates is:

$$\nabla^2 p + \frac{\omega^2}{c^2(r)} p = -\delta(r - r_s) \tag{5.1}$$

where $r = (x, y, z)$, p is the sound pressure, $c(r)$ is the sound speed in liquid, and ω is the frequency of the δ-source located at r_s. To obtain the ray equations, we seek a solution to (5.1) in the form of a ray series:

$$p(r) = e^{i\omega\tau(r)} \sum_{j=0}^{\infty} \frac{A_j(r)}{(i\omega)^j} \tag{5.2}$$

Substitution of (5.2) into (5.1) yields the following infinite sequence of equations for the functions $\tau(r)$ and $A_j(r)$:

Reproduced with permission of the copyright owner. Further reproduction prohibited without permission.

$$
\begin{aligned}
O(\omega^2) &: |\nabla\tau|^2 = c^{-2}(r), \\
O(\omega) &: 2\nabla\tau\cdot\nabla A_0 + (\nabla^2\tau)A_0 = 0, \\
O(\omega^{1-j}) &: 2\nabla\tau\cdot\nabla A_j = -\nabla^2 A_{j-1}, j = 1, 2, \ldots
\end{aligned}
$$

In the high-frequency approximation we can ignore all of the equations except the first one, which is the *eikonal* equation. The vector $\nabla\tau$, perpendicular to the wavefronts, defines surfaces of constant phase $\tau(r)$. The rays in geometrical acoustics are also defined as curves perpendicular to the wavefronts, which means that $\nabla\tau$ is always tangent to the ray. The eikonal equation can be rewritten in terms of the arc length along the ray:

$$
\frac{d}{ds}\left(\frac{1}{c(r)}\frac{dr}{ds}\right) = -\frac{1}{c(r)^2}\nabla c(r) \tag{5.3}
$$

Equation (5.3) for the ray trajectories can be also derived from Fermat's principle stating that the travel time for the ray path is stationary [81]. Since $|dr(s)/ds|^2 = 1$, we can write for the travel time along the ray curve:

$$
t = \int_{s_0}^{s_1} \frac{1}{c(s)} ds = \int_{s_0}^{s_1} \frac{\sqrt{x_s^2 + y_s^2 + z_s^2}}{c(s)} ds = \int_{s_0}^{s_1} F(r, r', s) ds \tag{5.4}
$$

The last equation is made stationary when F satisfies the Euler-Lagrange equations

$$
\frac{\partial F}{\partial r} - \frac{d}{dx}\left(\frac{\partial F}{\partial r'}\right) = 0 \tag{5.5}
$$

Reproduced with permission of the copyright owner. Further reproduction prohibited without permission.

which are the same as (5.3). This means that both approaches discussed above are equivalent and we may use either one for ray tracing.

Another useful starting point for tracing rays was proposed by Dynes and Lytle in [82]. They derived a two-dimensional differential equation for the ray trajectory from the local form of Snell's law:

$$\frac{d\theta}{ds} = \frac{1}{c(r)}\left(\frac{\partial c(r)}{\partial y}\cos\theta - \frac{\partial c(r)}{\partial x}\sin\theta\right) \tag{5.6}$$

where θ is an angle between the ray tangent and positive $x - axis$, c is the material sound velocity and s is the coordinate along the ray (Fig. 5.1, adapted from [65]).

Snell's law holds in a wide range of media, even with severe discontinuities in the the index of refraction (sound velocity). It is difficult to formulate in anisotropic media [66] due to the fact that Snell's law is associated with wave normals while the ray paths are defined by the energy propagation (group velocity). Although these two can be collinear when the wave propagates along some degenerate directions, this is not a general case in anisotropic media. Wang and Kline [66] adapted Fermat's principle for ray tracing in anisotropic media. They used second order Euler equation to minimize the ray travel time expressed in the form:

$$t(y) = \int_A^B m(x, y, y')ds = \int_{x_A}^{x_B} m(x, y, y')\sqrt{1 + y'^2}dx \tag{5.7}$$

where x_A, x_B are the x-coordinates of points A and B of the ray, $y(x)$ is any admissible path between A and B, $m(x, y, y')$ is the inverse of the group velocity (not phase velocity). m is also considered to be a function of the slope of the ray y' to reflect the

Reproduced with permission of the copyright owner. Further reproduction prohibited without permission.

directional dependence of the group velocity. Solution to the Euler equation yields the minimum transit time ray path for both isotropic and anisotropic media.

As demonstrated above, the eikonal equation and the concept of the acoustic rays result from a high frequency approximation to the solution of the wave equation. More generally, they are valid only for wavelengths much shorter than characteristic dimensions of the defect or inhomogeneity in the medium of propagation. On the other hand both Born and Rytov approximations assume low contrast velocity variations in the background medium and a small size of defect compared to the wavelength of the insonifying field. In all intermediate cases we have to use higher order methods to calculate acoustic travel times. For example, we can use full field models [41] for wave propagation and calculate quantities of interest with finite difference or finite element methods [83]. We may also resort to scattering theory [33] and predict directional dependence of travel times and amplitudes. Although these methods will naturally account for ray bending correction, they require either detailed analysis of the wavefront progression through media or *apriori* information on the defect symmetry and shape.

5.3 Ray tracing algorithms

The next task was to choose a fast and reliable method capable of tracing rays between any two transducers in a square perimeter array. The terrain to be traced is a discrete velocity map of the plate area surrounded by the array. This map is the output of the straight ray ART/SIRT reconstruction routine, and as a result, it may display artificial inhomogeneities of regular or random character, which

Reproduced with permission of the copyright owner. Further reproduction prohibited without permission.

complicate or even abort the ray tracing process. One common practice is to smooth the original image by convolving it with a small averaging mask. The size of the mask determines the quality of smoothness and can be chosen interactively. The influence of smoothing and interpolation on the anomalous behavior of traced rays was discussed by Chapman [84].

The existing ray tracing methods can be divided into shooting, bending (perturbation) and searching classes. In order to link two points, ray shooting methods [65, 82] solve a differential equation for the ray trajectory with systematically changing initial conditions until the ray passes within an acceptable error distance from destination point. However, choosing appropriate initial conditions is often difficult since the receiver position may be an ill-behaved function of them. There exists a possibility, proposed by Andersen [85], to significantly speed up the ray linking procedure by converting the complicated boundary value problem to a much faster initial value problem. This procedure is based on the observation that all paths found as integral curves of the ray equation are indeed valid geometrical rays – but correspond to different pairs of transmit and receive positions. One therefore needs to trace rays only once and then map the results to the new "fictive" geometry using interpolation where needed. The described method does not support multiple linking rays, but it can be modified to handle that situation as well.

Ray bending methods [86–93] first link the endpoints with an arbitrary ray and then perturb it until the minimum travel time is achieved. It is possible to miss the global minimum with this method when several linking rays exist, since the solution depends on the first guess.

Reproduced with permission of the copyright owner. Further reproduction prohibited without permission.

The searching family consists mainly of graph-theoretical methods [94]. Here the image is represented as a graph of discrete points joined by weighted segments. The minimum-time path is then obtained using graph searching algorithms like the priority-first search. These methods can be very fast since the weights can be pre-computed and stored in memory for subsequent search. The disadvantage is that the ray is forced to travel along predetermined segments. The problem of multiple paths can be solved by imposing natural additional constraints on the ray behavior.

5.3.1 Simulated annealing ray tracing

Velis and Ulrych, [95] proposed a hybrid Monte Carlo method for ray tracing which incorporates features from shooting and bending algorithms and uses a very fast simulated annealing technique [96] for the travel time minimization. Simulated annealing converges to a global minimum in a statistical sense and can be combined with any available initial value ray tracing system. Although it cannot find all possible local minima or all paths with equal traveltimes in some pathological cases, the method has numerous advantages and we have applied it to our Lamb wave tomography data sets.

For simplicity we assumed that the refractive index profile to be traced is cell-wise constant and used Snell's law to propagate the ray between cell boundaries, starting from arbitrary initial conditions. Tracing stops when the ray reaches either a receiver or any of the image boundaries. In the latter case we complete the ray by joining its last point and the receiver with a straight line. Since the cell values represent local slownesses $\frac{1}{v}$, the travel time along the piecewise constant ray can be

Reproduced with permission of the copyright owner. Further reproduction prohibited without permission.

calculated as:

$$t = \sum_{segments} \frac{segment\_length}{v_{seg}} \tag{5.8}$$

Our simulated annealing routine uses the Metropolis algorithm from [97] and can be summarized in Table 5.1:

Simulated Annealing Ray Tracing
1. Trace a random ray, compute traveltime t and initialize $t_{min} = t$;
2. Determine temperature T from the annealing schedule;
3. Choose random shooting angle, trace the ray and calculate t;
4. Calculate $\Delta t = t - t_{min}$;
5. If $\Delta t \leq 0$ accept the change: $t_{min} = t$;
6. Else if $rnd \leq \exp(-\frac{\Delta t}{T})$ accept the change: $t_{min} = t$;
7. Do 3 for the sufficient number of Monte Carlo steps;
9. Do 2 according to the annealing schedule;
10. Output t_{min}.

Table 5.1: Simulated Annealing Ray Tracing Algorithm

The speed and the accuracy of this method are determined by the annealing schedule – the rate of lowering temperature. It it has been proven [96] that it suffices to obtain a global minimum of traveltime t if temperature T is selected to decrease not faster than

$$T(k) = \frac{T_0}{ln(k)} \tag{5.9}$$

where k is the iteration step. Such a slow schedule combined with exhaustive Monte Carlo sampling ensures thorough exploration of the local extrema and gradual jump-

Reproduced with permission of the copyright owner. Further reproduction prohibited without permission.

ing into lower-energy states. Lowering the temperature more rapidly is called simulated quenching – a common approach to speeding up the conventional simulated annealing, but it does not provide a guarantee of finding an optimal solution [98].

We applied the conventional Simulated Annealing algorithm with temperature schedule (5.9) to the problem of ray tracing for Lamb wave tomography. It worked well for all possible rays in a 100×100 square perimeter array of transducers. On the other hand, the Snell's law ray propagator in the above form demonstrated poor performance because refraction on cell boundaries introduces artificial features into the ray behavior. Computational speed was an additional problem because it took overnight processing to trace the whole set of 10^4 rays on the $Pentium - Pro^{TM}$ PC whereas the straight ray reconstruction of the same data set took only several seconds on the same computer. We tried to use simulated quenching, but the temperature schedule had to be manually adapted to every particular image since some of them allow for several linking rays and it is easy to get trapped in a local minimum.

5.3.2 Discrepancy minimization ray tracing

We needed to improve both the quality of the ray tracer and the speed of the calculations. The local form of Snell's law (5.6) introduced in [82] is independent of the cell boundaries and can be integrated numerically to compute ray paths through a given digital image of the refractive index. We chose a classical fourth order Runge-Kutta method [99] to integrate (5.6) for a given shooting angle θ. Since rays are not restricted to pass only through the image sample points, a suitable interpolation routine should be used to evaluate both the index of refraction (slowness) and its

Reproduced with permission of the copyright owner. Further reproduction prohibited without permission.

partial derivatives at arbitrary location. Lytle and Dynes, [82] used cubical spline interpolation which involves 16 neighboring samples. For the sake of speed we use the simple bilinear interpolation requiring only 4 nearest neighbors A,B,D and C [65]:

$$\hat{n}(x,y) = n(A) + [n(B) - n(A)]\frac{x - x_0}{\Delta x} + [n(C) - n(A)]\frac{y - y_0}{\Delta y} + \\ +[n(A) - n(C) + n(D) - n(B)]\frac{x - x_0}{\Delta x}\frac{y - y_0}{\Delta y} \qquad (5.10)$$

where $\hat{n}(x,y)$ is a refractive index in the point E (Fig. 5.2), Δx and Δy are cell dimensions, x_0, y_0 are the coordinates of the point A.

This improved ray tracer worked well for a wide range of sample backgrounds. The only bottleneck was the simulated annealing minimization procedure. We ultimately replaced it with another routine that corrects the shooting angle until the ray passes within a specified error distance from the receiver point. Initially we used a bisection algorithm to minimize this distance in a small number of steps. We marked the discrepancy distance positive or negative depending on the relative positions of the crossing point and the receiver, but it turned out that for some backgrounds, and especially for points close to the image border, this discrepancy distance is not a single-valued function of the shooting angle. In those cases the bisection routine fails. It is also clear that the convergence speed of this method depends highly on the choice of the initial shooting angle.

To avoid the latter, in our current implementation we shoot multiple rays at equiangular intervals and trace them until they reach the border. Then for each ray we calculate discrepancy distance from the border crossing point to the receiver and extract all the triplets that could possibly bracket minima. In the case of multiple

Reproduced with permission of the copyright owner. Further reproduction prohibited without permission.

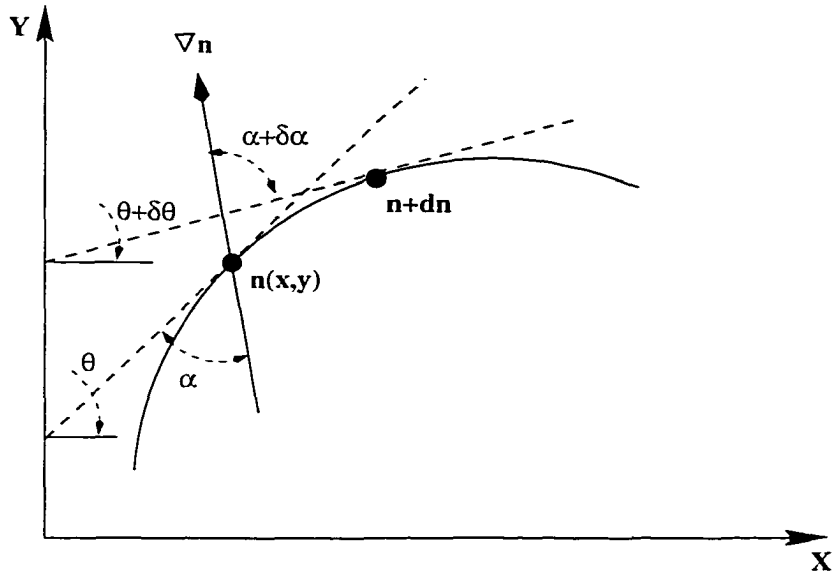

Figure 5.1: To the derivation of the local form of Snell's law.

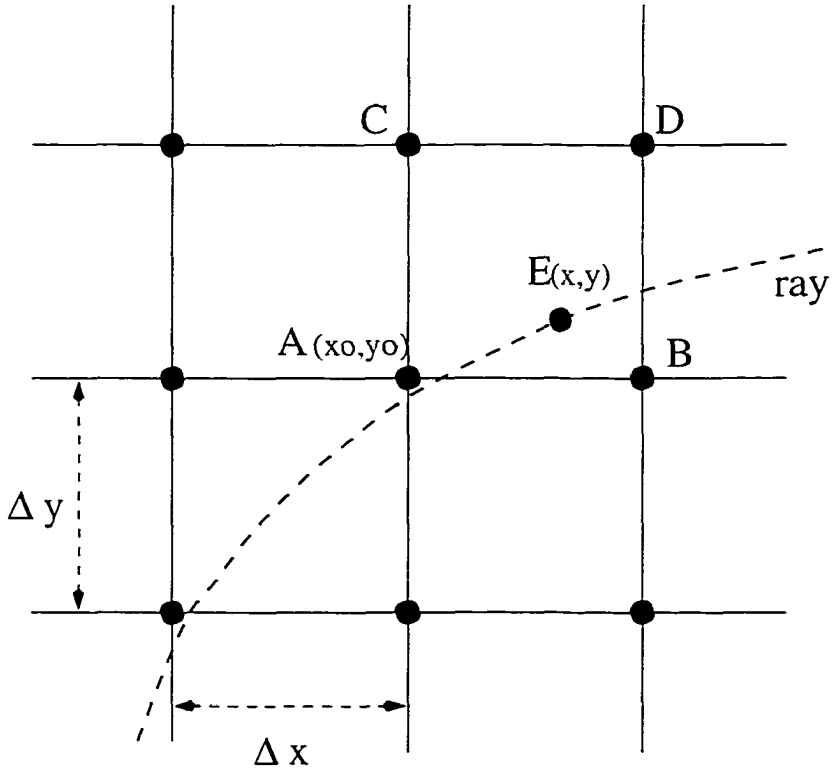

Figure 5.2: Ray path and bilinear interpolation.

Reproduced with permission of the copyright owner. Further reproduction prohibited without permission.

linking rays several minima may exist and the sampling rate has to be high enough to detect all of them. Then for each triplet we use a golden section minimum-finding routine adapted from [99] to return a corresponding shooting angle for a linking ray. Finally, the ray with the smallest travel time is identified and retraced to find its intersection points with the image cells. Fig. 5.4 demonstrates several typical rays traced by the above method.

In ill-behaved cases when no linking rays are found the above procedure counts failures and makes a thresholded decision to use higher degree of smoothing. This feedback can be used for tailoring the contrast of the straight ray SIRT image to the needs of the ray tracing program. The raw output from the straight ray ART and even SIRT routine (Fig. 5.3a) suffers from noise and artifacts causing abrupt changes in gray level from pixel to pixel. Even interpolation does not save the ray tracing program from failures, and smoothing of the original image is often required. We smooth the image automatically, trying to keep the percentage of failures less than 1%. To fit this requirement the image in Fig. 5.3A should be smoothed with a 21×21 averaging mask (Fig. 5.3B). Typical results of ray tracing on this image are shown in Fig. 5.4. Lower degrees of smoothing usually lead to stronger ray bending and the same time increase the number of failures.

Reproduced with permission of the copyright owner. Further reproduction prohibited without permission.

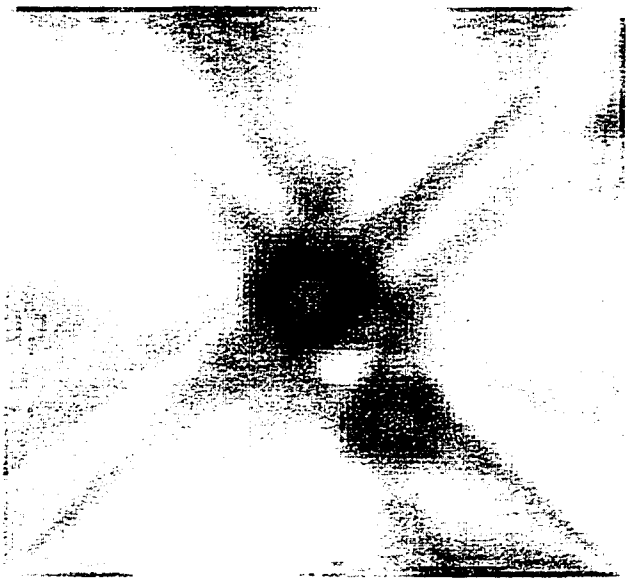

A. Raw straight ray SIRT reconstruction.

B. Image (A) smoothed with a 21x21 mask

Figure 5.3: Image preparation for ray tracing: smoothing with averaging mask.

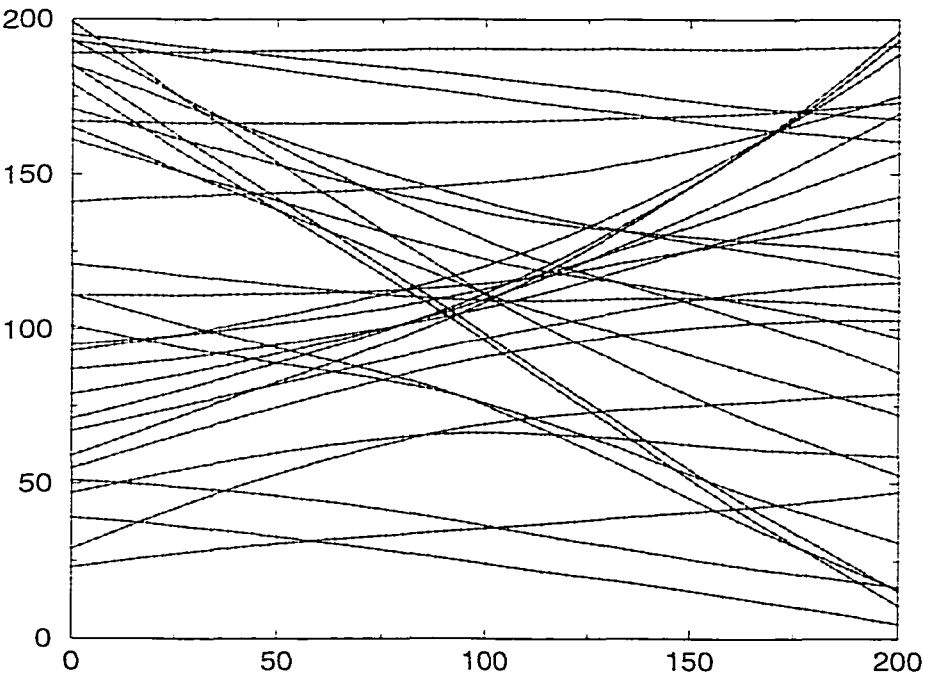

Figure 5.4: Typical rays traced from left (transmitters) to right (receivers) on a smoothed terrain (Fig. 5.3B).

Reproduced with permission of the copyright owner. Further reproduction prohibited without permission.

5.4 Iterative image reconstruction

5.4.1 Curvilinear SIRT

The curved ray SIRT is conceptually very similar to the straight ray one [100] except that it stores all the ray data in memory instead of computing them analytically. It is indeed impossible to know in advance the number of pixels the bent ray will cross as well as the lengths of the pixel segments it will cut. We therefore have to compute these quantities for each traced ray and accumulate them into a huge array. After the tracing of all the rays is completed we invert the matrix using the same ART or SIRT algorithm as for the straight rays. This means that reconstruction from curved rays preserves all tomographic artifacts specific for a given data acquisition geometry and reconstruction algorithm. In addition, refraction at defects often creates severe focusing (or defocusing depending on the difference of the wave speed inside and outside the defect). Due to these effects the resulting ray density and wave vector coverage often become highly nonuniform throughout the scanned area making the resolution of the reconstruction algorithm depend on the size and location of the defects.

As we have already pointed out, the degree of ray bending is determined by the size and properties of the smoothing mask. This approach is not as artificial as it seems because the smoothed image can be treated as an initial guess for the slowness map. Lower degrees of smoothing leave artifacts that strongly distort ray paths and make accurate tracing impossible. This is in some sense equivalent to the presence of strong scatterers for which the whole geometrical acoustics approach fails. On

Reproduced with permission of the copyright owner. Further reproduction prohibited without permission.

the other hand, very high degrees of smoothing blur out defects and ray paths more closely resemble straight lines. It seems possible to empirically find the optimal size of a smoothing mask allowing for realistic modeling of the ray paths and thus for the most accurate reconstruction of defects with chosen inversion algorithm.

5.4.2 Integrated reconstruction procedure

Below we include the complete routine for the iterative image reconstruction from Lamb wave traveltime data. The image upgrading concept, used by the algorithm, is similar to that described by Wang and Kline [101]. The procedure is currently implemented in "C" programming language and designed as a modularized package to allow for a fast replacement of different ray tracing, image processing and tomographic reconstruction blocks (Table 5.2):

Bent ray iterative reconstruction scheme
1. Collect waveforms from 1, 2 or more crosshole projections
2. Extract arrival times of the fastest mode from each waveform
3. Do straight ray SIRT until acceptable image quality is achieved
4. Build the image from the previous step and smooth it
until the ray tracer accepts it with a specified accuracy
5. Trace all the rays and store corresponding pixel segments in memory
6. Do bent ray SIRT one or several times
7. Do 4. until acceptable quality is achieved or image stops changing
8. Output the final image

Table 5.2: Bent ray SIRT reconstruction scheme

Reproduced with permission of the copyright owner. Further reproduction prohibited without permission.

5.5 Double crosshole reconstructions

Figures 5.5, 5.6 and 5.7 illustrate the application of our algorithm to the inversion of double crosshole data acquired on three aluminum plate samples with machined defects using the apparatus described in [100]. Figures (A) in each triplet show the positions and shapes of the defects on the reconstruction square of the size 20×20 cm. Figures (B) are straight ray SIRT reconstructions of these defects. In each case we ran only a single SIRT iteration. The output images, smoothed with an averaging mask of order 21, were used as input velocity maps for the ray tracing algorithms. Figures (C) are bent ray SIRT reconstructions of the corresponding defects. All the (B) and (C) images were equally contrast stretched to lower the level of residual reconstruction artifacts.

Visual comparison of the double crosshole reconstructions with straight and bent ray SIRT yields several important conclusions:

- Defect size: The size of defects reconstructed with straight ray SIRT (Figures 5.5(B), 5.6(B), 5.7(B)) often exceeds reality (Figures 5.5(A), 5.6(A), 5.7(A)). The sizes of defects reconstructed with bent ray SIRT (Figures 5.5(C), 5.6(C), 5.7(C)) appear to be smaller and closer to their real size.

- Defect centers: Inner areas of defects reconstructed with straight ray SIRT often have different color than the rest of the defect. For the through holes where Lamb waves do not propagate at all, this is not a real effect of change of the Lamb wave velocity inside the defect, but rather a reconstruction artifact. It occurs because straight rays inadequately model reality and any slowdown due

Reproduced with permission of the copyright owner. Further reproduction prohibited without permission.

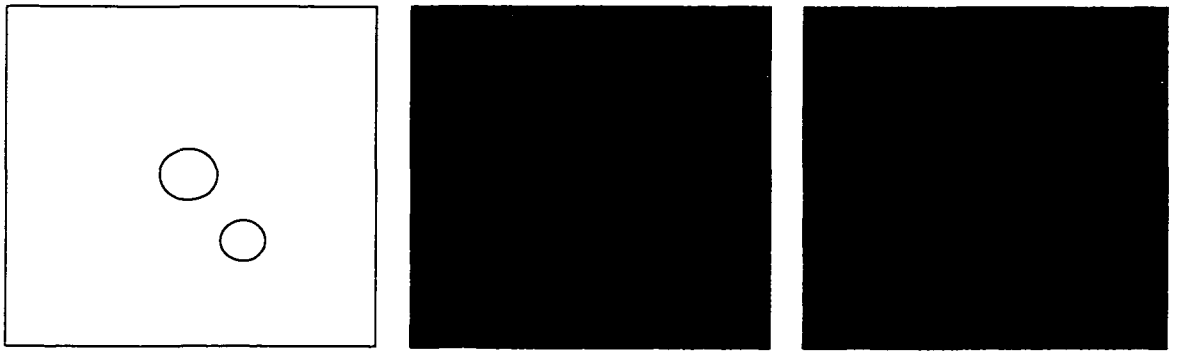

A. Defect location B. Straight ray SIRT C. Curved ray SIRT

Figure 5.5: Aluminum plate with two circular thinnings. Image size: 200 × 200 mm.

A. Defect location B. Straight ray SIRT C. Curved ray SIRT

Figure 5.6: Aluminum plate with five through holes. Image size: 200 × 200 mm.

A. Defect location B. Straight ray SIRT C. Curved ray SIRT

Figure 5.7: Aluminum plate with oblong thinning. Image size: 200 × 200 mm.

Reproduced with permission of the copyright owner. Further reproduction prohibited without permission.

to ray bending is interpreted as smaller wave speed inside the defect. Curved ray SIRT partially eliminates these artifacts proving that the ray tracing approach is physically more accurate and applicable to the Lamb waves. For the thinning defects, the different color of their inner areas may have a different origin. It may be caused by the actual difference in the propagation velocity of the waves traveling through the defect center and those refracting around the defect boundary. Nevertheless, the bent ray SIRT reduces the size of differently colored inner spots.

- Ray density and reconstruction artifacts: Both straight and curved ray SIRT images bear reconstruction artifacts showing up as a diagonal-stretched and star-like patterns surrounding the defects. These patterns result from nonuniform ray density and wave vector area coverage for a given data collection geometry. They can be reduced by making ray density high and uniform throughout the image – a realistic goal for straight ray tomography. Ray bending distorts this uniformity bringing the effects of acoustic lensing and shadowing [80], when some areas are covered with rays more or less densely than the others. These phenomena depend on the size and severity of defects and result in additional reconstruction artifacts. Indeed, the most intensive artifacts are observed on Fig. 5.7(C) with the largest defect area and the weakest artifacts are on Fig. 5.6(C) where defects are small and don't introduce large changes to the ray density.

Reproduced with permission of the copyright owner. Further reproduction prohibited without permission.

5.6 Reconstruction from six crosshole projections

For a single crosshole projection the ray density and the wave vector coverage are extremely nonuniform throughout the scanned area. This leads to severe reconstruction artifacts [47]. To improve the ray pattern we combined two mutually perpendicular crosshole projections into a double crosshole data set and built series of images of a much higher quality. However, rather wide peripheral areas of the image still suffer from relatively low ray density and narrow range of wave vector directions in each particular pixel. The only remaining way to fix this problem is to use the rays connecting all possible pairs of points in a discrete square perimeter array. These rays can be split into six sets of projections as shown in Figure 5.8. The four corner projections (Fig. 5.8c-f) seem to be a natural addition to the previously tried double crosshole configuration. They augment the ray density along the sides of the square and contribute significantly to the wave vector directivity pattern over the entire area.

Implementation of the complete six-projection crosshole tomography with our laboratory scanner was a laborious task. To acquire all data we needed to carefully move one or both sliders with attached transducers to different locations and measure projections one by one. In addition, because of the finite dimensions of the transducer holder arms, we found it impossible to take measurements when both source and receiver are very close to the corner. In such cases we substituted missing arrival times with theoretically calculated ones. Moreover, if the source and receiver are very close to each other the embryonic guided waves are still in the formation stage and relatively stable mode envelopes are not formed yet. This introduces errors into

Reproduced with permission of the copyright owner. Further reproduction prohibited without permission.

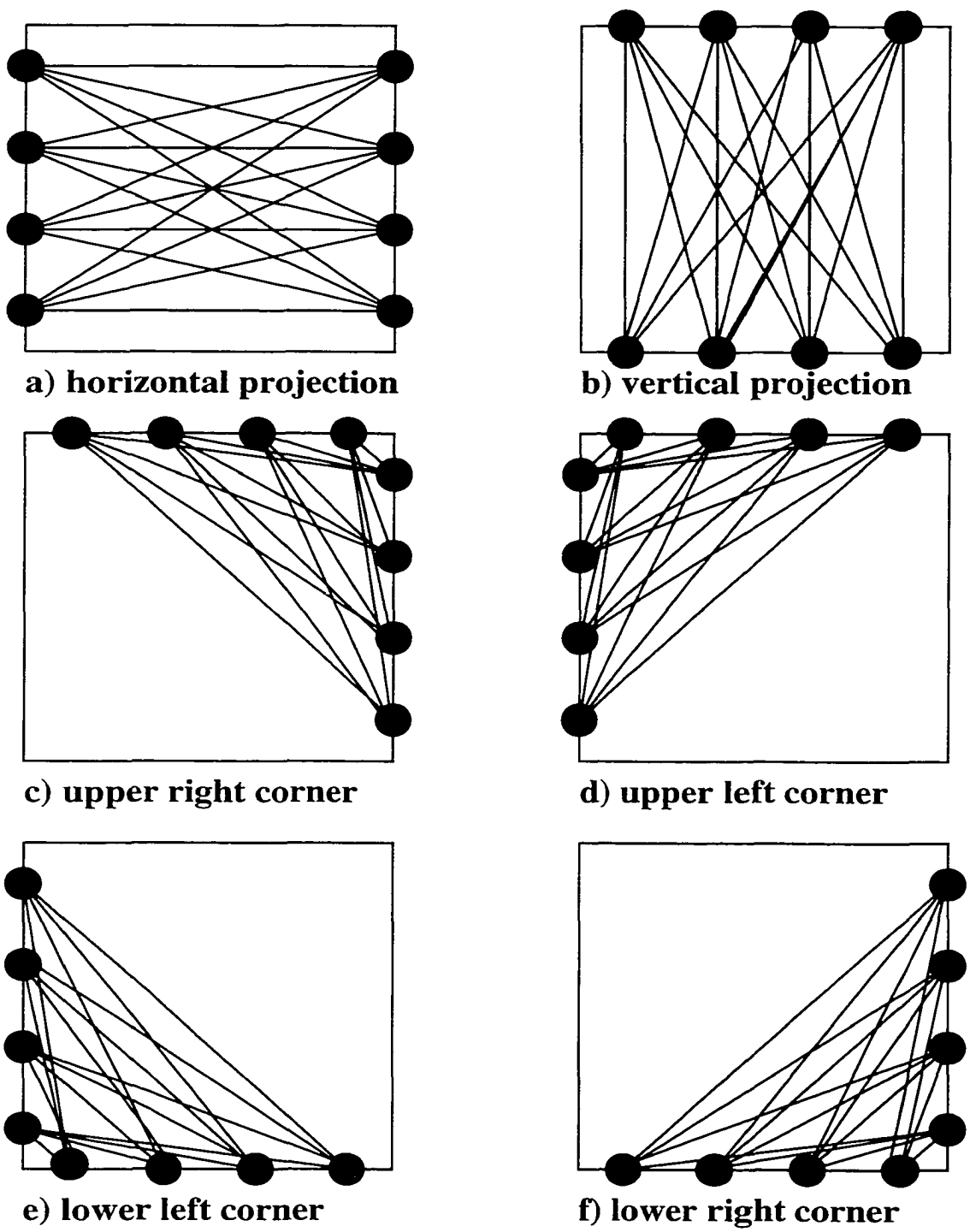

Figure 5.8: Six possible crosshole projections.

Reproduced with permission of the copyright owner. Further reproduction prohibited without permission.

measured arrival times. All ray tracing, data processing, storage, and reconstruction code had to be adapted to the new configuration.

At the same time we modernized the data acquisition equipment by substituting all the rack-mount and block devices with two PC ISA plug-in boards, a tone burst pulser-receiver TB-1000 board by $Matec^{TM}$ and a $GAGE^{TM}$ CS8012A DAQ board with 12-bit resolution and up to 100 MHz sampling rate. We partly wrote and partly adapted free third-party software to make all the equipment work under Linux RedHat-6.0 Operating System. A block diagram of the new fully computerized tomographic system is drawn on Fig. 5.9.

Below we present our most recent results on the Lamb wave tomography. All the experiments included measurement of all six crosshole projections on the 100×100 square matrix with a step size of 2 mm. The total number of captured waveforms for each sample was $N_{tot} = 6 \cdot 10^4$. All the measurements were performed on the new hardware (Fig. 5.9). The arrival times were extracted with our most accurate time domain group delay measurement routine. After extraction, they were transformed into velocity domain using known distances between transducers. In this domain the data are less scattered and we can identify the points with outlying velocities as erroneous and truncate them using empirical rules. The projection data were then transformed back into time domain and fed the reconstruction algorithm. We found this truncation in the velocity domain quite useful while other manipulations such as filtering or smoothing time domain data produced unsatisfactory results. All the samples under study were made out of 1.2 and 2.3 mm-thick aluminum plates with machined defects including one 25.4 mm-diameter through hole, five 15 mm-diameter

Reproduced with permission of the copyright owner. Further reproduction prohibited without permission.

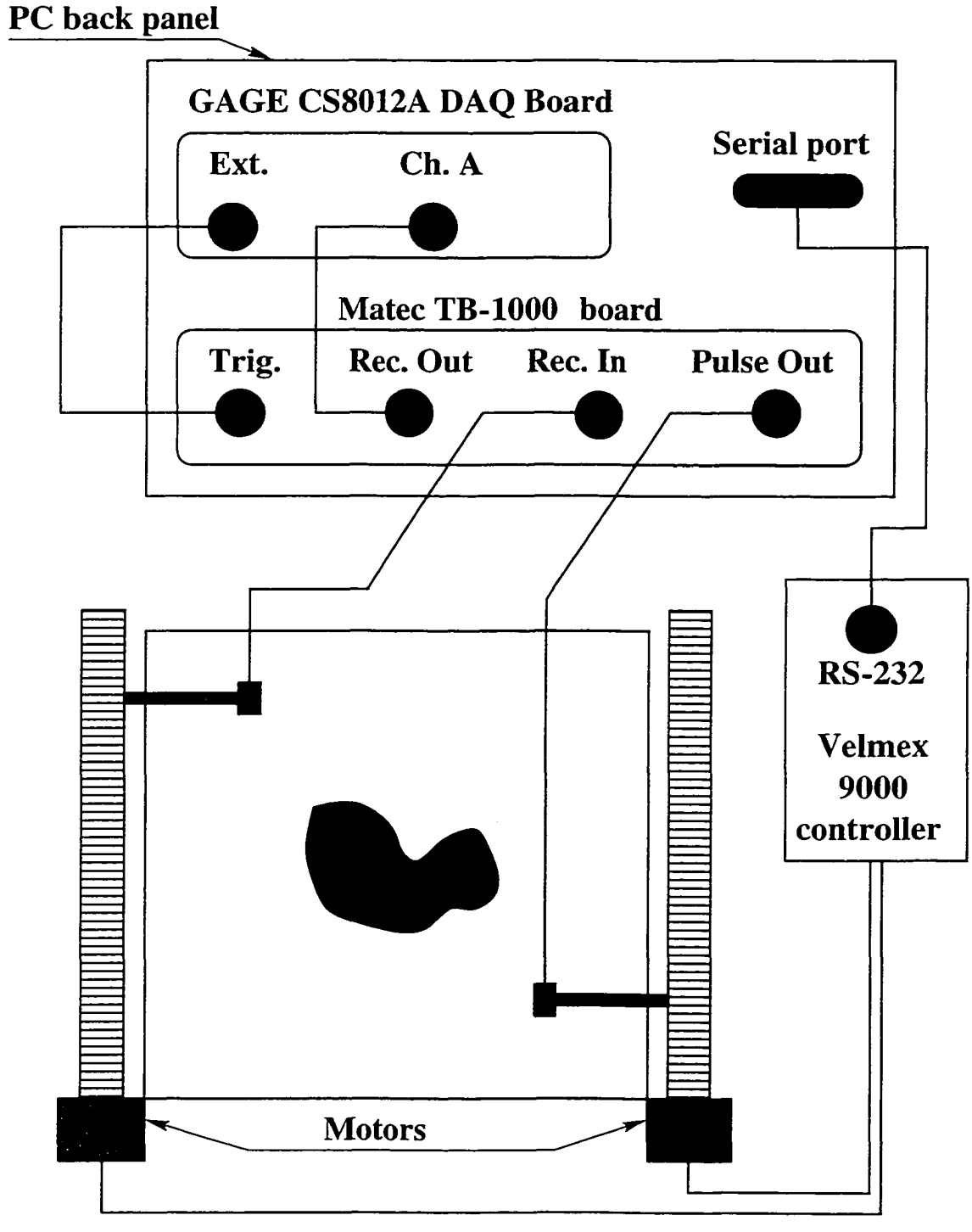

Figure 5.9: Lamb wave traveltime tomography with computer plug-in boards.

Reproduced with permission of the copyright owner. Further reproduction prohibited without permission.

A. Defect-free plate B. 25.4 mm through hole C. Difference B-A

Figure 5.10: Subtracting SIRT reconstruction artifacts. Image size: 200 × 200 mm.

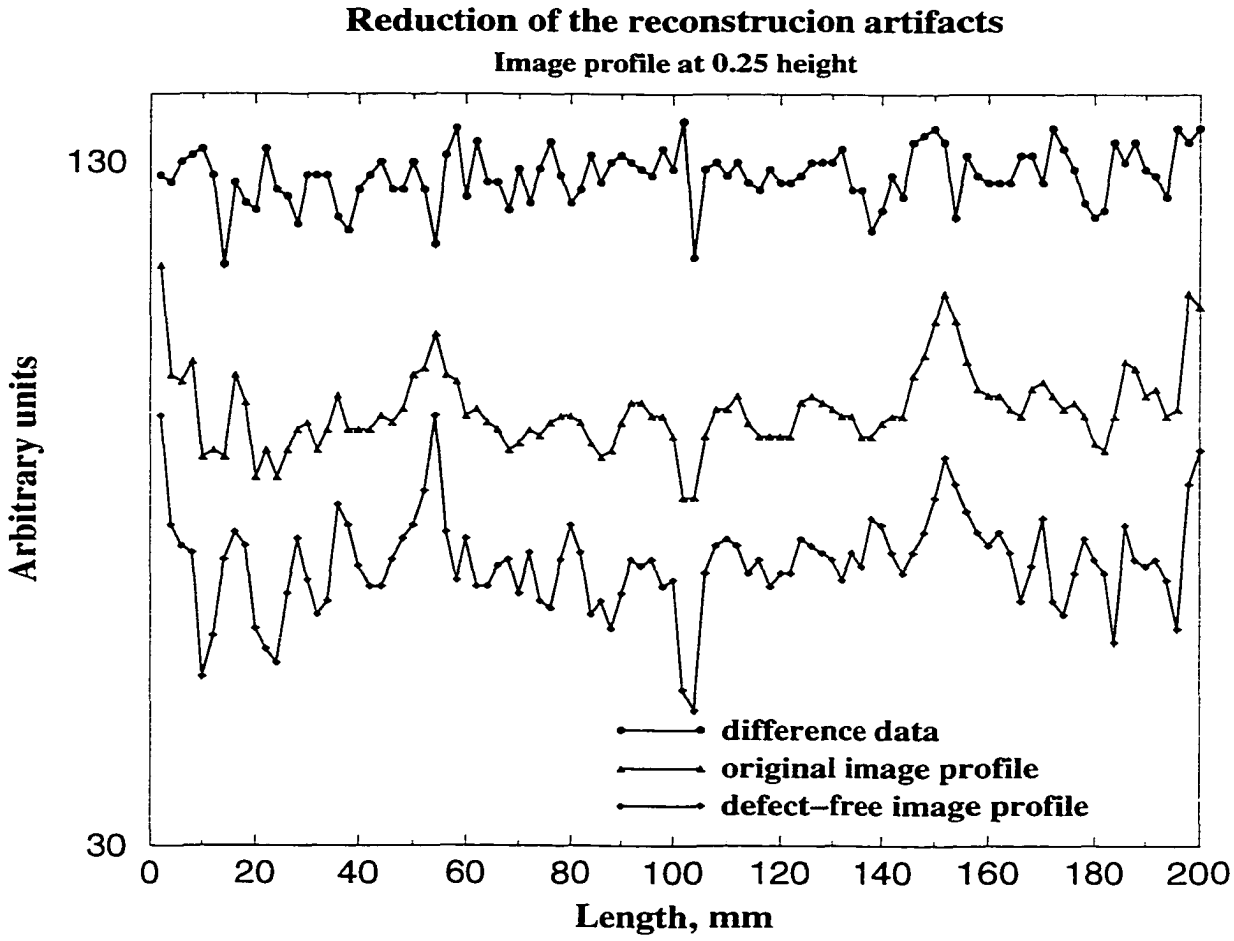

Figure 5.11: Horizontal artifact profiles taken at image quarter-height.

Reproduced with permission of the copyright owner. Further reproduction prohibited without permission.

through holes, two circular flat bottom holes, one oblong thinning with rounded edges, and a defect-free plate for the test purposes.

The first reconstruction step involved 50 iterations of straight ray SIRT, modified to handle all 6 projections. Figures 5.10A,B show the corresponding reconstructions for the defect-free plate and a plate with a 25.4 mm-diameter through hole in the center. Both images bear diagonal and arc-shaped artifacts specific for the cross-hole geometry. Fig. 5.10C is the result of subtraction of the images B and A. The majority of the artifacts were eliminated and the visual quality was drastically improved. Fig. 5.11 shows the profiles of the above three images taken at 50 mm above the bottom (1/4 of the image height). It demonstrates the effect of the subtraction of persistent artifacts near the edges, on the diagonals and in the central area. The resulting image profile is much less noisy and more uniform. We decided to include the background subtraction as a necessary step of the reconstruction software. However, the background image of the defect-free plate should be created with the same number of straight and bent ray SIRT iterations as the image of interest. Otherwise the artifact patterns will be different and the subtraction will be less efficient.

The second reconstruction step involved ray tracing on the smoothed velocity pattern obtained at a previous step. The resulting matrix was inverted with 50 iterations of a six-projection bent ray SIRT. A key issue on this stage is a choice of a smoothing filter. To study dependence of the image quality on the degree and type of smoothing we convolved the straight ray image with a combination of a median and averaging masks of various orders. The action of both filters on the image pixels can be explained as follows: the median operator substitutes the pixel value with a median

Reproduced with permission of the copyright owner. Further reproduction prohibited without permission.

value of the pixels in a chosen neighborhood while the average operator substitutes it with the mean value over the neighborhood. As a result, the median filter produces smoother images with emphasized edges, and the average filter uniformly blurs the whole image.

In our study we used combinations of median masks of orders 11, 15, and 17 and average masks of orders 5, 11, 13, 15, 17, and 21. We observed that averaging orders higher than 21 blurred our images so completely that ray paths were almost straight and corresponding reconstructions were almost the same as with a straight ray SIRT. We also noticed that low order averaging (≤ 9) made accurate ray tracing impossible because of the wild ray bending on the artificial scatterers. In addition, we observed that the median filter produced negligibly small effect on the image quality compared to that of the averaging filter, and decided not to use it for further analysis. The following results were obtained with averaging masks of of the orders 11 and 17.

Figures 5.12B,C represent the bent ray SIRT reconstructions of a 25.4 mm-diameter through hole with averaging masks of the orders 17 and 11 correspondingly. Fig. 5.12A is the straight ray reconstruction for the comparison purposes. In all cases the appropriate backgrounds were subtracted. It is clearly seen that the degree of averaging affects the size of the reconstructed defect and the number of artifacts on the resulting image. Fig. 5.13 allows for quantitative comparison of reconstructed velocity profiles. The blue line indicates position and size of the defect. The straight ray reconstruction (black line) oversizes the defect, the green line (averaging order 11) undersizes it, and the red line (averaging order 17) matches the defect closer than the other. In all cases we estimated the width of the defect at the level of 3.75 $mm/\mu s$

Reproduced with permission of the copyright owner. Further reproduction prohibited without permission.

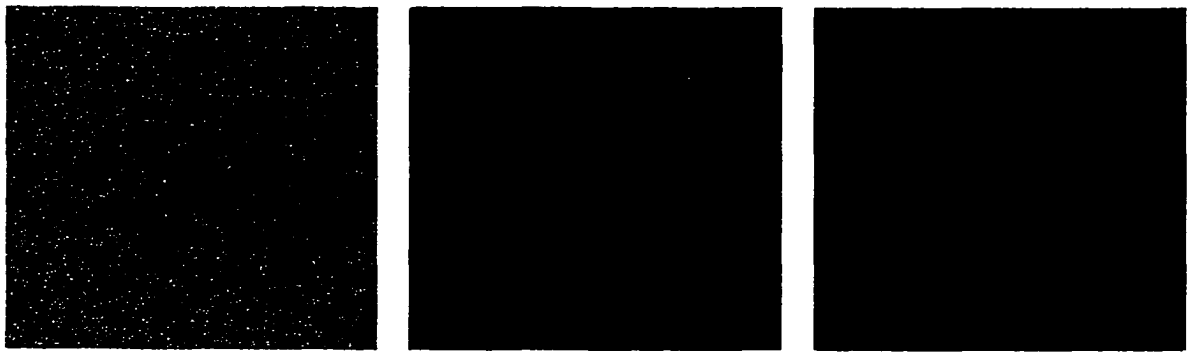

A. Straight rays B. Curved, average 17 C. Curved, average 11

Figure 5.12: Straight and bent ray reconstructions of a 25.4 mm-diameter through hole in aluminum plate. Orders of averaging masks used: B - 17; C - 11. Image size: 200 × 200 mm.

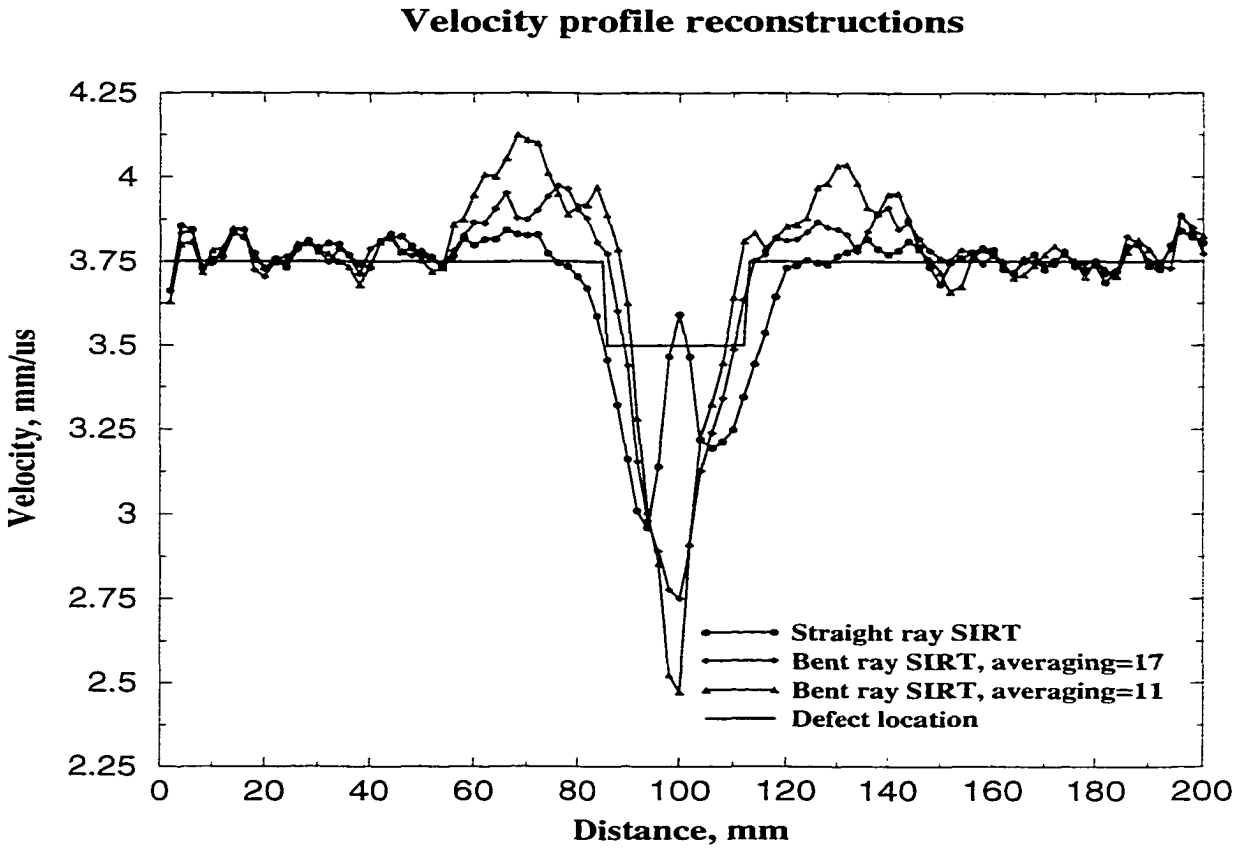

Figure 5.13: Horizontal profiles of images (Fig. 5.12A,B,C) taken at half-height.

Reproduced with permission of the copyright owner. Further reproduction prohibited without permission.

which is equal to the background velocity. It therefore seems possible to empirically choose the averaging order so that the reconstructed defect will have the same size as the original one.

Figures 5.14B,C represent the bent ray SIRT reconstructions of the five 15 mm-diameter through holes with averaging masks of the orders 17 and 11 correspondingly. Fig. 5.14A is the straight ray reconstruction for the comparison purposes. Its quality is clearly superior to that of a double crosshole SIRT (Fig. 4.16), especially when the shapes of the two holes at the extreme top and bottom of the image are compared. This improvement is due to the six projection data acquisition scheme with higher ray density and better wave vector directivity pattern on the edges. Fig. 5.14B also demonstrates significant improvement in defect sizing (compare to Fig. 5.6A). However, further reduction of the smoothing order produces multiple intractable artifacts. Fig. 5.15 with vertical velocity profiles supports this analysis quantitatively. It is worth mentioning that areas with multiple defects are a big problem for ultrasound tomography since multiple reflections and mode conversions make accurate interpretation of the arrival times sometimes impossible.

Figures 5.16B,C represent the bent ray SIRT reconstructions of the 25x100 mm 50% oblong thinning with averaging masks of the orders 17 and 11 correspondingly. Fig. 5.16A is the straight ray reconstruction for the comparison purposes. Its quality is much better than that of a double crosshole SIRT (Fig. 4.18), especially when the horizontal dimensions are compared. As in the previous case, this improvement is due to the six projection data acquisition scheme. However, bent ray inversion (Figures 5.14B,C) with averaging masks of orders 17 and 11 clearly undersized the

Reproduced with permission of the copyright owner. Further reproduction prohibited without permission.

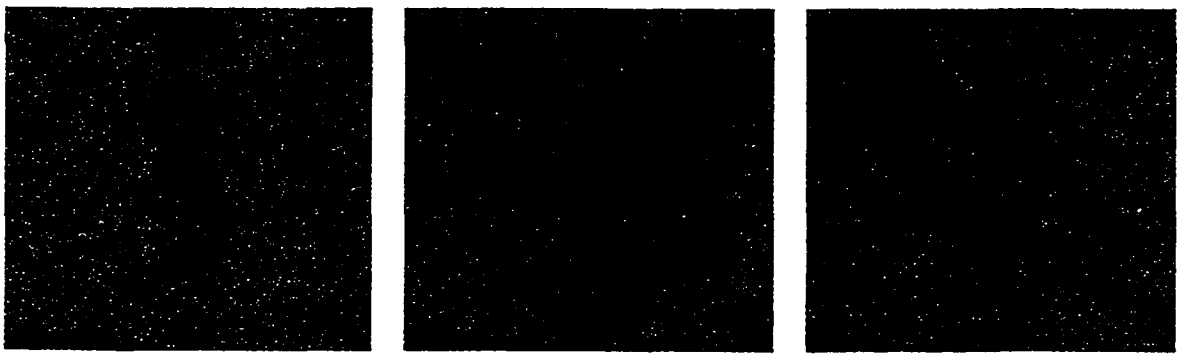

A. Straight rays B. Curved, aver17 C. Curved, aver11

Figure 5.14: Straight and bent ray reconstructions of the five 15 mm-diameter through holes in aluminum plate. Orders of averaging masks used: B - 17; C - 11. Image size: 200 × 200 mm.

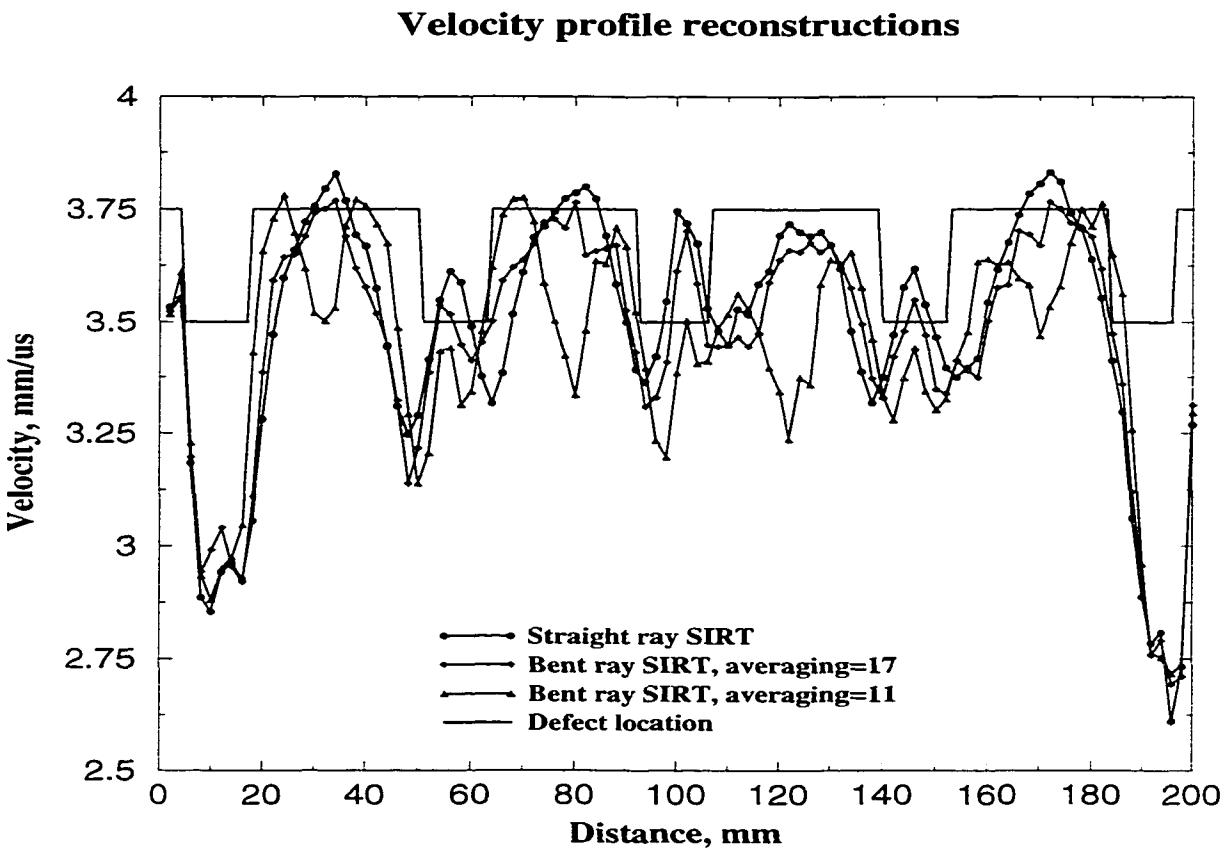

Figure 5.15: Horizontal profiles of images (Fig. 5.14A,B,C) taken at half-height.

Reproduced with permission of the copyright owner. Further reproduction prohibited without permission.

A. Straight rays B. Curved, aver17 C. Curved, aver-11

Figure 5.16: Straight and bent ray reconstructions of an oblong 25x100 mm thinning region in aluminum plate. Orders of averaging masks used: B - 17; C - 11. Image size: 200 × 200 mm.

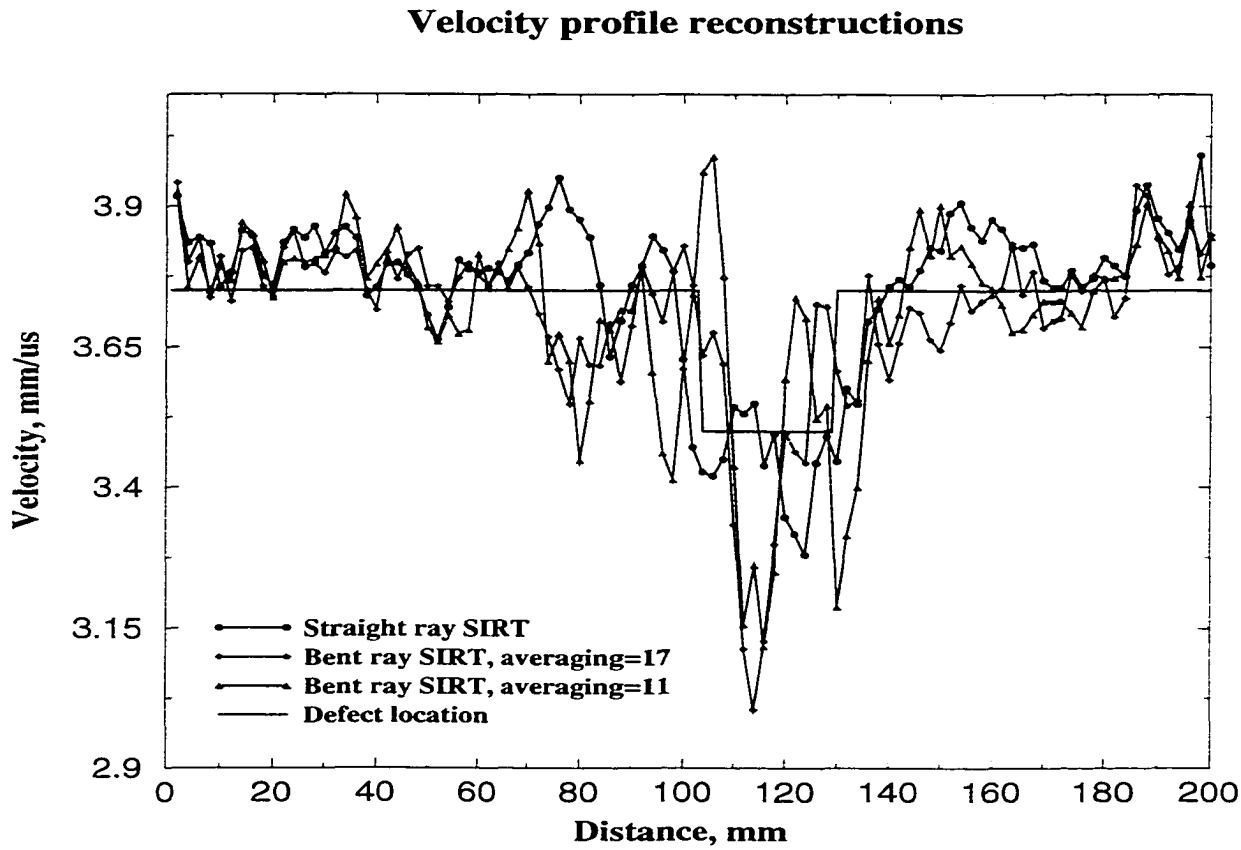

Figure 5.17: Horizontal profiles of images (Fig. 5.16A,B,C) taken at half-height.

Reproduced with permission of the copyright owner. Further reproduction prohibited without permission.

defect (compare to Fig. 5.7A) and created multiple artifacts. It seems probable that the higher smoothing order (19 or 21) will do a better job. Fig. 5.15 shows vertical velocity profiles of the above three images.

Figures 5.18A,B show the straight and bent (averaging order 17) ray SIRT reconstructions of plate area with two regions simulating multiple corrosion pits. Each region contains 23 flat bottom holes drilled along parallel rows with 5 or 4 holes in the row. The upper array has holes with diameters of 2 and 3 mm, the lower one has holes with diameters of 3 and 4 mm. As the images show, individual holes are not resolved. Instead, in agreement with expectations for transmission tomography (Fig. 1.8), the whole arrays are reconstructed as "shadowgrams". However, this does not mean that Lamb wave transmission tomography can never resolve individual holes. In our experiment the wavelength of the first-arriving mode is

$$\lambda = \frac{V_p h}{f} \simeq \frac{4}{1.2} mm \simeq 3.3 mm$$

which is bigger than the size of a single hole in the array and the wave field senses the array as a whole. The lower array with larger holes affects wave propagation more than the upper one and thus shows a larger footprint on the reconstructed image. In order to increase sensitivity we must use a smaller wavelength which can be achieved by selecting a different mode at a different frequency. And finally we may have to use reflection tomography because multiple interactions with the array of strongly scattering defects could make the interpretation of arrival times an impossible task.

Reproduced with permission of the copyright owner. Further reproduction prohibited without permission.

5.7 Discussion

This chapter has described our newly developed integrated iterative tomographic procedure using both straight and curved ray SIRT to reconstruct Lamb wave velocity maps for isotropic plates. We studied several ray tracing and linking methods and identified those most applicable to the tasks of Lamb wave tomography. Currently we use the fast and efficient shooting method for tracing rays because of the slowness of the simulated annealing approach. However, several versions of the simulated annealing algorithm, such as adaptive simulated annealing and very fast simulated annealing [96] have been reported to be relatively fast and, due to the numerous advantages of the technique, can be used as a main ray linking routine in further implementations.

This procedure was tested on aluminum plate samples with machined thinnings and through holes, and the results were compared to those obtained with a straight ray approach. We found that success of the ray tracing approach strongly depends on the degree of smoothing of the image, reconstructed with a straight ray SIRT. Changing this degree affects the size of the reconstructed defects and it is possible to find optimal smoothing conditions where defect dimensions will be reconstructed correctly. This is an important step towards improving the resolution of the Lamb wave tomography. At the same time ray bending always distorts the uniformity of the ray density and introduces additional artifacts into the final image. This distortion, however, is proportional to the size and severity of the defect. It does not occur for smaller defects and can be minimized even for larger ones by sufficient smoothing of the input image.

Reproduced with permission of the copyright owner. Further reproduction prohibited without permission.

The six projection crosshole geometry seems to be the best among the family of crosshole data acquisition schemes on a square perimeter array. Its high and uniform ray density plus broad local wave vector directivity pattern throughout the scanned area insure satisfactory resolution over the entire image. Some minor difficulties in the corners occurred mainly because of the imperfections of our scanning apparatus. They can be overcome if a square perimeter array of transducers is used for data acquisition.

All tomographic reconstruction methods produce geometry-related regular artifact patterns that complicate data interpretation. We found it useful to reduce their effect through background image subtraction. To create the background image one must reconstruct the defect-free plate using exactly the same routine as for the image of interest. Of course, the material and thickness of the defect-free calibration plate should be identical to those of the defective plate.

Reproduced with permission of the copyright owner. Further reproduction prohibited without permission.

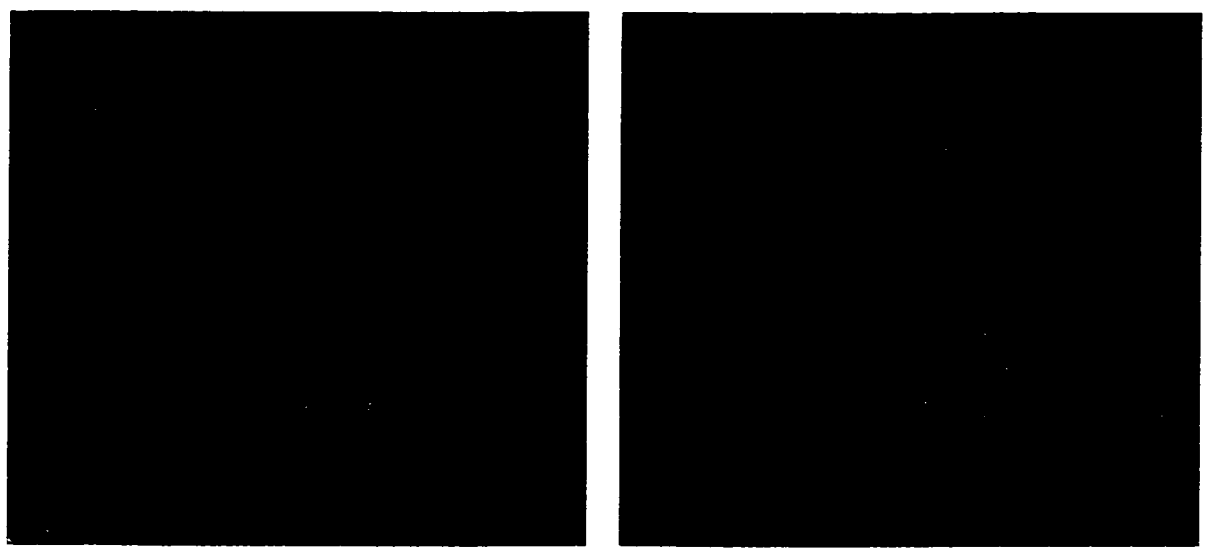

A. Straight rays B. Curved, aver17

Figure 5.18: Straight and bent ray reconstructions of two simulated corrosion pits in aluminum plate with 23 shallow holes in each. Image size: 200 × 200 mm.

Reproduced with permission of the copyright owner. Further reproduction prohibited without permission.

Chapter 6

Conclusions and Future Work

The main motivation for this work was the need for a fully automatic inspection system capable of fast and efficient monitoring of large areas of metal plate and producing high resolution images of hidden defects such as corrosion, cracks, holes, delaminations and other possible kinds of structural damage. Lamb waves were chosen as the information carrier due to the extensive set of properties that make them highly sensitive to all possible plate defects, and the ability to propagate over long distances and thus effectively cover large areas. Tomography was chosen as a faster and a more convenient alternative to a conventional C-scan and other point-inspection methods. More specifically, we decided to use traveltime tomography since arrival time remains the only dependable quantity when coupling problems do not allow for the accurate amplitude measurements.

There currently exist a wide variety of tomographic techniques and image reconstruction algorithms, but not all of them are applicable to our problem. We started this work with a study of the parallel projection and single crosshole techniques de-

Reproduced with permission of the copyright owner. Further reproduction prohibited without permission.

veloped in our lab by McKeon and Hinders.

Lamb wave parallel projection tomography based on the convolution-backprojection reconstruction algorithm and using the Pulsed Phase Lock Loop to determine changes in the phase velocity of the first arrivals, is a fast and complete high-resolution technique capable of accurately imaging defects in plate-like structures. However, certain features make it not fully correspond to our goals. Among such features are:

- Low fill-factor of the imaged area;
- Difficulties with direct interpretation of the reconstructed image data because of the unknown P_2L_2 output;
- Impossibility of the array implementation as a limitation of the parallel projection geometry.

A so called Fan Beam data acquisition geometry seemed to be a promising substitute for the parallel projection scheme. We adapted the convolution-backprojection algorithm to the fan beam geometry and conducted an extensive study of its performance on a number of simulated objects. The study revealed excellent performance and accuracy, and we began experimental testing. Implementation in a circular array of transducers became possible after some changes to the original fan beam reconstruction algorithm. We used a specially designed fan beam scanning apparatus to mimic the behavior of a circular array with a pair of transducers and accomplished a series of test measurements using different techniques to extract arrival time of the fastest mode. However, all attempts to use the P_2L_2 for this purpose failed because a bias of unknown nature was introduced into measured data. The most probable cause

Reproduced with permission of the copyright owner. Further reproduction prohibited without permission.

for this bias is the systematic internal frequency drift that causes Lamb wave velocity to change. At the same time we created a series of time delay estimation software routines and with their help were able to get satisfactory results for individual fan beam projections. Although we could resolve multiple artifacts within separate projections, the convolution-backprojection algorithm tended to produce reconstructions of extremely low quality. Our only successful reconstruction of a single flat bottom hole in the center of the scanned area was possible only after smoothing projection data with a moving average filter. This high sensitivity to the measurement noise was a key issue preventing us from further use of the convolution-backprojection algorithm in combination with a fan beam geometry.

Another issue was the relatively low area coverage of the fan beam geometry. The area most densely covered with rays and thus allowing for the best reconstruction quality turned out to be a rather small circle, which is quite inconvenient for the inspections of large areas. Because of this we didn't think it productive to implement some iterative reconstruction algorithm for fan beam tomography.

After rejection of the Fan Beam and the Parallel Projection data acquisition tomographic schemes based on the convolution-backprojection inversion algorithm we focused our attention on a crosshole geometry used together with Algebraic Reconstruction Technique. After testing the performance of the available single crosshole Lamb wave tomographic equipment we discovered the following reasons for the low quality of the reconstructed images:

1. The computer hardware and driving software were outdated;

2. The algorithms for the accurate time delay estimation did not exist;

Reproduced with permission of the copyright owner. Further reproduction prohibited without permission.

3. A single crosshole projection provided nonuniform ray density and limited local wave vector directivity pattern thus causing poor and nonuniform resolution throughout the image;

4. The sequential ART algorithm created unacceptable levels of the "salt and pepper" noise.

We solved the first problem by upgrading computer hardware and writing faster driving software under Linux Red Hat-5.0 operating system. To solve the third problem we built the multi-projection crosshole scanner which allowed us to increase the ray density and drastically improve the wave vector directivity pattern. The new ART code and all related data processing software were also written to handle increased amounts of data and different projections. After extensive testing of the code on synthetic data sets we observed sufficient improvement in resolution in support of our further actions. To eliminate the "salt and pepper" noise we transformed sequential ART algorithm into the SIRT, which is known for much lower level of artifacts due to simultaneous updating of pixels levels during reconstruction.

The problem of time delay estimation was rather challenging and required a deep insight into the nature and behavior of guided waves. We created several algorithms using time-frequency search, time domain search, pattern matching and group delay estimation methods. Among other promising algorithms we identified those using generalized traveltime concepts, neural network approaches and wavelet transform-based methods. We were able to reach required accuracy with time-frequency and group delay estimation algorithms and left the others for the further research as necessary.

Reproduced with permission of the copyright owner. Further reproduction prohibited without permission.

With all four problems fixed we successfully used the new crosshole scanner and data acquisition software to collect data from two mutually perpendicular crosshole projections, extracted arrival times, and eventually reconstructed a series of images with a straight ray SIRT. The quality of these images was far superior to that from original single crosshole technique based on sequential ART. At this stage, however, we still identified two important problems:

1. Artifacts near the image borders were still severe due to the problems with low ray density and wave vector directivity pattern;

2. The reconstructed defects were always larger and sometimes of different shape than the real ones.

To solve the first problem we decided to measure all six crosshole projections possible for the square array. This required substantial modifications to the existing data processing and reconstruction software. The second problem, we believed, was related to the limitations of the SIRT reconstruction based on the straight ray assumption. To solve it we conducted an extensive study of existing methods in the area of diffraction tomography. We aimed to find a computationally affordable technique which would correct for the diffraction/refraction of Lamb waves on defects and thus provide higher reconstruction quality.

We chose a method based on the assumptions of geometrical acoustics allowing ray paths to bend around defects according to the Fermat's principle of a minimum arrival time. The key portion of this method was the ray tracing algorithm. We found the method based on simulated annealing theory very robust but slow, and resorted

Reproduced with permission of the copyright owner. Further reproduction prohibited without permission.

to a faster shooting method instead. Then we adapted our SIRT algorithm to handle bent rays and created an iterative image reconstruction technique that accepts the output of a straight ray SIRT as a starting velocity model and sequentially updates it through tracing ray paths and running the bent ray SIRT.

The new procedure was tested on the aluminum plate samples with machined thinnings and through holes, and the results were compared to those obtained with a straight ray approach. We found that success of the ray tracing approach strongly depends on the degree of smoothing of the image reconstructed with a straight ray SIRT. Changing this degree affects the size of the reconstructed defects and it is possible to find optimal smoothing conditions when defect dimensions will be reconstructed correctly. The size of defects can be initially estimated from a straight ray reconstruction. The appropriate degree of smoothing can then be chosen depending on the estimated size. This is an important step towards maximizing the resolution of the Lamb wave tomography. At the same time ray bending always distorts the uniformity of the ray density and introduces additional artifacts into the final image. This distortion, however, is proportional to the size and severity of the defect. It does not occur for smaller defects and can be minimized even for larger ones by sufficient smoothing of the input image.

The six projection crosshole geometry seems to be the best among the family of crosshole data acquisition schemes on a square array. Its high and uniform ray density plus broad local wave vector directivity pattern throughout the scanned area insure satisfactory resolution over the entire image. In addition, this geometry has the highest possible fill-factor of 100% and the reconstructed area is a square coincident

Reproduced with permission of the copyright owner. Further reproduction prohibited without permission.

with the transducer array

All tomographic reconstruction methods produce geometry-related regular artifact patterns that complicate data interpretation. We found it useful to reduce their level through the background image subtraction. To create the background image one must reconstruct the defect-free calibration plate using exactly the same routine as for the image of interest. Of course, the material and thickness of the defect-free plate should be identical to those of the defective plate.

This work resulted in identification and development of a Lamb wave tomographic technique that:

1. Is based on the noise-insensitive SIRT reconstruction algorithm;
2. Has all its measurement hardware inside the PC box;
3. Provides high quality velocity maps represented as images;
4. Can improve its resolution by means of diffraction tomography;
5. Can be implemented as a multiplexed array of transducers;
6. Has the highest possible area fill-factor;
7. Automatically extracts group arrival times of the fastest mode;
8. Can produce acceptable results in a near-real-time mode.

The future work may involve additional search for the efficient time delay estimation algorithm, better understanding of the reconstructed velocity values within defects, selection and work with higher order modes, smoothing and error correction

Reproduced with permission of the copyright owner. Further reproduction prohibited without permission.

in data, optional employment of various diffraction tomography algorithms, building square perimeter array of transducers with embedded multiplexing electronics, transforming existing software into a fully autonomous expert system package, and further improvement of the existing reconstruction algorithms. The real-time performance of highly parallel ray tracing algorithms can be achieved even with moderate-speed computers via parallel processor networks [102]. It is also possible to significantly speed up [85] or completely bypass [103–105] the time-consuming ray tracing procedure using alternative techniques.

Another direction for future research is finding the inversion algorithm superior to the algebraic technique. The latter is a local optimization technique requiring a good starting model and optimizing the result in the mean square sense which is a rather rough measure of accuracy. A global optimization technique based on the concept of simulated annealing, proposed by Weber [106] was reported to be a very robust and stable method suitable for almost any type of inversion problems and capable of outperforming SIRT - the most popular reconstruction technique today.

Reproduced with permission of the copyright owner. Further reproduction prohibited without permission.

Bibliography

[1] DC National Transportation Safety Board, Washington. *Aircraft accident report: Aloha Airlines, Flight 243, Boeing 737-200, N73711, Near Maui, Hawaii, April 28, 1988.* U.S. Department of Commerce, NTTS, 1989.

[2] J. Krautkramer and H. Krautkramer. *Ultrasonic Testing of Materials, 4th edition.* Springer-Verlag, 1990.

[3] J.C.P. McKeon. *Tomography applied to Lamb wave contact scanning nondestructive evaluation.* Ph.D. in Applied Science Thesis, College of William and Mary, Williamsburg, VA, U.S.A., 1998.

[4] I.A. Viktorov. *Rayleigh and Lamb Waves: physical theory and applications.* Plenum Press, New York, 1967.

[5] J.D.Achenbach. *Wave propagation in elastic solids.* North-Holland, Netherlands, 1984.

[6] K.E.Graff. *Wave Motion in Elastic Solids.* Dover, New York, 1991.

[7] L.Brekhovskikh and V.Goncharov. *Mechanics of Continua and Wave Dynamics.* Springer-Verlag, New York, 1994.

Reproduced with permission of the copyright owner. Further reproduction prohibited without permission.

[8] V.T.Grinchenko and V.V.Meleshko. *Garmonicheskie kolebania i volny v uprugih telah.* Naukova Dumka, Kiev, Ukraine, 1981.

[9] J.L.Rose. *Ultrasonic Waves in Solid Media.* Cambridge University Press, Cambridge, U.K., 1999.

[10] B.A. Auld. *Acoustic Fields and Waves in Solids.* Kreiger, Malabar, Fl, 1990.

[11] J.D. Achenbach. Lamb waves as thickness vibrations superimposed on a membrane carrier wave. *Journal of the Acoustical Society of America*, 103(5):2283–2286, 1998.

[12] I. Nunez, R.K. Ing, C. Negreira, and M. Fink. Transfer and green functions based on modal analysis for lamb waves generation. *Journal of the Acoustical Society of America*, 107(5):2370–2378, 2000.

[13] Y. Bar-Cohen, Z. Chang, and A. Mal. Characterization of defects in composite material using rapidly acquired leaky lamb wave dispersion data. *NDT.net*, 3(9):online article, 1998.

[14] W. Zhu and J.L. Rose. Lamb wave generation and reception with time-delay periodic linear arrays: a bem simulation and experimental study. *IEEE Transactions on Ultrasonics, Ferroelectrics, and Frequency Control*, 46(3):654–664, 1999.

[15] J.L. Rose. Guided wave nuances for ultrasonic nondestructive evaluation. *IEEE Transactions on Ultrasonics, Ferroelectrics, and Frequency Control*, 47(3):575–583, 2000.

[16] T.Demol, P. Blanquet, and C. Delebarre. Lamb waves generation using a flat

Reproduced with permission of the copyright owner. Further reproduction prohibited without permission.

multi-element array device. In *IEEE Ultrasonics Symposium*, pages 791–794, 1995.

[17] L.F. Degertekin, B.V. Honein, and B.T. Khuri-Yakub. Efficient excitation and detection of lamb waves for process monitoring and nde. *IEEE Ultrasonics Symposium*, 6:787–790, 1995.

[18] J. Pei, M.I. Yousuf, F.L. Degertekin, B.V. Honein, and B.T. Khuri-Yakub. Lamb wave tomography and its application in pipe erosion/corrosion monitoring. In *IEEE Ultrasonics Symposium*, pages 795–798, 1995.

[19] J.Pei, M.I.Yousuf, F.L.Degertekin, B.V. Honein, and B.T. Khuri-Yakub. Plate tomography with dry contact lamb wave trasducers. *Acoustical Imaging*, 22:725–730, 1996.

[20] B.P. Hildebrand, T.J. Davis, G.J. Posakony, and J.C. Spanner. Lamb wave tomography for imaging erosion/corrosion in piping. *Review of Progress in QNDE*, 18:967, 1999.

[21] J.O. Strycek, W.A. Grandia, and H. Loertscher. Wave modes produced by air coupled ultrasound. *NDT.net*, 2(5):online article, 1997.

[22] D.E. Bray and R.K. Stanley. *Nondestructive Evaluation. A tool in design, manufacturing and service. Revised edition.* CRC Press, 1997.

[23] C.B. Scruby and L.E. Drain. *Laser Ultrasonics : Techniques and Applications.* Adam Hilger, 1990.

[24] A. Friedman. *Theoretical and experimental study of generation mechanisms for laser ultrasound in woven graphite/epoxy composites with translaminar*

Reproduced with permission of the copyright owner. Further reproduction prohibited without permission.

stitching. Ph.D. in Applied Science Thesis, College of William and Mary, Williamsburg, VA, U.S.A., 2000.

[25] H. Tretout. Review of advanced ultrasonic techniques for aerospace structures. *NDT.net*, 3(9):Online article, 1998.

[26] W.Zhu, J.L. Rose, J.N. Barshinger, and V.S. Agarwala. Ultrasonic guided wave ndt for hidden corrosion detection. *Research in Nondestructive Evaluation*, 10:205–225, 1998.

[27] A. Chahbaz, V. Mustafa, and D. Hay. Corrosion detection in aircraft structures using guided waves. *NDT.net*, 1(11):online article, 1996.

[28] K.J. Sun and P.H. Johnson. Disbond detection in bonded aluminum joints using lamb wave amplitude and time-of-flight. *Rev. Prog. in QNDE*, 13:1507–1514, 1994.

[29] W.H. Prosser and M.D. Seale. Time-frequency analysis of the dispersion of lamb modes. *Journal of the Acoustical Society of America*, 105(5):2669–2675, 1999.

[30] M.D. Seale and E.I. Madaras. Lamb wave stiffness characterization of composites undergoing thermal-mechanical aging. *Review of progress in QNDE*, 18(B):1233–1240, 1999.

[31] V. Mustafa, A. Chahbaz, D.R Hay, M. Brassard, and S. Dubois. Imaging of disbond in adhesive joints with lamb waves. *NDT.net*, 2(3):online article, 1997.

Reproduced with permission of the copyright owner. Further reproduction prohibited without permission.

[32] M.D. Seale and B.T. Smith. Lamb wave propagation in thermally damaged composites. *Review of progress in QNDE*, 15:261, 1996.

[33] J.C.P. McKeon and M.K. Hinders. Lamb wave scattering from a through hole. *Journal of Sound and Vibration*, 224(5):1999, 843-862.

[34] T. Liu, W. Karunasena, S. Kitipornchai, and M. Veidt. The influence of backward wave transmission on quantitative ultrasonic evaluation usin lamb wave propagation. *Journal of the Acoustical Society of America*, 107(1):306–314, 2000.

[35] R. Murayama. Nondestructive evaluation of formability in thin steel sheets using fundamental lamb wave. *Nondestructive Testing and Evaluation International*, 33:245–251, 2000.

[36] R. Murayama. Study of driving mechanism on electromagnetic acoustic transducer for lamb wave using magnetostrictive effect and application in drawability evaluation of thin steel sheets. *Ultrasonics*, 37:31–38, 1999.

[37] K.L. Telschow, V.A. Deason, R.S. Schley, and S.M. Watson. Direct imaging of traveling lamb waves using photorefractive dynamic holography. *Journal of the Acoustical Society of America*, 106(5):2578–2587, 1999.

[38] F.Natterer. *The Mathematics of Computerized Tomography.* Wiley, New York.

[39] S.Webb. *The physics of medical imaging.* IOP Publishing Ltd, 1988.

[40] N.D. Bregman, R.C. Bailey, and C.H. Chapman. Crosshole seismic tomography. *Geophysics*, 54(2):200–215, 1989.

[41] R.G. Pratt and N.R. Goulty. Combining wave-equation imaging with traveltime

Reproduced with permission of the copyright owner. Further reproduction prohibited without permission.

tomography to form high resolution images from crosshole data. *Geophysics*, 56(2):208–224, 1991.

[42] T.A. Dickens and G.A. Winbow. Spatial resolution of diffraction tomography. *Journal of the Acoustical Society of America*, 101(1):77–86, 1997.

[43] T.J. Gomm and J.A. Mauseth. State of the technology: Ultrasonic tomography. *Materials Evaluation*, July:747–752, 1999.

[44] W. Mao and G.W. Stuart. Transmission-reflection tomography: application to reverse vsp data. *Geophysics*, 62(3):884–894, 1997.

[45] I.D. Hall, A. McNab, and G. Hayward. Improved ultrasonic image generation through tomographic image fusion. *Ultrasonics*, 37:433–443, 1999.

[46] M.K.Hinders and J.C.P.McKeon. Lamb wave tomography for corrosion mapping. In *2nd joint NASA/FAA/DoD Conference on Aging Aircraft*, 1998.

[47] M.K.Hinders, E.V.Malyarenko, and J.C.P.McKeon. Contact scanning lamb wave tomography. *Journal of the Acoustical Society of America*, 104(3, part 2):1790, 1998.

[48] J.C.P.McKeon and M.K.Hinders. Parallel projection and crosshole lamb wave contact scanning tomography. *Journal of the Acoustical Society of America*, 106(5):2568–2577, 1999.

[49] M.Tohyama and T.Koike. *Fundamentals of Acoustic Signal Processing*. Academic Press, CA, U.S.A.

[50] H.Medwin and C.S.Clay. *Fundamentals of Acoustical Oceanography*. Academic Press, U.S.A.

Reproduced with permission of the copyright owner. Further reproduction prohibited without permission.

[51] R. Kumaresan and A. Rao. Model-based approach to envelope and positive instantaneous frequency estimation of signals with speech applications. *Journal of the Acoustical Society of America*, 105(3):1912–1924, 1999.

[52] M.T. Taner and F. Koehler. Estimation of unbiased delays. *Geophysics*, 63(2):738–742, 1998.

[53] X. Lin. *Numerical computation of stress waves in solids.* Akademie Verlag, Berlin, 1996.

[54] J. Pan and J.B. Wang. Acoustical wave propagator. *Journal of the Acoustical Society of America*, 108(2):481–487, 2000.

[55] K.R.Leonard. *Neural Network Technology and Lamb Wave Tomography.* BS in Applied Science Thesis, College of William and Mary, Williamsburg, VA, U.S.A., 1999.

[56] L.Cohen. *Time-Frequency Analysis.* Prentice Hall, New Jersey, U.S.A., 1995.

[57] X.L. Xu, A.H. Tewfik, and J.F. Greenleaf. Time delay estimation using wavelet transform for pulsed-wave ultrasound. *Annals of Biomedical Imaging*, 23:612–621, 1995.

[58] J.B. Han, J.C. Cheng, T.H. Wang, and Y. Berthelot. Mode analyses of laser-generated transient ultrasonic lamb waveforms in a composite plate by wavelet transform. *Materials Evaluation*, August:837–840, 1999.

[59] S. Legendre, D. Massicotte, J. Goyette, and T. Bose. Wavelet-transform-based method of analysis for lamb wave ultrasonic nde signals. *IEEE Transactions on Instrumentation and Measurement*, 49(3):524–530, 2000.

Reproduced with permission of the copyright owner. Further reproduction prohibited without permission.

[60] G.Herman. Generalization of traveltime inversion. *Geophysics*, 57(1):9–14, 1992.

[61] J.C.M. Goudswaard, F.P.E. ten Kroode, R.K. Snieder, and A.R. Verdel. Detection of lateral velocity contrasts by crosswell traveltime tomography. *Geophysics*, 63(2):523–533, 1998.

[62] F.Ernst and G.Herman. Tomography of dispersive media. *Journal of the Acoustical Society of America*, 108(1):105–116, 2000.

[63] F. Natterer. Sampling in fan beam tomography. *SIAM Journal of Applied Mathematics*, 53(2):358–380, 1993.

[64] A.C. Kak and M. Slaney. *Principles of Computerized Tomographic Imaging.* IEEE Inc., New York, 1988.

[65] A.H. Andersen and A.C. Kak. Digital ray tracing in two-dimensional refractive fields. *J. Acoust. Soc. Am.*, 72(5):1593–1606, 1982.

[66] Y.Q. Wang and R.A. Kline. Ray tracing in isotropic and anisotropic materials: Application to tomographic image reconstruction. *J. Acoust. Soc. Am.*, 95(5):2525–2532, 1994.

[67] L.-J. Gelius, I. Johansen, N. Sponheim, and J.J. Stamnes. A generalized diffraction tomography algorithm. *Journal of the Acoustical Society of America*, 89(2):523–528, 1991.

[68] L.-J. Gelius. Generalized acoustic diffraction tomography. *Geophysical Prospecting*, 43:3–29, 1995.

Reproduced with permission of the copyright owner. Further reproduction prohibited without permission.

[69] D.M. Pai. Crosshole seismics using vertical eigenstates. *Geophysics*, 55(7):815–820, 1990.

[70] T.A. Dickens. Diffraction tomography for crosswell imaging of nearly layered media. *Geophysics*, 59(5):694–706, 1994.

[71] K.T. Ladas and A.J. Devaney. Generalized art algorithm for diffraction tomography. *Inverse Problems*, 7:109–125, 1991.

[72] K.T. Ladas and A.J. Devaney. Application of an art algorithm in an experimental study of ultrasonic diffraction tomography. *Ultrasonic Imaging*, 15:48–58, 1993.

[73] M. Almqvist, A. Holm, T. Jansson, H.W. Persson, and K. Lindstrom. High resolution light diffraction tomography: nearfield measurements of 10 mhz continuous wave ultrasound. *Ultrasonics*, 37:343–353, 1999.

[74] B. Chen and J.J. Stamnes. Validity of diffraction tomography based on the first born and the first rytov approximations. *Applied Optics*, 37(14):2996–3006, 1998.

[75] T.D. Mast, A.I. Nachman, D.L. Liu, , and R.C. Waag. Quantitative imaging with eigenfunctions of the scattering operator. *Proceedings of the IEEE Ultrasonics Symposium*, 2:1507–1510, 1997.

[76] T.D. Mast, A.I. Nachman, and R.C. Waag. Focusing and imaging using eigenfunctions of the scattering operator. *Journal of the Acoustical Society of America*, 102(2):715–725, 1997.

[77] D.T. Mast. Wideband quantitative ultrasonic imaging by time-domain diffrac-

Reproduced with permission of the copyright owner. Further reproduction prohibited without permission.

tion tomography. *Journal of the Acoustical Society of America*, 106(6):3061–3071, 1999.

[78] S. Delamare, J.-P. Lefebvre, and A. Wirgin. Ghosts in the born images of a layer probed by acoustic waves. *Ultrasonics*, 37:633–643, 2000.

[79] A. Tsihrintzis and A.J. Devaney. Higher-order (nonlinear) diffraction tomography: reconstruction algorithms and computer simulation. *IEEE Transactions on Image Processing*, 9(9):1560–1572, 2000.

[80] A.H. Andersen. Ray tracing for reconstructive tomography in the presence of object discontinuity boundaries: A comparative analysis of recursive schemes. *Journal of the Acoustical Society of America*, 89(2):574–582, 1991.

[81] F.B. Jensen, W.A. Kuperman, M.B. Porter, and H. Schmidt. *Computational Ocean Acoustics*. AIP Press, New York, 1994.

[82] R.J. Lytle and K.A. Dines. Iterative ray tracing between boreholes for underground image reconstruction. *IEEE Trans. Geosci. Remote Sensing*, GE-18(3):234–240, 1980.

[83] T. Hayashi and S. Endoh. Calculation and visualization of lamb wave motion. *Ultrasonics*, 38:770–773, 2000.

[84] C.H. Chapman. Ray theory and its extensions: Wkbj and maslow seismograms. *Journal of Geophysics*, 58:27–43, 1985.

[85] A.H. Andersen. Ray linking for computed tomography by rebinning of projection data. *J. Acoust. Soc. Am.*, 84(4):1190–1192, 1987.

[86] S.K. Nath, S.K. Singh, A. Pani, and S. Sengupta. Cross-hole tomographic

Reproduced with permission of the copyright owner. Further reproduction prohibited without permission.

velocity estimation by rey tracing and back projection methods. *Indian Journal of Geology*, 67(4):263–272, 1995.

[87] A.L. Vesnaver. Ray tracing based on fermat's principle in irregular grids. *Geophysical Prospecting*, 44:741–760, 1996.

[88] A.L. Vesnaver. Irregular grids in seismic tomography and minimum-time ray tracing. *Geophysical Journal International*, 126:147–165, 1996.

[89] R.T. Coates and C.H. Chapman. Ray perturbation theory and the born approximation. *Geophysical Journal International*, 100:379–392, 1990.

[90] R. Sneider and M. Sambridge. The ambiguity in ray perturbation theory. *Journal of Geophysical research*, 98(B12):20,021–20,034, 1993.

[91] P.R. Saastamoinen. Construction of algorithms for optimal fermat ray tracing. *Geophysica*, 30(1-2):31–40, 1994.

[92] J. Pulliam and R. Sneider. Ray perturbation theory, dynamic ray tracing and the determination of fresnel zones. *Geophysical Journal International*, 135:463–469, 1998.

[93] J. Pulliam and R. Sneider. Fast, efficient calculation of rays and travel times with ray perturbation theory. *Journal of the Acoustical Society of America*, 99(1):383–391, 1996.

[94] D.P. Jansen, D.A. Hutchins, P.J. Ungar, and R.P. Young. Acoustic tomography in solids using a bent ray sirt algorithm. *Nondestr. Test. Eval.*, 6:131–148, 1991.

Reproduced with permission of the copyright owner. Further reproduction prohibited without permission.

[95] D.R. Velis and T.J. Ulrych. Simulated annealing two-point ray tracing. *Geophysical Research Letters*, 23(2):201–204, 1996.

[96] L. Ingber. Very fast simulated re-annealing. *Math. Comput. Modeling*, 12(8):967–973, 1989.

[97] Harvey Gould and Jan Tobochnik. *Introduction to Computer Simulation Methods Applications to Physical Systems, second edition.* Addison-Wesley, 1996.

[98] L. Ingber. Simulated annealing: Practice versus theory. *Math. Comput. Modeling*, 18(11):29–57, 1993.

[99] W.H. Press et al. *Numerical Recipes in Fortran: The Art of Scientific Computing.* Cambridge University Press, 1992.

[100] E.V. Malyarenko and M.K. Hinders. Fan beam and double crosshole lamb wave tomography for mapping flaws in aging aircraft structures. *Journal of the Acoustical Society of America*, 108(4):1631–1639, 2000.

[101] R.A. Kline and Y.Q. Wang. A technique for ultrasonic tomography in anisotropic media. *J. Acoust. Soc. Am.*, 91(2):878–884, 1992.

[102] M. Yang, H.I. Schlaberg, B.S. Hoyle, M.S. Beck, and C. Lenn. Parallel image reconstruction in real-time ultrasound process tomography for two-phased flow measurements. *Real-Time Imaging*, 3:295–303, 1997.

[103] L. Lines B. Du. Crosswell seismic tomography without ray tracing. *Exploration Geophysics*, 31:359–365, 2000.

[104] S.A. Enright, S.M. Dale, V.A. Smith, R.D. Murch, and R.H.T. Bates. Towards solwing the bent-ray tomographic problem. *Inverse Problems*, 8:83–94, 1992.

Reproduced with permission of the copyright owner. Further reproduction prohibited without permission.

[105] P.O. Ecoublet, S.C. Singh, G.M. Jackson, and C.H. Chapman. Seismic tomography and migration without ray tracing. *SPIE*, 2571:87–96, 1995.

[106] Z. Weber. Seismic traveltime tomography: a simulated annealing approach. *Physics of the Earth and Planetary Interiors*, 119:149–159, 2000.

Reproduced with permission of the copyright owner. Further reproduction prohibited without permission.

Vita

Eugene Malyarenko was born on January 8, 1969 in Poltava, Ukraine. He attended High School 171 in Kiev, Ukraine, and graduated with Honors in 1985. In 1988 he completed four semester course work in the Department of General and Applied Physics, Moscow Institute of Physics and Technology, and then served in the Soviet Army for two years 1988-1990. During the period 1990-1994 he continued education in the Physics Department of Kiev National University, Ukraine, and graduated with diploma of physicist, teacher. After graduation he worked as a Research Assistant in the Acoustics track of the Physics Department, studying properties of backward Lamb waves in isotropic and piezoelectric plates. In 1995 he started working as a fire-technical expert in the Forensic Research Center, Ukrainian Ministry of Interior, being also a part-time graduate student in the Physics Department of Kiev University. In 1997 Eugene became a full-time graduate student in the Department of Applied Science, College of William & Mary, U.S.A., and earned Ph.D. degree in Applied Physics in October, 2000.

Reproduced with permission of the copyright owner. Further reproduction prohibited without permission.